Development of sol-gel derived bioactive glass-ceramics for bone regeneration and hyperthermia applications

A thesis submitted in partial fulfillment of the requirement for the award of the degree of

Doctor of Philosophy in Physics

By

Nitu

Under the supervision of

Prof. A. Srinivasan

Department of Physics

Indian Institute of Technology Guwahati

Guwahati – 781039, India

June 2024

Dedicated to

my parents

Declaration statement

I, Nitu, hereby declare that the research work presented in the thesis, entitled "**Development of sol-gel derived bioactive glass-ceramics for bone regeneration and hyperthermia applications**" has been carried out by me under the supervision of Prof. A. Srinivasan, at the Department of Physics, Indian Institute of Technology Guwahati. I further confirm that no part of this work has been submitted elsewhere for the award of any other degree/diploma or any other academic award.

June 24th 2024

Nitu

Roll No.: 176121023

Department of Physics

Indian Institute of Technology Guwahati

Guwahati – 781039, India

Certificate

It is certified that the work contained in the thesis entitled "**Development of sol-gel derived bioactive glass-ceramics for bone regeneration and hyperthermia applications**" submitted by Nitu (Roll No. 176121023), a Ph D student of the Department of Physics, Indian Institute of Technology Guwahati for the award of the degree of Doctor of Philosophy has been carried out under the supervision of Prof. A. Srinivasan. This work has not been submitted elsewhere for the award of any degree.

June 24th 2024

Prof. A. Srinivasan

Professor

Department of Physics

Indian Institute of Technology Guwahati

Guwahati – 781039, India

Acknowledgments

As I reflect on this significant milestone, I am overwhelmed with gratitude for all the individuals who have played a pivotal role in my journey.

First and foremost, I extend my deepest appreciation to my supervisor, Prof. A. Srinivasan. His mentorship has not only nurtured my intellectual curiosity but also cultivated a culture of discussion and debate on diverse topics, which was instrumental in developing my scientific mindset. His insightful advice, innovative ideas, and broad vision have profoundly expanded my understanding. His vision and guidance transformed me from a Ph.D. scholar into an independent researcher, providing me with the liberty to explore my work unconditionally.

I am profoundly grateful to my doctoral committee members, Prof. Sunil K. Khijwania, Prof. D. Pamu, and Prof. S. Kanagraj, for their continuous academic guidance and meticulous monitoring of my research progress. Their instructive comments and feedback significantly enhanced the quality of my thesis and illuminated the path toward my research objectives.

I extend my heartfelt thanks to the current and former Heads of the Department of Physics for their substantial administrative support and for granting me unrestricted access to all the departmental resources.

My appreciation extends to the Department of Physics (including the facility acquired under the Department of Science and Technology, Government of India for project no: SR/FST/PSII-037/2016), the Central Instrument Facility (CIF), the Centre for Environment, and other departments of the Indian Institute of Technology Guwahati. Their provision of sample preparation, characterization, and research facilities was invaluable to my work.

I am deeply thankful to my collaborators, Prof. L.M. Pandey and R. Foapse, for their assistance in collecting and analyzing cell culture data. Additionally, I extend my gratitude to Dr. J.P. Borah, P. Seal, K. Hazarika, and J. Molongnela for their support in collecting induction heating measurements data, which significantly enriched my research.

I am immensely grateful to Dr. Sidananda Sarma for his consistent support throughout various stages of my Ph.D. journey. I also thank Mr. Aditya Kalita and Dr. Arnab Kumar Das for upskilling me in operating X-ray diffractometer, electrospinning, and other equipment. Furthermore, I appreciate Dr. Sidananda Sarma, Mr. Aditya Kalita, Mr. Chandan Borgohain, Dr. Kula Kamal Senapati, Dr. Kh. Kesho Singh, Mr. Sujit Kumar Deb, A. Malakar, and Dr. Dolly Gogoi for allowing me to use the XRD, VSM, SEM, TEM, BET, ESR, and other instruments whenever required, even at odd hours. My thanks also go to the non-teaching staff of the Department of Physics and the IIT campus for their kind assistance in various ways. The technical support from Mr. Bhaskar, Mr. Kishor, Mr. Milan, Mr. Rupak, and other instrument operators was instrumental in performing measurements under the desired conditions. Special thanks to Dinesh and Alok for their efforts in EDS and TEM measurements, even at odd hours.

I am indebted to my seniors, Dr. Arnab Kumar Das, Dr. Rajkumar Modak, Dr. Aneeta Manjari Padhan, and Dr. Dolly Taparia, who enriched me with their valuable inputs in the research field even during their short time on campus. I also acknowledge my amazing school-time instructor, the late Shivtaj Singh Sir, whose captivating teaching guided me to where I am today.

I am extremely fortunate to have had a wonderful lab group that provided a comfortable and stress-free working environment. I take this opportunity to thank Amritava Bhaiya, Sunil Bhaiya, Manisha, Subrata, Pushpesh, Alok, Madhav, Dev, Didwmsha, Debraj, Dinesh, Aritra, Harekrushna, Sourav, Tandrima, Nidhi, Praduman, Pratibha, Abul, Abhinath, and Franky.

Their homely care and selfless assistance in both research and personal matters are priceless. They have been companions in my joys and sorrows, making me feel like part of a family. I began my journey with Manisha as a labmate and am concluding it having gained a best friend. She assisted me with sample preparation and taught me how to use the VSM instrument. She was always available to help, both personally and academically, whenever I needed her. I am deeply grateful to Debraj for upskilling me with the TEM analysis, which will undoubtedly help me throughout my research career. I am indebted to my grandparents for their valuable teachings during my childhood, which have greatly helped me complete this journey. I am deeply thankful to my father-in-law and mother-in-law for their wholehearted blessings, care, and trust in me, which made me strong. I am blessed to have a loving and understanding family, which made it easier for me to balance research and personal life. I am eternally grateful to my entire family, who have always been a constant source of happiness. Special thanks to Shantanu ji, whose unwavering belief in me carried me forward. He always stood by my side and backed me in every possible way, sustaining me through the challenges and obstacles along the way. He always encouraged and inspired me to follow my dreams. Words are not enough to express my profound emotions for his togetherness. Vikrant, my younger brother, has always been a source of motivation for me throughout this journey.

Finally, I express my heartfelt gratitude to everyone who has assisted me directly or indirectly in any way and helped me reach this milestone. For those I may have inadvertently skipped, I thank you all for enabling me to achieve this accomplishment.

Nitu

Preface

Developments in bioglass and glass-ceramics are extending patients' lifespans by regenerating damaged or diseased organs or replacing them with implants through tissue engineering applications. Bulk 45S5 bioglass has been used for small bone regeneration due to its exceptional bioactivity. Even after 50 years of its invention, 45S5 bioglass remains the preferred composition for bone regeneration, particularly for soft tissue applications. However, sustaining the vitreous state in sol-gel derived 45S5 nanopowders has posed a challenge. The possibility of achieving enhanced surface properties in 45S5 nanopowders is a strong motivation to tackle this problem. A systematic investigation is needed to (a) determine the threshold amount of Na_2O that can sustain a vitreous state in SiO_2-CaO-Na_2O-P_2O_5 system and to (b) assess role of atomic structure and Na_2O content on the bioactivity of this ceramic system. It is relevant to point out here that 45S5 glass-ceramic with a combeite crystal phase is recognized as a biodegradable bone regenerative material. Additionally, magnetic hyperthermia (MH) treatment is gaining prominence for addressing deep rooted malignant cells while preserving the health of adjacent normal cells. An efficient thermoseed, which is basically a magnetic glass-ceramic with optimum magnetic and bioactive properties is required for this application. Although various magnetic bioactive glasses and glass-ceramics have been explored in the past, none of them are based on the 45S5 composition in nanopowder form. Hence, this work attempts to fill a significant gap in the field of magnetic bioglass-ceramics based on the 45S5 composition. The strategy followed and the results achieved are briefly summarised below.

To address the vitreous state issue associated with the Na_2O content in 45S5 ceramic, a sol-gel synthesis route was developed to synthesize (69.5-x)SiO_2-CaO-P_2O_5-xNa_2O ($0 \leq x \leq$ 24.5 wt.%) ceramic nanopowders. The maximum Na_2O concentration that can maintain the vitreous state was found through controlled heat treatment of sol-gel-derived nanopowders. The

impact of devitrification on the bioactive properties of these compositions was also studied. The thermal stability of the vitreous bioglass-ceramic was studied as a function of x (Na_2O wt.%). Upon confirming that the vitreous state could not be achieved with the full Na_2O content in the 45S5 composition through the sol-gel route, the focus of this thesis research shifted to glass-ceramics with 45S5 composition (since preserving the high bioactivity of this ceramic is more important than maintaining the vitreous state).

Next, to develop an efficient thermoseed, iron oxide was introduced in 45S5 glass-ceramics by replacing SiO_2. It was observed that iron oxide-substituted 45S5 glass-ceramic turned toxic to osteoblast cells when its iron oxide content exceeded 10 wt.%. Since iron oxide was introduced in the sol-gel process through a precursor ($Fe(NO_3)_3$. $9H_2O$), its magnetic properties were limited by the presence of the weakly magnetic hematite (Fe_2O_3) along with the strongly magnetic magnetite (Fe_3O_4). In order to improve the magnetic proprieties, MNP were directly introduced in the sol-gel process to yield MNP-substituted 45S5 glass-ceramics. With appropriate heat treatment, the magnetite to hematite conversion was prevented. This led to MNP-substituted 45S5 glass-ceramics with better induction heating capacity and similar bioactivity as the iron oxide-substituted 45S5 glass-ceramics. However, the 10 wt.% iron oxide cytotoxicity limit persisted in the MNP-substituted 45S5 glass-ceramics too. To improve the magnetic characteristics further without diminishing bioactive properties, an 8 wt.% MNP substitution for different oxide constituents of 45S5 composition was attempted. The best combination of magnetic induction heating and bioactive properties emerged when MNP was substituted for the glass modifier CaO in the 45S5 glass-ceramics. Heat treatment of the as-synthesized MNP-substituted 45S5 bioglass-ceramic nanopowders played a crucial role in balancing its magnetic and bioactive properties. Therefore, a systematic heat treatment was performed to identify the processing conditions which yields the best thermoseed from MNP-substituted (for CaO) 45S5 glass-ceramics.

Apart from addressing the Na_2O content versus vitreous state issue in 45S5 nanopowders, an MNP-substituted 45S5 glass-ceramic whose performance far superior to that of commercially available thermoseed fluid, FluidMag-CT has been demonstrated in this thesis work. Several new insights on the sol-gel derived 45S5 ceramics including their processing conditions and the role of various magnetic and non-magnetic crystalline phases in these bioglass-ceramics have also emerged from this work.

Table of Contents

Chapter 1

Introduction

Evidence of implanted materials such as sutures made from animal sinew, low reactive metals such as gold, silver and wood, have been found in ancient Chinese and Egyptian civilizations [NIH0]. This demonstrates an early awareness of using substances that exhibited minimal reactivity within the body. These historical examples have laid the foundation to the contemporary concept of biomaterials. The term "biomaterial" is derived from "bio" and "material," indicating a biological material. Although these materials have been utilized since ancient times, they have not been commonly used in clinical trials until the 1860s. It was during this period that Lister invented a surgical technique involving biomaterials [LIST1867]. Much later, the European Society of Biomaterials defined a biomaterial as a nonviable material used in medical devices, intended to interact with the biological system [WILL1986]. In the modern times, biomaterials are defined as substances employed to create devices that can safely, reliably, economically, and physiologically replace or augment a specific part or function of the body. Biomaterials can be synthetic or natural materials [NIH02017]. They have the tendency to function like the tissues that they replace. These biomaterials mostly work by enhancing, repairing, or restoring the functions of the tissue they are intended to replace [CHON2023]. They function either by replacing the body component completely or by providing mere support. Various materials including metals, ceramics, composites, and polymers are drawing the attention of researchers for their properties that can be exploited in making biocompatible biomaterials [BOSE2018].

Biomaterials can be classified as bioinert, porous, bioactive and bioresorbable [AGRA2023]. Table 1.01 lists their characteristics.

Table 1.01: Classification of biomaterials on the basis of tissue attachment [HENC1991].

Type of implant	Type of attachment	Example
Nearly inert	Mechanical interlock (morphological fixation)	Metals, alumina, zirconia, and polyethylene
Porous	In growth of tissues into pores (biological fixation)	Hydroxyapatite (HAp) coated porous metals
Bioactive	Interfacial bonding with tissues (bioactive fixation)	Bioactive glasses, bioactive glass-ceramics and HAp
Resorbable	Replacement with tissues (bioabsorbable fixation)	Tricalcium phosphate and polylactic acid

Bioinert biomaterials exhibit no response or minimal interaction with the body when inserted, such as those composed of titanium, zirconium, ultra-high molecular weight polyethylene, and stainless steel [RAO02022]. These materials are utilized when minimal interaction with the body is desired. Porous materials are characterized by pores typically larger than 10 μm, enabling biological fixation since the bone can grow into these pores [JIAN2020]. The increased surface area resulting from these pores enhances the implant's integration with the body, facilitating strong fixation. However, their mechanical strength is lower than the nonporous bulk materials [HUO02020, LIU02020, YANG2020], rendering them unsuitable for long-term implantation where high mechanical strength is crucial. Nonetheless, they find application in specific contexts where mechanical strength is not a concern. Bioresorbable materials like calcium oxide and polylactic-polyglycolic copolymers, dissolve in the body fluid and are removed from the body within a designed time period, [PRAK2017, MCKE2021]. However, balancing the resorption rate with cellular metabolism poses a significant challenge in practical applications of these biomaterials [GROO1983]. On the other hand, bioactive biomaterials evoke ion-exchanges with the body fluids surrounding the material, leading to the formation of a carbonate apatite layer on their surface [RAO02022]. The surface layer of this implant is physiologically active and resembles the mineral phase of human bone. Examples

of bioactive materials include bioactive glasses, bioactive glass-ceramics, and HAp [ASTH2014, BANS2023].

1.1. Bioactive Materials

Hench's criteria for the evolution of bioactivity help in classifying bioactive materials into categories, viz., Class A (osteoproductive and osteoconductive) and Class B (only osteoconductive), as outlined in Table 1.02 [CAO01996, HENC1998a].

Table 1.02: Broad classification of bioactive materials [CAO01996, HENC1998a].

Class A	Class B
Osteoproductive and osteoconductive	Only osteoconductive
Rapid bonding with bone	Slow bonding with the bone
Enhanced bone proliferation	No enhancement in bone proliferation
Bonding to soft connecting tissue	No bonding to soft tissue connective
Example: 45S5 bioglass	Example: Synthetic HAp

Osteoproductive materials actively stimulate and promote bone regeneration by releasing bioactive molecules or growth factors. These materials play a more active role in the bone healing process by initiating or enhancing bone formation such as in the case of Hench's Bioglass® [CAO01996]. In contrast, osteoconductive materials provide a framework for bone cell proliferation and differentiation, thereby facilitating bone regeneration without directly participating in bone formation. Examples of this category include HAp, β-tricalcium phosphate, calcium sulfate and certain bioactive glasses [CAO01996]. Bioactive materials serve as an intermediary between inert materials and bioresorbable materials. Bioactive materials are used for extracellular matrix simulation and are biocompatible without exhibiting any critical cytotoxic effects. They are widely used in treatments for their ability to promote biological functions of the body and cell activity [XIAO2023]. Bioactive materials have significance in soft tissue regeneration such as demonstrated in cardiac, epithelial, and lung

tissues regeneration [JOY02019]. Bioactive material coatings materials on metallic implants serve to effectively bond the implant with the host tissue [JOY02019]. Bioactive materials are extensively studied, and they are critically utilised in association with personalised therapies due to their ability to degrade and show compatibility with the immune system [MAZZ2021]. Thus, these materials are widely studied for their role in curing different diseases and thus have significance in medical science. Advancements in the field of nanotechnology have further promoted the use of bioactive nanomaterials. Nanobiomaterials are very effective because of their nanometer size, precise structure and high surface area that allow significant interaction between the implant material and the biological system [ZHAO2021].

1.2. Bioglass and bioglass ceramics

Bioglass and bioglass ceramics fall under the category of bioactive biomaterials. However, due to their biodegradable nature, they also meet the partial criteria for bioresorbable biomaterials. Before delving into their properties, it's important to understand what a glass is. As per Shelby's definition, glass is described as an amorphous solid devoid of long-range order and periodic atomic structure, while showcasing a region of glass transformation behavior [SHEL1997]. The glass transformation (*a.k.a*. glass transition) can be comprehended by examining the volume (or enthalpy) change in a molten liquid as a function of temperature, as depicted in Figure 1.01. When the molten liquid is cooled below its melting temperature (T_m) at a slow cooling rate, there is a sudden decrease in volume, characteristic of a first order phase transition. This leads to the conversion of the melt into a crystalline solid with a long-range ordered atomic arrangement, as indicated by the red line in Figure 1.01. On the other hand, when the melt is cooled below T_m at a higher cooling rate (*a.k.a*. quenching), a gradual decrease in volume is observed without any abrupt change, as shown by the blue line in Figure 1.01. When this path is taken, the melt cools without undergoing crystallization, and so it is referred to as a supercooled liquid. Further cooling of the supercooled liquid results in an

increase in viscosity. Eventually, the viscosity becomes too high (~10^{13} poise) for any long-range atomic order to be maintained at that cooling rate. When the supercooled liquid attains a viscosity comparable to that of a solid and its volume approaches saturation, the metastable supercooled liquid is called a glass. The kinetic nature of the glass can be understood by recording either the temperature (or heat flow) change as a function of temperature using a differential thermal analyzer (or differential scanning calorimeter). Figure 1.02 shows a differential scanning calorimeter heating curve of a typical glass. Initially, an endothermic baseline shift is observed at the glass transition temperature (T_g). Upon further heating of the glass, an exothermic peak corresponding to the crystallization of the glass appears at crystallization temperature (T_c), where the disordered glass transforms into ordered crystal. This is followed by an endothermic peak signalling the melting of crystal at its melting point (T_m). In the case of multicomponent glasses, more than one exothermic and endothermic peaks may be observed. From the above explanation, it is apparent that when a glass is heated above T_g, it undergoes partial or full crystallization into a glass-ceramic. It has been extensively researched and established that glass-ceramics exhibit superior mechanical strength as compared to the brittle glass samples [SHEL1997]. Some of the commonly used bioglass ceramics include mica, apatite, combeite and wollastonite [SHEA2023]. Controlled-crystallization of a bioglass enhances its biocompatibility apart from retaining its bioactivity. Arstila *et al.* proposed a classification of glasses into two categories based on their T_g and T_c [ARST2007]. The first category consists of glasses with a T_g of ~500 °C and an onset of T_c below 750 °C. The second category comprises of glasses with T_g ranging from 550 to 600 °C, and onset of crystallization ~900 °C.

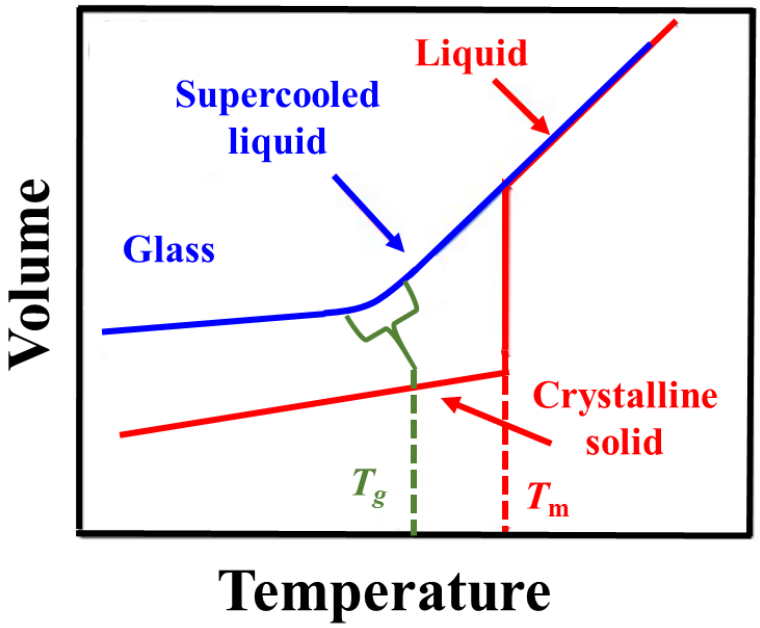

Figure 1.01: The influence of temperature on the enthalpy of a glass undergoing melt transformation [SHEL1997].

The story behind the invention of the first bioglass with the composition $45SiO_2$-$24.5CaO$-$24.5Na_2O$-$6P_2O_5$ (wt.%) is fascinating. This first bioglass was formulated by Dr. Larry L Hench in 1969 and later became known as Hench's glass or 45S5 Bioglass® [HENC1982a, HENC1982b]. Dr. Hench presented a review article detailing the story and adoption of the 45S5 glass composition [HENC2006]. The invention of 45S5 composition sparked the development of a broad field of bioactive materials and ceramics, including synthetic hydroxycarbonate apatite, calcium sulfate, and A/W glass-ceramics [PEIT2012, FU002011, KOKU1990a, JONE2013, WORK2022], leading to numerous studies aimed at enhancing implant performance [MONT2016, BAIN2018, CANN2021]. The 45S5 composition formulated by Hench has been found to be the best bioactive material among the researched materials due to its exceptional bioactivity for bone regeneration applications [CANN2021].

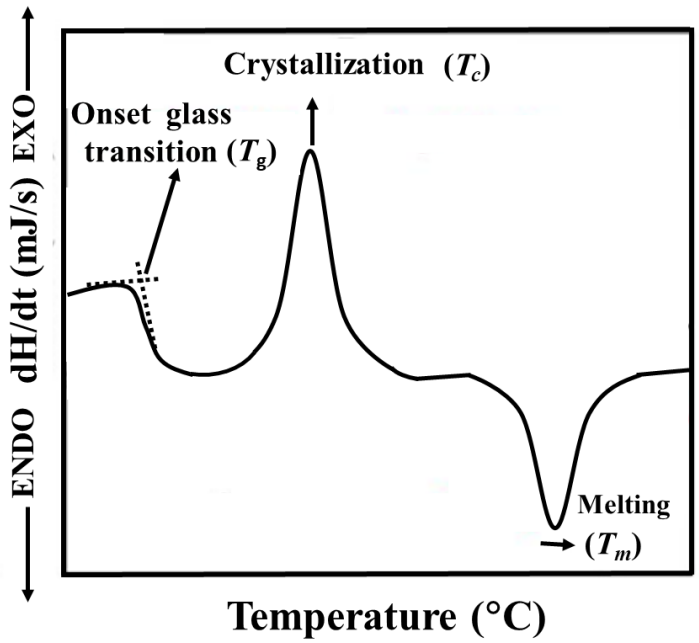

Figure 1.02: A typical heating curve of glass with its characteristic features [MUSG2014].

1.3. Mechanism of bioactive bonding

Upon immersion of a bioactive glass or bioactive glass-ceramic specimen in simulated body fluid (SBF), ions such as Na^+, Ca^{2+}, and Si^{4+} migrate from the specimen surface via exchange with H_3O^+ ions to the SBF solution . These inorganic ions released from the specimen surface play an essential role in stimulating genes involved in tissue regeneration. This process initiates the formation of a hydrated silica layer over the bioglass surface.

The migration of alkali and alkaline metal ions increases the local pH of the SBF surrounding the specimen surface, further promoting the hydrolysis of the hydrated layer and the formation of Si-OH groups. Through the polycondensation of Si-OH groups, a SiO_2-rich layer is formed over the bioglass surface. Additionally, due to the presence of Ca^{2+} and HPO_4^- ions in both SBF and bioglass, a heterogeneous amorphous calcium phosphate layer (ACP) is deposited on the specimen surface. This layer then undergoes crystallization, forming a hydroxy carbonate apatite layer or hydroxyapatite layer (HAp). Kokubo *et al.* [EBIS1990] established that the ionic exchange leads to the formation of a HAp layer on the bioglass or bioglass-ceramic surface, mimicking the interaction of human bone with human blood plasma,

as shown in Figure 1.03. Furthermore, bioactive glasses and glass-ceramics degrade over time, and a new HAp layer is deposited with longer immersion time, a process dependent on the composition of bioglass-ceramic constituents. Recent studies by Kaur *et al.* [KAUR2019] and Joy-Anne *et al.* [JOY02019] have also reported the formation of an apatite surface layer on bioactive glass and glass-ceramic coated implant materials, in a manner resembling the surface interactions of human bone.

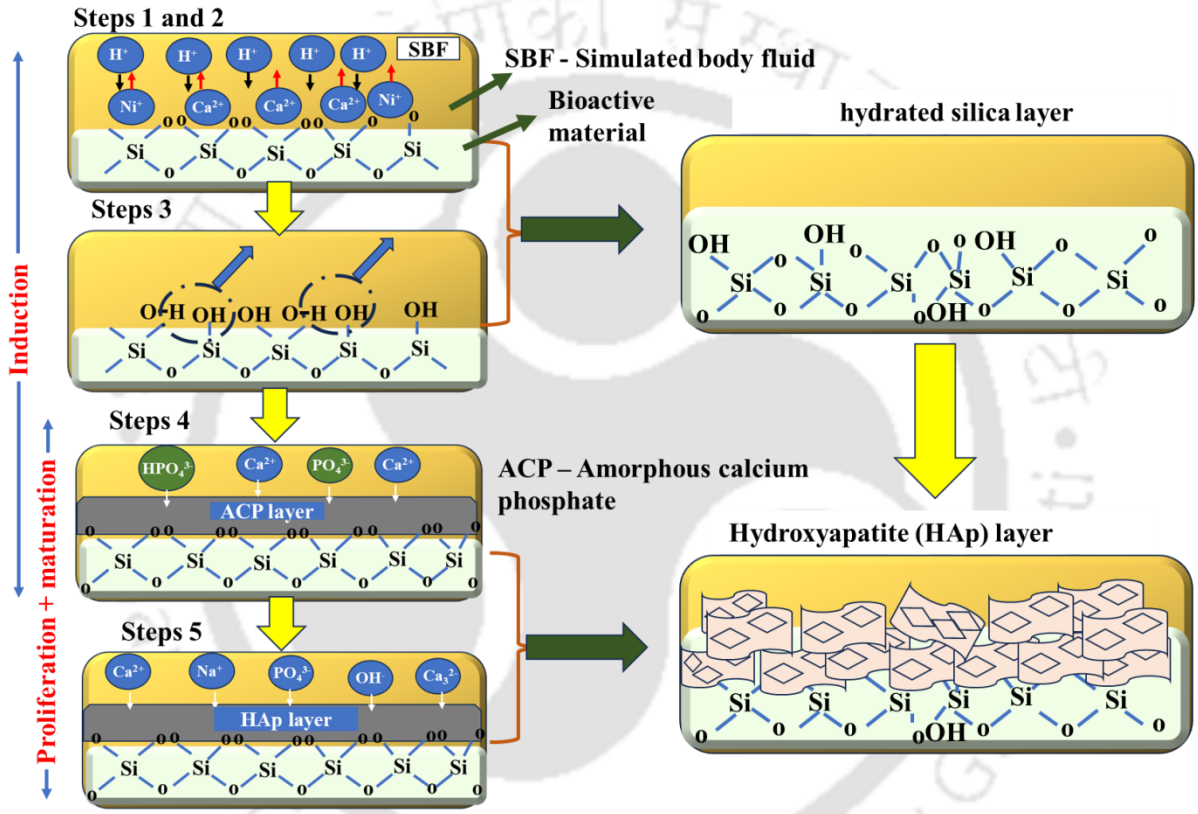

Figure 1.03: Schematic depiction of Hench's ion exchange mechanism [HENC1991, FERR2020] for HAp layer formation on the surface of a bioglass.

1.4. Sol-gel derived bioglass and glass-ceramics

45S5 bioglass was first utilized in solid form in middle ear surgery in 1980, serving as a replacement for small bones [HENC2002, HENC2006, HENC1991]. Subsequently, researchers have proposed various clinical applications for bulk 45S5 glass, including its use in periodontology and as a coating on metallic orthopedic implants. Among the various

reported bioglass compositions, 45S5 Bioglass has been recognized as one of the most effective biomaterials for bone regeneration, particularly in non-load-bearing applications [HENC1998b, HENC1991]. Currently, only a few bulk bioglass compositions based on SiO_2-CaO-Na_2O-P_2O_5 have been utilized as implant materials [JONE2015, HUSL2017]. Interestingly, these compositions commonly include SiO_2, CaO, Na_2O, and P_2O_5. This suggests that a narrow range of these oxides promote bioactive fixation [HENC1982c, LI001991]. Hence, a limited variation in bioglass constituent oxides composition has been found in the literature. Therefore, further discussions are limited to SiO_2-CaO-Na_2O-P_2O_5 based bioglasses. These bioglasses exhibit not only rapid formation of a HAp layer but also degrade in the physiological environment, due to the high Na_2O or other alkali cations content present in the compositions [CLAR1974]. All such bioglasses are synthesized in the bulk form by the conventional melt quench method. This method involves melting all the oxide constituents in a platinum crucible and rapidly quenching the molten state to obtain the glass. However, this process has some disadvantages such as high temperature processing, compositional limits (bioglasses containing above 60% SiO_2 exhibit no bioactive bonding), and low surface area [ARCO2003b, LI001991, FIUM2020]. Consequently, researchers have turned their attention to alternative methods for producing mesoporous powders of bioglass. Among these, the sol-gel method has emerged as a viable alternative to conventional melt quench technique along with certain distinct advantages [SAKK1985, CANN2021, ORGA1988].

In this method, a sol (colloidal suspension) is prepared through hydrolysis reactions of the constituent oxide precursors. Subsequently, a series of condensation reactions takes place, either simultaneously or sequentially, depending on the catalyst's nature. The hydrolysis and polycondensation phases portrayed below are essential elements of the precise mechanism that drives the sol-gel process [BADA2012, JUNG2000].

$$Si\ (OR)_4 + H_2O \rightarrow HO - Si(OR)_3 + R - OH \qquad (1.01)$$

In equation 1.01, tetraethyl orthosilicate ($Si(OC_2H_5)_4$) serves as the precursor for SiO_2, with the substitution of C_2H_5 by R.

$$Si\ (OR)_4 + 4H_2O\ \rightarrow Si(OH)_4 + 4R - OH \qquad (1.02)$$

$$(OR)_3 - Si - OH + HO - Si - (OR)_3\ \rightarrow [(OR)_3Si - O - Si(OR)_3] + H - O - H \qquad (1.03)$$

$$(OR)_3 - Si - OR + HO - Si - (OR)_3\ \rightarrow [(OR)_3Si - O - Si(OR)_3] + R - O - H \qquad (1.04)$$

Equations 1.01 and 1.02 depict the hydrolysis reactions, while equations 1.03 and 1.04 represent the condensation reactions within the sol-gel process. As a consequence of polycondensation, siloxane groups ([Si-O-Si]) are generated along with side products like H-O-H and R-O-H. These reactions occur at room temperature, resulting in gel formation. The gel represents a colloidal state where the liquid (H-O-H and R-O-H) is trapped within a 3-dimensional network of silica bonding and behaves like a semi-solid. It can be dried using supercritical and ambient temperature conditions. In supercritical condition, the gel solidifies without entering a liquid phase, allowing the liquid to evaporate. In ambient condition, mild temperatures are sufficient to evaporate the liquid phase present in the gel. Hench *et al.* and others have explored this method and observed that the use of metal alkoxide precursors, such as tetraethyl orthosilicate for silica and triethyl phosphate for P_2O_5 [HENC1990, RWJO1989], is favorable for this approach. The sol-gel process can be utilized to acquire fibers, films, and powders at various stages, as depicted in Figure 1.04.

It has been observed that high Na_2O-containing bioglasses exhibit bioactivity comparable to the 45S5 ($45SiO_2$-$24.5CaO$-$24.5Na_2O$-$6P_2O_5$) composition. However, careful examination of Table 1.03 reveals that compositions with high amounts of Na_2O content are structurally devitrified due to the presence of crystalline inclusions in the glassy matrix [PEIT2001, CART2006, CHEN2010, CACC2012, PIRA2013, ADAM2013, SIQU2011, THOM2016]. The predominant crystalline phase identified in high Na_2O-containing bioglass ceramics is sodium calcium silicate ($Na_2Ca_2Si_3O_9$). Some reports have described glassy

networks with compositions different from the 45S5 composition [LI001991, CART2005, GIRO2011, CATT2013]. There are only a few reports on attempts to synthesize sol-gel derived 45S5 Bioglass without the use of templates or complex processing steps [REZA2014]. They used nitrate-free organic precursors for sodium and calcium oxides to make 45S5 glass using the sol-gel method. However, their process is very time consuming with the gel forming process itself taking about 46 days. Though 45S5 bioglass is generally considered to be the best bioactive glass, it is very brittle with low fracture toughness which makes it fail under a load as encountered in biomedical applications [BAIN2019]. It has been demonstrated that sol-gel derived 45S5 glass-ceramic with $Na_2Ca_2Si_3O_9$ phase exhibits better mechanical strength than bulk 45S5 Bioglass [KARI2018]. Since the sol-gel 45S5 glass-ceramic powder exhibits similar bioactivity, it can serve as a better implant material with enhanced surface related properties than its bulk counterpart. Chapter 3 of the thesis addresses challenges in synthesizing 45S5 glass and optimizing the Na_2O content.

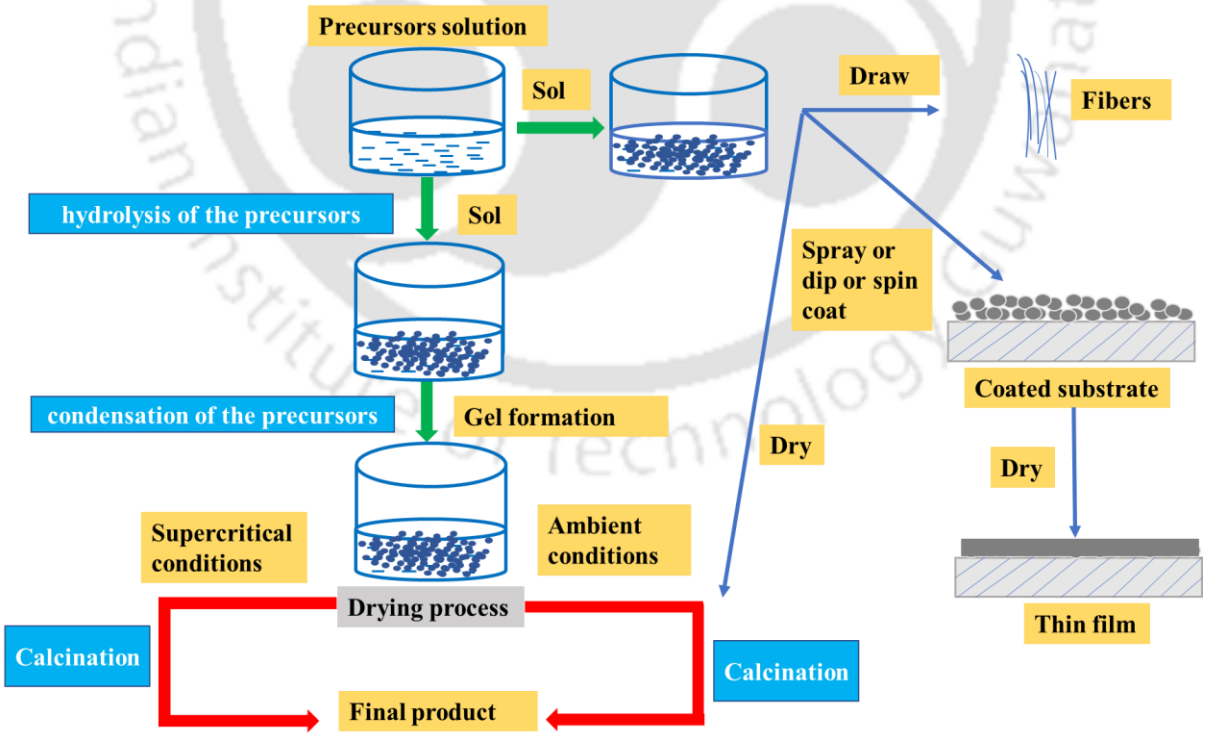

Figure 1.04: Schematic diagram of sol-gel process.

Table 1.03: Sample, composition, with structural details of SiO_2-CaO-Na_2O-P_2O_5 (mol%) bioglasses and glass-ceramics.

Sample ID	SiO_2	CaO	Na_2O	P_2O_5	Final product	References
49S	50.0	46.0	0.0	4.0	Glass	[LI001991]
45Ca40Si15	15.0	40.0	0.0	45.0	Glass	[CART2005]
52S4	52.3	32.3	13.7	1.7	Glass	[GIRO2011]
Si47C	47.0	26.5	21.5	5.0	Glass	[CATT2013]
45S5	49.2	26.9	24.4	2.6	Glass	[REZA2014]
1.07N2C3S	51.1	29.6	19.3	0	Glass-ceramic	[PEIT2001]
SSP4	48.6	22.2	24.5	4.7	Glass-ceramic	[PEIT2001]
SSP6	46.3	21.2	23.3	9.2	Glass-ceramic	[PEIT2001]
P45Ca20Na10Si25	25.0	20.0	10.0	45.0	Glass-ceramic	[CART2005]
45S5	46.1	26.9	24.4	2.6	Glass-ceramic	[CHEN2010], [CACC2012], [PIRA2013], [ADAM2013]
Bio(1)_TEP_Na	49.2	25.8	23.3	1.7	Glass-ceramic	[SIQU2011]
No name	49.2	25.5	23.4	1.7	Glass-ceramic	[THOM2016]

1.5. Iron oxide-substituted glass-ceramics

Researchers have extensively investigated the coating of biomaterials with magnetite. Such coatings are biocompatible but not bioactive [MADH2022, HUI02011, YETI2020, CAI02020, ALTE2021, NIKM2019, ZELE2017]. An alternative method involves precipitating the magnetic phase within a bioactive glassy matrix to attain both magnetic properties and bioactive fixation. Several researchers have shifted their focus towards these magnetic bioglass-ceramics which hold promise for diverse biomedical applications. These include hyperthermia treatment of cancer cells [IAVE2015, AJAY2007, QIUH2015, YOLA2015], targeted drug delivery [ANAN2023], and serving as contrast agents for magnetic resonance imaging [BRET2006a, SHCH2020], *etc*. Borrelli *et al.* have investigated magnetic properties of bulk magnetic glass-ceramic of composition Fe_2O_3-P_2O_5-Li_2O-SiO_2-Al_2O_3-MnO-B_2O_3-MgO [BORR1981]. Following that, Luderer *et al.* fabricated bulk 11.6Li_2O-0.4Al_2O_3-3.4SiO_2-23.7P_2O_5-60.5Fe_2O_3 glass-ceramic with saturation magnetization (M_s) of 8.69 emu/g

[LUDE1983]. Kukubo *et al.* developed a P_2O_5-free bulk glass-ceramic of composition $40Fe_2O_3$-$60(CaO\text{-}SiO_2)$ (wt.%) and demonstrated its magnetic properties with different compositions [KOKU1990b]. Bretcanu *et al.* found both magnetite and hematite phases along with a glassy matrix in their bulk $CaO\text{-}SiO_2\text{-}P_2O_5\text{-}Na_2O\text{-}Fe_2O_3$ ceramics [BRET2006a, BRET2006b, BRET2005]. Ebisawa *et al.* reported temperature dependent magnetic properties of this sample and the influence of small amounts of Na_2O, B_2O_3, and P_2O_5 addition in its bioactivity [EBIS1992]. Levenouri *et al.* investigated the structural and magnetic properties of bulk $CaO\text{-}SiO_2\text{-}P_2O_5\text{-}Na_2O\text{-}Fe_2O_3$ glass-ceramic [LEVE2005]. They also studied the influence of preparative conditions on the magnetic and heat generation properties of $CaO\text{-}SiO_2\text{-}P_2O_5\text{-}Na_2O\text{-}Fe_2O_3$ glass-ceramic prepared by melt quenching and co-precipitation methods. Singh *et al*. made a systematic study on bulk $(45\text{-}x)CaO\text{-}34SiO_2\text{-}16P_2O_5\text{-}4.5MgO\text{-}0.5CaF_2\text{-}xFe_2O_3$ (x = 5–20 wt.%) ferrimagnetic bioglass-ceramics and identified HAp, magnetite, akermanite, and wollastonite as the major crystalline phases in all compositions [SING2010]. Additionally, Singh *et al.* studied another series of bulk glass-ceramics with the composition $41CaO\text{-}(52\text{-}x)SiO_2\text{-}4P_2O_5\text{-}xFe_2O_3\text{-}3Na_2O$ (x = 0, 2, 4, 6, 8, and 10 mol%) and found that the M_s (H_c) varied from 0.17 emu/g (523 Oe) to 7.95 emu/g (91 Oe) as was x increased from 0 to 10 mol% [SING2008b]. Nisha *et al.* examined the change in magnetic properties of bulk $CaO\text{-}P_2O_5\text{-}Na_2O\text{-}Fe_2O_3\text{-}SiO_2$ glass and glass-ceramics with heat treatment temperature [SHAN2014].

The magnetic glass and glass-ceramics studied above are in bulk form. There are a few reports on nanostructured $SiO_2\text{-}CaO\text{-}Na_2O\text{-}P_2O_5\text{-}Fe_2O_3$ bioglass and glass-ceramics. Nisha *et al.* reported on sol-gel derived bioglass and glass-ceramics with the composition $(45 - x)SiO_2\text{-}24.5CaO\text{-}24.5Na_2O\text{-}6P_2O_5\text{-}xFe_2O_3$ ($0 < x \leq 3$ wt.%) and found combeite, magnetite, and maghemite as the main ceramic phases. M_s of the bioglass-ceramic with x = 2 was reported to be 1.36 emu/g [SHAN2016]. Rahman *et al.,* who initially developed (MNP) using the coprecipitation process, published the only report on sol-gel-generated magnetic iron oxide

glass-ceramic [RAHM2020]. They then used the P123 copolymer as a template using the sol-gel process to produce a mesoporous magnetic glass with a composition of $7Fe_3O_4$-$51SiO_2$-$18CaO$-$20Na_2O$-$4P_2O_5$ (mol%). They have also discussed the prospect of using Fe_3O_4 nanoparticles instead of iron oxide, which opens up the possibilities for a better glass or glass-ceramic for hyperthermia as well as bone regeneration applications. This proposal is explored in chapter 5 of the thesis.

1.6. Selected biomedical applications

The extensive applications of biomaterials in healthcare encompass a wide range of areas, making it challenging to detail each one. However, this review concentrates on selected biomedical applications closely associated with the biomaterials developed in this thesis. The investigations presented in this thesis were conducted with these specific applications in consideration.

1.6.1. Tissue Engineering

Tissue engineering emerges as a potent approach for organ and tissue repair [RAHA2011, LANG1993, NERE1991, GAO02023]. Tissue engineering enables the creation of organs from synthetic implants. The scaffold must possess specific properties to effectively support tissue regeneration, including biocompatibility, promotion of cell adhesion, mechanical properties comparable to the target tissue, appropriate architecture, and an appropriate degradation rate [RAHA2011]. Bioactive glass-ceramics or composites meet many of these requirements, making them highly suitable for tissue engineering applications. Bioactive materials, particularly in the form of scaffolds, play a crucial role in this process by providing a framework for bone regeneration. The porous nature of these scaffolds allows bone cells to migrate and proliferate, while the rough texture facilitates cell attachment. As cells multiply, they populate the scaffold, leading to the formation of 3-dimensional tissue structures.

Table 1.04: Clinical applications of bioactive materials [CAO01996].

Materials	Clinical applications	References
Bioglass ($45SiO_2$-$24.5CaO$-$24.5Na_2O$-$6P_2O_5$) (wt.%)	Middle ear device, Tooth root replacement, Periodontal treatment, Maxillo-facial reconstruction, Bone defect filler	[WILS1994] [WILS1993] [LOBE1995] [STAN1995]
Ceravital (SiO_2-CaO-Na_2O-P_2O_5-MgO-K_2O)	Middle ear device	[RECK1994], [LOBE1995] [GROS1993]
Bioverit $40(SiO_2$-$Al_2O_3)$-$60(MgO$-K_2O-F) (wt.%)	Middle ear device, Tooth root, Spacer	[HOLA1993] [HOLA1983]
A/W bioglass ceramic ($34SiO_2$-$44.7CaO$-$16.2P_2O_5$-$4.6MgO$-$0.5CaF_2$) (wt.%)	Vertebrae prosthesis, Vertebral spacer, Iliac crest prosthesis, Bone defect filler	[YAMA1984] [ONO01988] [YAMA1993]
Hydroxyapatite (HAp) $Ca_{10}(PO_4)_6(OH)_2$	Middle ear device, Tooth root, Periodontal treatment, Maxillo-facial reconstruction, Percutaneous device, Bone defect repair	[LOBE1995] [LEGR1991] [LACE1986] [BLIT1990] [DENI1989] [GALG1990]
Polyethylene / HAp	Orbital floor	[DOWN1991] [BONF1995] [STAN1995]

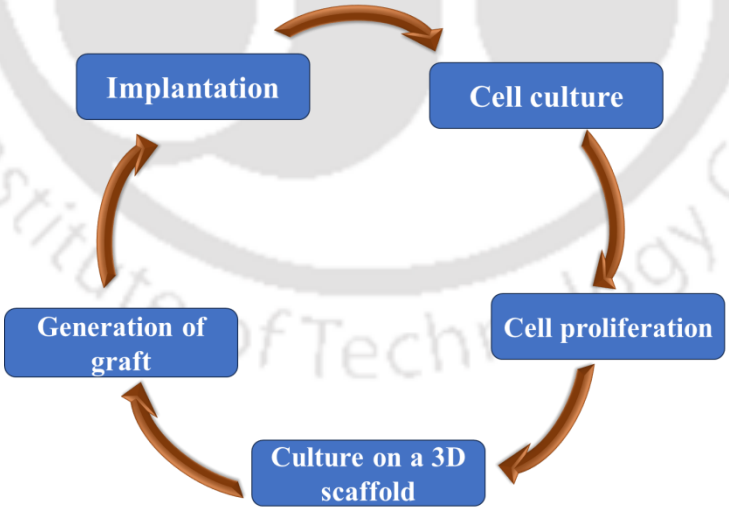

Figure 1.05: Schematic representation of bone tissue engineering.

Additionally, bioactive materials release ions such as calcium, phosphorus, and silicon, which stimulate bone formation and enhance bone regeneration. This process promotes the

bioactive fixation of the implant material with the surrounding tissue, ultimately facilitating the integration of the scaffold and promoting successful bone regeneration. Eventually, the scaffold dissolves, allowing the newly formed tissue to blend seamlessly with its surroundings. From a biological perspective, bone growth necessitates cellular engagement, extracellular matrix (ECM) deposition (3-D scaffold), cell-ECM interactions, and the presence of growth factors, as depicted in the schematic diagram of tissue engineering in Figure 1.05. Furthermore, Table 1.04 provides an overview of bioactive glasses and glass-ceramics employed in various clinical applications.

1.6.2. Hyperthermia treatment of cancer cells

Cancer is one of the leading causes of death. Preventing and curing it poses a huge challenge to the medical fraternity. The World Health Organization (WHO) data [MAUR2020] indicates that in the next 20 years, the prevalence of this condition will rise to 75%. The four main treatments for cancer utilized in clinical practice are radiation therapy, chemotherapy, hyperthermia (HT), and surgery [DANE2021]. Each method comes with its own set of advantages and drawbacks, influenced by factors like cancerous tumor/tissue size, location and the patient's overall health condition. Most of these therapies do not give a selective solution because they destroy cancer cells along with healthy cells. These days, combinations of therapies are often selected for their increased effectiveness in treating patients. HT, also known as thermal therapy, is gaining attention as a promising treatment for small, deeply rooted tumors that are a few centimeters in size. HT involves raising the temperature of the tumor to between 41-45 °C. This elevated temperature helps in cancer treatment by causing protein denaturation in cancer cells, which impairs their ability to repair themselves. Additionally, the increased temperature can disrupt the blood vessels supplying the tumor, reducing oxygen delivery, and further contributing to tumor shrinkage and destruction. While the primary goal of HT is to target and destroy cancer cells, it is equally important to minimize damage to healthy

tissues. However, completely avoiding harm to healthy cells is often challenging. If cancer is not detected early, primary cancer cells can spread through the bloodstream and form new tumors in other parts of the body. Among the organs that can be affected, the bone is the third most common site of metastasis, after liver and lungs [MAUR2020, VELA2019]. Further, HT can be applied in three ways, viz., whole body hyperthermia (WBH), regional hyperthermia, and localized hyperthermia [VELA2019]. The body temperature is raised to at least 43 °C in WBH, usually by submerging the body in hot water or by exposure to radiant heat sources like ultraviolet (UV) radiation. In regional hyperthermia, a portion of the individual's blood is removed, subjected to heat, and then reintroduced into a targeted limb or organ, accompanied by anticancer drugs. Meanwhile, localized hyperthermia or magnetic hyperthermia treatment (MHT) employs a more targeted approach. For this thesis work localized MHT is useful hence discussed in detail.

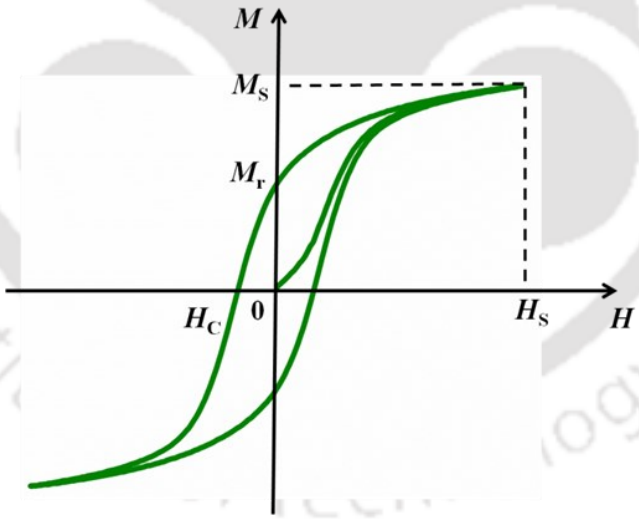

Figure 1.06: A typical *M-H* loop for ferromagnetic material.

In MHT, magnetic particles, such as iron oxide nanoparticles, are surgically inserted into the tumor site through a minimally invasive procedure. After implantation, an external alternating magnetic field is applied, which induces localized heat within the tumor, leading to temperature-mediated cell destruction. The heat generation capacity of iron oxide nanoparticles

is highly dependent on their particle size, which determines the dominant heat generation mechanism. Generally, there are three primary mechanisms for heat generation in magnetic materials: Relaxation mechanisms (Néel and Brownian relaxation), eddy currents, and hysteresis losses [DEAT2014, KAFR2016].

- Relaxation mechanisms: The relaxation mechanisms involve two different processes:
  - Néel relaxation: This refers to the reorientation of the magnetic moment (spin orientation) within the nanoparticles. This mechanism dominates in superparamagnetic nanoparticles with sizes typically ≤ 20 nm. In these particles, heat is primarily generated by the flipping of the internal magnetic moment. Heat loss due Néel relaxation can be described by the relation,

$$P_{Neel} = \frac{\mu_0 M_s^2 \, V \, \tau_N H^2 f^2}{k_B \, T \left(1 + \left((2 \, \pi \, f \tau_N)\right)^2\right)} \qquad (1.05)$$

where μ_0, M_s, V, τ_N, H, f, k_B, and T represent permeability of free space, saturation magnetic moment, volume of the nanoparticle, Néel relaxation time, amplitude of applied magnetic field, frequency of the applied field, Boltzmann constant, and temperature, respectively. Also, Néel relaxation time τ_N is defined as [KAFR2016],

$$\tau_N = \tau_0 \, exp \left(\frac{KV}{k_B \, T}\right) \qquad (1.06)$$

where τ_0, and K, indicating attempt time (~ 10^{-9} seconds), and magnetic anisotropy constant, respectively.

  - Brownian relaxation: This refers to the physical rotation of the particle itself in response to the alternating magnetic field. Brownian relaxation dominates in larger nanoparticles (typically > 20 nm), where the entire nanoparticle physically rotates within the surrounding medium to align with the external

magnetic field. Heat loss generated through Brownian relaxation can be calculated by the following equation [ROSE2002].

$$P_{Brownian} = \frac{\mu_0 M_s^2 \, V \, \tau_B H^2 f^2}{k_B \, T \left(1 + \left((2 \, \pi \, f \tau_B)\right)^2\right)} \qquad (1.07)$$

Here, τ_B represents the Brownian relaxation time, which can be estimated using,

$$\tau_B = \frac{3 \, \eta \, V_H}{k_B \, T} \qquad (1.08)$$

Here η, and V_H indicate the viscosity of the surrounding medium, and hydrodynamic volume of the nanoparticle, respectively.

- Eddy current: This mechanism involves heat generation resulting from induced circulating currents within a conductive material when it is subjected to an alternating magnetic field. The amount of heat produced by eddy currents is influenced by the electrical conductivity of the material and the size of the particles. Eddy current loss is often negligible due to the small size of the nanoparticles.
- Hysteresis loss: When ferromagnetic materials or iron oxide nanoparticles are exposed to an external alternating magnetic field (H), the magnetic domains within the material attempt to align with the field's direction. As the magnetic field strength increases, more magnetic domains align, reaching a point where nearly all domains are aligned in the direction of the field. This state is referred to as saturation magnetization (M_s). As the magnetic field decreases, not all domains immediately return to their original orientations, leaving a residual magnetic moment known as remnant magnetization (M_r), even when the applied field is reduced to zero. To completely eliminate this remnant magnetization, a reverse magnetic field is required, which is referred to as the coercive field (H_c). This cyclic behavior of magnetization and demagnetization creates a characteristic hysteresis loop on an *M-H* curve, where the area enclosed by the loop

represents the energy loss due to hysteresis as illustrated in Figure 1.06. This energy loss is dissipated as heat. A larger hysteresis loop area correlates with greater heat loss. The hysteresis loss can be mathematically expressed as [CARR2011],

$$Hysteresis\ loss = \int_0^{Hmax} \mu_0 M.dH \qquad (1.09)$$

Hysteresis loss accounts for heat generation that depends on the applied alternating frequency, effective anisotropy, and particle volume. Therefore, power loss is determined entirely by the material's properties.

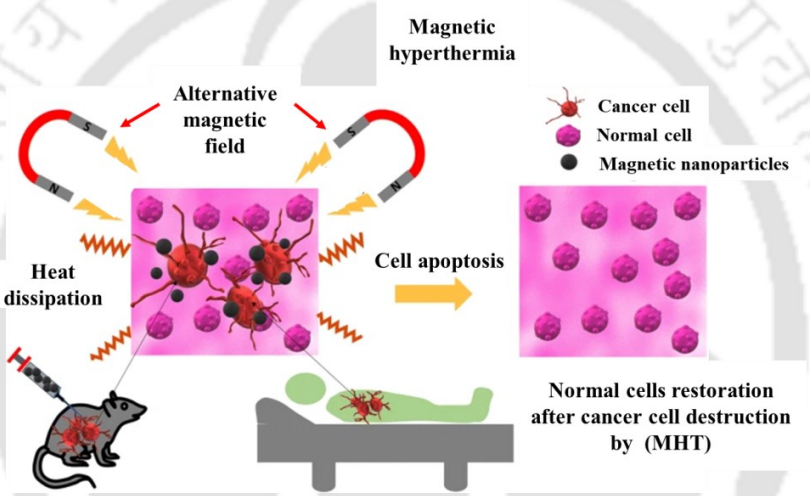

Figure 1.07: Schematic view of procedure adapted in MHT to treat cancer cells [GERH2010].

Figure 1.07 illustrates the basic mechanism of how cancer cells can be eradicated through this localized MHT. This innovative approach shows promise in enhancing treatment efficacy while minimizing adverse effects, marking a significant stride in cancer therapy. The magnetic phase within the magnetic glass-ceramic helps in the destruction of cancer cells, whereas the non-magnetic composition of magnetic glass-ceramics shows potential as cavity fillers for post-removal of cancerous tumors, as depicted in Figure 1.07. Figure (1.08) illustrates their role in promoting bone regeneration and their potential application in MHT. Velasco *et al.* have described the systematic evolution of magnetic materials starting from magnetite to

magnetic glass-ceramics in a review article which includes almost 70 magnetic glass-ceramic papers [VELA2019]. In 1957, for the first time, Gilchrist *et al*. administered magnetic nanoparticles (47 mg of Fe_2O_3 per gram of tissue) of size 20-100 nm and demonstrated the process of inductively killing of lymphatic metastases [GILC1957]. In this experiment, an increment in the temperature of 14º was observed after exposure to alternating magnetic field of 200-240 Oe at a frequency of 1.2 MHz. Since no control experiments were reported, cytotoxicity remained as a serious concern for frequent application on 20 patients. Later, it was recognized that bare magnetic materials, including nanoparticles, have limited biocompatibility. This issue led to efforts to minimize the dosage of the material required for MHT. In the mid-1990s, the utilization of magnetic particles in conjunction with glasses and glass-ceramics re-emerged. Borrelli *et al.* patented the first bulk magnetic glass-ceramic for MHT with a composition of Fe_2O_3-P_2O_5-Li_2O-SiO_2-Al_2O_3-MnO-B_2O_3-MgO [BORR1981]. After initial investigations, this field transitioned from bulk magnetic glass-ceramic to nanoporous and then mesoporous materials with varying oxide constituents [VELA2019].

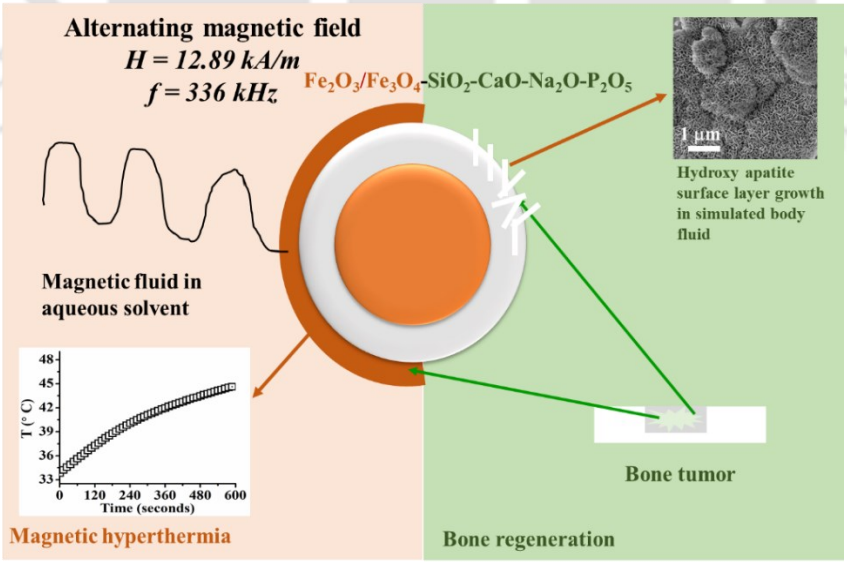

Figure 1.08: A schematic diagram illustrating the use of magnetic glass-ceramics for bone regeneration and MH applications.

1.7. Motivation behind the thesis

Upon a careful review of the literature surveyed, it is evident that synthesizing Hench's 45S5 bioglass composition ($45SiO_2$-$24.5CaO$-$24.5Na_2O$-$6P_2O_5$ (wt.%)) by sol-gel method encounters serious challenges. However, despite these challenges, the preference for bioglass-ceramics with a combeite phase persists strongly due to their unparalleled bioactivity. Consequently, this thesis maintains its emphasis on the 45S5 composition. This work addresses the following critical issues related to bioglass and bioglass-ceramics, specifically focusing on bone regeneration and magnetic hyperthermia (MH) applications:

- The literature survey shows that 45S5 Bioglass exhibits unparalleled bioactivity and devitrification of sol-gel derived 45S5 bioglass cannot be avoided [CART2005, CHEN2010, SIQU2011, LUCA2011, PIRA2013, ADAM2013, CATT2013, THOM2016, PEIT2012, NOVA2022, ADHI2023]. However, factors impeding the vitreous state in the sol-gel derived 45S5 composition and the role of atomic structure on bioactivity of this ceramic is not understood.
- An early study on bulk iron oxide-based glass-ceramics has extensively investigated and presented varying phase percentages, including magnetite, hematite, and combeite, which are temperature-dependent [SING2008b, SING2010, SHAN2014, SHAN2016]. However, no systematic investigation has been published so far that includes the iron oxide-based 45S5 composition obtained by sol-gel route.
- Only limited iron oxide could be substituted in bioglass or bioglass-ceramics without making the material toxic. An alternative methodology to improve the magnetization of the magnetic bioglass-ceramics without making it toxic has not been explored.
- Selective substitution of iron oxide for 45S5 oxide components for achieving optimal heating capacity without compromising bioactivity has not been investigated so far.

- Since both the heat treatment temperature and the relative phase percentages impact the heating capacity and bioactivity, the selection of the optimal heat treatment temperature may become a crucial consideration.

This thesis work aims to address the above crucial issues with the following objectives:

1) Address the hurdles associated with producing Hench's 45S5 bioglass in nanopowder form through the sol-gel route.
2) Explore the potential of iron oxide-substituted 45S5 glass-ceramic for MH by incorporating both Fe_2O_3 and MNP.
3) Scrutinize the substitution of MNP for SiO_2 (glass former), CaO, and Na_2O (glass modifiers) in the 45S5 ceramic for optimal MH.
4) Determine the optimal heat treatment conditions to yield the best possible combination of ceramic phases and magnetic properties in a multicomponent 45S5 glass-ceramic substituted with MNP.

With the above objectives, the research work aims to create an optimal thermoseed for use in both bone regeneration and MH applications, pushing forward the frontiers of biomaterial synthesis and biomedical uses.

Chapter 2

Experimental details

The synthesis process is crucial in achieving high-quality materials and each synthesis route comes with its own advantages and limitations. A variety of experimental methods and instruments have been utilized for characterizing MNP, mesoporous bioglass, and glass-ceramics prepared in this thesis work. The first part of this chapter will delve into the methodology employed for the synthesis of MNP, as well as mesoporous glass and glass-ceramic materials. The second segment will briefly describe the characterization techniques applied to analyse the properties of MNP, bioglass, and glass-ceramics.

2.1. Sample preparation

Nanoparticles have garnered significant attention owing to their enhanced properties across various fields [SING2000]. Many methods have been developed for the synthesis of nanoparticles [FADL2019] including co-precipitation [OKUD2009], hydrothermal [LIU02006], thermal evaporation [SARI2018], sol-gel process [ASUH2011], *etc*. In this study, the coprecipitation method was selected for synthesizing MNP, while the sol-gel method was chosen for producing bioactive mesoporous glass and glass-ceramics.

2.1.1. Co-precipitation method for magnetite nanoparticles synthesis

The co-precipitation method involves the production of a mixed precipitate comprising two or more insoluble species. These chemical species are simultaneously removed from the precursor's solution. This method primarily utilizes inorganic salts such as nitrates, chlorides, and sulfates, which readily dissolve in water or other solvents to form a homogeneous solution. Subsequently, a high-pH (basic) solution is employed as a precipitant, causing the salts to precipitate into hydroxides or oxalates. Following precipitation, a solid powder is obtained, which is collected through washing and gradual drying processes. The procedures of drying and washing impact

the degree of particle aggregation. To obtain the final product, the dried powder needs to undergo calcinations to facilitate growth of the desired crystalline phase.

In this work, precursors of Fe^{3+} ($FeCl_3$, HIMEDIA, 99%) and Fe^{2+} ($FeCl_2.4H_2O$Thermo Scientific, Chemicals, 98%) were added to deionized water in a molar ratio of 2:1, and the mixture was homogenized by stirring at 80 °C under inert atmosphere. After stirring for 30 minutes, ammonia solution ($NH_4(OH)$) was gradually added to the mixture until the solution turned black. Subsequently, the mixture was stirred for 3 h followed by overnight aging to complete the synthesis of the MNP. Equation 2.01 indicates the chemical reaction leading to the formation of MNP.

$$2FeCl_3 + FeCl_2 + 8NH_4(OH) \rightarrow Fe_3O_4 + 6H_2O + 8NH_4Cl \qquad (2.01)$$

To eliminate any remaining traces of ammonia, the resultant MNP were repeatedly cleaned with ethanol and deionized water. After cleaning, the MNP were dried overnight and stored under vacuum for further use.

2.1.2. Preparation of glass-ceramics by sol-gel route

The sol-gel method was selected for the preparation of glass ceramic nanopowder. The process is explained in detail in section 1.4 of chapter 1. To prepare sol-gel derived nanopowder, the amount of each precursor was calculated using batch calculation [SHEL1997].

A magnetic glass ceramic (MGC) sample with the composition of $43SiO_2$-24.5CaO-$24.5Na_2O$-$6P_2O_5$-$2Fe_2O_3$ (wt.%) was prepared. For this, tetraethyl orthosilicate [TEOS, $Si(OC_2H_5)_4$, purity > 99%, Sigma-Aldrich], calcium nitrate tetrahydrate [$Ca(NO_3)_2 \cdot 4H_2O$, purity > 98%, Loba Chemie], triethyl phosphate [TEP, $C_6H_{15}O_4P$, purity > 99%, Sigma-Aldrich], sodium nitrate [$NaNO_3$, purity > 98%, Loba Chemie], and iron nitrate [$Fe(NO_3)_3 \cdot 9H_2O$, purity

> 98%, Loba Chemie] were used as sources of SiO_2, CaO, P_2O_5, Na_2O, and iron oxide, respectively. The batch calculation involves the following steps:

- Mol. wt. of MGC = [(MW of SiO_2× 43) +(MW of CaO × 24.5) + (MW of Na_2O × 24.5) + (MW of P_2O_5× 6) + (MW of Fe_2O_3× 2)] /100 = 66.46 g/mol.
- Weight fraction of SiO_2 = (MW of SiO_2× 43) / MW of MGC *100 = 0.38867.
- Thus, the desired compound is not directly employed as a source compound as it is a by-product of the precursor compounds. Therefore, a gravimetric factor (G.F.) is multiplied with the weight fraction of the source compound. In this manner, the precise amount of the precursor required is calculated.
- G.F. = MW of precursor (batch compound) / MW of source compound.
- G.F. of SiO_2 = MW of TEOS / MW of SiO_2 = 208.33 / 60.08 = 3.46.
- TEOS = 0.38867 × 3.46 = 1.34480 g = 1.34480/.933 = 1.44 ml.
- All precursors' amounts were calculated using this approach.

The batch calculation provided above is for 1 g of the MGC. Initially, the molar ratio between TEOS and water was fixed at 1:18 for all the samples. The aqueous TEOS solution was mixed in 1M HNO_3 aqueous solution using a magnetic stirrer with programmable heater. After allowing for completion of hydrolysis, other precursors such as TEP, $NaNO_3$, $Ca(NO_3)_2.4H_2O$ and $Fe(NO_3)_3.9H_2O$ were introduced into the TEOS solution. This mixture (sol) was consistently stirred for 24 h until a clear and homogeneous sol was obtained. The homogenized sol was then aged for 3 days at room temperature. The aged gel was dried either by heating (at 100 °C for 24 h) or by lyophilization (at -40 °C for 24 h). The dried gel powder was placed in an air oven for 3 days at 70 °C for thermal stabilization. Subsequently, a systematic heat treatment procedure was conducted using a raising hearth furnace. This controlled heat treatment of glass and glass-ceramic powder samples facilitated the control/optimization of various desired crystalline phase in the ceramic powders.

2.2. Characterization techniques

Advanced characterization methods are crucial to understanding the physics and material behavior of the synthesized nanoparticles to assess their application potential. In this section, a detailed account of the characterization methods and tools used to examine these materials.

2.2.1. Powder X-ray Diffractometer

Determination of atomic structure is the first step in characterising a material. While certain materials have only short-range periodic atom configurations known as amorphous solids, others have long-range periodic patterns known as crystalline solids. X-ray diffraction patterns serve as the primary tool for distinguishing between the amorphous and crystalline nature of materials and identifying the crystalline phase (s) present in the investigated sample. Additionally, the XRD technique allows one to obtain structural information about crystalline materials, including strain (ε), average crystallite size (D_v), lattice parameters (a, b, c, α, β, γ), and more.

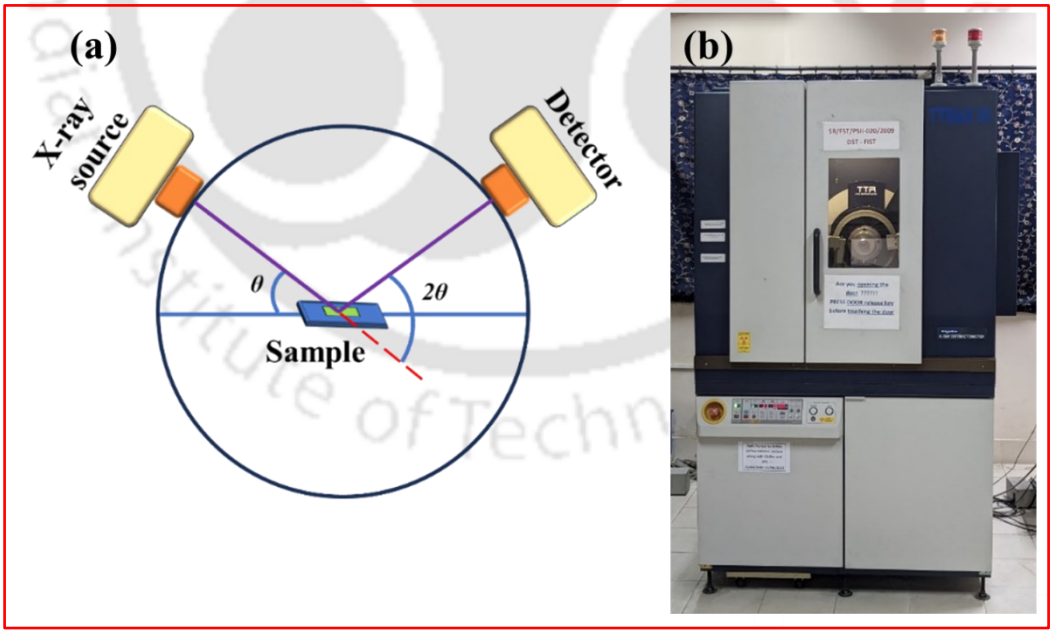

Figure 2.01:(a) Schematic diagram of the X-ray goniometer, and (b) photograph of the rotating anode-based Rigaku TTRAX III X-ray diffractometer.

The Bragg's law as its fundamental premise of X-ray diffraction studies [CULL1956]. It is commonly known that atoms are arranged periodically in crystals. X-ray diffraction is caused by the constructive interference of scattered X-rays from a series of parallel atomic planes within the crystal that interact with incident X-rays at certain angles. The relation commonly referred to as Bragg's law is expressed as

$$2dsin\theta = n\lambda \qquad (2.02)$$

Here, d represents the spacing between atomic planes characterized by the Miller indices h, k, l, θ is the diffraction angle, n is an integer (representing the order of diffraction, generally taken as 1), and λ denotes the wavelength of the incident X-rays. If both the X-ray source and the X-ray detector in an X-ray diffractometer travel in the same direction with each step of angular displacement, it is said to have θ-2θ geometry. This arrangement guarantees that the detector gathers diffracted photons from a certain set of parallel crystal planes.

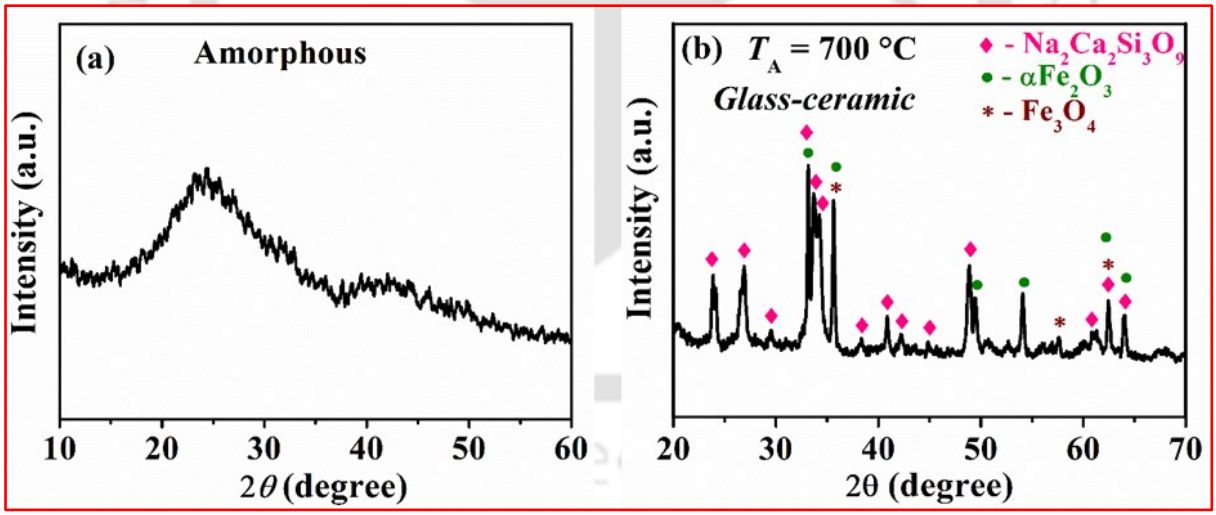

Figure 2.02: Typical XRD pattern of (a) $69.5SiO_2$-$24.5CaO$-$6P_2O_5$ glass, and (b) S_{Fe10} MSGC sample.

A Rigaku TTRAX III powder X-ray diffractometer operating in θ-2θ geometry was used in the current studies (Figure 2.01 (a)). Cu-K_α X- radiation with a wavelength (λ) of 1.5406 Å is

generated with an input power of 5 kW. A scintillation counter acting as the detector, pyrolytic graphite serving as the monochromator and a Ni-Cu-K_β filter are also used. All the measurements have been performed with scan speed 2°/min and with step size 0.02°. A photograph of the instrument is shown in Figure 2.01 (b). Figure 2.02 (a) and (b) presented the XRD patterns of glass and S_{Fe10} MSGC nanopowder samples, respectively. If the atomic arrangements are extended up to infinity, the peaks in X-ray diffraction (XRD) patterns should ideally show up as Dirac delta functions. In actuality, though, XRD peaks of nanocrystalline materials show broadening because of several variables, including the size of the nanocrystallite, internal strain, and contributions from the instrument. The peak width is often represented as the full width at half maximum (FWHM) increases as the size of the nanocrystallites decreases.

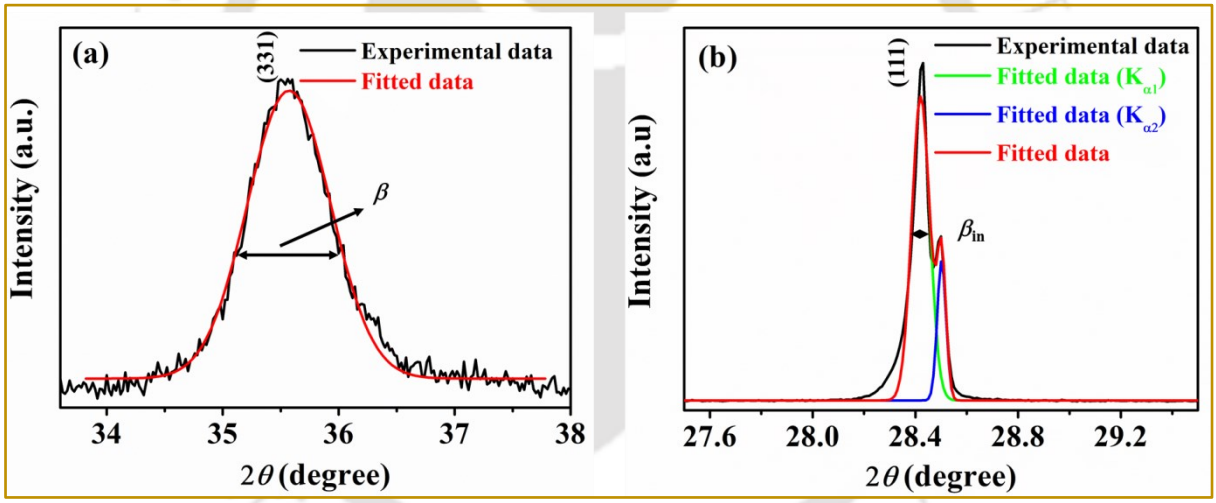

Figure 2.03: Procedure followed to fit normal distribution (Gaussian) function to (a) (331) peak in the XRD pattern of MNP, and (b) (111) peak in the XRD pattern of standard Si.

The average crystallite size (D_v) of the synthesized nanoparticles was calculated using the Debye-Schërrer equation [CULL1956]. Although this method may not be entirely reliable for semi-crystalline materials, it provides a reasonable approximation of crystallite size for the purposes of this study.

$$D_v = \frac{k\lambda}{\beta \cos\theta} \qquad (2.03)$$

Here k is a constant which takes the value 0.9 if the nanoparticles are spherical with cubic symmetry, λ (= 1.5406 Å) is the X-ray wavelength, θ is the Bragg angle and β is the FWHM of the Bragg peak, expressed in radians. θ and β corresponding to the strongest peak of a particular phase in the XRD pattern is chosen for the estimate. The peak profile fitting procedure used to determine β from the most intense peak (331) in the XRD pattern of MNP is illustrated in Figure 2.03 (a). The FWHM obtained from the fit (0.8445°) is converted into radians (= 0.0147 rad). This observed value of β also includes a contribution from the instrumental broadening (β_{ib}) arising from non-monochromaticity of X-ray beams, finite X-ray beam size, limitations in collimator to yield a perfectly parallel beam of X-rays, resolution (pixel size) of the detector, *etc.*

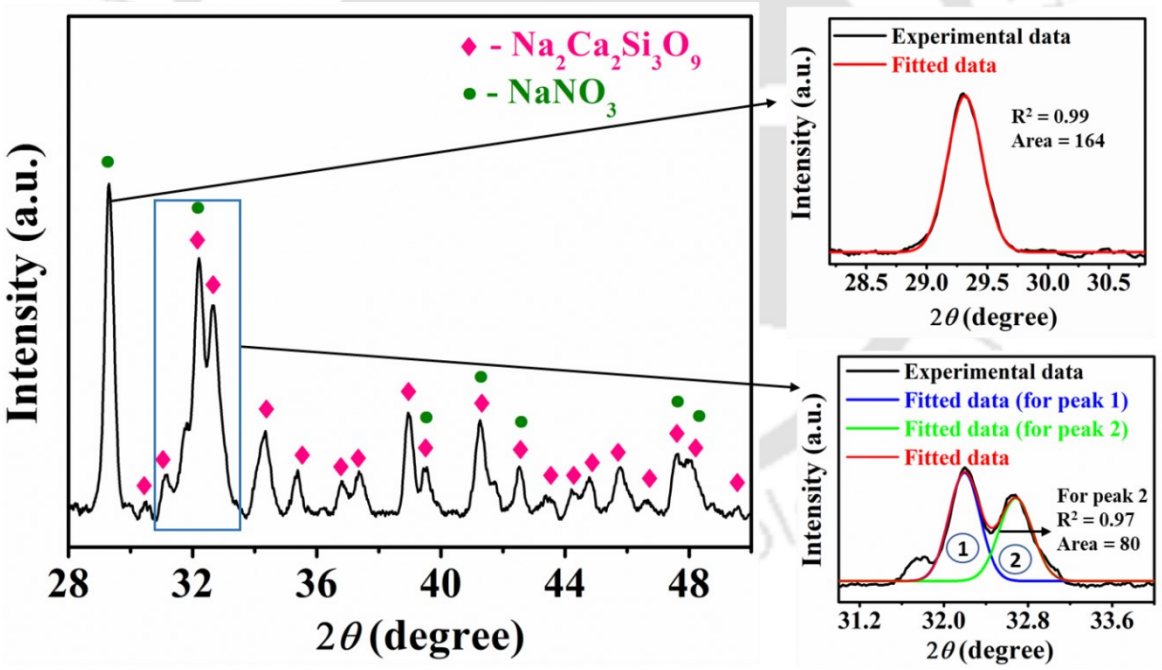

Figure 2.04: XRD pattern of S6 (53.5SiO_2-24.5CaO-6P_2O_5-16Na_2O) glass-ceramic showing the procedure followed to estimate the area under the peak and hence the percentage of the two crystalline phases in it.

In order to obtain the actual FWHM corresponding to the nanocrystallite size, β_{ib} should be subtracted from the β. To obtain a good estimate of β_{ib}, the XRD pattern of the fully crystallized standard Si sample supplied as a reference by Rigaku is recorded under the same experimental conditions. It is presumed that the peak broadening in the Si XRD pattern is entirely due to instrumental effects. Hence, the FWHM (= 0.08259° = 0.001887 rad.) of the strongest Si peak (111) peak appearing at $2\theta \approx 28.4°$ is taken as β_{ib}.

Figure 2.03 (b) shows the procedure used to estimate β_{ib}. Now the actual FWHM of MNP is

$$\beta_{act} = \beta - \beta_{ib} \quad (2.04)$$

Using this β_{act} in equation 2.03, an estimate of D_v (= 9 nm ±1 nm) is obtained.

In the analysis of multiphase glass-ceramics, an estimate of the relative phase percentage of each crystalline phase in the sample is required. In the typical XRD pattern of S6 sample shown in Figure 2.04, two crystalline phases, namely, combeite and sodium nitrate are identified. Origin software was used to estimate the integrated area under the strongest peak of each phase as shown in the inset in the Figure 2.04. From the integrated area, the percentage of combeite and sodium nitrate phases are estimated as ~33% and ~67%, respectively.

2.2.2. Scanning Electron Microscopy

When an incident electron beam interacts with a sample, several processes can occur: (a) some electrons get scattered, (b) some get absorbed, and (c) some transmit through the sample as depicted in Figure 2.05 (a). The scattered electrons that interact with the object are sensibly captured and used by the scanning electron microscope (SEM) for imaging and analysis. Low-energy secondary electrons are formed close to the surface and are employed in topographic imaging when incident electrons contact with the outer electrons of a specimen.

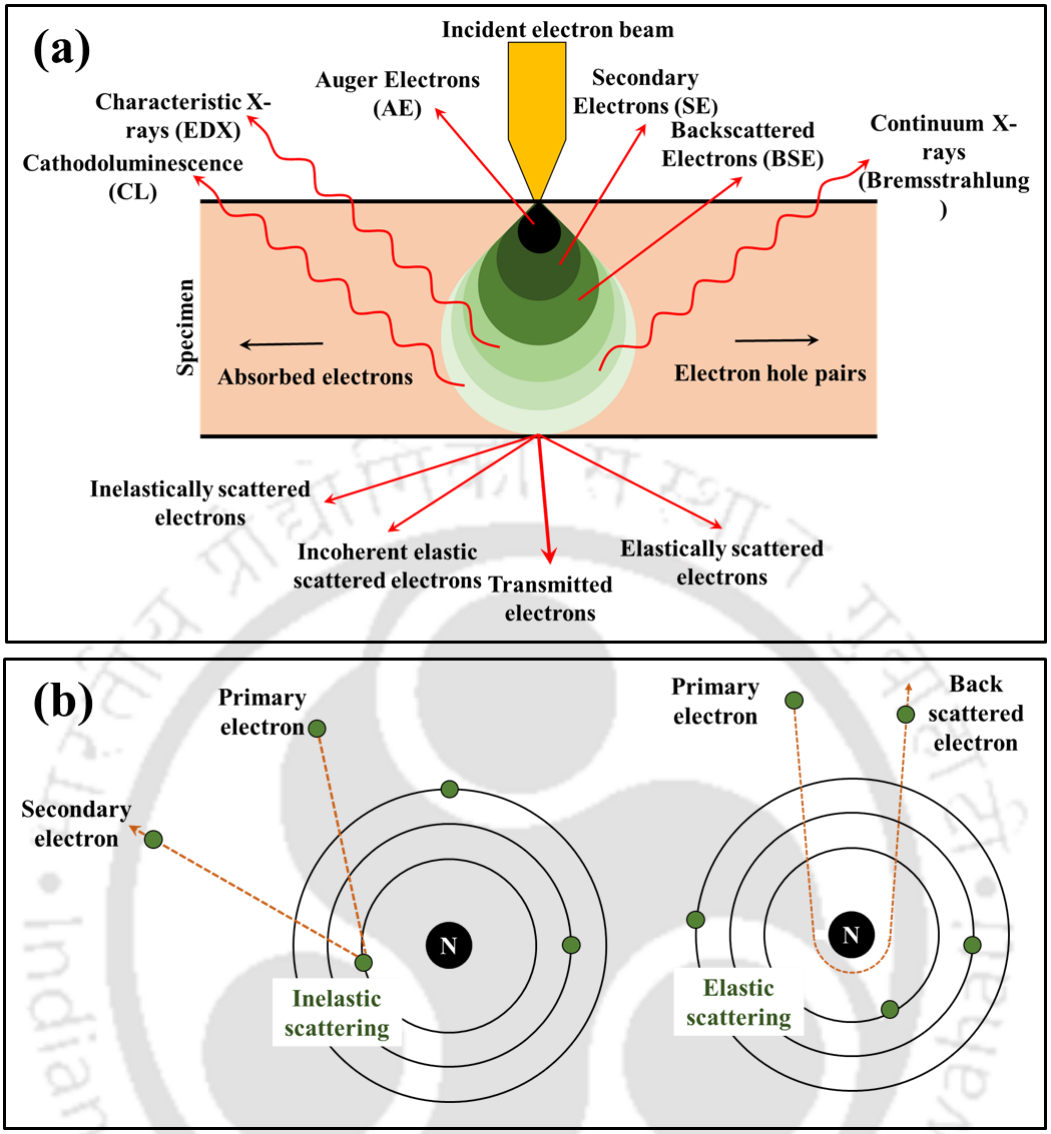

Figure 2.05: (a) A schematic representation of the interaction between electrons, and (b) the processes of elastic and inelastic electron scattering.

Electrons can be scattered elastically by the atomic system, producing greater energy backscattered (or reflected) electrons (Figure 2.05 (b)), which can penetrate deeper and provide contrast according to atomic number. Photon emission for composition analysis can also be produced by energetic electron interactions. As will be discussed later, energetic electrons can also cause photon emission when they contact the specimen This process is helpful for estimating the elemental composition of the specimen.

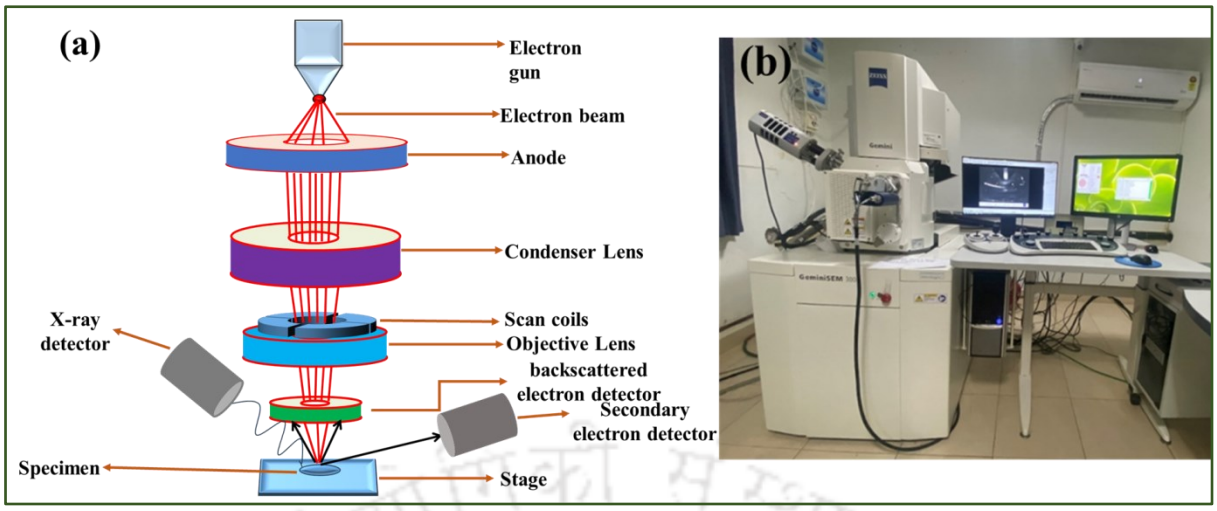

Figure 2.06: (a) Schematic diagram, and (b) photograph of a typical FESEM setup.

As shown in the schematic in Figure 2.06 (a), an electron source (electron gun), condenser lenses, objective lenses, scan coils, and detectors are some of the fundamental parts of SEM. A field emitter is used in the electron gun in a FESEM, unlike the thermionic emitter in a SEM. The thermionic emitter functions according to the principles of thermionic emission. However, the field emitter used here offers better resolution because of its smaller beam diameter. Electromagnetic lenses are used in electron microscopes whose focal length can be changed by adjusting the current flowing through a solenoid coil. For these studies, a Zeiss Gemini 300 Field Emission Scanning Electron Microscope (FESEM) was employed. Figure 2.06 (b) shows the image of the instrument. The particle size distribution of the synthesized nanoparticles was estimated from the recorded FESEM images using ImageJ software. Subsequently, a particle size histogram was plotted. The average particle size was calculated by fitting the histogram data with a normal distribution (Gaussian) function. Figure 2.07 (a) is a typical FESEM micrograph of a glass-ceramic powder sample designated as S_{Fe8}, revealing its particle morphology. A particle size histogram was plotted using the data obtained from the FESEM images, as displayed in Figure 2.07 (b).

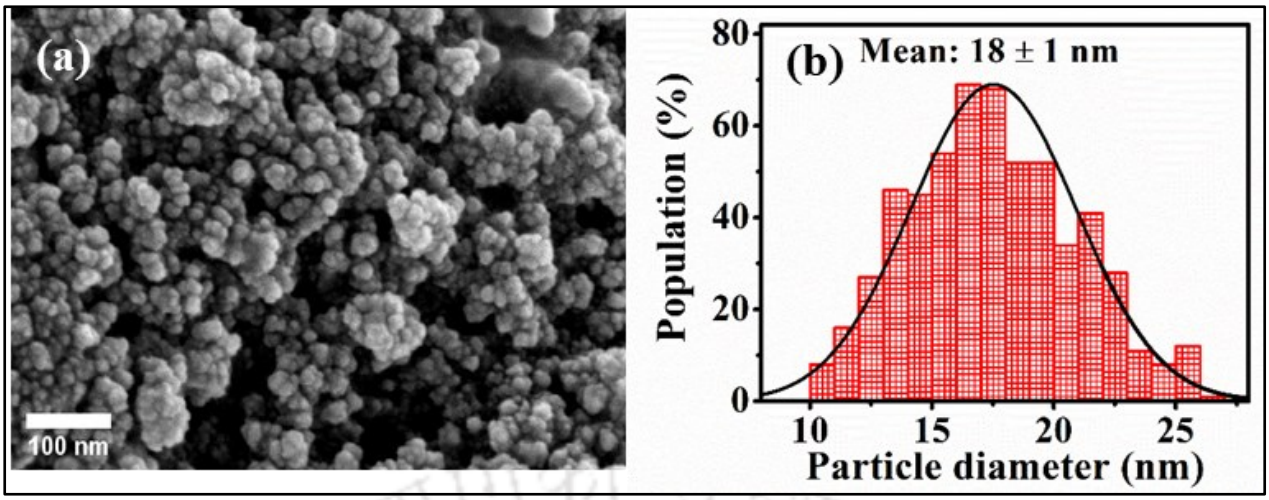

Figure 2.07: (a) FESEM micrograph, and (b) particle size histogram of S_{Fe8} ($37SiO_2$-$24.5CaO$-$24.5Na_2O$-$6P_2O_5$-$8Fe_3O_4$) powder sample.

Determining the elemental composition of the glass-ceramic nanopowder is the next important characterization step after its structural identification. As seen in Figure 2.05 (a), a number of events can take place in the SEM following the interaction of the incoming electrons with the specimen. As seen in Figure 2.08 (a), these interactions entail excitations of core electrons, which result in the emission of distinctive X-rays. Identification of the elements present in the material and their relative concentrations is made possible by the distinct energies at which each element emits the characteristic X-rays. These distinctive X-rays are collected by an X-ray detector in a SEM coupled with an energy dispersive spectrometer (EDS) attachment as a function of energy. The EDS spectrum obtained for an element by the instrument is shown in Figure 2.08 (b). The EDS spectrum was recorded using the same Zeiss Sigma instrument depicted in Figure 2.06 (b) and operated at an accelerated voltage of 20 kV. A raw EDS spectrum of glass-ceramic nanopowder is shown in Figure 2.09. The weight % of each element contained in the material can be found by analysing the spectra. The estimated elemental composition of x = 2 MGC sample in wt.% and at. % are also shown.

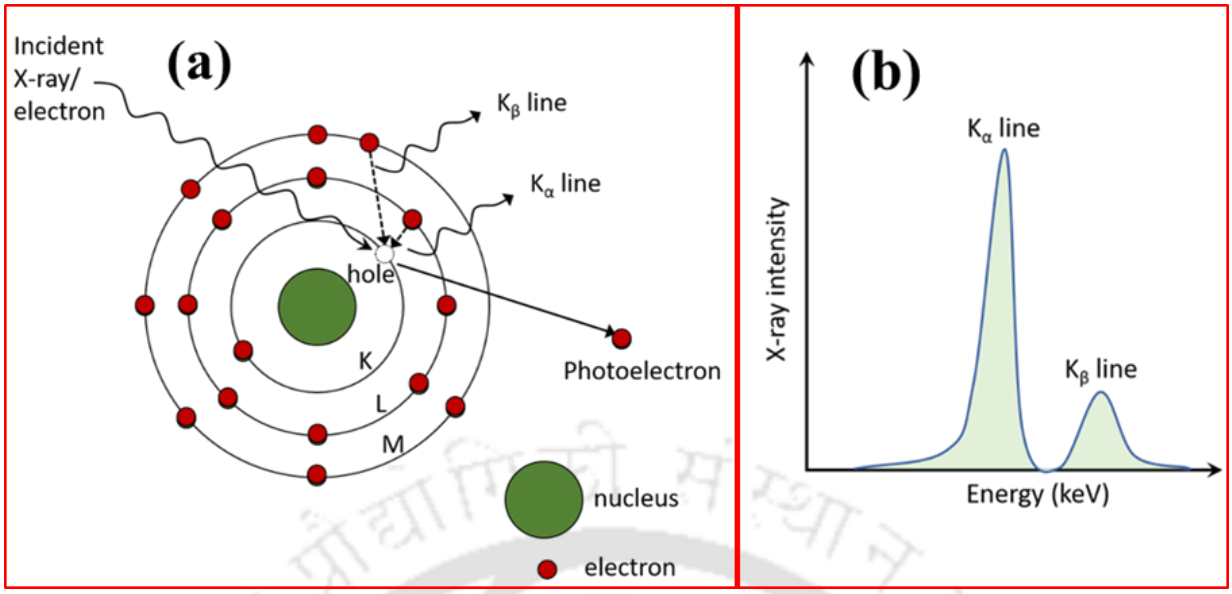

Figure 2.08:(a) Schematic of characteristic X-ray generation process from an atom, and (b) the corresponding EDS spectrum.

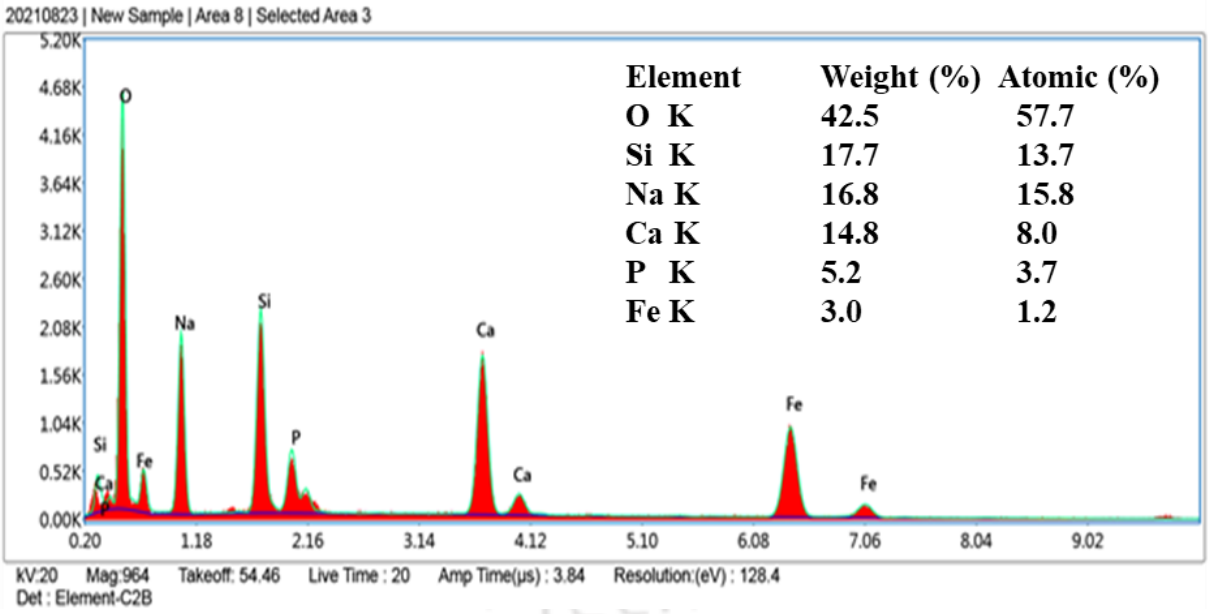

Figure 2.09: Raw EDS spectrum of x = 2 ((45-x)SiO_2-24.5CaO-24.5Na_2O-6P_2O_5-xFe_2O_3) sample.

2.2.3. Transmission Electron Microscopy

Figure 2.05 (a) illustrates the different ways in which the incoming electrons can interact with the specimen. After meeting with a thin specimen, a portion of the incoming intense electron beam may pass through (transmit) it. These transmitted electrons are examined in a transmission electron microscope (TEM) to determine the atomic structure. Electromagnetic condenser lenses in a TEM are used to accelerate and project electrons from the electron gun toward the thin specimen. As the electrons pass through the specimen, they (a) pass through without any obstructions, (b) scatter elastically (without losing any energy) as a result of their interaction with the atom/ion core potential field, creating electron diffraction patterns, and (c) scatter inelastically (due to the presence of defects, dislocations, grain boundaries, and other elements), causing variations in the intensity of the scattered electrons. The transmitted beams are further magnified using a set of intermediate and projector lenses before being shown on a fluorescent screen. To gather various data about the specimen, the transmitted electrons are detected using sensors. Data can be collected in diffraction or imaging modes by the TEM as schematically depicted in Figure 2.10. The field emission transmission electron microscope (FETEM, JEOL-2100F) shown in Figure 2.11 has been utilised in this thesis work.

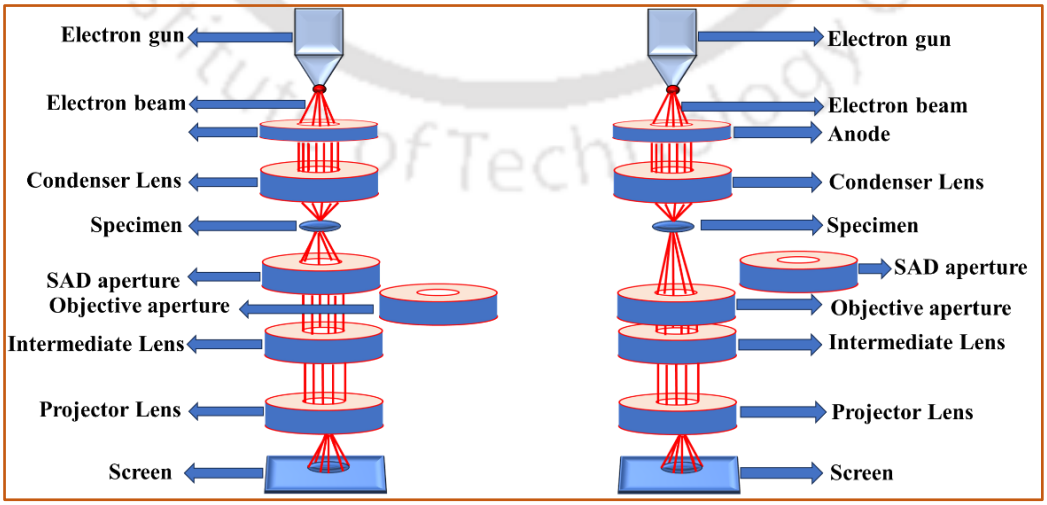

Figure 2.10: Schematic of a TEM operating in diffraction (left) and imaging (right) modes.

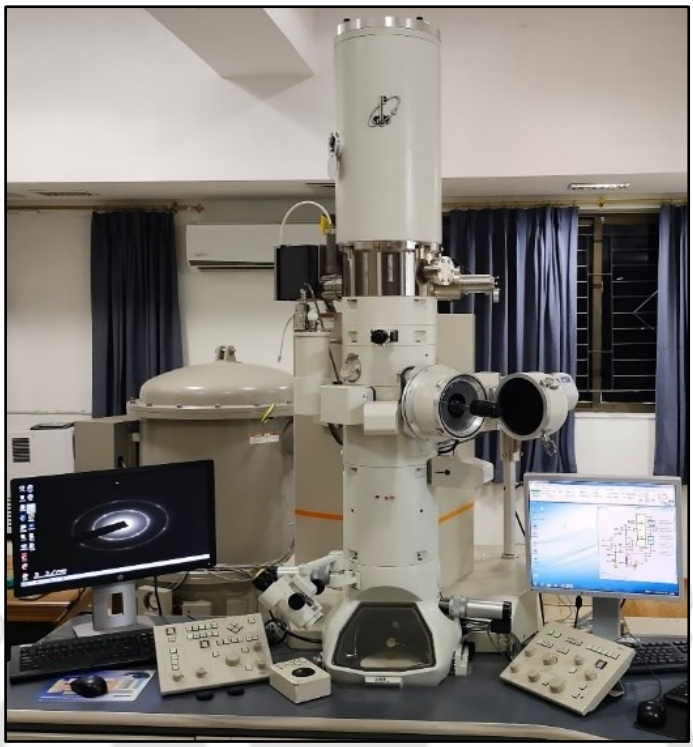

Figure 2.11: Photograph of JEOL-2100F FETEM utilized in this work.

In transmission electron microscopy, bright field images are produced by purposefully obstructing diffracted beams so that only the central beam is monitored. To achieve this, appropriately sized apertures are placed in the objective lens's back focal plane. On the other hand, dark field images are created by utilizing an aperture that blocks the central beam and only allows selected diffracted beams. Recombining the primary transmitted beam with one or more diffracted beams while maintaining their phases and amplitudes is another imaging technique. This high-resolution transmission electron microscopy (HRTEM) method is used to identify the atomic arrangements and lattice planes within a specimen. For assessing crystallographic structures and lattice parameters, HRTEM images are useful. Selective area electron diffraction (SAED), on the other hand, is accomplished by gathering all the diffracted beams to create a diffraction pattern and blocking the core beam. SAED patterns show unique spots in the case of single crystals, whereas concentric rings of distinct spots are produced in the case of polycrystalline specimens. For FETEM experiments, a small amount of nanoparticles is finely

dispersed in solvent. Next, a few drops of this colloid transferred to a copper TEM grid covered in carbon. After allowing for the solvent to dry, the TEM grid containing the dry particles is loaded into the TEM. Bragg's law simplifies into the following form where the Bragg angle is small such that $\sin\theta \approx \theta$ and when $n = 1$:

$$2\theta d_{hkl} = \lambda \qquad (2.05)$$

In a SAED pattern, as illustrated in Figure 2.12, L represents the distance between the sample and the screen (camera length), while r stands for the radius of the circle connecting the diffraction spots from a plane

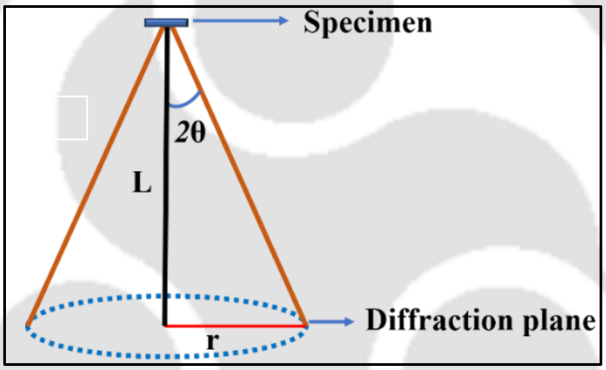

Figure 2.12: Schematic diagram of the geometry of an SAED pattern.

From the above Figure, for small θ,

$$2\theta = \frac{r}{L} \qquad (2.06)$$

Combining equations 2.05 and 2.06,

$$rd_{hkl} = L\lambda \qquad (2.07)$$

$$\therefore \quad d_{hkl} = \frac{L\lambda}{r} \qquad (2.08)$$

If the TEM is operated at 200 kV, $\lambda \approx 0.0027$ nm. Now, L and r depend upon each other, which shows that the camera length L can modify the radius of the ring pattern corresponding to a

particular plane. Adjusting the camera length allows us to control the magnification of the diffraction pattern to optimize the visibility of a specific diffraction spot or ring. Rewriting equation 2.08, we get,

$$d_{hkl} = \frac{1}{\left(\frac{r}{L\lambda}\right)} \qquad (2.09)$$

Now, the length scale given in SAED image is a measure of $\frac{r}{L\lambda}$ in nm^{-1}. This procedure eliminates the need to calculate the individual values of r, L and λ. The value of d_{hkl} can be determined by measuring the radius of the ring in nm^{-1} scale. Figure 2.13 (a) displays the SAED pattern of the MGCC sample processed at 550 °C. The radius of the first ring (from (003) plane) in the observed SAED pattern is 4.6 nm^{-1}, which corresponds to a d_{003} value of 0.43 nm.

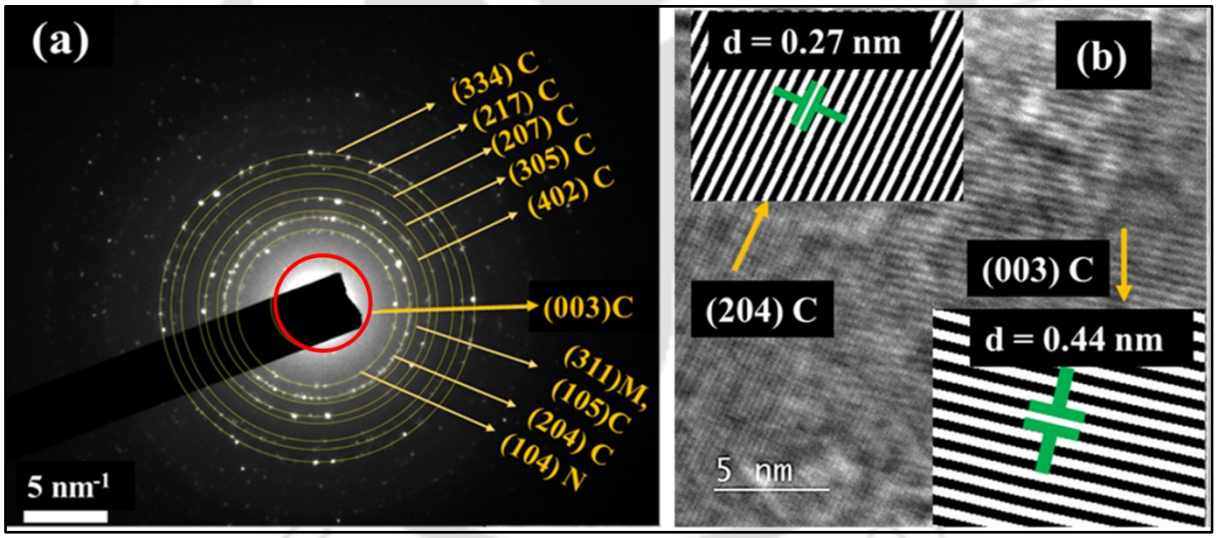

Figure 2.13: (a) SAED pattern, and (b) HRTEM and iFFT images of MGCC ($45SiO_2$-16.5CaO-$24.5Na_2O$-$6P_2O_5$-$8Fe_3O_4$) heat treated at 550 °C. C, M, and N refer to combeite, magnetite and sodium nitrate phases in the sample, respectively.

The first step in analysing the HRTEM micrograph is to choose the region of interest by using the crop or duplicate tool. Next, the fast Fourier transform (FFT) of the image HRTEM image is taken. One can then observe different sets of bright spots in the FFT image, which

correspond to distinct crystal plane. To create an inverted fast Fourier transformed (iFFT) image, a specific spot is selected from the FFT image and the lattice fringes corresponding to the chosen crystal plane is obtained. One can calculate the interplanar spacing (d_{hkl}) from these lattice fringes image using the line tool available in the software. Figure 2.13 (b) illustrates the two different planes, (003) and (204) of the combeite phase visible in the HRTEM image.

2.2.4. Differential Thermal Analysis

The technique known as differential thermal analysis (DTA) is used to detect thermal transition temperatures such as melting or sublimation temperature (T_m), onset glass transition temperature (T_g), and crystallization temperature (T_c). The current investigation used a commercial DTA (Hitachi STA7200) similar to the one depicted in Figure 2.14 (a). The DTA technique was developed for the first time in the 1950s [MULL1957].

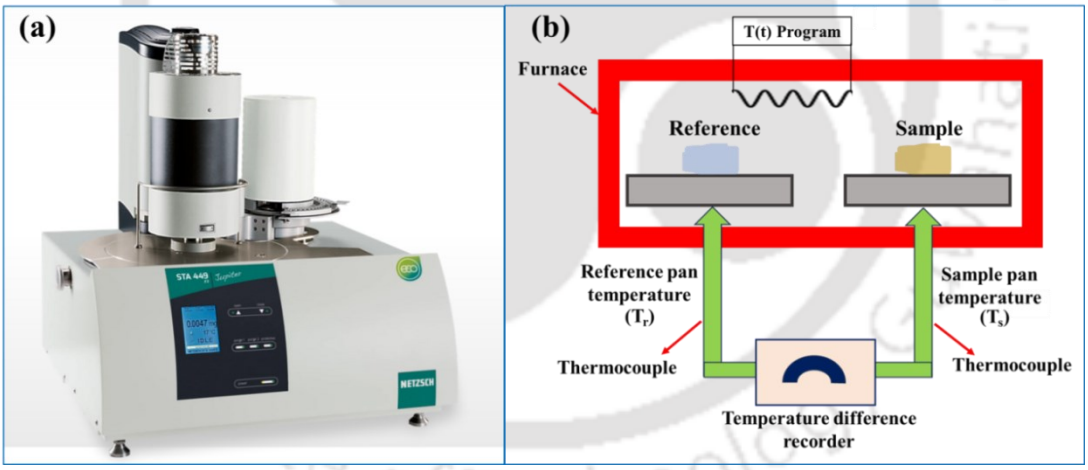

Figure 2.14: (a) Photograph, and (b) schematic functional diagram of STA7200 DTA.

Figure 2.14 (b) describes the functional parts of the DTA, namely, the sample holder (including sample pan and reference pan), furnace, thermocouple, temperature programming, and data recording system. In DTA, the sample material experiences a constant heat flow (dH/dt) relative to the reference, and the temperature difference between them is recorded over time or temperature at a constant heating rate. An empty alumina pan was used as reference in this

investigation. Both exothermic (when the sample releases heat) and endothermic (when the sample absorbs heat) in comparison with the thermally inert reference material can be observed in these studies. While glass to crystal transformation (or crystallization) is an exothermic reaction, melting of the crystal is endothermic. Glass transition is identified by an endothermic baseline shift. After performing baseline corrections, DTA curves were recorded up to 1000 °C at a constant heating rate of 10 K/minute. The DTA curve of the S5 ($57.5SiO_2$-$24.5CaO$-$6P_2O_5$-$12Na_2O$) glass sample is shown in Figure 2.15. The onset glass transition temperature (T_g) was estimated using the procedure illustrated in Figure 1.02 in chapter 1. Further heating of the sample revealed an exothermic peak (T_c). The peak value of the exothermic reaction is noted as T_c. The T_g and T_c were found to be 540 °C and 555 °C, respectively, for the S5 sample.

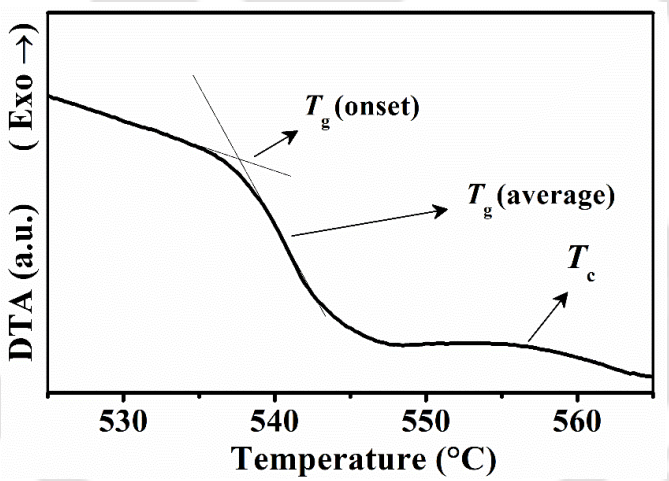

Figure 2.15: (a) DTA curve of S5 ($57.5SiO_2$-$24.5CaO$-$6P_2O_5$-$12Na_2O$) sample recorded at 10 K/minute.

2.2.5. Surface area analysis

The BET technique, developed in 1938 by Brunauer, Emmett, and Teller, is an extension of Langmuir's adsorption theory [PAVA2019]. This technique is popularly used for measuring the surface area of porous materials like porous solids, polymer catalysts, and powder samples. To facilitate analysis, the following assumptions are made: gas molecules can infinitely adsorb onto

the sample surface, these adsorbed layers do not interact with each other, adsorption at one site is independent of others, and all surface sites exhibit the same adsorption energy for the adsorbed gas (e.g., N_2 gas). Figure 2.16 illustrates the adsorption and desorption phenomena for N_2 gas. Before conducting measurements, the powder samples were placed in an oven at 100 °C for one day to eliminate physically adsorbed water. Following this step, an additional precautionary measure was taken in accordance with the instrument protocol. The samples underwent a degassing process at 150 °C for 3 h to remove any remaining physically adsorbed moisture.

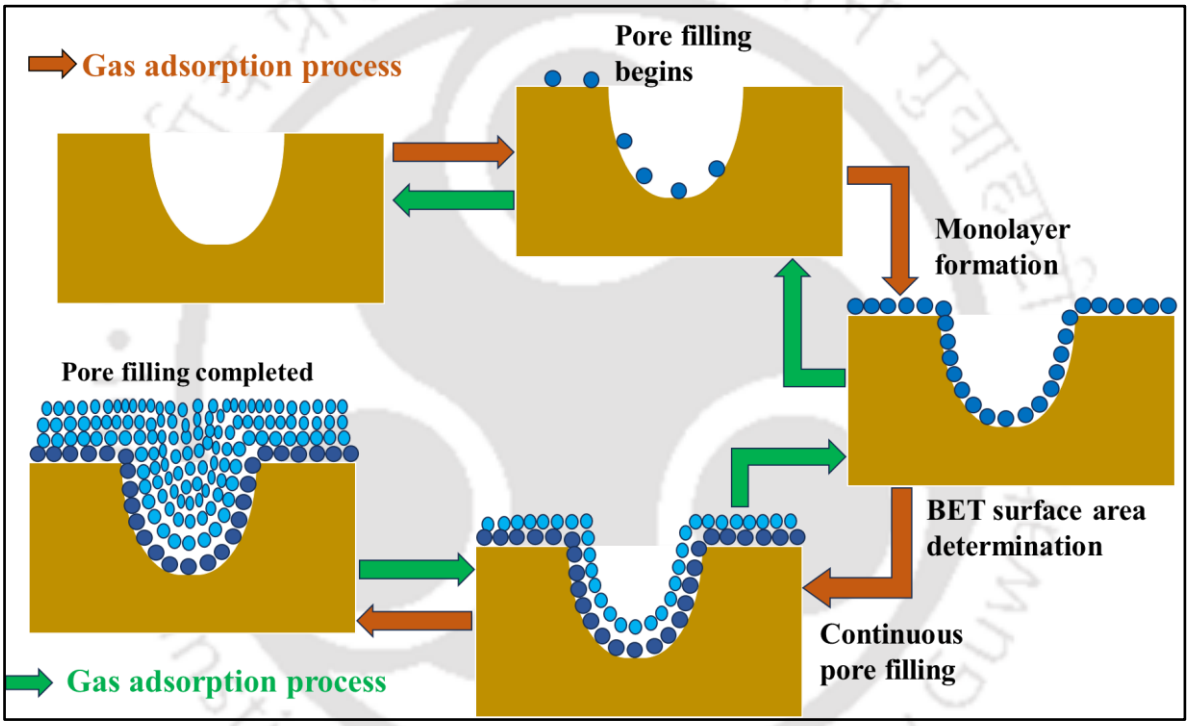

Figure 2.16: N_2 gas adsorption and desorption process in BET method.

The procedure involves exposing the powder sample to a controlled environment where gas molecules, typically N_2, are allowed to be adsorbed. As pressure increases, adsorption advances until the formation of the first monolayer. A partial vacuum is created to achieve a relatively lower pressure than atmospheric pressure. Once saturation pressure is reached, further adsorption ceases even with increased pressure. Following the adsorption of the monolayer, the sample is heated to remove the adsorbed molecules. The resulting data is plotted as a function of

relative pressure, yielding an isothermal Barrett-Joyner-Halenda (BJH) curve, as illustrated in Figure 2.17 (a). The recorded adsorption and desorption data exhibit hysteresis, indicating significant implication on material textural properties. Through this method, five types of isothermal curves can be attained, each describing various possible porous structures of the material under study [FU002020, FORO2021]. BJH isothermal curve of S_{Fe5} MSGC illustrated in Figure 2.17 (a) resembles a type-IV isotherm, which is associated with a mesoporous linked worm-like structure.

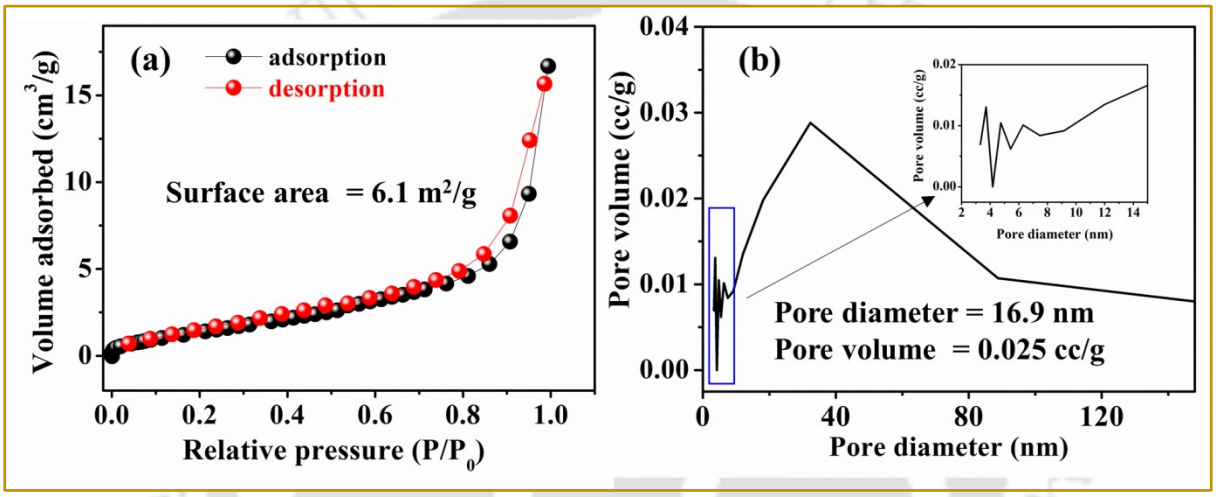

Figure 2.17: (a) Isothermal BJH curve, and (b) N_2 adsorption and desorption curve of S_{Fe5} MSGC ($45SiO_2$-$24.5CaO$-$24.5Na_2O$-$6P_2O_5$-$5Fe_3O_4$). Inset in (b) gives an enlarged view of data in the selected region.

To calculate the surface area, the BET equation given below is used [LADA2012]:

$$\frac{1}{W[(P_0/P)-1]} = \frac{1}{W_m C} + \frac{(C-1)}{W_m(P/P_0)} \qquad (2.10)$$

where W, (P_0/P), W_m and C represent the adsorbed N_2 at a given P_0/P, relative pressure, weight of monolayer adsorbate, and BET constant at 273 K and 1 atmospheric pressure, respectively.

*Multi-Point BET - Notepad

File Edit Format View Help

```
                    Quantachrome® ASiQwin™- Automated Gas Sorption Data
                                  Acquisition and Reduction
                            © 1994-2012, Quantachrome Instruments
                                        version 3.0

Analysis                                        Report
Operator:      IIT-GHY       Date:2023/03/21    Operator: IIT-GHY            Date:2023/03/23
Sample ID:     45S5_Fe304_21_03_2023 Filename:  45S5_Fe304_21_03_2023.qps
Sample Weight: 0.1456 g           Instrument:    Autosorb iQ Station 1            _
Outgas Time:   3.0 hrs            Outgas Temp.:  150 °C
Analysis gas:  Nitrogen           Non-ideality:  6.58e-05 1/Torr     CellType:     6mm w/o rod
Analysis Time: 3:42 hr:min        Bath temp.:    77.35 K
Analysis Mode: Standard                                            VoidVol Remeasure:off
VoidVol. Mode: He Measure         Cold Zone V:   1.54772 cc        Warm Zone V:   7.49439 cc
                                    Data Reduction Parameters
               Thermal Transpiration: onEff. mol. diameter (D): 3.54 ÅEff. cell stem diam. (d): 4.0000 mm

Adsorbate      Nitrogen               Temperature    77.350K
               Molec. Wt.: 28.013     Cross Section: 16.200  Å²    Liquid Density: 0.808  g/cc

           Relative                     Volume @ STP              1 / [ W((Po/P) - 1) ]
           Pressure
             P/Po                           cc/g

               6.72545e-02                  0.8033                      7.1821e+01
               7.43631e-02                  0.8429                      7.6256e+01
               8.87836e-02                  0.9110                      8.5574e+01
               1.14143e-01                  1.0194                      1.0113e+02
               1.63257e-01                  1.2061                      1.2943e+02
               2.13193e-01                  1.4017                      1.5467e+02
               2.38960e-01                  1.5044                      1.6699e+02
               2.63703e-01                  1.5984                      1.7928e+02
               2.88874e-01                  1.6999                      1.9120e+02
               3.13760e-01                  1.7985                      2.0341e+02

                                        BET summary
                                  Slope =       533.497
                                Intercept =       3.854e+01
                      Correlation coefficient, r =       0.999031
                                C constant=       14.841
```

Figure 2.18: Multipoint BET data file of S_{Fe5} MSGC sample recorded from the instrument.

To calculate the surface area, a linear portion of the data with about 10 data points in the range $0.05 < P/P_0 < 0.3$ was plotted. A typical multipoint output data file obtained for S_{Fe5} MSGC is presented in Figure 2.18. The slope and intercept obtained from the data file are related to W_m as follows [LADA2012]:

$$W_m = 1/(slope + intercept) \qquad (2.11)$$

The surface is then given by the relation [LADA2012],

$$S = (W_m A_m N)/M_v \qquad (2.12)$$

where N, A_m, M_v are the Avogadro's number, adsorbate cross section (=16.2 Å for N_2) and molecular weight of adsorbate, respectively.

The BJH analysis also covers the estimates of cumulative pore volume as a function of pore size. The derivative of the cumulative pore volume gives the pore size distribution in the material. In Figure 2.17 (b), the pore size distribution is illustrated, showcasing the range of pore sizes present in the investigated sample. Additionally, the inset of Figure 2.17 (b) provides further detail by depicting the multipore distribution at lower pore diameters. The inset highlights the broad range of pore diameters observed within the sample, indicating a diverse distribution of pores across different size categories.

2.2.6. Vibrating Sample Magnetometer

A vibrating sample magnetometer (VSM), invented by Foner in 1959, functions according to Faraday's law of electromagnetic induction and is employed to investigate the magnetic qualities of the samples [FONE1959]. Figure 2.19 shows a schematic of one such device. The induced electromotive force is directly proportional to the rate of change in magnetic flux through the coil, *i.e.*,

$$\varepsilon \propto -\, d\varphi/dt \qquad (2.13)$$

Figure 2.19 (b) shows a schematic diagram of a contemporary VSM. The VSM is made up of a (a) sample vibration excitation unit, (b) quartz rod sample holder, (c) electromagnet with bipolar power supply, (d) hall probe (e) pickup coil duos, (f) lock in amplifier, (g) control unit, and (h) programmable computer interface. The sample vibration exciter unit is used to vibrate the specimen at a set frequency while it is in a uniform magnetic field. Through electromagnetic induction, the flux variation within the pickup coils causes an electromotive force to be induced while the magnetic specimen vibrates. By comparing this generated voltage to a piezoelectric vibration frequency signal, a lock-in amplifier measures the induced voltage. The induced voltage measured by lock-in amplifier is directly proportional to the sample vibration frequency and amplitude. Through the use of the lock-in amplifier and feedback techniques, isolation is

achieved just for the magnetic moment signal component. After that, this signal is transformed into electromagnetic units, or emu, and it is shown on a digital panel metre or stored in the interfaced computer.

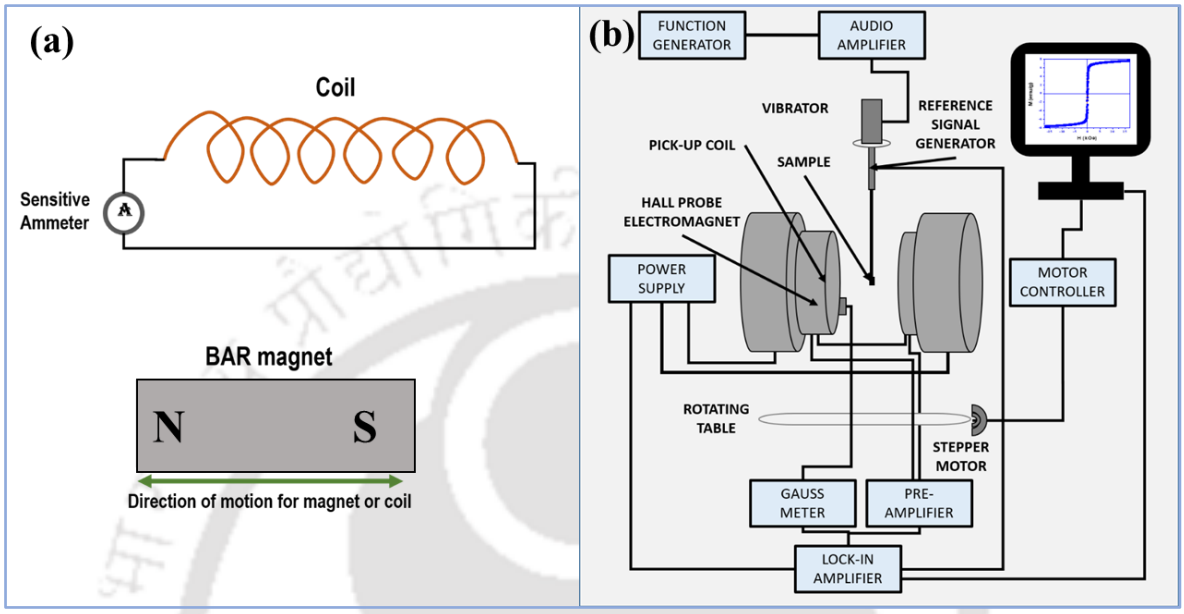

Figure 2.19: Schematic diagram representing (a) electromagnetic induction (Faraday's law), and (b) VSM set up.

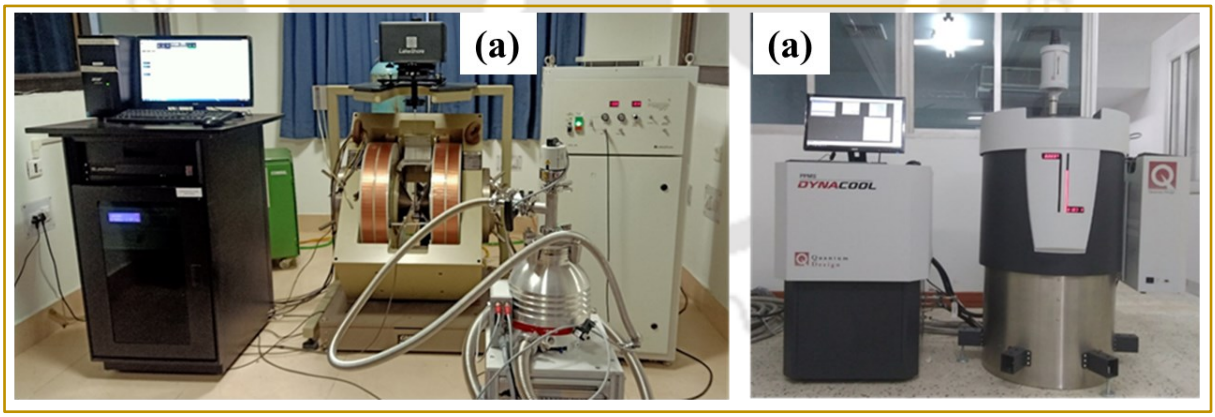

Figure 2.20: Photograph of (a) the electromagnet based Lakeshore 7410 VSM, and (b) the 9T PPMS (Quantum Design, DynaCool) with a VSM attachment.

Before performing measurements on materials, the instrument is usually calibrated using a standard nickel spherical specimen with a known magnetic moment (M = 6.92 emu at H = 5

kOe). With the instrument's software, the user creates a program sequence based on predetermined criteria. To minimize errors in obtaining magnetic parameters such as M_s, M_r, H_c, T_C, and so on, this sequence is tailored to contain the best steps and limits of magnetic fields or temperatures to obtain isothermal *(M-H)* or thermo-magnetic *(M-T)* curves. Considerable progress has been achieved in VSM instrumentation to improve sensitivity while preserving the core idea. In the current work, an electromagnet-based VSM (Lakeshore 7410) was used for high-temperature (300-1273 K) measurements, whereas a 9 Tesla Physical Property Measurement System (PPMS, Quantum Design, DynaCool) VSM was used for low-temperature (5–300 K) magnetic measurements. Figure 2.20 (a), and (b) show the VSM and PPMS configurations, respectively. Polychlorotrifluoroethylene (Kel-F) sample holders and polypropylene capsules were placed inside a brass holder container in the PPMS. The sample was held in place for high temperature measurements by a sturdy quartz rod. Attaching the sample to the quartz rod required the application of high temperature ceramic putty. In addition, the oven was constantly purged with argon gas to prevent the sample from oxidising at such high temperatures.

The *M-H* hysteresis loop of MNP was recorded at room temperature, and the *M-T* curve of the magnetite S_{Fe5} MSGC sample was recorded from 5 to 310 K under zero field cool (ZFC) and field cooled (FC) conditions, as depicted in Figure 2.21 (a) and (b), respectively. The S_{Fe5} MSGC sample is first cooled to 5 K in the ZFC (zero-field cooled) condition without the use of a magnetic field. The magnetization is then monitored while the temperature is raised in the presence of 500 Oe magnetic field. On the other hand, the sample is first subjected to a magnetic field of 500 Oe in the FC condition. Then, the sample is cooled to 5 K while the magnetic field is maintained. Subsequently, the magnetization is measured as the temperature is raised. Mainly, two phenomena can be observed from the ZFC and FC curves: (1) a broad peak, the maximum value of which can be related to the blocking temperature (T_B) below which the spins are blocked,

and (2) the splitting of the ZFC and FC curves at the bifurcation temperature (T_{BF}), above which all spins are unblocked, as displayed in Figure 2.21 (b).

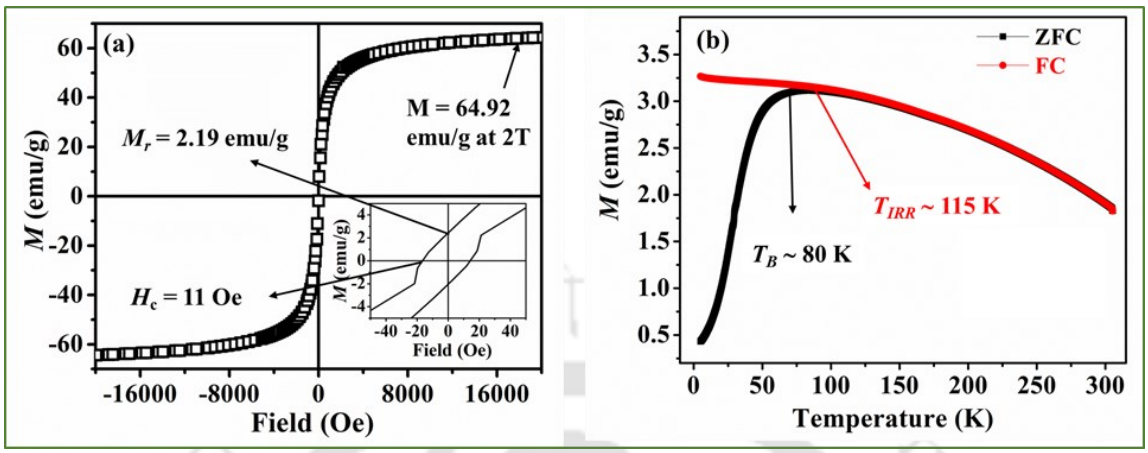

Figure 2.21: (a) Room temperature *M-H* curve of MNP. (b) Temperature dependent magnetization (*M-T*) curves of S_{Fe5} MSGC ($40SiO_2$-$24.5CaO$-$24.5Na_2O$-$6P_2O_5$-$5Fe_3O_4$) recorded under ZFC and FC modes.

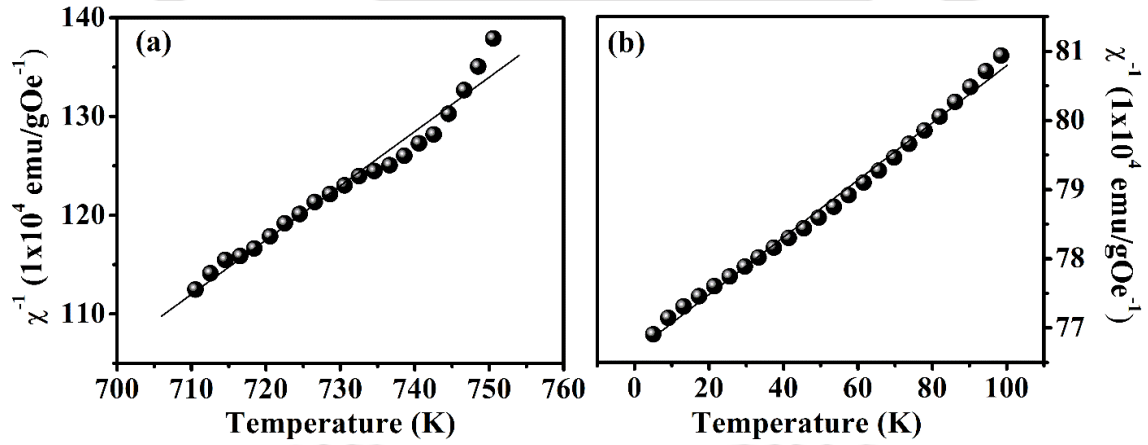

Figure 2.22: Temperature dependent inverse susceptibility of S_{Fe8} MSGC ($37SiO_2$-$24.5CaO$-$24.5Na_2O$-$6P_2O_5$-$8Fe_3O_4$) in (a) high, and (b) low temperature regimes.

Figure 2.22 (a and b) depict the temperature-dependent reciprocal magnetic susceptibility (χ^{-1}) of S_{Fe8} MSGC nanopowder in the high and low temperature regimes. The linear behavior of these $\chi^{-1} - T$ plots is described by the Curie-Weiss law.

$$\chi^{-1} = \frac{T - T_C}{C_M} \qquad (2.14)$$

In equation (2.14), T_C represents the Curie temperature, while C_M denotes the molar Curie constant. Solid lines in Figure 2.22 (a and b) represent the least squares fits to the χ^{-1}-T data as per equation (2.14). The fraction of iron ions can be estimated using equation (2.15) and equation (2.16) [ILON1988].

$$x\left(\mu_{exp}\right)^2 = x_1\left(\mu_{Fe^{3+}}\right)^2 + x_2\left(\mu_{Fe^{2+}}\right)^2 \qquad (2.15)$$

$$x = x_1 + x_2 \qquad (2.16)$$

In equations (2.15) and (2.16), $\mu_{exp} = 2.827(^{C_M}/_{2x})^{\frac{1}{2}}$ is the effective magnetic moment which can be estimated from the data in Figure 2.22, x_1 and x_2 are the weight fractions of Fe^{3+} and Fe^{2+} ions and x is the total weight fraction of Fe ions. The effective magnetic moment values of free Fe^{2+} and Fe^{3+} ions, viz., $\mu_{Fe^{2+}} = 4.90\mu_B$ and $\mu_{Fe^{3+}} = 5.92\mu_B$ [BURZ1979] were used to calculate μ_{exp}.The slopes of the linear fits to the high and low temperatue data shown in Figure 2.22 (a and b) were used to calculate C_M values of 3.8×10^4, and 5.6×10^4 emuK/Oemol, respectively. The corresponding μ_{exp} calculated using the C_M values are $5.51\mu_B$ and $5.27\mu_B$, respectively, which differed by ~5%. Considering the difficulty in accessing a high-temperature system, μ_{exp} is estimated for the low temperature data with relative ease [NAG0A2019, PAVI2014]. Subsequently, the fraction of iron ions within the S_{Fe8} MSGC can be estimated using equations 2.15 and 2.16.

2.2.7. Analysis of magnetic fluids (aqueous colloids)

Magnetic fluids have been prepared to investigate the heating capacity of the MGC samples for assessing them for MH application. To delve into the stability and surface charge of the MGC

powder in an aqueous solvent, a Zetasizer instrument was utilized. The system comprises of three key components, namely, an optical unit, a dispersion unit, and a computer, as depicted in Figure 2.23. The optical unit houses two distinct wavelength lasers (usually, red and green) for probing the colloidal sample. The cell area denotes where cells (cuvettes) containing the colloidal samples are placed for analysis. The MPT-2 titrator enables automated titration during data recording. The Zetasizer software governs the measurement conditions and provides options to set them. The instrument facilitates two types of analyses: static and dynamic. In static analysis, the surface charge over the sample surface, termed zeta potential, and molecular weight of the fluid are determined. Dynamic analysis offers a deeper understanding of colloidal particle behavior, by focusing on characteristics such as mobility, stability, aggregation and response to external factors like pH, temperature, *etc*. To conduct measurements, MGC powder sample weighing 1 mg was dispersed in 1 ml of Milli-Q water to form a magnetic fluid. The same instrument was used in two different modes to gather information about zeta potential and colloidal particle size. Notably, the sample holder or cuvette for both measurements are different as displayed in Figure 2.23.

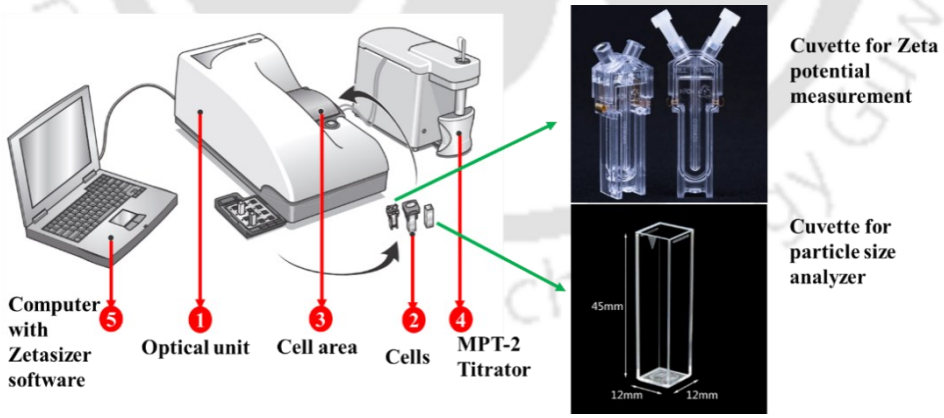

Figure 2.23: Zetasizer set up with all components.

In static analysis, when a powder sample is dispersed, a hydrodynamic layer forms over the sample surface with different charges. In the presence of an electric field, charged particles

are attracted towards the opposite electrode. The velocity of this movement is utilized to measure the zeta potential, computed using the equation (2.17).

$$\zeta = (3\eta\mu e)/(2\varepsilon f(ka)) \qquad (2.17)$$

Here, η is the viscosity of the suspension, μe is the mobility of the colloidal particles, ϵ is the dielectric constant of the solution, f is the Henry function, k is the Debye length (where the inverse is the thickness of the charge layer), and a is the equivalent spherical diameter of the particles.

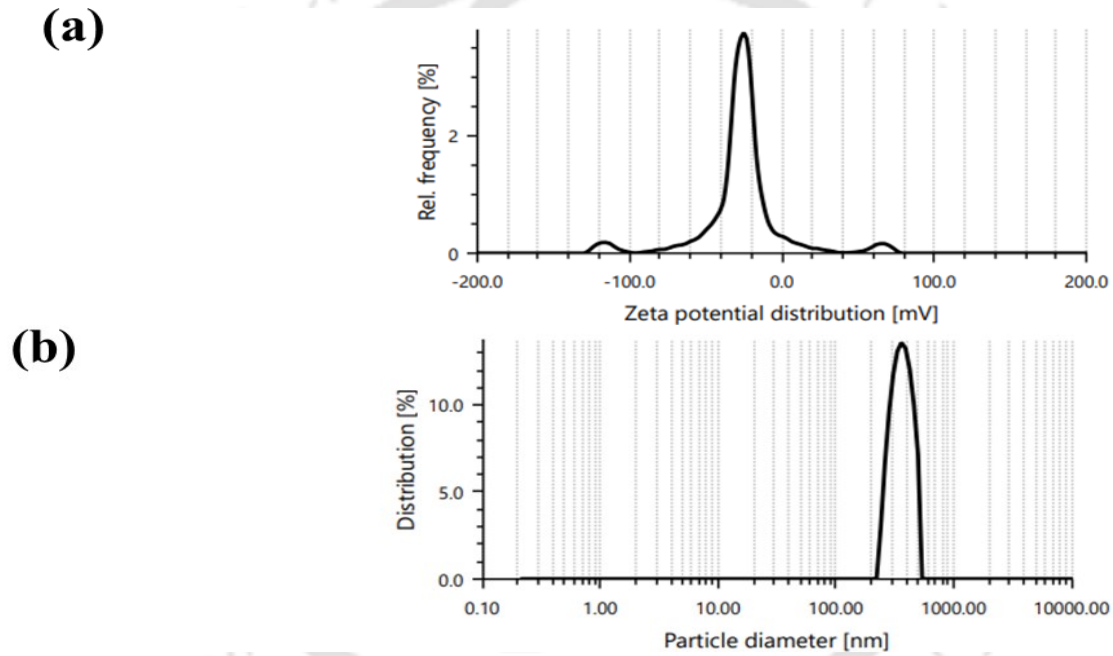

Figure 2.24: Output profile of (a) zeta potential distribution of aqueous colloid of S_{Fe8}, and (b) aqueous particle size distribution of x =10 MGC sample recorded at room temperature.

Figure 2.24 (a) illustrates the distribution of zeta potential of aqueous S_{Fe8} MSGC, from which ζ = -27.4 mV was determined. In dynamic analysis, light is allowed to fall on a well-dispersed aqueous fluid and the scattered light at different angles is collected. The intensity of scattered light fluctuates due to Brownian motion and this fluctuation intensity is analysed to determine the average size distribution of aqueous particles (colloidal). The recorded data of the

aqueous colloidal size distribution of aqueous x = 10 MGC colloid is illustrated in Figure 2.24 (b). Analysis yielded a size distribution of ~900 nm.

2.2.8. Electron Paramagnetic Resonance

A useful tool for examining the environment of transition metal species containing one or more unpaired electrons is electron paramagnetic resonance (EPR) [ANTU2019]. EPR is utilized to determine the type of the interaction between the iron ions within the glass and the glass-ceramic network. Every electron is associated with magnetic moment, a spin quantum number (s = ½), and corresponding magnetic quantum number (m_s = ±½). Two states are formed in response to applied field B_0: one parallel (m_s = +½) to the applied field's direction and other antiparallel (m_s = -½). The parallel state represents the lower energy level, while the antiparallel state represents the higher energy level. The energy difference between these states (ΔE) can be denoted as $\Delta E = g\mu_B B_0$, in which g, μ_B, and B_0 represents the electron's g-factor, the Bohr magneton, and the applied magnetic field, respectively. The relationship between the applied magnetic field B_0 and the frequency v of the EPR transition is established by the resonance condition, often represented as,

$$h\nu = g\mu_B B_0 \qquad (2.18)$$

This equation serves as the fundamental principle behind EPR spectrometry. Two approaches can be employed for achieving the resonance condition, viz., (i) varying the magnetic field while maintaining a constant frequency, or (ii) varying the frequency while maintaining the same magnetic field. It is usually more convenient to vary the magnetic field by adjusting the current in a coil, making the variable magnetic field approach more popular. In typical EPR experiments, microwave frequency in the range of 9 - 10 GHz and a varying applied magnetic field of 0 to 0.9 T are employed. When paramagnetic species containing sample such as MGCs are subjected to this applied field at a fixed microwave frequency of 9.4 GHz, the resonance

condition occurs when the energy gap matches with the appropriate field value. This condition elucidates the absorbed energy through the spectrum. Generally, the first derivative of the spectrum is used in the analysis.

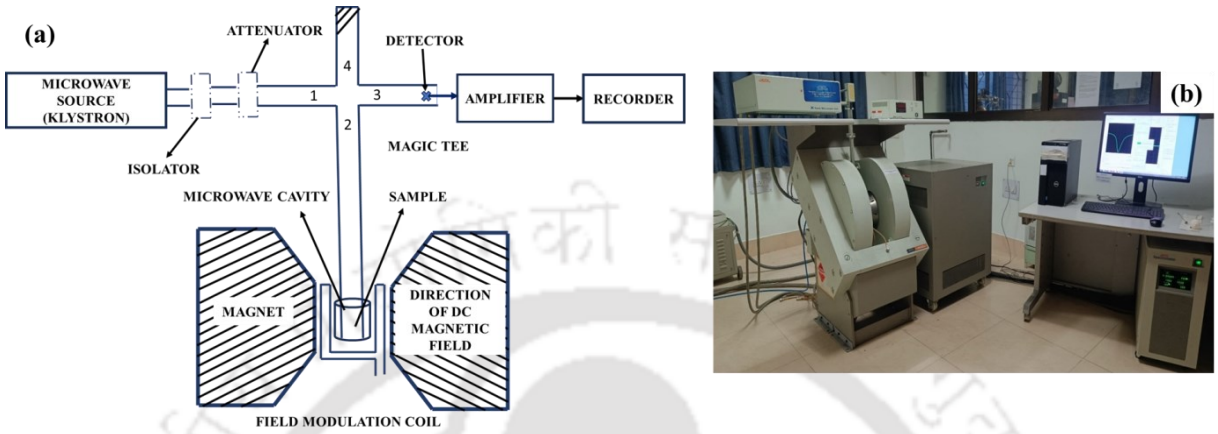

Figure 2.25: (a) Schematic Figure, and (b) photograph of JEOL-JES-FA200 EPR spectrometer.

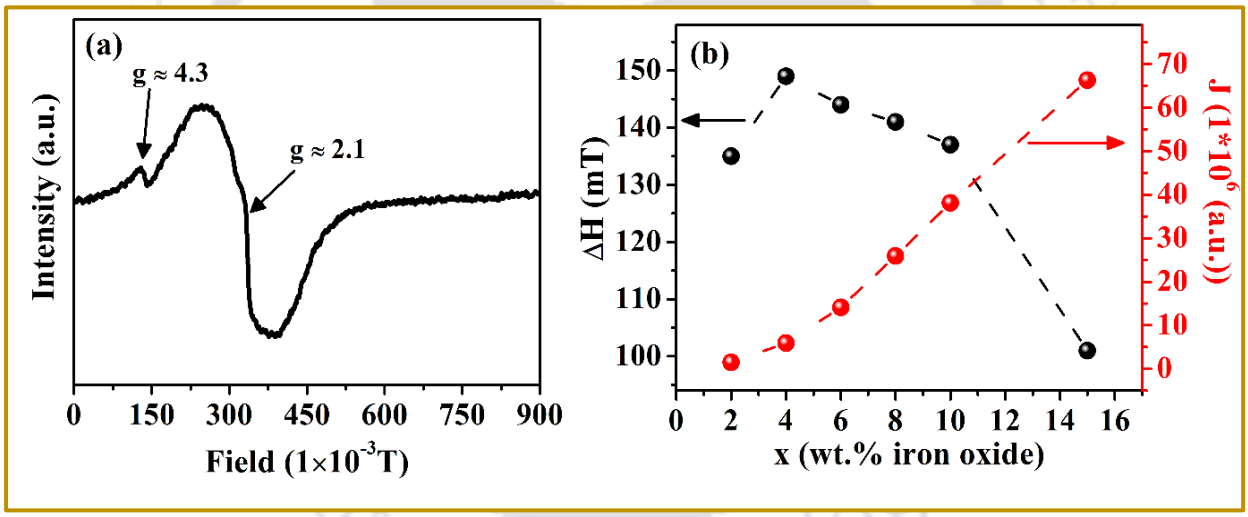

Figure 2.26: (a) EPR spectrum of x = 2 MGC powder, and (b) variations of integral line intensity *J* and linewidth *ΔH* of g ≈ 2.0 spectral line of (45-x)SiO_2-24.5CaO-24.5Na_2O-6P_2O_5-xFe_2O_3 (wt.%) (2 ≤ x ≤15) MGC powders.

The instrumentation of the EPR spectrometer requires (a) an electromagnet to generate a stable, homogeneous, and strong magnetic field, (b) a sample container to retain the sample, (c) a Klystron oscillator to generate the desired frequency in microwave range, (d) a pick-up coil to

receive the microwave signal from the specimen and couple it to the detector, (f) a recording device with signal processing unit, *i.e.* a computer with an appropriate software as shown in schematic diagram (Figure 2.25 (a)). Figure 2.25 (b) displayed the photograph of the EPR spectrometer used for this work. EPR spectra of the processed ceramic powders were recorded at room temperature with the JEOL EPR Spectrometer (model JESFA200) operating at 9.4 GHz. The MnO spectrum was used as a reference to calibrate the spectrometer with the help of built-in software. For the EPR measurement, a power of 1mW and a magnetic field ranged from 0 to 900 mT were set, and ~20 mg of x = 2 MGC powder sample was placed in a sample holder (quartz tube). Figure 2.26 (a) presents the EPR spectrum acquired for the x = 2 MGC. Fe^{2+} ions do not directly contribute to EPR absorption spectra, but they can influence the absorption lines' characteristics through their interaction with Fe^{3+} ions. EPR spectral line at $g \approx 4.3$ in the x = 2 MGC system signify presence of isolated Fe^{3+} ions located at different sites, whereas absorption at $g \approx 2.0$ indicates clustering behavior of Fe^{3+} ions within the ceramic network. The absorption line intensity (J) and other EPR parameters can be computed using the formula $J = I(\Delta H)^2$ based on the peak-to-peak height (I) and linewidth (ΔH) of the EPR absorption profiles. Figure 2.26 (b) illustrates the variation of EPR parameters corresponding to the $g \approx 2.0$ absorption lines of a ceramic sample with different iron oxide concentrations. This depiction allows for insights into the alterations in the local environment surrounding Fe^{3+} ions in the MGC at various iron oxide concentrations.

2.2.9. Magnetic induction heating capacity measurement

The induction heating capacity of magnetic glass-ceramics was analysed using the EasyHeat Ambrell 8310 UK setup. It consists of a power supply, induction coil, temperature measurement system. The inducting heating set up is depicted in Figure 2.27. The RF power supply provides the required electrical power to the coil. The helical copper coil acts as the magnetic field generator, offering precise and uniform magnetic field strength through adjustments in coil

turns and configuration. An optical fibre sensor was used to measure the temperature rise in the magnetic fluid accurately. This sensor ensured high precision temperature readings for in-depth analysis of the heating process.

Figure 2.27: Induction heating measurement system.

Before conducting the measurement, MGC powder was dispersed properly in 1 ml of Milli-Q water and sonicated for 10 minutes to ensure uniform dispersion. The magnetic fluid was then subjected to an alternating magnetic field, causing heat loss from hysteresis to be measured in terms of temperature rise. In this experiment, the magnetic field strength, current, and frequency were set at 12.89 kA/m, and 336 kHz, respectively. The temperature rise of the x = 15 MGC fluid was recorded using specialized software, and the data were plotted against time, as illustrated in Figure 2.28 (a). The specific absorption rate (*SAR*), which measures absorbed energy, was used to evaluate the heating capacity of the magnetic fluid. As observed in Figure 2.28 (b), factors such as the system's operating conditions (adiabatic or non-adiabatic) and the initial temperature rise have an impact on *SAR* values. In an adiabatic system, temperature rises

linearly as there's minimal heat exchange with the surroundings, while in a non-adiabatic system, temperature may saturate due to equilibrium with the surroundings. Consequently, adiabatic systems exhibit higher *SAR* values than non-adiabatic systems.

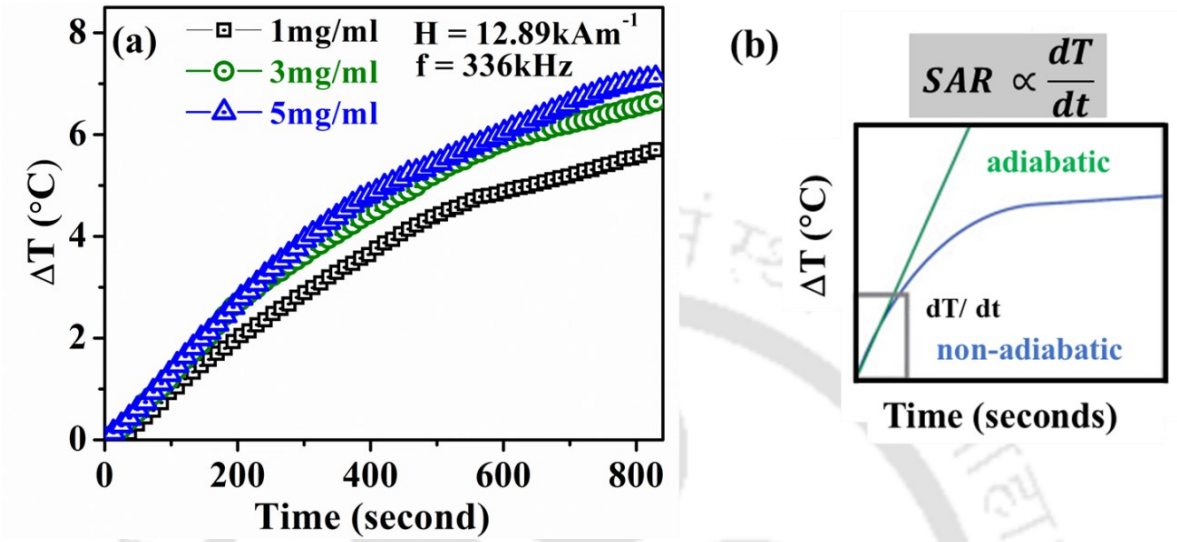

Figure 2.28: (a) Temperature rise of x = 15 MGC fluid with various fluid concentration. (b) A typical heating curve describing the data analysis procedure.

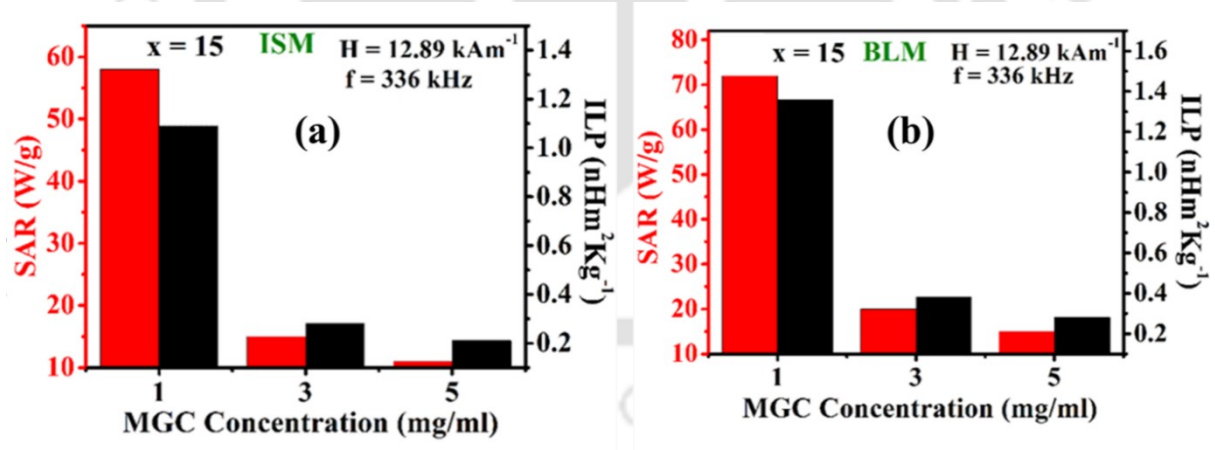

Figure 2.29: Calculated *SAR* and *ILP* values of MGC fluids of x = 15 ((45-x)SiO_2-24.5CaO-24.5Na_2O-6P_2O_5-xFe_2O_3) using (a) ISM, and (b) BLM for various fluid concentration.

Initial slope method (ISM) and Box Lucas method (BLM) are two common methods used to calculate *SAR* value [DEAT2014]. The *SAR* value (in W/g) was estimated from the initial linear slope (dT/dt) using the ISM relation (2.19) [LANI2019]

$$SAR = C\frac{V_s}{m} \times \frac{dT}{dt} \qquad (2.19)$$

where C (= 4.186 j/g °C) is the specific heat capacity of the solvent, V_s is the sample volume and m is the sample mass. BLM was also used to characterize the heating capacity of magnetic fluid by using the relation (2.20) [SOET2017, RING2020],

$$\Delta T = A(1 - e^{(-B\Delta T)}) \qquad (2.20)$$

In the above expression, A and B represent fitting parameters. Then, the *SAR* was computed by employing equation (2.21).

$$SAR = \frac{ABC_v m_i}{m_{Np}} \qquad (2.21)$$

In equation (2.21), m_{Np}, m_i, and C_v represent the mass of magnetic material, the entire mass of the magnetic fluid, specific heat capacity of aqueous solvent, respectively. Direct comparison between the reported and observed *SAR* values is not straight forward as determination of *SAR* depends on various factors, including the magnetic fluid's mass, size, shape, and applied frequency of the particles as well as the strength of the field. In order to facilitate comparison with available literature, the *SAR* was normalized with *f* and *H,* yielding the intrinsic loss power (*ILP*) which is expressed as,

$$ILP = \frac{SAR}{f \times H^2} \qquad (2.22)$$

Figure 2.29 (a) and (b) depict the *SAR* and *ILP* values of x = 15 MGC, calculated using the ISM and BLM methods, respectively, at different fluid concentrations.

2.2.10. Bioactivity Test (*In vitro* apatite formation)

Bioactivity assessment can be defined by the capacity of a material which can have the potential to mimic or replace the human body in physiological environment. *In vitro* bioactivity test is performed before a biomaterial is tested on animal or human. To achieve this, the Kokubo's recipe was followed to produce a modified simulated bodily fluid (SBF) solution [HENC1982a, KOKU2006]. Both SBF and human body plasma (HBP) contain comparable amounts of inorganic ion concentrations, as shown in Table 2.01. Therefore, it is considered that *in vitro* test based on SBF mimic *in vivo* testing in animal or human models.

Table 2.01: The ion concentrations of SBF and HBP [OYAN2003, TAKA2004].

Ion (mM)	Na^+	K^+	Mg^{2+}	Ca^{2+}	Cl^-	HCO_3^-	HPO_4^{2-}	SO_4^{2-}
SBF	142.0	5.0	1.5	2.5	17.8	4.2	1.0	0.5
HBP	142.0	5.0	1.5	2.5	103.0	27.0	1.0	0.5

2.2.10.1. *In vitro* bioactivity assessment

To prepare 1000 ml of SBF, 700 ml of Milli-Q water was taken in a conical flask and heated to 35 °C using a heating mantle. The reagents numbered 1 through 8 as listed in Table 2.02 are sequentially introduced into the flask. After adding each reagent, the solution is stirred for 30 minutes to ensure homogenous mixing. Following the addition of the eighth reagent, tris buffer is introduced into the flask. The solution was then made up to 1000 ml of SBF by adding ~300 ml of Milli-Q water. Then the pH of SBF is adjusted to 7.4 using appropriate amounts of 1M HCl and 1M NaOH solutions. After preparation, the SBF is transferred into a dark-colored plastic bottle and stored at 5 °C. Freshly prepared SBF is used to ensure viability.

To conduct *in vitro* test, glass and glass-ceramic powder samples are made into pellets measuring 10×10×2 mm^3 dimensions using a hydraulic press. The pellets are gently polished

with silicon carbide (emery) paper with a fine grit size of 4000 and washed with acetone. Subsequently, the pellets were immersed in 30 ml of SBF in a beaker and placed in an oven set at 37 °C. Upon immersion in SBF, the dissolution mechanism as explained in section 1.3 of chapter 1 occurs. pH of the solution was recorded with an accuracy of ± 0.05, and the mean pH was computed. The pH was monitored as a function of soaking time using a calibrated pH meter (Systronic pH meter 335). Figure 2.30 represents the change in pH of S8 ($45SiO_2$-24.5CaO-$24.5Na_2O$-$6P_2O_5$) in SBF with immersion time.

Table 2.02: Regent Order, amounts, purities and formula weights for preparing 1000 ml of SBF [HENC1982a, KOKU2006].

Order	Reagent	Amount (g)	Purity (%)	Formula unit
1	NaCl	8.035	99.5	58.443
2	$NaHCO_3$	0.355	99.5	84.007
3	KCl	0.225	99.5	74.552
4	$K_2HPO_4 \cdot 3H_2O$	0.231	99.0	228.222
5	$MgCl_2 \cdot 6H_2O$	0.3110	98.0	203.303
6	1.0M-HCl	39 ml	—	—
7	$CaCl_2$	0.292	95.0	110.985
8	Na_2SO_4	0.0720	99.0	142.043
9	Tris buffer	6.118	99.0	121.136

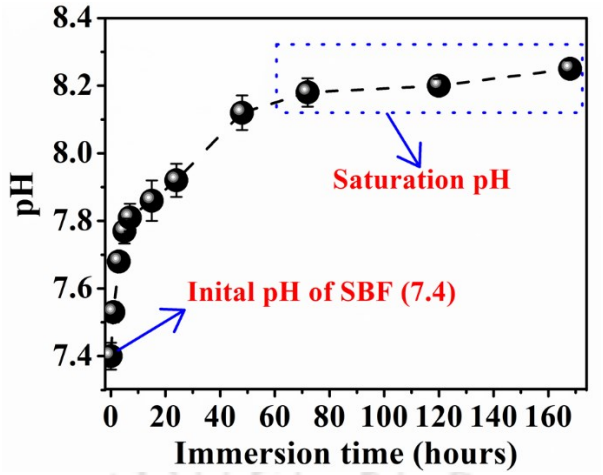

Figure 2.30: Change in pH of SBF with soaking time of $45SiO_2$-24.5CaO-$24.5Na_2O$-$6P_2O_5$ glass-ceramic pellet.

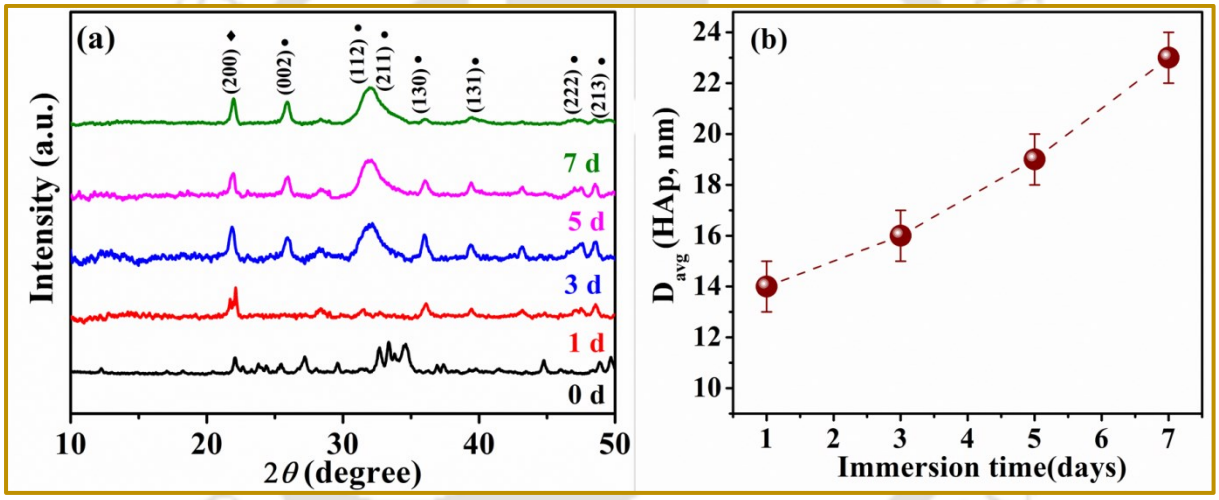

Figure 2.31: (a) GI-XRD patterns from the surface of S8 ($45SiO_2$-24.5CaO-$24.5Na_2O$-$6P_2O_5$ glass-ceramic) immersed in SBF for 0 to 7 days. (b)Variation in average crystallite size of HAp surface layer on SBF treated S8 pellet as function of immersion time. Symbols ♦, •, represent combeite and HAp phases, respectively.

Grazing Incidence X-Ray diffraction (GI-XRD) is a method used to examine the structure of thin films or surface layers. In this work, GI-XRD patterns have been collected using CuKα radiation (λ = 1.5418 Å) at a grazing angle of 0.5° and a scan rate of 2°/minute, covering the 2θ range from 20° to 50°. The X-ray source maintained a power of 9 kW (operating at 45 kV and

200 mA) in the analysis of all the samples. The GI-XRD patterns of SBF treated glass-ceramic samples are depicted in Figure 2.31 (a). The presence of a HAp surface layer on the glass-ceramic samples treated with SBF is indicated by peaks observed at 26° and 32°. The average crystallite size of HAp was estimated, as explained in the XRD section, and plotted against immersion time, as shown in Figure 2.31 (b). To explore the morphology and mineral composition of this HAp surface layer, FESEM (SIGMA-300) was utilized, whose details are provided in section 2.2.2. Figure 2.32 depicts the FESEM micrograph of the x = 2 MGC sample surface after immersion for 30 days in SBF. The presence of a HAp layer suggests that glass-ceramic samples exhibit bioactivity in physiological conditions.

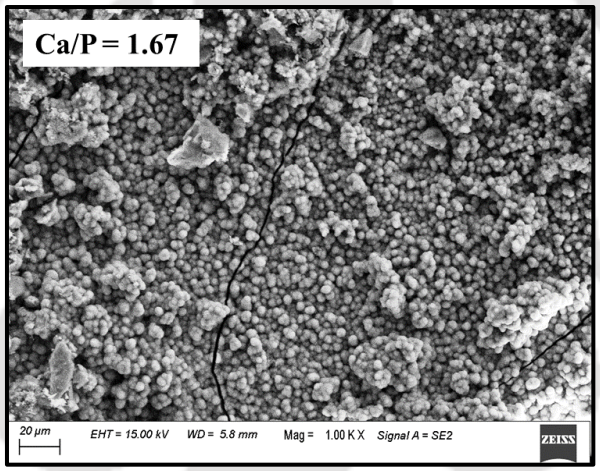

Figure 2.32: FESEM micrograph of x = 2 MGC ((45-x)SiO_2-24.5CaO-24.5Na_2O-6P_2O_5-xFe_2O_3) after soaking in SBF for 30 days.

2.2.10.2. Cell viability test with MG-63 cells

Tim Mosmann first introduced 2,5-diphenyl-2H-tetrazolium bromide (MTT) test in 1983, and since then, it has proven to be a very useful tool for determining cell viability [MOSM1983]. To perform cell viability test, 5000 cells (osteoblast MG-63 cells) were added to each well of a 96-well culture plate. The plates were incubated with Dulbecco's Modified Eagle Medium (DMEM, pH-7.4) along with 10 % phosphate-buffered saline (PBS) in a CO_2 incubator for 1, 3 and 5 days. After completing the incubation periods, the media from the wells were replaced with fresh

media along with MTT (5 mg/ml), and the mixture was then further incubated for an additional 4 h. During the incubation, the added MTT reduces to formazan crystals through oxidoreductase enzymes secreted by live cells in the wells. The formazan crystals were allowed to dissolve in dimethyl sulfoxide (DMSO), and the absorbance of the solution at 570 nm was measured using a multi-plate reader (Fluostar Omega, BMG, Germany). The cell viability was estimated using the relation (2.23),

$$Cell\ viability\ (\%) = \frac{Absorbance\ of\ Sample\ at\ 570\ nm}{Absorbance\ of\ Control\ at\ 570\ nm} \times 100 \qquad (2.23)$$

Figure 2.33 (a) presents the results of cell viability test performed on x = 2 MGC sample.

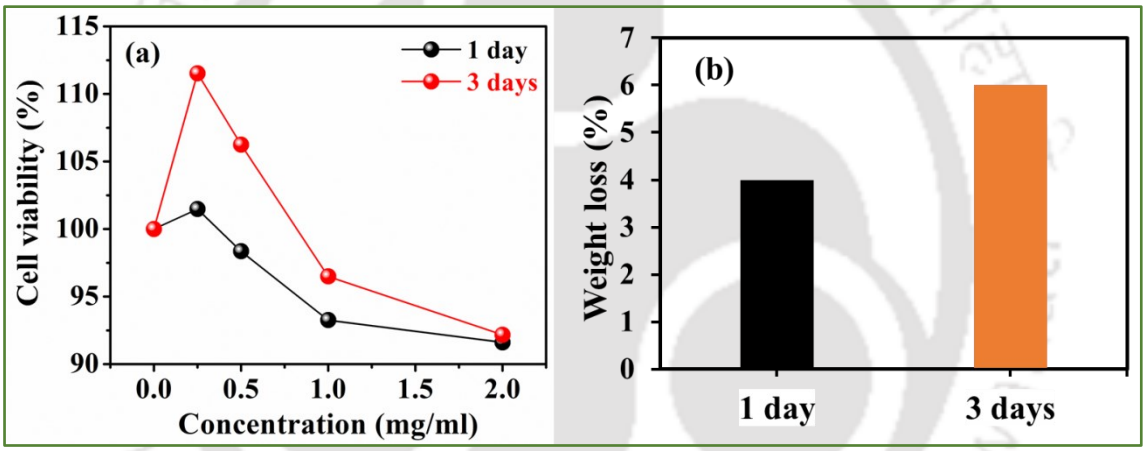

Figure 2.33: (a) Cell viability, and (b) degradation of x = 2 MGC ((45-x)SiO_2-24.5CaO-24.5Na_2O-6P_2O_5-xFe_2O_3) after 1, 3 days of incubation in PBS media.

A two-tailed t-test with unequal variance was conducted to assess the statistical significance of the collected cell viability data. In this test, three key hypotheses, viz., (1) No effect or difference is observed (null hypothesis, H_0), (2) an effect or difference is present (alternative hypothesis, H_1), and (3) whether rejection regions are located at both tails of the distribution (Critical regions).

To perform the comparison, two independent cell viability data sets, one from the control group (without treatment) and one from the treatment group were analyzed. The t-statistic for comparing the two groups was calculated using the formula:

$$t = \frac{X_1 - X_2}{\sqrt{\left({s_1}^2/n_1\right) + \left({s_2}^2/n_2\right)}} \qquad (2.24)$$

Where X_1 and X_2 represent the average cell viability for the control (without treatment) and treatment groups, respectively. ${s_1}^2$ and ${s_2}^2$ represent the variances of the two data sets, and n_1 and n_2 represent the sample sizes for each group.

$$degree\ of\ freedom\ (df) = \frac{\left({s_1}^2/n_1 + {s_2}^2/n_2\right)^2}{\left(\left(\frac{{s_1}^2}{n_1}\right)^2 \Big/ n_1 - 1\right) + \left(\left(\frac{{s_2}^2}{2}\right)^2 \Big/ n_2 - 1\right)} \qquad (2.25)$$

For the MGCC sample, X_1 = 100.2%, X_2 = 87.6%, ${s_1}^2$ =18.1, and ${s_2}^2$ = 25.4. Using these in equation (2.25) with df = 8, a t-value of 4.4 was found. The p-value from a two-tailed t-test was found to be 0.00222, which is smaller than the typical significance level (α) of 0.05.

The significance of the result is evaluated as follows:

- α = 0.05: Significant (*), indicating rejection of the null hypothesis.
- α = 0.005: Highly significant (**), indicating strong evidence against the null hypothesis.
- α = 0.001: Very highly significant (***), indicating very strong evidence for null hypothesis rejection.

In addition to assessing cell viability, another significant process observed is the degradation of the sample in the medium. To mimic the cellular environment, PBS media with a pH of 7.4 was utilized. The mass of the pellet was measured both before and after immersion in PBS, allowing the calculation of weight loss (a measure of sample degradation) using the following formula:

$$Weight\ loss\ (\%) = (w_0 - w_t)/w_0 \times 100\ \% \qquad (2.26)$$

In relation (2.26), w_0 and w_t are the weight of the sample before and after immersion for a particular time in PBS, respectively. The weighed pellets were then placed in PBS medium in a

20-well plate and subsequently incubated in an oven at 37 °C for 1 and 3 days. After 1 and 3 days, the pellets were taken out of the PBS and allowed to dry for 5 h at 37 °C in an oven. Then, the weight was measured. Using the equation, the weight loss was measured as presented in percentage form in Figure 2.33 (b).

The investigations carried out on various bioactive glass and glass-ceramic samples are described in the following chapters. These investigations use the above described techniques.

Chapter 3

Investigation of (69.5-x)SiO_2-24.5CaO-6P_2O_5-xNa_2O glass and glass-ceramics

As highlighted in chapter 1, 45S5 (45SiO_2-24.5CaO-24.5Na_2O-6P_2O_5) (wt.%) composition is a well-researched material which has the ability to bond with bone by development of the HAp layer under physiological environment [JONE2013]. It has also been pointed out in section 1.4 that stabilizing the glassy state in sol-gel derived bioglass-ceramics with a high Na_2O content (24.5 wt.%) such as in the 45S5 composition is a significant challenge [PEIT2001, CART2005, CHEN2010, CACC2012, PIRA2013, ADAM2013, SIQU2011, THOM2016]. Compositions with such high Na_2O content often experience structural devitrification due to the precipitation of crystalline inclusions. Moreover, inclusion of high amounts of Na_2O amplifies the alkalinity of the SiO_2-CaO-P_2O_5-Na_2O system during the dissolution process, which in turn promotes bone regeneration [CHAJ2015].

Though the difficulties associated with sol-gel derived glass-ceramics containing high Na_2O have been reported, the factors influencing the vitreous state or the maximum amount of Na_2O that can be incorporated in 45S5 composition without inducing devitrification has not been examined so far. Additionally, the impact of devitrification on the physical properties of 45S5 glass remains underexplored. It has been found that 45S5 glass devitrifies into a combeite phase ($Na_2Ca_2Si_3O_9$), which exhibits properties beneficial for bone regeneration. The presence of the $Na_2Ca_2Si_3O_9$ crystal phase, along with phosphorous ions, enhances the bioactivity and mechanical strength of the material [FILH1996, KARI2018]. As a result, sol-gel derived 45S5 glass-ceramic, with its comparable bioactivity and superior mechanical strength than its bulk counterpart, shows substantial promise as an advanced material for implants. This chapter

presents the structural and bioactive characteristics of sol-gel derived ceramics obtained by a systematic substitution of Na_2O for SiO_2, in the 45S5 composition.

3.1. Sample preparation

(69.5-x)SiO_2-24.5CaO-6P_2O_5-xNa_2O ($0 \leq x \leq 24.5$ wt.%) glass and glass-ceramics were prepared through the sol-gel route as detailed in section 1.1.3 of this thesis. The amounts of precursors (viz., TEOS, TEP, $Ca(NO_3)_2.4H_2O$, $NaNO_3$) were calculated as per the batch calculation for 5 g of (69.5-x)SiO_2-24.5CaO-6P_2O_5-xNa_2O ($0 \leq x \leq 24.5$ wt.%) glass and glass-ceramics as described in section 2.1.2 of this thesis. The synthesis follows the same process described in section 2.1.2. The aged gel was dried in a freeze drier and stored for 3 days at 70 °C for thermal stabilization. Table 3.01 lists eight samples, labeled as S1 to S8, produced by varying the Na_2O concentration in the (69.5-x)SiO_2-24.5CaO-6P_2O_5-xNa_2O ($0 \leq x \leq 24.5$ wt.%) composition. The dried powders with higher Na_2O concentration contained unreacted sodium nitrate. So, each set of as-synthesized ceramic powder was processed at temperatures ranging from 500 °C to 700 °C for 2 h each to ensure that no unreacted sodium nitrate remained in the samples.

3.2. Structural analysis

Figure 3.01 (a - d) display the recorded XRD patterns of all the samples as prepared and after processed at different temperatures as described in the sample preparation section 3.1. As-prepared samples S1 and S2 show only a broad hump at $2\theta = 20°$, which is characteristic of their amorphous nature. But the XRD patterns of S3, S4 and S5 show a weak crystalline peak of unreacted precursor superposed on the broad hump. The Na_2O content in S3, S4, and S5 is 4, 8 and 12 wt.%, respectively.

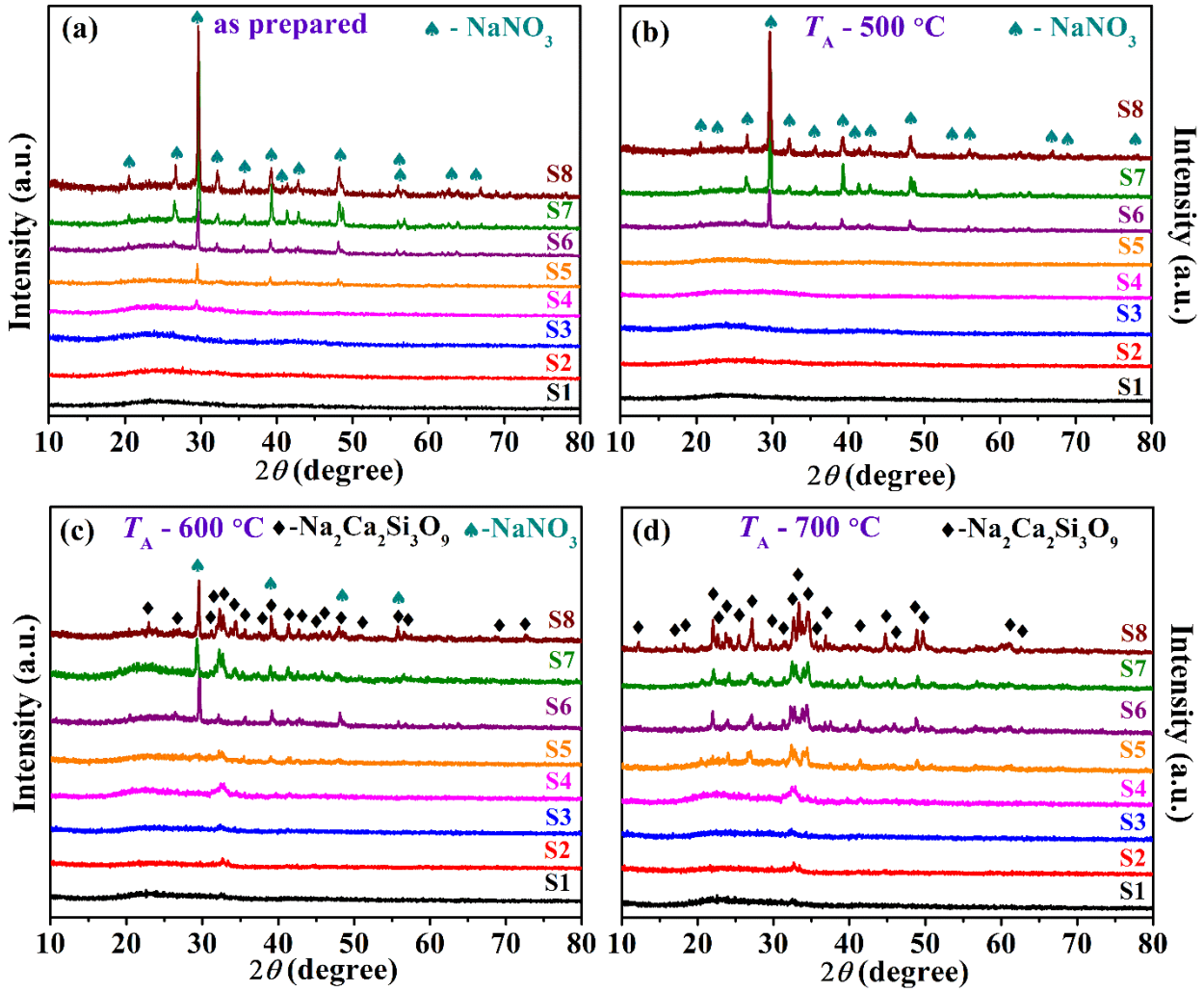

Figure 3.01: XRD patterns of (a) as prepared and processed nanopowder samples at (b) 500 °C, (c) 600 °C, and (d) 700 °C with compositions of (69.5-x)SiO_2-24.5CaO-6P_2O_5-xNa_2O ($0 \leq x \leq$ 24.5 wt.%). Combeite (♦), sodium nitrate (♠) peaks are marked.

It can be inferred from the Figure 3.01 (a) that the thermal stabilization performed at 70 °C was insufficient to convert all the sodium nitrate ($NaNO_3$) into Na_2O and integrate it in the glassy matrix in these samples. XRD patterns of as prepared S6, S7, S8 reveal prominent Bragg peaks corresponding to unreacted $NaNO_3$ crystalline phase confirming the difficulty in preparing glasses with high content of Na_2O. In order to introduce higher amount of Na_2O (x > 12 wt.%), proportionally higher quantities of $NaNO_3$ were used in their preparation as compared to S1, S2, S3, S4, and S5. It is apparent that the residual $NaNO_3$ did not dissolve into the matrix during the

thermal stabilization process and remains as an impurity phase. It can also be noticed that the intensity of the primary peak of this phase increases with an increase in $NaNO_3$ wt.% in the nominal composition. In order to understand the heat treatment required to dissolve the $NaNO_3$ precursor in samples with different amounts of the precursors, all the as-prepared samples were processed at 500 °C, 600 °C, and 700 °C for 2 h each.

Figure 3.01 (b) illustrates that heat treatment at 500 °C for 2 h completely suppressed the $NaNO_3$ phase in samples S1 to S5, which had Na_2O contents ranging from 0 to 12 wt.%. This indicates that the residual $NaNO_3$ precursor dissolved into the amorphous network upon this heat treatment. It is also obvious that processed at 500 °C for 2 h reduced the residual $NaNO_3$ phase in S6, S7, and S8, but could not completely dissolve the precursor in the amorphous network. Figure 3.01 (c) shows that the $NaNO_3$ phase persisted in S6, S7, and S8 samples processed at 600 °C for 2 h. Heat treatment at 700 °C removed all traces of $NaNO_3$ in all samples, but on the other hand induced stronger crystallization of the sodium calcium silicate (combeite, $Na_2Ca_2Si_3O_9$) phase in all the samples as depicted in Figure 3.01 (d). It can be observed that compositions with Na_2O content of up to 12 wt.% can be obtained in the vitreous state by processed of as-prepared powders at 500 °C for 2 h. In compositions with higher Na_2O content i.e., for x > 12 wt.%, the sol-gel procedure followed does not completely dissolve $NaNO_3$ in the vitreous network, thereby leaving it as a crystalline residue in the ceramic. Attempts to dissolve this residue by processed at a higher temperature of 700 °C is successful, but this heat treatment also induces crystallization of the combeite phase, thereby turning the sample into a glass-ceramic. This explains the challenges faced by researchers in obtaining the 45S5 composition with x = 24.5 wt.% Na_2O in completely vitreous state through sol-gel route.

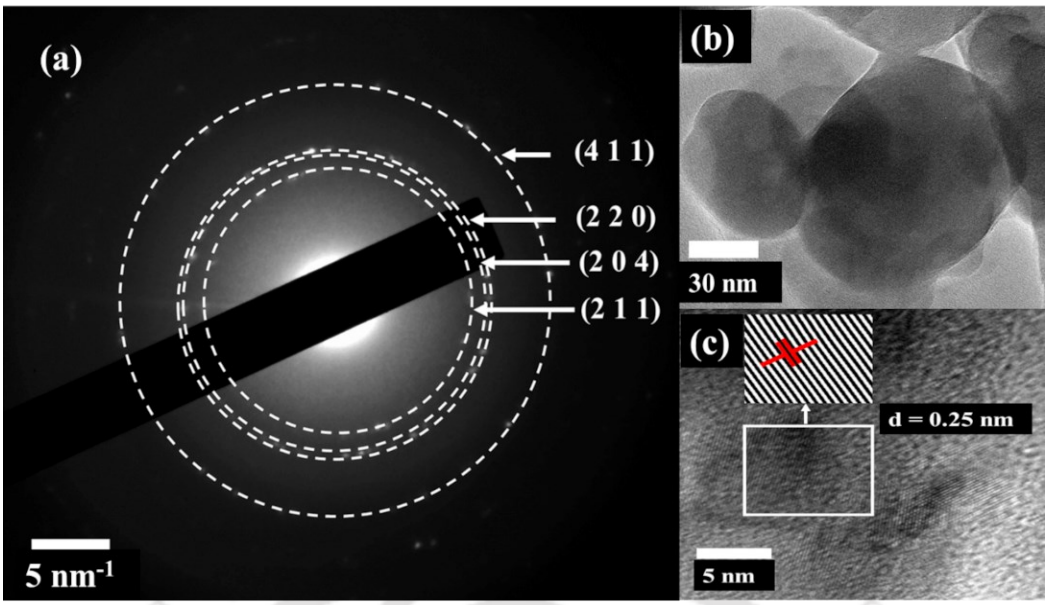

Figure 3.02: (a) SAED pattern, (b) FETEM image, and (c) HRTEM image of S8 processed at 700 °C. Inset of (c) shows iFFT of (220) plane of combeite phase in S8.

Figure 3.02 (a) displays the SAED pattern of S8 sample processed at 700 °C in which the reflections from (220), (204), (211), and (411) planes of the combeite phase (JCPDS Card No: 022-1455) have been identified. HRTEM image and inverse fast Fourier transform (iFFT) of the HRTEM image reveal the lattice fringes corresponding to (220) plane of combeite phase as displayed in Figure 3.02 (c). This study also confirms that combeite is the only crystalline phase present in this sample with 45S5 composition.

Table 3.01 presents EDS data that reveals a slight discrepancy between the measured and nominal values of elements such as O, Si, Ca, Na, and P in the (69.5-x)SiO_2-24.5CaO-xNa_2O-6P_2O_5 powders. This deviation is predominantly due to the presence of physically adsorbed oxygen. The adsorbed oxygen results in a higher measured oxygen content, which in turn lowers the observed percentages of the other elements compared to their nominal values. This adsorption effect is a key factor in the lower than expected measured composition of the glass and glass-ceramic components.

Table 3.01: Nominal and measured compositions of as-prepared (69.5-x)SiO_2-24.5CaO-6P_2O_5-xNa_2O ($0 \leq x \leq 24.5$ wt.%) glass and glass-ceramic samples.

Sample code (Na_2O content)	Nominal Compositions (wt. %)					Measured Compositions (wt. %)				
	O	Si	Ca	P	Na	O	Si	Ca	P	Na
S1 (x = 0)	48.6	30.4	15.3	5.8	0.0	52.0	28.6	14.4	5.0	0.0
S2 (x = 2)	48.3	29.6	15.5	5.8	0.8	51.8	27.9	14.8	4.9	0.5
S3 (x = 4)	46.3	29.7	15.3	5.9	2.8	51.2	27.5	14.5	4.7	2.1
S4 (x = 8)	46.3	26.9	15.3	5.8	5.7	50.4	25.8	14.7	4.6	4.5
S5 (x = 12)	45.1	25.2	15.3	5.8	8.6	49.5	23.9	14.9	4.5	7.2
S6 (x = 16)	44.8	23.4	15.3	5.8	10.7	46.0	22.9	15.1	5.6	10.4
S7 (x = 20)	43.0	21.6	15.3	5.8	14.3	45.2	20.4	15.0	5.5	13.9
S8 (x = 24.5)	41.9	19.6	15.2	5.8	17.5	42.6	19.3	15.2	5.7	17.2

3.3. Thermal analysis

Figure 3.03 displays the DTA curves of the S1, S2, S3, S4, and S5 samples. S1-S5 exhibit amorphous nature with the characteristic glass transition temperature (T_g). Four distinct features marked as a, b, c, and d were observed in the DTA curves. Feature "a" indicates the elimination of physically adsorbed water, while feature "b" represents the condensation of OH groups. Endothermic baseline shift represented by 'c' indicates the T_g, and the exothermic marked as 'd' indicates crystallization of the combeite phase. The thermal behavior observed can be correlated with the influence of the network modifier Na_2O on the glassy network. The ternary glass sample S1 (0 wt.% Na_2O) exhibits the highest T_g of 605 °C among all the tested samples. Samples S2, S3, S4, and S5, containing 2, 4, 8, and 12 wt.% Na_2O, respectively, display T_g at 583 °C, 570 °C, 558 °C, and 540 °C, respectively. The addition of Na_2O to the silicate glassy network leads to a significant decrease in T_g. Samples with higher SiO_2 content have a larger network connectivity, which promotes the formation of glassy networks. However, the introduction of Na_2O causes polymerization of the silicate network, resulting in a reduction in T_g.

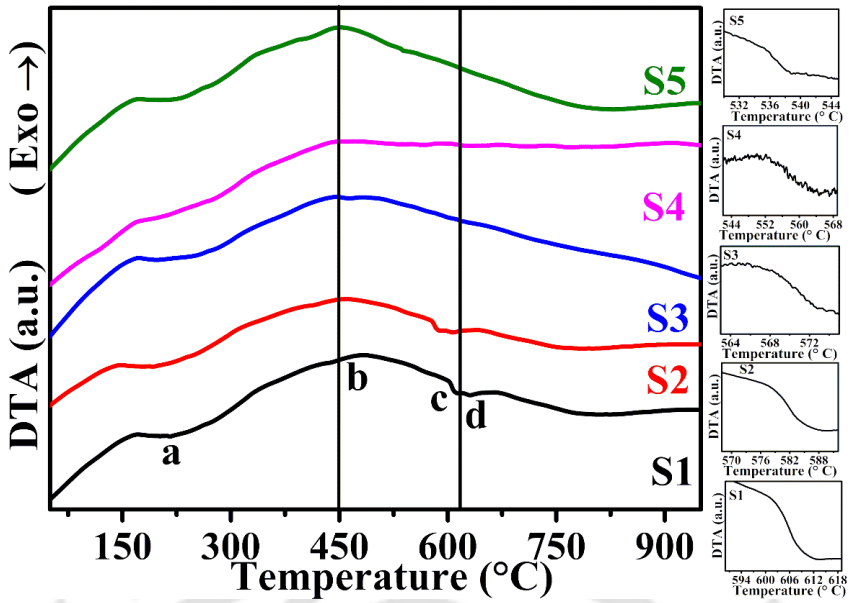

Figure 3.03: DTA curves of S1, S2, S3, S4, and S5 samples. The endothermic baseline shift corresponding to the glass transition of S1-S5 samples are shown in the right.

This is in line with the observations reported on SiO_2-Na_2O-CaO-P_2O_5-Al_2O_3-B_2O_3 glasses [ANDE1992]. The thermal stability of the glasses can be coarsely assessed through the measurement of ΔT,

$$\Delta T = (T_c - T_g)$$

Here, T_g is the glass transition temperature and T_c is the crystallization temperature [HUSS2022]. A higher ΔT is indicative of a more thermally stable glass since its crystallization and glass transition temperatures are wide apart. ΔT values for vitreous samples with x = 0, 2, 4, 8 and 12 were found to be 60 °C, 50 °C, 30 °C, 20 °C, and 15 °C, from DTA runs. Thus, the stability of the glasses declined with the addition of Na_2O, as indicated by the diminishing values of ΔT. It may be noted that as the Na_2O content exceeds 12 wt.%, the glass undergoes a transformation into a glass-ceramic state. In summary, the system with the lowest Na_2O content exhibits the highest thermal stability, and the glassy state is not sustainable in compositions with Na_2O content higher than 12 wt.%.

3.4. Surface area analysis

Figure 3.04 (a) and (b) depict the isotherms of S1 and S8 powder samples. The insets display the distribution of pore sizes. S1 glass displays an H1-type isotherm while S8 glass-ceramic shows H2-type isotherm in their hysteresis loops. Both isotherms are part of type-IV isotherm which symbolizes the mesoporous linked worm-like structure. S1 and S8 have specific surface area, average pore sizes, and total pore volumes ranging from 15 m^2/g to 1.81 m^2/g, 5.15 nm to 3.13 nm, and 0.021 cc/g to 0.012 cc/g, respectively. S1 shows mono-modal distribution, whereas the S8 shows bi-modal type of pore size distribution (inset of Figure 3.04 (a) and (b)). Considering these attributes, S8 may offer some advantage in the osteointegration process involving proteins of various sizes. Overall, the data shows that the ternary glass (S1) without Na_2O has higher surface area and bigger pore size with higher pore volume than the glass-ceramic sample (S8) with 45S5 composition. These results lead us to the following conclusions about the textural properties of the glass (S1) and glass-ceramic (S8) samples: (1) the differences in textural properties are mainly due to their different atomic network and composition, (2) Na_2O functions as a fluxing agent and lowers the amount of pore residue in the glass-ceramic structure, and (3) Na_2O influences particle size and crystal growth during heat treatment. In general, glass-ceramics often have a higher surface area compared to glass with the same composition [HENC2006] although in this case, S1 and S8 have different compositions. Textural parameters along with other factors contribute to the bioactivity of glasses and glass-ceramics. It is apparent that addition of Na_2O decreases the system's porosity and makes the ceramic more soluble in biological fluids, which in turn improves the HAp layer formation ability under physiological conditions.

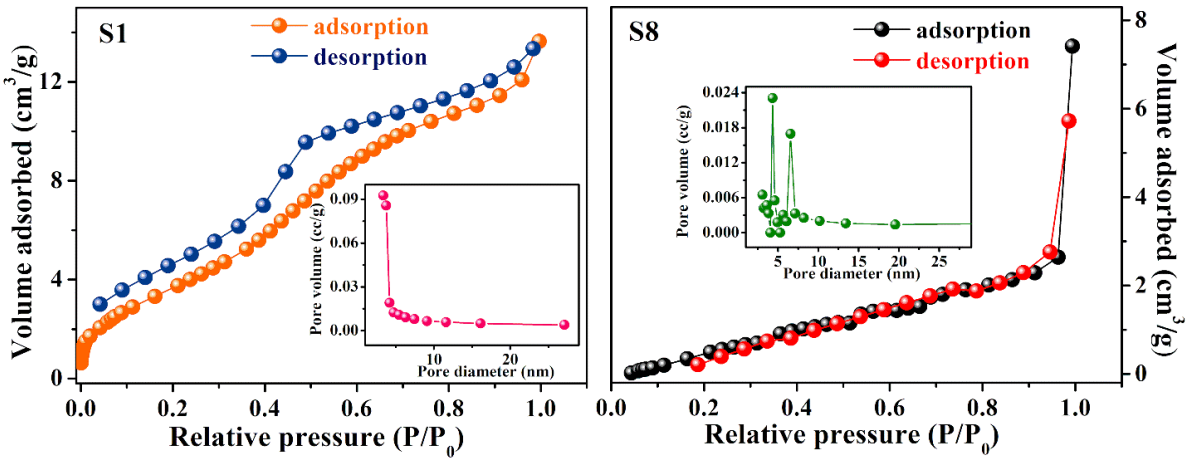

Figure 3.04: N_2 adsorption-desorption isotherm curves of samples (a) S1, and (b) S8. The insets of (a) and (b) show the pore size distribution curves of the respective samples.

3.5. Zeta potential

The zeta potential (ζ) of nanopowder samples in aqueous suspensions are presented in Figure 3.05. The ζ of glass and glass-ceramic powders initially exhibits a decrease in magnitude from -22.0 to -10.6 mV, as the Na_2O concentration is increased from 0 wt.% (in S1) to 12 wt.% (in S5). Subsequently, an increase in the magnitude of ζ from -13.3 to -25.4 mV is observed as the Na_2O content is progressively increased from 16 wt.% (in S6) to 24.5 wt.% (in S8). This decline in ζ is connected to the diminishing concentration of SiO_2 with increasing Na_2O, leading to a reduction in the presence of the negative functional group (Si-OH). Remarkably, beyond Na_2O > 12 wt.% (in S5), the surface charge experiences an increase despite the diminishing SiO_2 content. This phenomenon is attributed to the nucleation and growth of the combeite phase, contributing to an overall elevation in surface charge as Na_2O content is increased. ζ can be either negative or positive, thereby directly reflecting the charge type of the sample within the suspension. Doostmohammadi *et al.* discovered that bioactive nanoparticles exhibit a negative ζ potential, which becomes positive as the pH increases [DOOS2011]. Interestingly, osteoblast bone cells also exhibit a negative ζ potential, whereas HAp exhibits a positive ζ potential [OPPE1998]. However, some other reports have also documented a negative ζ for synthetic

bioglass and glass-ceramics [LU002000, GHAN2001, DOOS2011, MOST2021]. Higher ζ values are more favourable for bone regeneration.

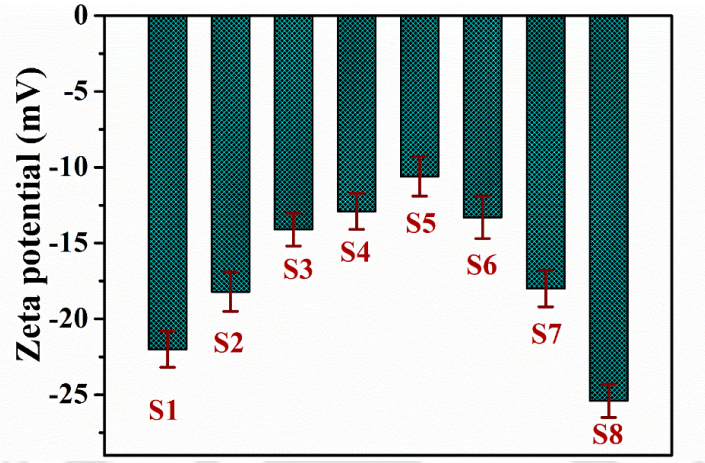

Figure 3.05: Zeta potential of glass and glass-ceramic samples in aqueous solvent.

3.6. *In vitro* bioactivity assessment

3.6.1. Ion exchange

Upon immersion of the bioglass and glass-ceramic pellets in SBF, a dissolution process occurs [PRYC2003]. Section 2.2.10.1 elaborates on this dissolution process. Figure 3.06 (a) shows the periodic variation of pH of the solution in which samples S1 to S8 were independently immersed. Initially, the pH was set at 7.4 corresponding to the ion concentration of the human body fluid. This is taken as the starting data point and marked as 0 h of immersion. If we closely check the pH test results, a quick pH change can be seen immediately upon immersion of the sample in SBF as shown in inset of Figure 3.06 (a). The leaching of Ca^{2+} and Na^{+} ions from the sample surface reaches saturation after 3 days of immersion, bringing the pH close to its maximum value. Composition dependent pH data was obtained to understand the exchange of more alkali and alkaline metal ions as a function of Na_2O content in the sample. After 7 days of immersion, the pH of the SBF solution increases from 7.40 to 7.88, 7.90, 7.98, 8.1, 8.13, 8.15, 8.2, and 8.25 for samples S1, S2, S3, S4, S5, S6, S7, and S8, respectively. S1 (ternary SiO_2-CaO-P_2O_5) glass

shows the minimum pH value of 7.88 while the quaternary S8 (SiO_2-CaO-P_2O_5-Na_2O) glass-ceramic sample shows the highest pH of 8.25 after 7 days of immersion. As the Na_2O concentration is increased, more alkali ions would be released from the sample surface resulting in higher pH. As expected, S8, the sample with the highest sodium content, exhibits the highest pH value among all samples. Increase in Na^+ ions in the glassy system also accelerates the dissolution process by breaking the bridging (Si-O-Si) links and creating additional non-bridging bonds. This enhances the sample's bioactivity and rate of degradation. A physiological environment similar to the *in vitro* tests performed in PBS media was maintained to investigate the hydrolytic degradation of the samples. Despite having different ions concentrations, PBS and SBF have a similar dissolving mechanism for bioactive materials [ISLA2017, LOH02023]. The PBS treated pellets were dried at 70 °C for 3 h before measuring their weight to estimate the weight loss.

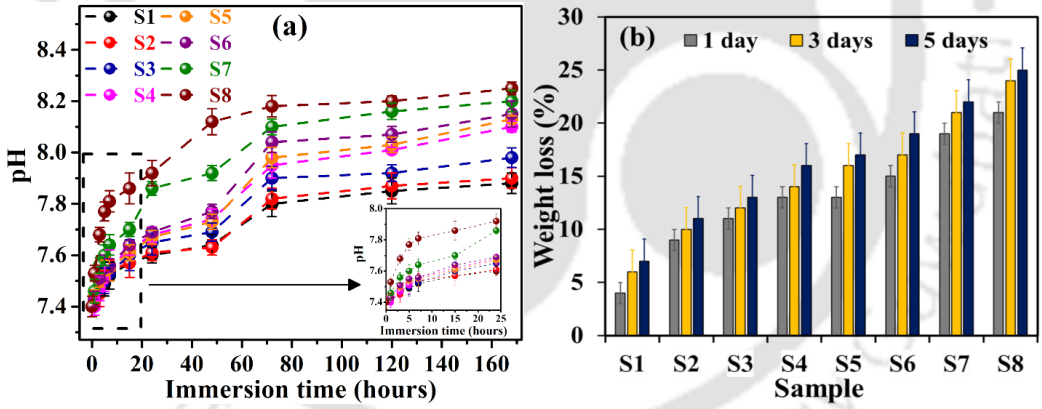

Figure 3.06: (a) Change in pH of glass and glass-ceramic in SBF with soaking time. (b) Weight loss in glass-ceramics measured before and after immersion in PBS for different days. Inset shows the rapid pH variation in the initial 24 h of immersion.

The measured weight loss of the sample pellets after immersion for different days are displayed in Figure 3.06 (b). The weight loss gradually increased with immersion time as well as Na_2O concentration. A rapid weight loss was observed after 1 day of soaking in PBS due to rapid degradation of the samples. It is evident that as Na_2O content escalates, the network

connectivity decreases, which in turn causes a rapid degradation of glass and glass-ceramic samples. These studies indicate that the degradation of glass-ceramics increased with an increase in Na_2O concentration. Simultaneously, the HAp layer formation also increased which counters the degradation by the deposition of the Ca-P rich layer on the surface of samples. As a result, considerable increase in pH saturation value and degradation are observed with increased Na_2O substitution. Overall, all the samples exhibit good ion exchange in SBF and degradation in PBS, qualifying them to be termed as degradable bioactive materials.

3.6.2. Surface apatite layer formation

Figure 3.07 (a) to (h) show the typical GI-XRD patterns of SBF treated glass and glass-ceramic samples after various immersion time periods (0, 1, 3, 5, and 7 days). The XRD pattern labeled as 0 days represents the untreated samples, clearly portraying the amorphous nature of S1, S2, S3, S4, and S5, and the crystalline nature of S6, S7, and S8 samples. Figure 3.07 (a - h) clearly demonstrate the growth of a crystalline HAp layer on the samples' surface following one or more days of immersion in SBF. The growth of this layer increases with immersion time for all the tested samples. The crystallinity of S6, S7, and S8 samples appears to be suppressed with increasing immersion time due to the formation of the HAp layer on the surface. According to the explanation given in chapter 2, the chemical reaction of surface ions with the physiological fluid controls the growth of the HAp coating (section 2.2.10.1). Formation of the HAp layer over the surface of the sample indicates the bioactive nature of the entire series of samples. The development of the HAp layer depends upon the amount of Ca and P ions available and the ion exchange mechanism with the sample. The Ca/P molar ratio after 7 days was nearly the same in all samples and the value was close to the ratio found in fully crystalline HAp. Though Si and Na influence the ion exchange process with SBF, Ca and P play a more impactful role in the dissolution mechanism of the sample. In addition, Na_2O influences the initial stage of dissolution in SBF. One can notice the reflections from the combeite phase along with those the HAp phase

in the GI-XRD patterns of S6, S7, and S8 samples after 7 days of soaking in SBF. This is due to the lower thickness or poor coverage of the HAp phase over the sample surface, resulting in the visibility of the combeite phase from the surface of the samples even after 7 days of soaking in SBF.

The relationship between the average crystallite size of the HAp phase and soaking time of samples with different Na_2O concentration is illustrated in Figure 3.08. It can be observed that the crystallite size of HAp increases with soaking time, due to the growth of HAp on the sample's surface. Only a small increase in crystallite size is seen with an increase in Na_2O content since Na_2O promotes the dissolution process and not directly involved in HAp formation.

The FESEM micrographs of the surfaces of S1 to S8 glass-ceramic samples after soaking in SBF for 1 and 7 days provide visual evidence of HAp layer evolution, as displayed in Figure 3.09. The newly formed layer on the surface of the submerged samples has a cauliflower-like shape, which is typical of the initial HAp layer [WU002015]. All the samples show sponge or cauliflower-like feature on their surface after one day of immersion, which denotes the formation of the HAp layer. As the immersion time increases, the growth rate of the HAp layer also increases. After 7 days of immersion, the previously formed cauliflower-like structure develops into a larger sphere composed of small petal-like structures. Rapid layer formation results from faster interchange of Ca^{2+} ions of a specimen with H_3O^+ ions in the physiological fluid. Due to the interchange of ions, silanol group Si-OH is formed on the surface of the pellets, which induces HAp nucleation. In addition, the rate of HAp layer formation mainly depends upon the composition of the biomaterial. The surface mineralization was confirmed by EDS analysis, which shows the Ca/P ratio for all the samples after 7 days of soaking. The Ca/P ratio of all tested samples is close to the Ca/P ratio of 1.67 of bulk HAp [JEON2019].

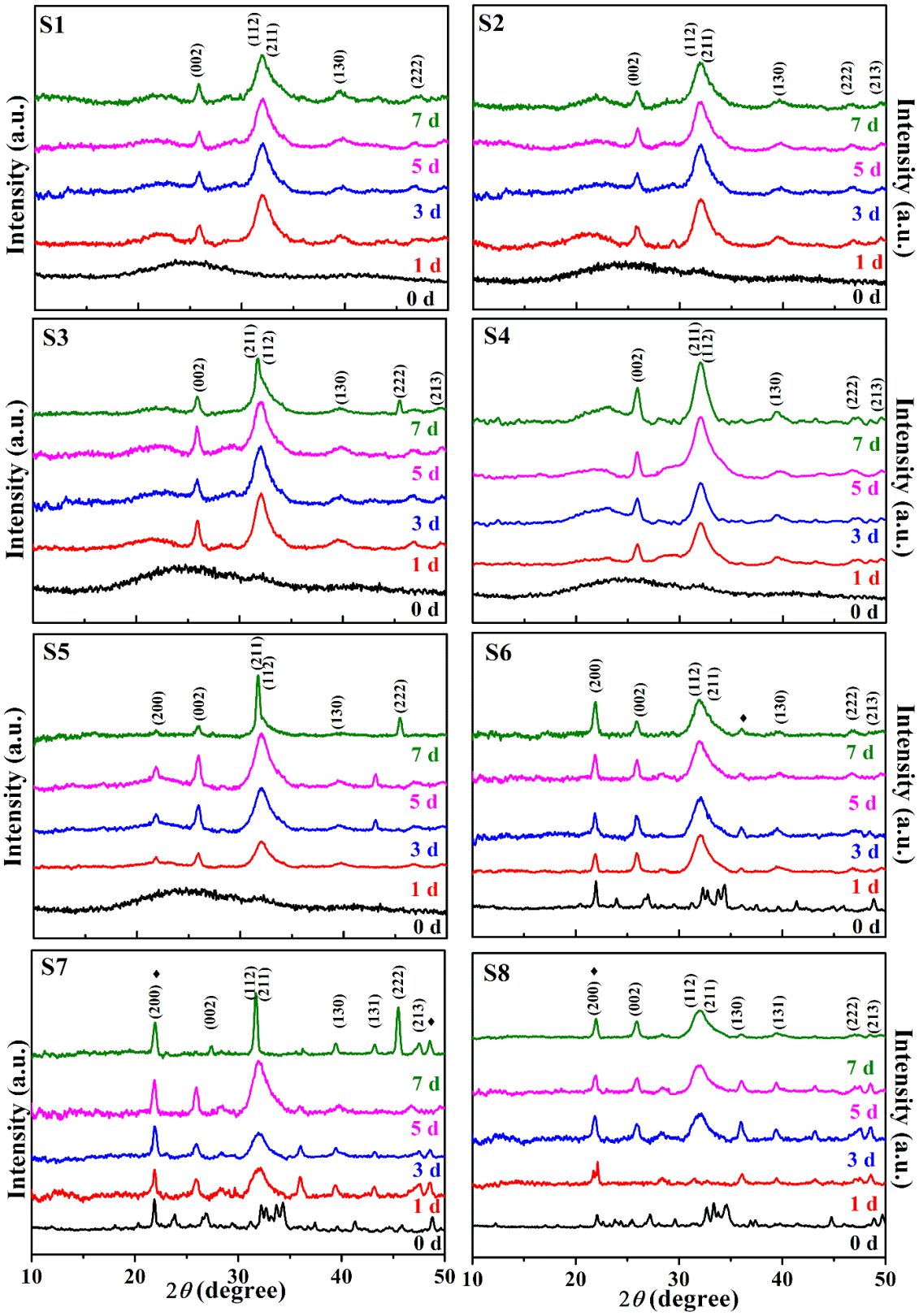

Figure 3.07: GI-XRD patterns of SBF treated (a) S1, (b) S2, (c) S3, (d) S4, (e) S5, (f) S6, (g) S7, and (h) S8 pellet surface. Symbols (♦) represents combeite phase.

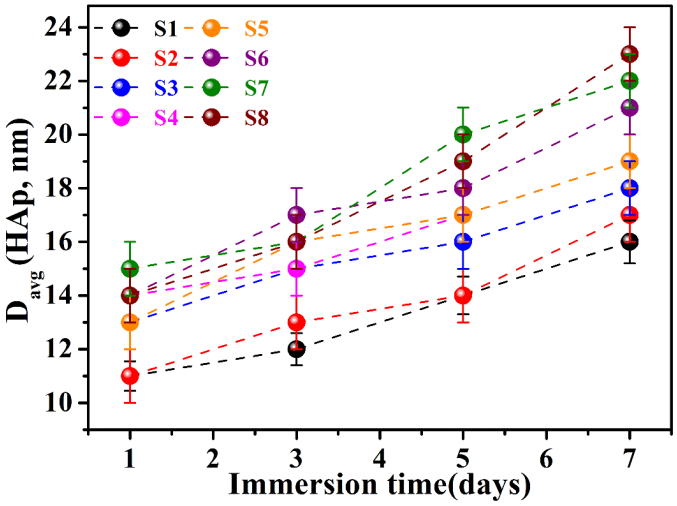

Figure 3.08: Variation of average crystallite size of HAp with soaking time of different samples.

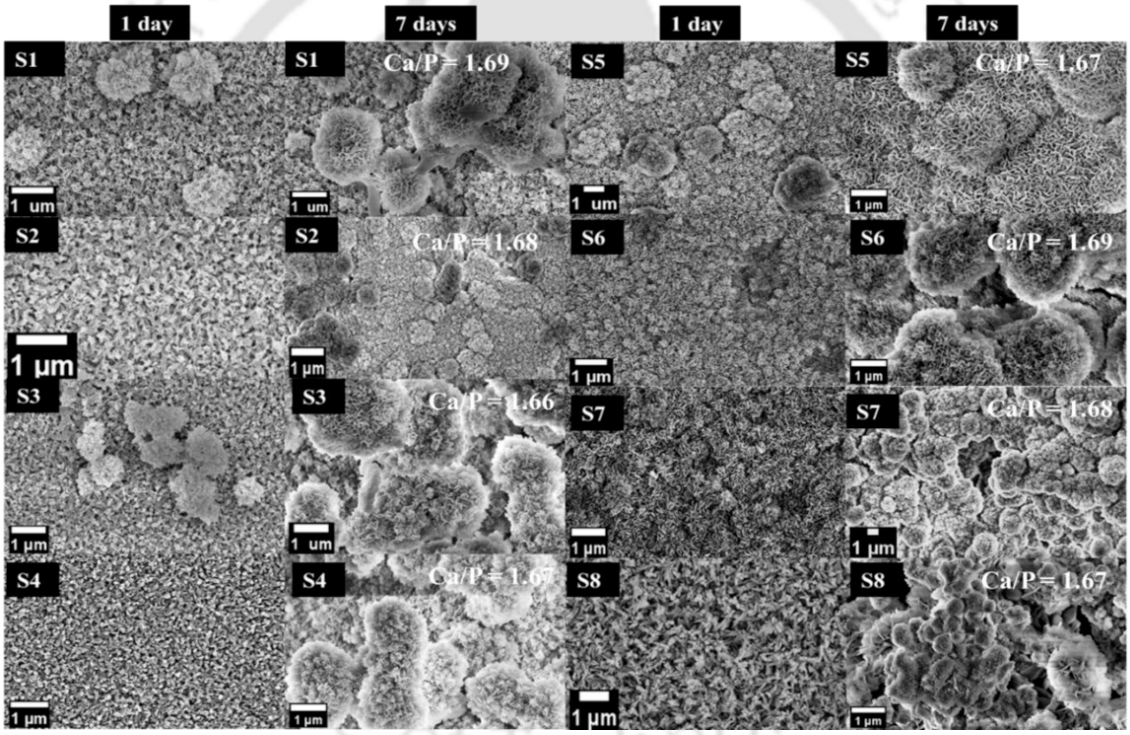

Figure 3.09: FESEM images of sample pellets after immersion in SBF for 1 day and 7 days.

3.6.3. Osteoblast cell viability

Figure 3.10 shows the survival viability of osteoblast cells, MG-63, in contact with the samples. The cells showed enhanced viability with increasing amount of Na_2O in the synthesized samples during the tested period of incubation. 1 day of incubation of sample S1 (without Na_2O) with 0.25 mg/ml concentration resulted in ~96% viability of osteoblast cells. Upon increasing Na_2O

content, the cell viability increased to ~98% for S8, the sample containing the highest amount of Na_2O (24.5 wt.%). Similarly, the 2 mg/ml sample concentration showed ~80% and ~91% cell viability after 1 day of incubation of S1 and S8 samples, respectively. Sample S1 showed maximum cell viability of ~101% with 0.25 mg/ml concentration after 5 days of incubation. Cell viability increased with higher amount of Na_2O in the sample as well as the duration of incubation. The cell viability after 1 day of incubation of sample S3 (4 wt.% Na_2O) was ~95% with 0.25 mg/ml concentration, whereas it increased to ~98% for sample S8. For the maximum tested concentration of 2 mg/ml, the cell viability increased from ~84% to ~91% in samples with increasing Na_2O content as observed in S3 to S8 samples. Further, the cell viability increased with incubation period (Figure 3.10 (a), (b), and (c)), probably owing to the formation of HAp on the samples. After 3 days of incubation of S8, the viability of the MG-63 cell line was boosted to ~116% for 0.25 mg/ml and ~98% for 2 mg/ml concentration, respectively. During a 5 days incubation period, the cell viability of MG-63 cells reached a maximum value of ~118% for the 0.25 mg/ml concentration and ~102% for the 2 mg/ml concentration of S8 sample. The effects of sample concentration on cell viability were also observed, as depicted in Figure 3.10 (d). S7 and S8 with a concentration of 0.25 mg/ml showed the highest cell viability of ~112% and ~118% after 5 days of incubation. On the other hand, increasing concentration to 2 mg/ml reduced the cell viability to ~98% and ~99% for S7 and S8, respectively. Overall, the osteoblast cells viability was observed to improve significantly with increasing Na_2O content in the samples, proving its excellent cytocompatibility with the cells. Also, as expected, the proportion of viable cells decreased with increasing sample concentrations. However, it is to be noted that the cell viability of all samples was well above the acceptable limit for biomaterials at all tested concentrations [LI002015].

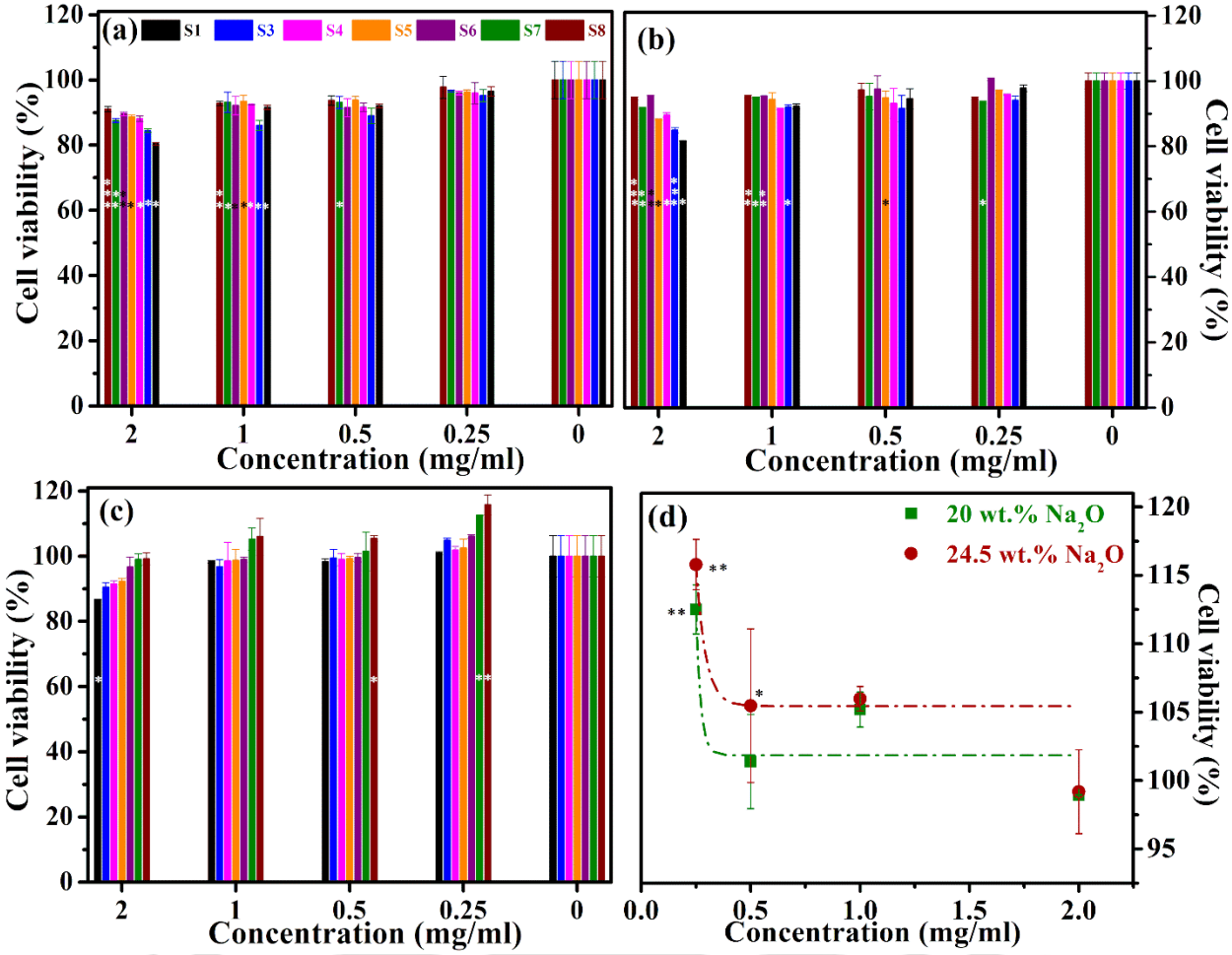

Figure 3.10: Viability of MG-63 osteoblast cells after incubation with synthesized samples for (a) 1 day, (b) 3 days, and (c) 5 days for various concentrations (2, 1, 0.5, 0.25 mg/ml). (d) Effect of concentration of different samples on the viability of MG-63 cells. An asterisk indicates a significant difference in cell viability between different samples and control group *(* $\rightarrow p < 0.05$, ** $\rightarrow p < 0.005$, *** $\rightarrow p < 0.001$, where p is the probability value or p-value).

As reported earlier, Si can stimulate osteoblast differentiation, collagen I production, and several pathways promoting osteogenesis [NEIL2018]. However, a high amount of Si induces the formation of a strong network within the bioglass, leading to prolonged biodegradation. Replacement of Si with Na in the bioglass weakens the network yielding to preferable degradation rate [STEP2021]. Increasing Na_2O content by replacement of SiO_2 showed improved cell growth and viability over the tested incubation period with an adequate

degradation rate. Na^+ is an essential cation in extracellular space which regulates the water movement across the cell membrane, thus maintaining osmolality [WU002017]. Na^+ plays a key role in numerous cellular functions, acting as a secondary messenger. Osteoblast cells possess epithelial and voltage-sensitive sodium channels which induce osteogenesis and participate in bone formation via cyclic guanosine monophosphate molecules [CHEN2014, WANG2016]. Further, Na^+ regulates the function of Na-Ca exchanger channels which are responsible for maintaining the intracellular concentration of Ca^{2+} ions within the cells and thus help regulate osteoporosis [LI002007]. Moreover, the observed results are in accordance with the formation of an apatite layer when incubated in SBF, as discussed in the previous sections. The extensively increased amount of apatite formation after 5 days of incubation stimulates the osteoblast cells' growth and proliferation, leading to the high number of viable cells. Thus, all the prepared samples are highly cytocompatible and can promote osteoblast cell growth.

3.7. Summary

- Bioactive glasses and glass-ceramics with compositions of (69.5-x)SiO_2-24.5CaO-6P_2O_5-xNa_2O (x = 0, 2, 4, 8, 12, 16, 20, 24.5) were obtained by optimal heat treatment of sol-gel derived ceramic powders.
- XRD analysis of the samples revealed that glassy nature of (69.5-x)SiO_2-24.5CaO-6P_2O_5-xNa_2O system is preserved up to $x \leq 12$. For $x > 12$, devitrification occurred with the crystallization of combeite phase, whose content increased with increase in Na_2O content.
- Thermal studies revealed that T_g decreased with increase in Na_2O content from 0 to 12 wt.%.
- The sol-gel derived sample S8 with 45S5 composition showed lower surface area, pore volume, and pore size than the glass without Na_2O (S1). However, its bi-modal pore size distribution offers more scope for binding proteins of different sizes in bone regeneration application.

- *In vitro* bioactivity tests indicated that all samples are bioactive and nontoxic to MG-63 osteoblast cells, indicating their biocompatibility. S8, the glass-ceramic sample with 45S5 composition, exhibited the best bioactivity among all the studied bioglass-ceramic compositions.
- This study (a) identifies the upper threshold Na_2O content for maintaining the vitreous glass in (69.5-x)SiO_2-24.5CaO-6P_2O_5-xNa_2O system, (b) shows that the glass-ceramic with 24.5 wt.% Na_2O yields the best MG-63 cell viability, and (c) concludes that the bioglass-ceramic composition is more critical than the atomic structure for bone regeneration applications.

Chapter 4

Investigation on SiO_2-CaO-Na_2O-P_2O_5-Fe_2O_3 glass-ceramics

In chapter 3, it was shown that 45S5 composition (i.e., component stoichiometry, especially, that of Na_2O wt.%) is more relevant for efficient bone regeneration rather than the atomic structure (i.e., glassy or glass-ceramic network) of the ceramic. The optimally heat treated sol-gel derived 45S5 glass-ceramic sample designated S8 with combeite crystal phase turned out to be the best specimen for bone regeneration application in the (69.5-x)SiO_2-24.5CaO-6P_2O_5-xNa_2O ceramic system. Therefore, further studies of this thesis work will use this 45S5 glass-ceramic as the base composition. Due to the absence of magnetic content in this composition, it cannot be used in MH treatment of cancer. To extend its applicability to MH, ferromagnetic or ferrimagnetic oxide should be incorporated into the nominal 45S5 composition. Of the available magnetic oxides, iron oxide was chosen as the magnetic oxide component for substitution in the Hench's 45S5 composition due to its biocompatible nature [SEDI2022]. The literature survey presented in chapter 1 extensively covers magnetic glass-ceramics that exhibit both bioactive and magnetic properties, especially in the realm of MH. However, as already mentioned, there is only one report in the literature on sol-gel derived iron oxide-based nanopowder of 45S5 ceramic, prior to this work. In the earlier work, the authors have only examined two different concentrations of iron oxide (2 and 3 wt.%) [SHAN2016]. Moreover, no investigation on the heating capacity of these nanopowders was conducted in that study. There are also no reports of sol-gel derived iron oxide-substituted 45S5 glass-ceramics that demonstrate optimal magnetic behavior along with bioactivity for use in both bone regeneration and MH therapies. In this chapter, systematic replacement of SiO_2 by iron oxide in the sol-gel derived 45S5 glass-ceramic composition has been carried out. Then, *in vitro* bioactivity and induction heating capacity of the iron oxide-

substituted 45S5 glass-ceramics have been investigated to assess them for use in bone regeneration and MH treatment.

4.1. Sample preparation

Magnetic bioactive glass-ceramic nanopowders (MGC) of compositions (45-x)SiO_2-24.5CaO-24.5Na_2O-6P_2O_5-xFe_2O_3 ($2 \leq x \leq 15$ wt.%) have been synthesized through the sol-gel route described in details in chapter 2 (section 2.1). TEOS, $Ca(NO_3)_3.4H_2O$, TEP, $NaNO_3$, $Fe(NO_3)_3.9H_2O$, were used as sources of SiO_2, CaO, P_2O_5, Na_2O, and iron oxide, respectively. The dried gel powder was kept in an air oven at 70 °C for 3 days for thermal stabilization. Subsequently, the dried powder was heat treated at 750 °C for 2 h and the resultant product was used for further studies.

4.2. Structural analysis

Figure 4.01 (a) displays the XRD patterns of MGC nanopowder samples with x = 2 to 15 wt.%. Three crystalline phases, viz., combeite ($Na_2Ca_2Si_3O_9$, ICDD 002-1445), hematite (α-Fe_2O_3, ICDD 1-072-0469), and magnetite (Fe_3O_4, ICDD00-019-0629) were identified in all the nanopowder samples. The percentage of each crystalline phase estimated according to the procedure outlined in section 2.2.1 of chapter 2 are presented in Table 4.01. It can be observed from Table 4.01 that the combeite phase is more pronounced in those samples having a low concentration of iron oxide. Equation 2.03 was used to estimate the average crystallite size (D_V) of the magnetite. The percentage of magnetic phases (both hematite and magnetite) and D_V of the magnetite nanocrystallites increased with increase in x as depicted in Figure 4.01 (b) and its inset, respectively. Iron oxide phases (magnetite and hematite) were found to significantly increase as more iron oxide precursor was added with a corresponding decrease in combeite phase. The combeite phase has been well studied and is found to have good mechanical strength and biodegradability [ADAM2013, THOM2016, PEIT2001]. Therefore, the combined presence

of combeite and the iron oxide phases ensures both biocompatibility and induction heating capacity of the iron oxide-substituted MGC nanopowders.

Table 4.01: Nominal composition, measured composition and estimated percentage of crystalline phase percentages in various samples. C, M, and H refer to combeite, magnetite and hematite, respectively.

Sample code	Nominal Compositions (wt. %)						Measured Compositions (wt. %)						% of crystalline phases present		
	O	Si	Na	Ca	P	Fe	O	Si	Na	Ca	P	Fe	C	M	H
x = 2	41.7	18.7	17.4	15.2	5.6	3.4	42.5	17.7	16.8	14.8	5.2	3	84.0	10.0	6.0
x = 4	40.5	16.8	16.5	14.3	5.4	6.5	41.9	16.5	16	14.2	5.1	6.3	80.0	13.0	7.0
x = 6	39.7	15.5	15.9	14.1	5.3	9.5	41.3	15	15.3	14.4	4.8	9.2	77.0	14.0	9.0
x = 8	39.1	14.3	15.6	13.6	5.1	12.3	40.2	13.9	15.1	13.3	5.0	12.5	71.0	18.0	11
x = 10	38.5	13.2	15.1	13.2	5.0	15.0	39.2	12.6	15.4	12.7	4.8	15.3	46.0	30.0	24.0
x = 15	37.1	10.5	14.2	12.4	4.7	21.1	37.8	10.2	13.8	11.8	4.5	21.9	23.0	43.0	34.0

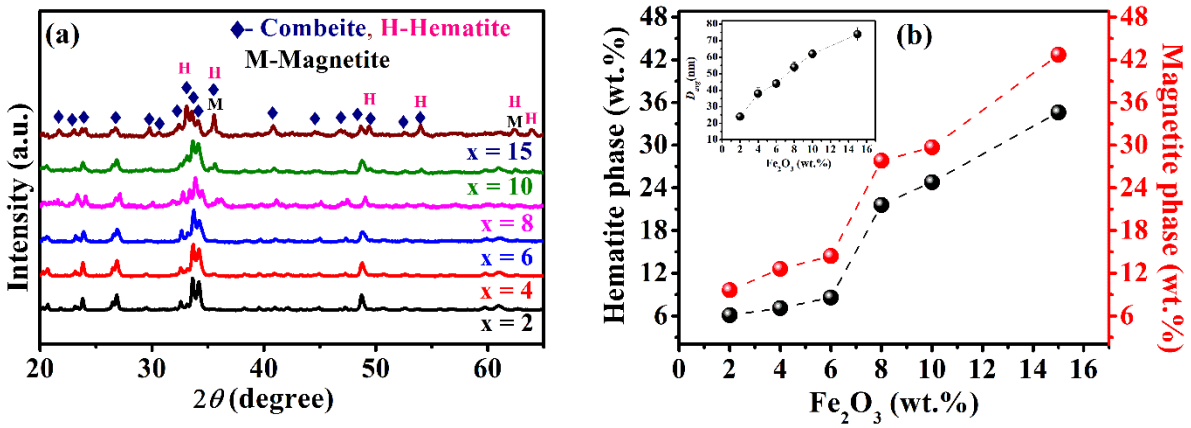

Figure 4.01: (a) XRD patterns, and (b) percentage of magnetic phases (magnetite and hematite) present in (45-x)SiO_2-24.5CaO-24.5Na_2O-6P_2O_5-xFe_2O_3 ($2 \leq x \leq 15$ wt.%) MGC samples as a function of iron oxide concentration. Inset of (b) shows the variation of average crystallite size of magnetite phase as a function of iron oxide content (x) in the MGC samples.

Morphology of dispersed MGC powder sample with x = 10 can be visualized in the FETEM image shown in Figure 4.02 (a). The near-spherical shape of a typical particle is illustrated as an inset in Figure 4.02 (a). Figure 4.02 (b) displays the particle size distribution of the MGC nanopowder sample with x = 10. Analysis of this distribution reveals an average particle size of 29 ± 1 nm with a FWHM of 16 nm. The SAED pattern of this sample shown in Figure 4.02 (c) shows diffraction spots emanating from (113), (006) and (217) planes of combeite and (311) and (440) planes of magnetite phase. It has to be noted that the (116) reflection from hematite is overlapping with the (217) reflection of combeite, and the (110) reflection of hematite is overlapping with the (311) of magnetite, due to the limited resolution of the SAED pattern. A weak isolated hematite reflection from the (1110) planes can also be noticed. The observed reflections in the SAED pattern may be compared with the corresponding ones in the XRD pattern of the sample [Figure 4.01 (a)]. HRTEM image and inverse fast Fourier transform (iFFT) of HRTEM image of this sample reveal the lattice fringes corresponding to the (311) plane of magnetite phase as displayed in Figure 4.02 (d). Table 4.01 presents a comparison between the measured composition and nominal composition of (45-x)SiO_2-24.5CaO-24.5Na_2O-6P_2O_5-xFe_2O_3 ($2 \leq x \leq 15$) MGC nanopowder. The EDS analysis indicates that, apart from O, the observed compositions of MGC elements such as Si, Ca, Na, P, and Fe are slightly lower than the nominal composition. This discrepancy is primarily attributed to the presence of physically adsorbed oxygen, which leads to an overestimate of O in comparison to its nominal value. This is the primary reason for the observed lower elemental composition in comparison to the nominal composition of MGC components.

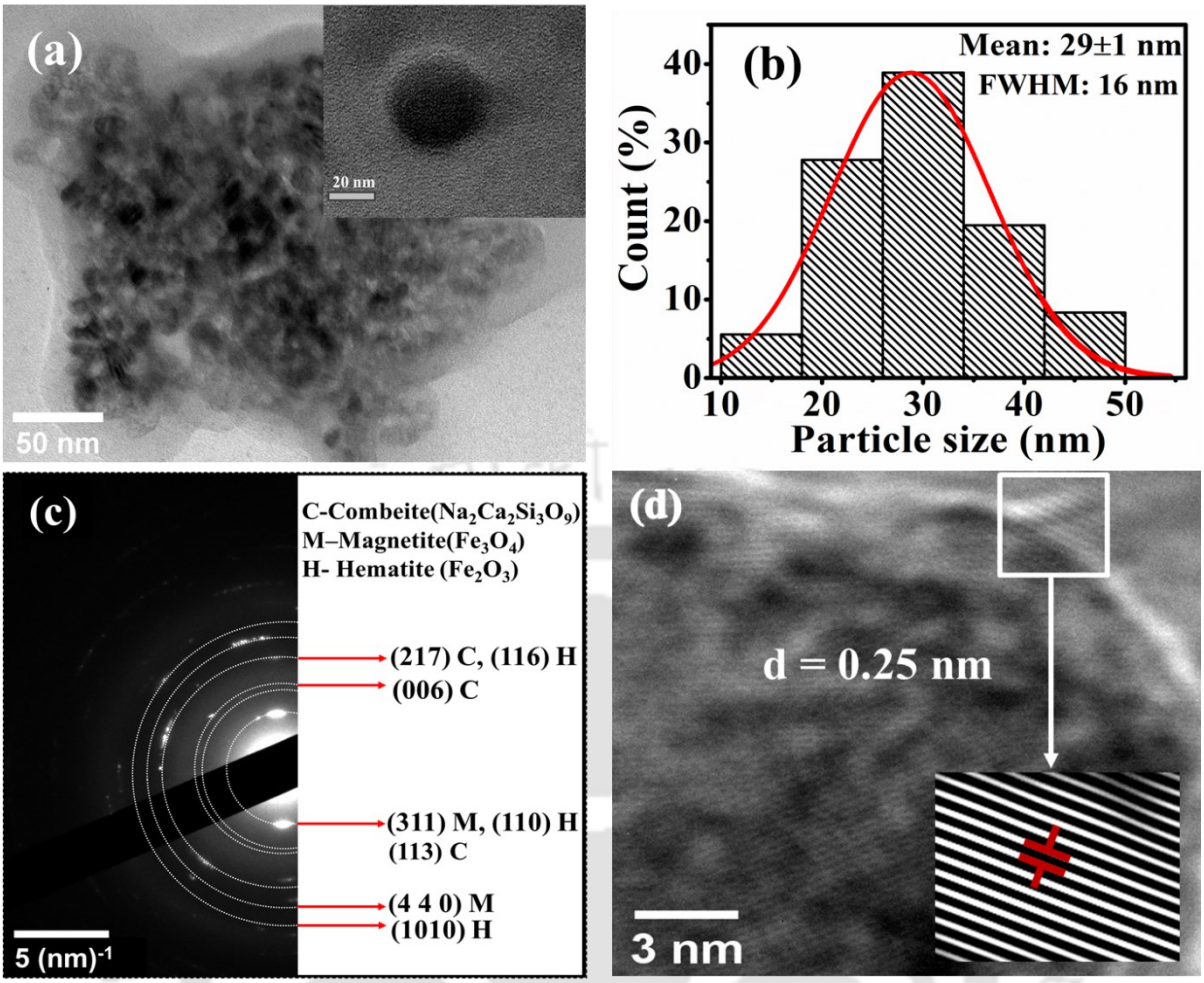

Figure 4.02: (a) FETEM image, (b) particle size distribution obtained from the TEM image, (c) SAED pattern, and (d) HRTEM image of x = 10 MGC sample. Inset of (d) shows iFFT of (331) plane of magnetite phase in x = 10 MGC sample.

4.3. Surface area analysis

Figure 4.03 (a) to (d) depict isotherm curves of the sol-gel derived MGC nanopowders. Inset in each Figure displays the pore size distribution of respective samples. All the nanopowder samples exhibited H2-type isotherm which is a part of type-IV isotherm which signifies a mesoporous interconnected worm-like structure. It is also evident from the data presented that progressive substitution of iron oxide for silica in the nominal 45S5 composition does not induce any significant change in the shape of the isotherm. Both BET and Barrett-Joyner-Halenda (BJH)

methods were used to calculate the specific surface area, mean pore size, and total pore volume, as shown in Table 4.02.

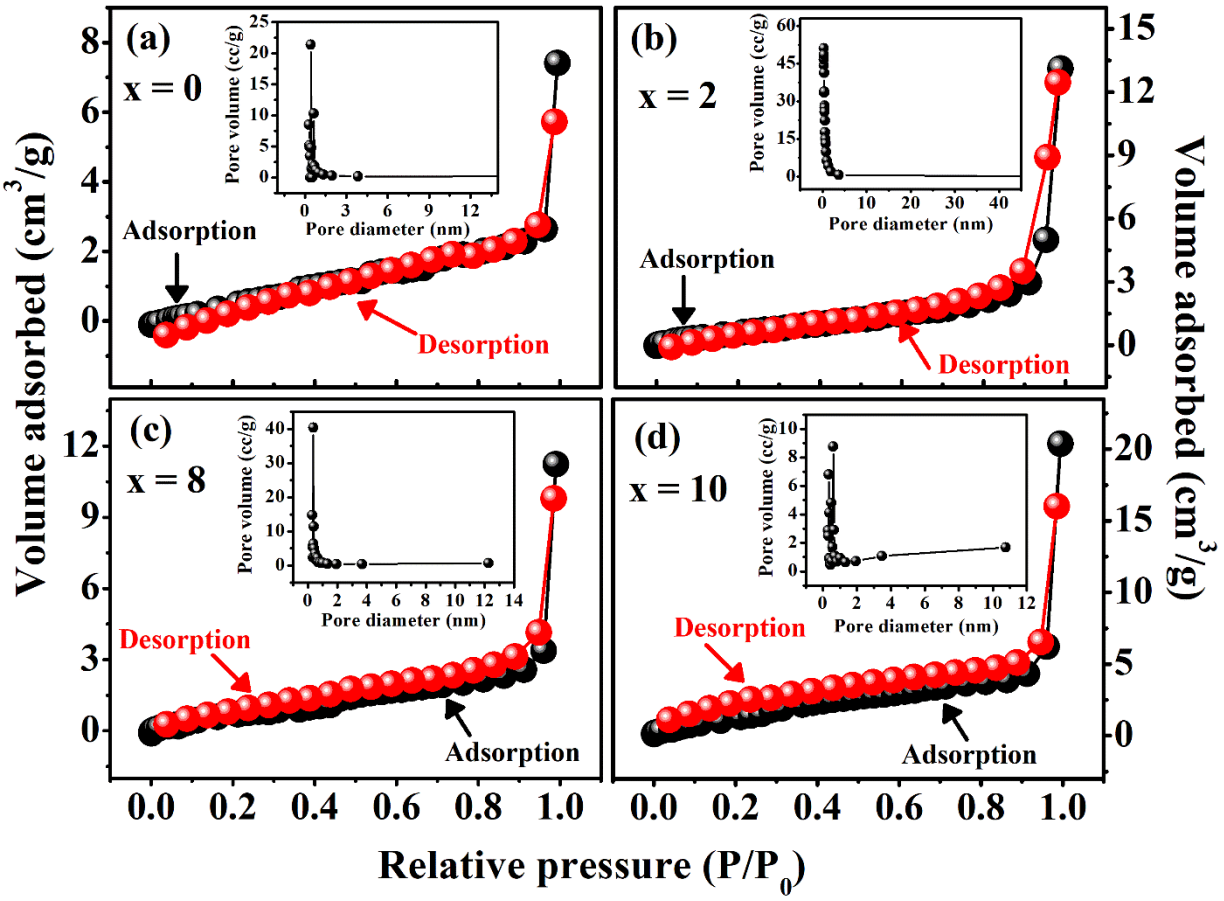

Figure 4.03: Nitrogen adsorption-desorption isotherms curves of (a) x = 0, (b) x = 2, (c) x = 8, and (d) x = 10 MGC samples. Insets present pore size distribution curve of respective samples.

A significant variation in the surface area, average pore size, and pore volume are noticed in the samples with an increase in x. The desorption isotherm in the BJH method was used to determine the pore size distribution presented here. Mono-modal type of distribution is observed for the x = 2 and x = 8 samples, while bi-modal type distribution has been observed for x = 0 and x = 10 (inset of Figure 4.03 (a) and (d)). The bi-modal distribution could have some advantage in osteointegration process involving proteins of different sizes [KOML2002]. The average pore size and total pore volume increased from 3.31 nm to 4.18 nm, and 0.012 cc/g to 0.031 cc/g,

respectively, when x was increased from 0 to 8 wt.%. As x was increased from 0 to 10 wt.%, surface area of the glass-ceramic powder increased from 1.81 m^2/g to 4.03 m^2/g. x = 0 MGC, which is devoid of iron oxide shows the minimum surface area of 1.81 m^2/g. The measured value of surface area shows slightly higher value with respect to the reported value of 0.9 m^2/g for nanopowders of 45S5 glass-ceramic [FAUR2015].

Table 4.02: Textural properties of x = 0, 2, 8 and 10 MGC nanopowder sample.

Sample code	Surface area (m^2/g)	Pore size (nm)	Pore volume (cc/g)
x = 0	1.81	3.31	0.012
x = 2	3.81	4.18	0.020
x = 8	3.86	4.18	0.031
x = 10	4.03	3.72	0.017

As iron oxide content (x, in wt.%) was gradually introduced into the 45S5 composition in the place of silicon oxide, the specific area of the glass-ceramic increased. This increase in the surface area is due to the larger size of iron ions as compared to Si ions. The experimental findings clearly show that the silica content of the material has a substantial effect on the porosity of the glass-ceramic. Thus, introduction of iron oxide content for silica not only increases the surface area but also influences its porosity of the of the sol-gel derived 45S5 based nanopowders. Therefore, the overall results arise from the complementary behavior of both SiO_2 and iron oxide. The overall enhancement of textural properties of the mesoporous x = 10 shows great promise for biomedical applications among the iron oxide-substituted 45S5 glass-ceramics.

4.4. Surface Zeta potential and analysis of colloidal particles

The ζ of aqueous suspensions of MGCs nanopowder was recorded and the corresponding data are displayed in Figure 4.04. ζ of MGC powders decreased in magnitude from -34.7 to -7.0 mV as x was increased from 2 to 15 wt.% in (45-x)SiO_2-24.5CaO-24.5Na_2O-6P_2O_5-xFe_2O_3

composition. A general hydrokinetic stability standard classifies a suspension in the ζ range of +25 mV to -25 mV as unstable and susceptible to form aggregation and agglomeration in water medium [MAHA2014]. According to this stable suspension classification, the ζ value of aqueous suspensions of MGCs nanopowder with x = 2 to 10 wt.% are stable suspensions [MAHA2014]. However, the aqueous suspension of x = 15 MGC is within the range of unstable suspensions and hence prone to aggregation and agglomeration in water medium. This reduction in ζ as a function of x can be explained by the interaction of the magnetic particles dispersed in water. According to structural investigations, the fraction of magnetic phases progressively increases as the x rises. So, with an increase in magnetic phase content, the magnetization increases, and hence the magnetic attraction between the particles. This in turn increases the aggregation and agglomeration of the particles. This results in the destabilization of the colloidal suspension, which is reflected in a decline in ζ with an increase in x. This destabilization mechanism becomes very strong for suspensions with magnetic content higher than x = 10 making them unstable as observed in the case of x = 15 MGC suspension.

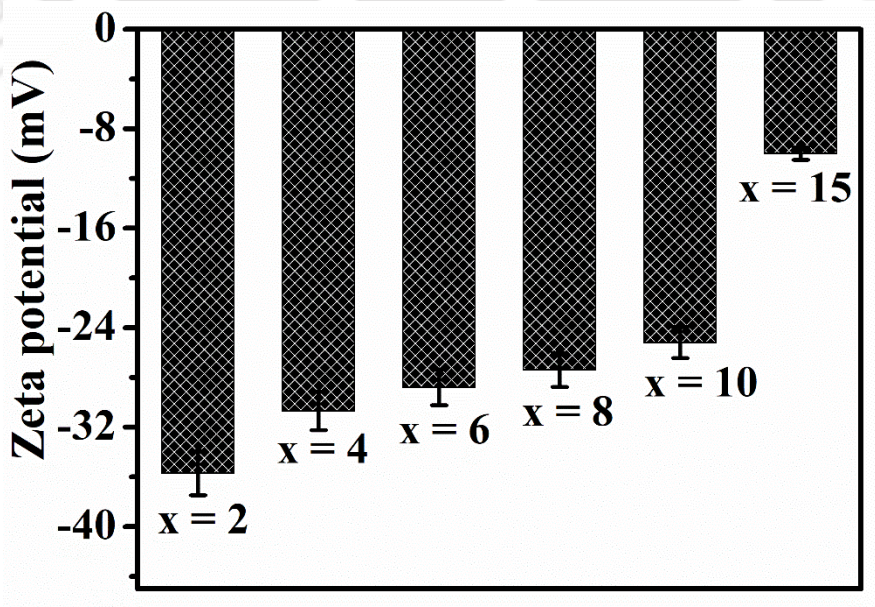

Figure 4.04: Zeta potential (ζ) of MGCs samples recorded at room temperature.

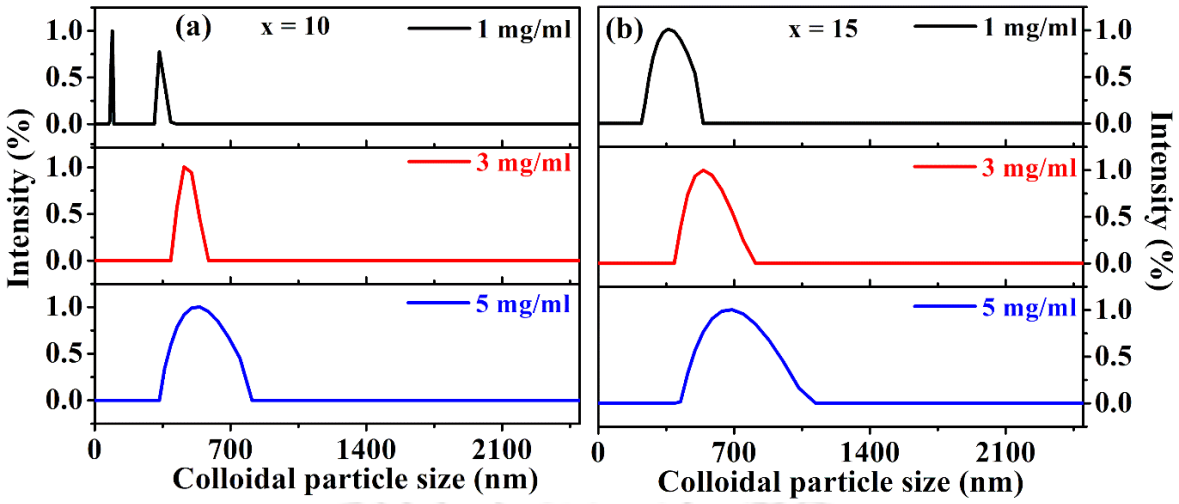

Figure 4.05: Colloidal particle size of (a) x = 10, and (b) x = 15 MGC nanopowder dispersed in deionised water with different solute concentration.

The colloidal particle size distribution of x = 10 and x = 15 MGC with three concentrations was measured using Dynamic Light Scattering (DLS), as depicted in Figure 4.05. At a concentration of 1 mg/ml, x = 10 MGC colloidal particles exhibited a bi-modal size distribution with a range of 67 nm to 100 nm and 301 nm to 398 nm, and average particle sizes of ~90 nm and ~330 nm, respectively. Similarly, with 3 mg/ml and 5 mg/ml concentrations, x = 10 MGC colloidal particles had larger size ranges of 385 nm to 590 nm and 320 nm to 810 nm, and average sizes of around ~480 nm and ~530 nm, respectively. Additionally, for x = 15 MGC colloidal particles, the average particle sizes varied from 200 nm to 520 nm, 380 nm to 810 nm, and 400 nm to 1100 nm at concentrations of 1 mg/ml, 3 mg/ml, and 5 mg/ml, respectively, with corresponding average sizes of ~370 nm, ~540 nm, and ~680 nm.

4.5. EPR studies

Room temperature EPR spectra due to Fe ions in (45-x)SiO_2-24.5CaO-24.5Na_2O-6P_2O_5-xFe_2O_3 ($2 \leq x \leq 15$ wt.%) MGC are shown in Figure 4.06. A strong dependence of EPR parameters, specifically total intensity (J) and line width (ΔH), on x has been observed. The resonance

absorption at g ≈ 2.0 is typical of a free electron, which signifies the lack of spin-orbit interactions [LOVE1971].

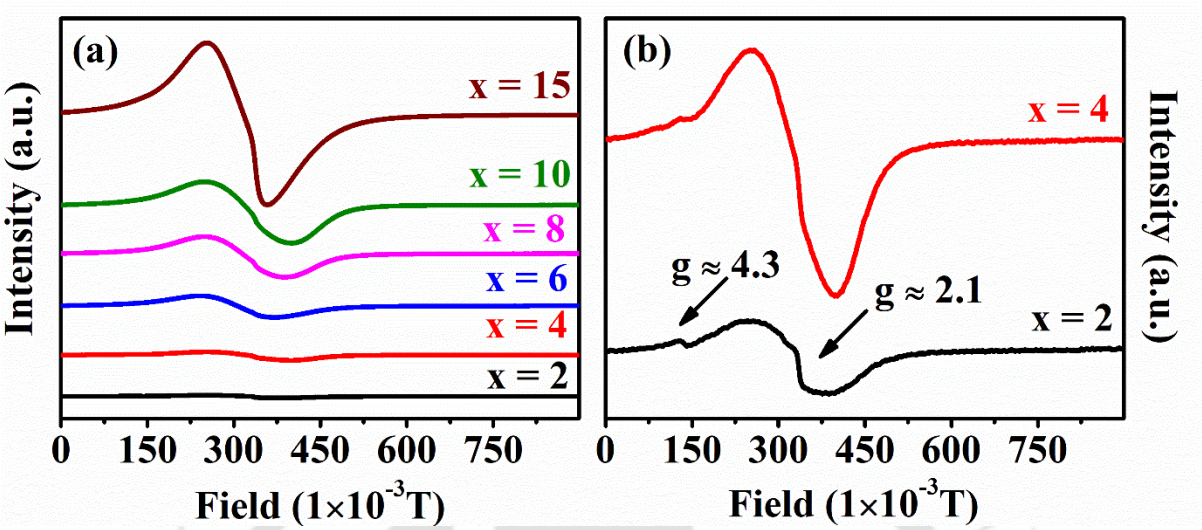

Figure 4.06: (a) Room temperature EPR spectra of all MGC nanopowder samples. (b) Enlarged view of EPR spectra of MGC nanopowders with x = 2 and x = 4 wt.% iron oxide content.

The literature also reports resonances at larger g values for materials containing iron, specifically at g ≈ 4.3, g ≈ 6.0, and g ≈ 9.7 [KOMA1980, RADA2011, RAJY2012]. The origin of these resonances can be explained by the spin Hamiltonian *H* presented in equation (4.01) [POPA2013].

$$H = g\beta\vec{B}.\vec{S} + D\left[S_z^2 - \left\{\frac{S(S+1)}{3}\right\}\right] + E\left(S_x^2 - S_y^2\right) \qquad (4.01)$$

In equation (4.01), the total spin of the Fe^{3+} system is 5/2, *B* is the applied magnetic field, and β is the Bohr magneton. The spin components along the x, y, and z axes are denoted as S_x, S_y, and S_z, while the rhombic and axial structural constants are represented by *E* and *D*, respectively. The first term in equation (4.01) represents the normal Zeeman term and the second is the crystal field term. The ratio of the rhombic to axial structural constant, λ = *E*/*D*, ranges from 1/3 to 0. The lower limit of λ (= 0) represents full axial symmetry and its increasing value reveals a

progression from axial to fully distorted rhombic symmetry for λ = 1/3. In the absence of a magnetic field, three degenerate energy levels (or Kramer doublets), viz., ±5/2, ±3/2, and ±1/2 are produced for the five unpaired electrons of the Fe system. If $E = D = 0$, the g value would be near the free-electron g value and for a small value of E and D, the perturbation theory might be used. The degeneracy is removed with a magnetic field and transition between +1/2 to −1/2 is not shifted in the first-order transition. Consequently, g ≈ 2.0 absorption will appear for weak crystal fields. The solution to the spin Hamiltonian presents challenges if the applied magnetic field is close to the crystal field. In order to solve equation (4.01), two assumptions, viz., the crystal field dominates when $2\beta H \ll D$ or $2\beta H \ll E$ are made. In the first limiting situation where E ≈ 0 and D = 0, the middle doublet exhibits an isotropic g ≈ 4.3 value. Conversely, the lowest doublet has a g value which is near 2.0 and 6.0 if $E = 0$ and $D \approx 0$. As previously noted, the presence of Fe^{3+} ions in deformed octahedral or tetragonal oxygen environments is characterized by absorption peaks around g ≈ 4.3, while Fe^{3+} ions within clusters typically exhibit absorption peaks around g ≈ 2.0.

In Figure 4.06 (a), it is observed that the resonance absorption at g ≈ 2.0 gradually intensifies with an increase in x. Conversely, the resonance absorption at g ≈ 4.3 weakens gradually upon the introduction of iron oxide and eventually disappears for samples with x > 4. Variations in the EPR parameters of the g ≈ 4.3 spectral line suggest a depletion of isolated Fe^{3+} ions as x increases, and that Fe^{3+} ions tend to occupy higher symmetry positions for x > 4. Figure 4.07 displays the variation in EPR parameters of the g ≈ 2.0 line with x. As x increases, the intensity of the g ≈ 2.0 spectral line grows, but the linewidth initially widens up to x = 4 before narrowing again for larger x. Enhanced super-exchange interactions between the iron ions are facilitated by the formation of iron clusters, as evidenced by the intensified g ≈ 2.0 absorption with increasing x. The super-exchange interaction tends to narrow the linewidth, while dipole-dipole interaction between the same type of Fe ions (Fe^{2+}-$Fe^{2+}$and/or Fe^{3+}-Fe^{3+}) favours the

broadening of the line. Hence, the observed spectral line width is a resultant of competing dipole-dipole and super-exchange type interactions. The behavior of ΔH of g ≈ 2.0 line shows that dipole-dipole interaction dominates in MGC with x ≤ 4 due to the presence of more Fe^{3+} paramagnetic spins whereas super-exchange type interaction dominates in MGC with higher x. As x increases, the number of spins also increases, resulting in a consistent rise in the total intensity of the g ≈ 2.0 line.

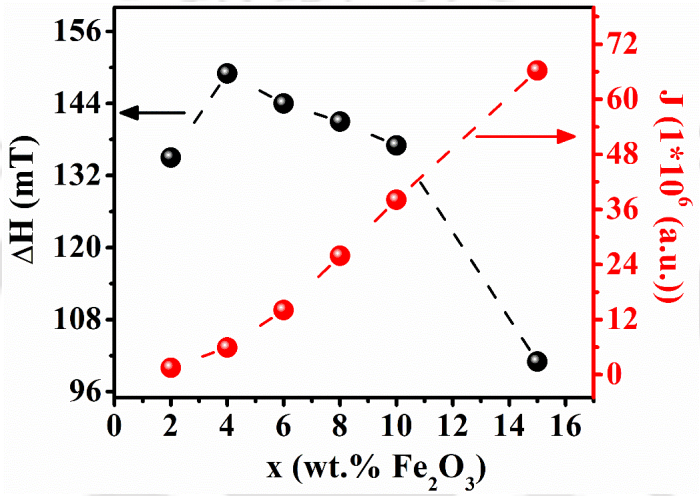

Figure 4.07: Variations of linewidth (ΔH) and intensity (J) of g ≈ 2.0 absorption line with x in (45-x)SiO_2-24.5CaO-24.5Na_2O-6P_2O_5-xFe_2O_3 MGC.

4.6. Magnetic properties

Figure 4.08 (a) shows the room temperature magnetic hysteresis loop (M-H curve) of all MGC nanopowder samples recorded under an applied magnetic field range of ±40 kOe. Figure 4.08 (b) depicts the minor hysteresis loops recorded in clinically viable field range of ±500 Oe. Low iron oxide containing samples such as x = 2 and x = 4 MGC did not exhibit magnetic saturation up to 40 kOe because of the relatively lower percentage of the magnetic phases present as compared to the combeite phase. As x was increased in the nominal composition, the percentage of magnetic phases increased and hence the saturation magnetization M_s of the samples. Low H_c and low M_r values indicate the soft magnetic behavior of the MGC nanopowder samples.

Magnetic parameters such as M_s, H_c, M_r, and hysteresis loop area of each sample are listed in Table 4.03. When x was increased from 2 to 15 in 45S5 composition, M_s improved from 0.094 emu/g to 1.543 emu/g. Two magnetic phases, viz., hematite and magnetite, have already been identified in these MGC samples (*cf*. Figure 4.01 and Table 4.01). The hematite phase (α-Fe_2O_3) exhibits antiferromagnetic nature below 260 K and shows a weak ferromagnetic behavior at room temperature (bulk M_s~ 0.4 emu/g), while the magnetite (Fe_3O_4) phase shows soft ferromagnetic nature (bulk M_s~ 92 emu/g) [ROBE2020]. Hence, the overall M_s of the MGC will depend on the relative percentages of the two magnetic phases. An analysis of the magnetic characteristics reveals that, M_r increases with an increase in x. But H_c increases for x up to 6 wt.% and then decreases for higher x values.

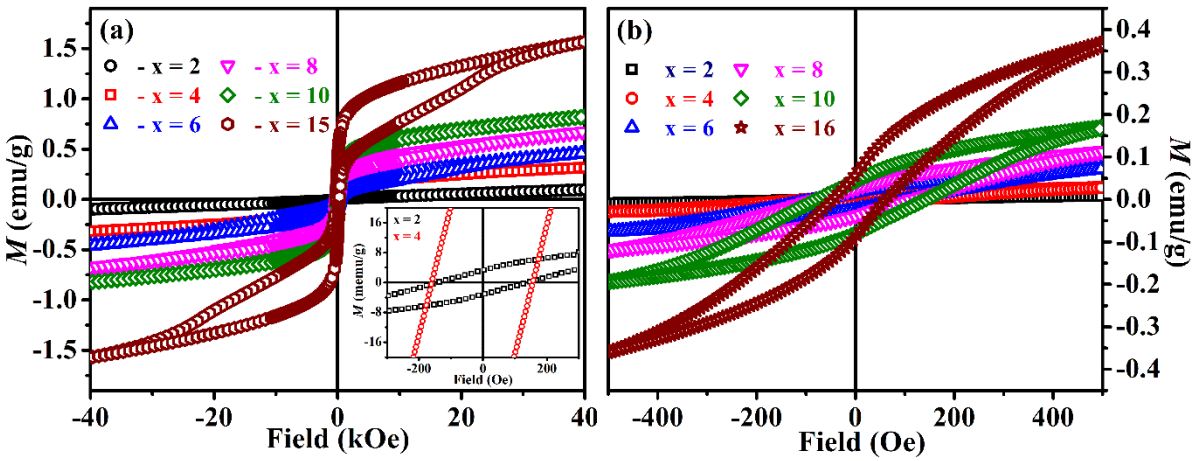

Figure 4.08: Room temperature *M-H* curves of (45-x)SiO_2-24.5CaO-24.5Na_2O-6P_2O_5-xFe_2O_3 (2 ≤x ≤ 15 wt.%) MGC recorded at (a) ±40 kOe and (b) ±500 Oe. Inset in (a) provides an enlarged view of the data close to the origin.

The area enclosed by the *M-H* loop varies significantly with increasing iron oxide levels. The energy loss leading to heat generation in an alternating magnetic field by the MGC is directly linked to this area. Based on the magnetic characteristics provided in Table 4.03, samples with high iron oxide concentrations (x = 10 and x = 15) are better suited for MH application. Since a

high magnetic field is not viable for clinical *in vivo* MH treatment, minor *M-H* loops have also been recorded at an amenable field range of ±500 Oe. A similar trend in magnetic parameters such as M_s, H_c, M_r, and hysteresis loop area has been observed in both the *M-H* loops recorded in ±40kOe and ±500 Oe field scans.

Table 4.03: Magnetic parameters of MGC samples.

Magnetic and structural parameters	**x = 2**	**x = 4**	**x = 6**	**x = 8**	**x = 10**	**x = 15**
Saturation magnetization, M_s (emu/g)	0.094	0.246	0.447	0.635	0.820	1.543
Coercive field, H_c (Oe)	137	234	306	214	149	107
Remnant magnetization, M_r (emu/g)	0.0032	0.0213	0.0685	0.1124	0.1169	0.1247
Area of major (±40 kOe) loop (erg/g)	57	725	2280	4352	8966	18041
Area of minor (±500 Oe) loop (erg/g)	2	8	22	35	62	74

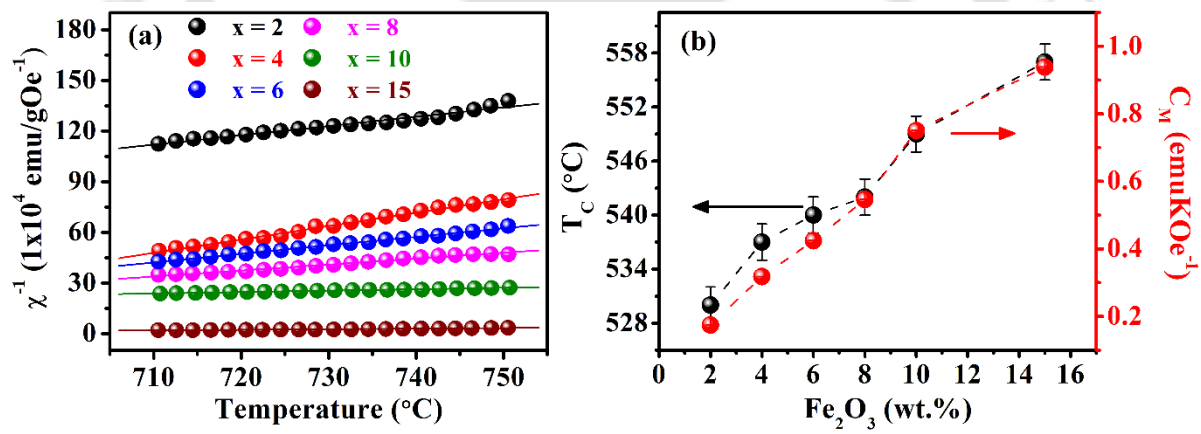

Figure 4.09: (a) Temperature dependence of reciprocal magnetic susceptibility, (b) Curie temperature and calculated molar Curie constant of various MGC compositions.

In Figure 4.09 (a), the temperature dependence of the reciprocal of magnetic susceptibility (χ^{-1}) corresponding to the MGC samples is illustrated. Lines in Figure 4.09 (a) represent the least squares fits to the χ^{-1}-T data as per equation 2.14. Above 677 °C, the bulk

CaO-SiO_2-P_2O_5-Na_2O-Fe_2O_3 glass-ceramics exhibit a linear variation in χ^{-1}-T curve with a distinctive downward deviation at lower temperature [SING2008a]. The deviation from linearity observed in the χ^{-1}-T graph indicates the onset of short-range magnetic order, occurring slightly above the ferromagnetic-paramagnetic transition temperature (*a,k,a*. Curie temperature T_C). The ferromagnetic nature of the bulk MGC is retained by these sol-gel MGC as well. The molar Curie constant was calculated from equation 2.14. Figure 4.09 (b) illustrates the molar Curie constant (C_M) and the dependency of T_C on composition for the magnetic glass-ceramics. T_C increases with iron content in these MGC. C_M was used to estimate the effective magnetic moment. Various valence states of iron ions in the ceramic network were estimated, as detailed in section 2.2.6 of chapter 2. Moreover, presence of Fe^{3+} and Fe^{2+}ions in these MGC has been confirmed by EPR studies.

Table 4.04: Experimental value of μ_{exp}, Molar Curie constant (C_M), weight fraction of iron ions in $(45-x)SiO_2$-$24.5CaO$-$24.5Na_2O$-$6P_2O_5$-xFe_2O_3 ($2 \leq x \leq 15$ wt.%) MGC.

x (wt.%)	C_M (emuKOe^{-1} mol^{-1})	μ_{exp} (μ_B)	x_1 (wt.%$Fe_2^{3+}O_3$)	x_2 (wt.%$Fe_2^{2+}O_3$)	$x_2/(x_1+x_2)$
2	0.1746±0.0001	5.90±0.01	1.96±0.01	0.04±0.01	0.02
4	0.3178±0.0001	5.64±0.01	2.87±0.01	1.13±0.01	0.28
6	0.4243±0.0001	5.31±0.01	2.41±0.01	3.59±0.01	0.60
8	0.5420±0.0001	5.20±0.01	2.35±0.01	5.65±0.01	0.71
10	0.7501±0.0001	5.03±0.01	1.36±0.01	8.64±0.01	0.86
15	0.9280±0.0001	4.97±0.01	1.03±0.01	13.97±0.01	0.93

It has been suggested that the presence of Si^{4+} and Ca^{2+} ions in the network could promote the existence of iron in the Fe^{2+} valence state in these glass-ceramics [SING2008a]. The composition dependence of C_M and the estimated percentage of Fe^{2+} and Fe^{3+} ions are given in

Table 4.04. C_M increased and effective magnetic moment decreased with an increase in x. Adrelean *et al.* showed that in magnetic glasses with more than 1 wt.% iron oxide, both Fe^{2+} and Fe^{3+} ions would be present [ARDE1997]. This has also been confirmed by other reports on iron oxide-based oxide glasses and glass-ceramics [BAND1980, KUMA1994, WEDG1976, ALBO2008, MEKK2001]. Table 4.04 clarifies that Fe ions exist in both Fe^{2+} and Fe^{3+} valence states in each glass-ceramic composition. x_2 (weight fraction of Fe^{2+}) increases with iron oxide content, while x_1 (weight fraction of Fe^{3+}) increases in samples with iron oxide content up to 4 wt.% and then decreases for higher iron oxide content. This finding is in line with the conclusions from the EPR investigations discussed earlier in this chapter. The ratio of Fe^{2+} ions (x_2) to total ions (x) in the MGC correlates with the iron oxide content, suggesting a corresponding decrease in the proportion of Fe^{3+} ions. This trend can be explained if we accept the existence of the Fe^{2+}-Fe^{2+}, Fe^{2+}-Fe^{3+}, and Fe^{3+}-Fe^{3+} exchange pairs in iron oxide based magnetic glass-ceramics. The research discussed above illustrates the existence of super-exchange and dipolar interactions among iron ions within the MGC network, highlighting how their relative dominance changes with the iron oxide content.

Figure 4.10 displays the temperature dependent magnetization (*M*-*T*) curves of all MGC samples from 5 K to 305 K under both FC and ZFC conditions. A noticeable distinction is observed between the ZFC and FC curves of MGC samples containing 2, 4, and 6 wt.% of iron oxide compared to those with higher iron oxide content (i.e., 8, 10, and 15 wt.%). In the case of MGC with 2 wt.% iron oxide, both the ZFC and FC curves overlap with each other completely in the entire (5 K to 305 K) temperature range. As iron oxide is progressively increased up to 6 wt.%, the ZFC and FC curves gently begin to deviate from the overlap. However, in MGC with iron oxide > 6 wt.%, the separation between the FC and ZFC increases drastically. Moreover, several new features appear in the ZFC curve of MGC with 8 wt.% iron oxide, which becomes more prominent in MGC with higher the iron oxide content.

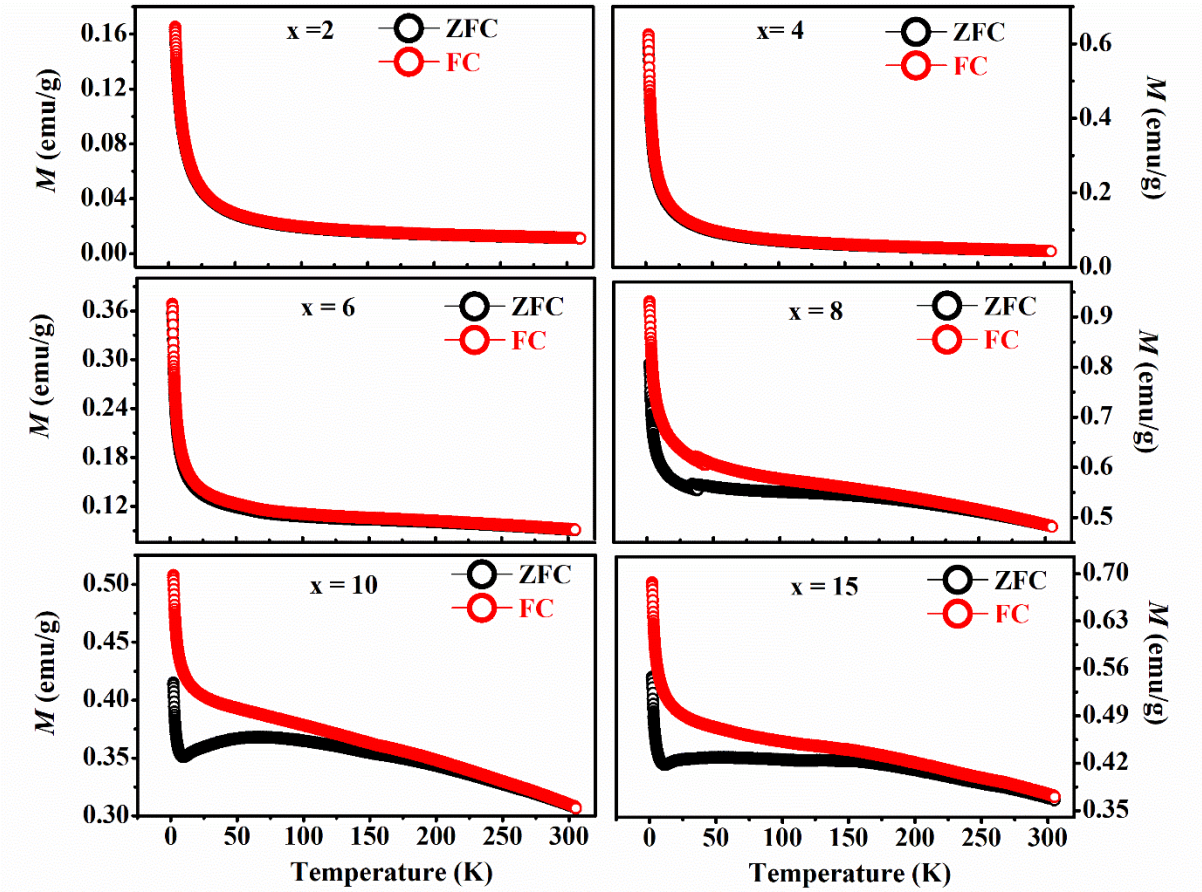

Figure 4.10: Thermo-magnetization *(M-T)* curves of (45-x)SiO_2-24.5CaO-24.5Na_2O-6P_2O_5-xFe_2O_3 ($2 \leq x \leq 15$ wt.%) MGC nanopowder recorded under ZFC and FC modes.

To understand the behavior of the ZFC-FC curves, let us first take a look at Figure 4.01 (b) which shows a step-like increase in the relative phase percentages of both magnetic phases in MGC with x > 6 wt.% iron oxide. Thus, one can classify the MGC with $x \leq 6$ wt.% iron oxide as weakly magnetic and those with $x \geq 8$ wt.% iron oxide and strongly magnetic in terms of the amount of magnetic phases present in them. Shapes of ZFC-FC curves resembling those observed in our weakly magnetic MGC (i.e., x = 2, 4, and 6 wt.%) have been reported for various oxides [DEY02016, LAFT2020, DATT2017]. It is apparent from the above reports that such ZFC-FC curves are observed in weak ferromagnetic or antiferromagnetic materials as observed in our weakly magnetic MGC. Conversely, the shape of the ZFC-FC curves of x = 8, 10, and 15 MGC sample, appear to mimic the behavior of ferromagnetic-like nanoparticles exhibiting

superparamagnetism. One can observe the well separated ZFC curve of MGC with x = 8, 10, and 15 exhibit three features: (a) A broad peak in the ZFC curve which is a signature of the blocking temperature (T_B) below which the spins are blocked, (b) bifurcation temperature (T_{BF}) of the ZFC and FC curves above which all spins are unblocked, and (c) a minimum followed by a significant increase in magnetization near ~10 K. The ZFC curve typically features a sharp maximum (designated as T_B) that depends on the size and shape of the superparamagnetic nanocrystallites [RUMP2012]. This peak broadens and shifts to higher temperatures if there is a wide range in particle sizes or if multiple magnetic nanoparticles are present [JOHN2021, HUAN2013]. In our case, magnetite, a strong nanomagnetic phase (M_s = 92 emu/g) and hematite, a weak magnetic phase (M_s = 0.4 emu/g) are present in these MGC samples. The peak-like feature observed in ZFC of MGC with x ≥ 8 wt.% iron oxide is primarily due to the magnetite nanoparticles. The broadening of this peak is attributed to the substantial presence of weakly magnetic hematite nanoparticles with varying particle sizes. T_B increases from 35 K to 170 K as x is raised from 8 to 15 wt.% in our MGC samples. The increase in T_B is related to an increase in D_V of magnetite phase with x in the MGC. There are a few reports on nanomagnetic particles exhibiting similar ZFC-FC curves as observed in our MGC with x = 8, 10 and 15 [LAFT2020, PROE2011, XU002019]. T_{BF} also increases with x in the MGC [T_{BF} ~ 265 K for the MGC with x = 8, T_{BF} ~ 275 K for the MGC with x = 10 and T_{BF}> 305 K for the MGC with x = 15]. The third feature observed below 15 K in the ZFC-FC curves shifts towards lower temperatures with increase in x. In this temperature range, the appearance of this feature can be attributed to pure paramagnetic contributions, or the presence of hematite nanoparticles, or the magnetic interaction between iron ions in their Fe^{2+} and Fe^{3+} valence states [XU002019]. Several reports have elucidated that this feature arises from the underlying double ferromagnetic exchange interaction among transition metal ions [XU002019]. One can also expect such double ferromagnetic exchange interaction in

our MGC containing Fe^{2+} and Fe^{3+}ions leading to Fe^{2+}- O - Fe^{3+} type of configuration in the glass-ceramic network.

4.7. Evaluation of induction heating capacity

Induction heating studies were carried out to assess the suitability of the MGC samples for use as thermoseeds in MH applications, following procedures detailed in chapter 2. Considering their high M_s and H_c, MGC with x = 10 and x = 15 were chosen for the test. Figure 4.11 illustrates the temperature-time curve and NIR camera images for three distinct concentrations of aqueous MGC fluids. The patient exposure safety limit, represented by the product, $H \times f$ (= 9.59×10^9 $Am^{-1}s^{-1}$), where H and f are the applied field strength and the frequency of the alternating magnetic field, respectively [PART2022]. Temperature rise of MGC fluids containing 10 and 15 wt.% iron oxide increased with increase in concentration of iron oxide in the MGC. For clinical application, the temperature rise of the magnetic fluid should be up to 42 °C. Different types of heat generation mechanisms are briefly discussed in section 1.6.2 of chapter 1 [DEAT2014]. In the case of magnetic nanoparticles, heat generation is primarily governed by hysteresis losses and relaxation mechanisms. Hysteresis loss is prevalent in multi-domain ferromagnetic particles or larger single-domain particles, while smaller particles contribute through Néel and Brownian mechanisms. It has been reported that particles ranging from above 17 nm to 100 nm exhibit predominantly Brownian contribution, whereas particles below 17 nm are prominently associated with the Néel mechanism [DEAT2014, KANG2022]. However, hysteresis loss becomes prominent in particles larger than 100 nm. It is obvious from the DLS data discussed in section 4.4 that colloidal particle sizes are dependent on concentration and are in general, higher than 100 nm. This clearly rules out Néel contribution and points towards a very low contribution from the Brownian component. Hence, the major contribution comes from hysteresis loss. In fact, Brownian contribution dominates only in MGC sample with x = 10 at a concentration of 1 mg/ml.

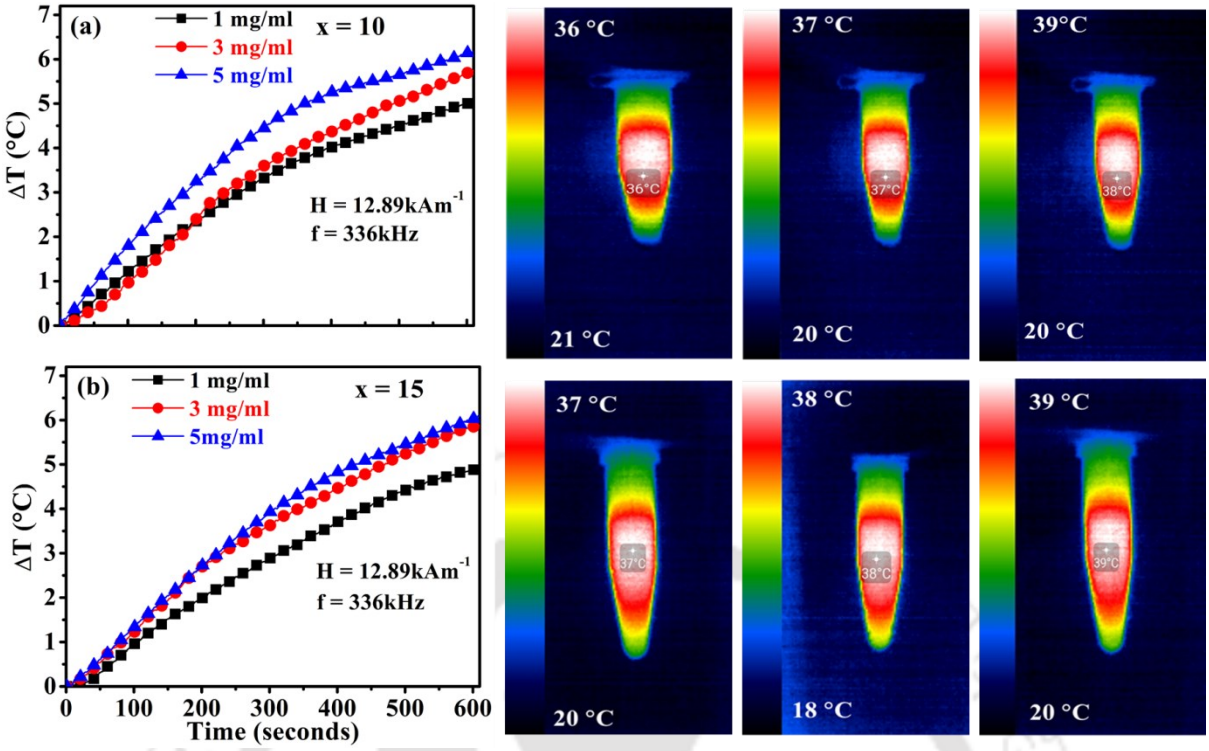

Figure 4.11: Curves depict the temperature rise (ΔT) as a function of time of magnetic fluids with x = 10 and x = 15. NIR camera images of each induction heated fluid is also displayed.

The BLM and ISM method is described in detail in section 2.2.9 of chapter 2. Figure 4.12 (a, and b) display the *SAR* and *ILP* values of the MGC fluids with x = 10 and x = 15 calculated using ISM, while Figure 4.12 (c) and (d) illustrate the *SAR* and *ILP* values calculated from BLM for different concentrations of magnetic fluids.

SAR values of the MGC fluids with x = 10 and x = 15 calculated using ISM are lower than the ones calculated using BLM because ISM considers only the initial linear data and neglects the higher temperature data of the heating curve, whereas BLM considers the data in the whole temperature range [KUMA2018]. There is a significant correlation between the *SAR* values and the MGC concentration in the magnetic fluids in both samples. The magnetic fluid with the lowest MGC content shows the highest *SAR* value which can be explained through the change in the dipolar interaction between the particles in the fluid [AHMA2018]. When the concentration of magnetic nanoparticles increases, the separation between particles decreases

which causes a reduction in the heat loss. However, the MGC fluids with x = 10 and x = 15 with 1mg/ml concentration exhibit *ILP* of 1.24 nHm^2kg^{-1} and 1.36 nHm^2kg^{-1} (estimated using BLM), respectively. These values are slightly higher than the *ILP* value of 1.0 nHm^2kg^{-1} reported for the commercially available magnetic fluid, FluidMag-CT [KUMA2018].

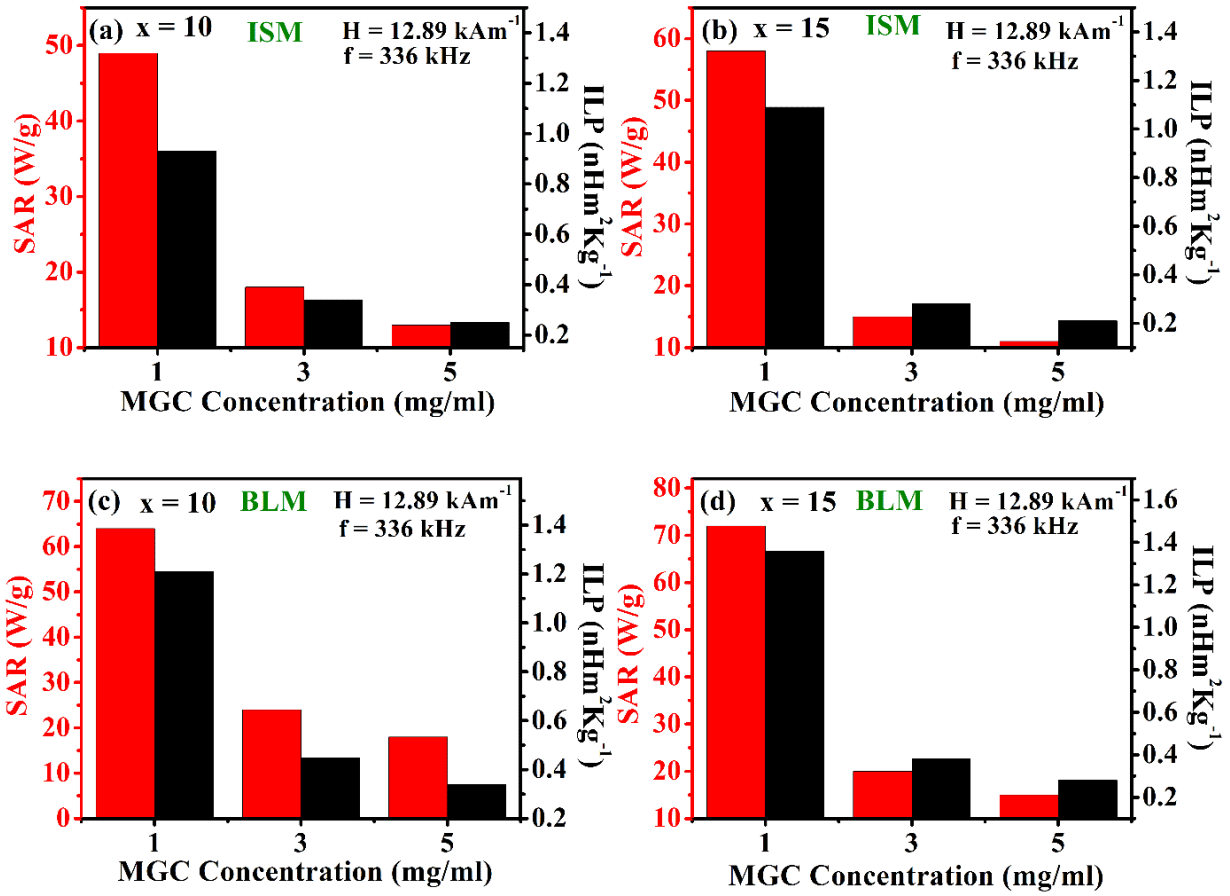

Figure 4.12: Calculated *SAR* and *ILP* values of MGC fluids with (a) x = 10, and (b) x = 15 using ISM and using BLM for fluids with (c) x = 10, and (d) x = 15.

Table 4.05 displays the estimated time required for the two MGC sample fluids with different concentrations to reach the crucial temperature of 42 °C. For MGC samples with concentrations of 5 mg/ml and x = 10 and x = 15, it takes 1280 s and 1200 s, respectively, to reach 42 °C from room temperature. MGC with x = 15 at a concentration of 5 mg/ml required the least time to reach 42 °C. Though the MGC fluid with x = 15 has better heating capacity than

the one with x = 10, it has unstable aqueous colloidal stability. So, if one considers both the *ILP* and colloidal stability factors, the MGC fluid with x = 10 MGC displays better potential for MH application.

Table 4.05: Estimated time for MGC fluids with x = 10 and x = 15 to reach 42 °C under H = 12.89 kAm^{-1} and f = 336 kHz.

Sample ID	Time (sec)		
	1 mg/ml	3 mg/ml	5 mg/ml
x = 10	1500	1320	1280
x = 15	1440	1300	1200

4.8. *In vitro* bioactivity assessment

4.8.1. Ion exchange

Figure 4.13 (a) shows the variation in pH of SBF as a function of time when (45-x)SiO_2-24.5CaO-24.5Na_2O-6P_2O_5-xFe_2O_3 ($2 \leq x \leq 15$) sample pellets are immersed in it. After 30 days of soaking, the pH of the SBF increased from 7.4 to 8.7, 7.4 to 8.5, 7.4 to 8.4, 7.4 to 8.3, 7.4 to 8.2, and 7.4 to 8.0 in the case of MGC with x = 2, 4, 6, 8, 10, and 15, respectively. The measured pH data of all MGC samples show a sharp increment in pH up to 5 days of immersion in SBF due to the rapid ion-exchange process occurring upon exposure to the body fluid. After this, the pH values slowly progress toward saturation due to the stabilization of released ions. The observed behavior of time dependent pH data shows that all the MGC compositions exhibit *in vitro* bioactivity expected from an implantable material. But, a comparative study of the pH curves of different MGC compositions show that the saturation value of pH decreases from 8.7 to 8.0 as iron oxide content is increased. The MGC with x = 2 shows the maximum variation of 1.3, which slowly decreases to 0.6 as we move to the MGC with x = 15. The silanol group (Si-

OH) formed in the intermediate stage of the dissolution mechanism is considered to be the nucleating site for a calcium phosphate layer, which can crystallize into a HAp layer. As iron oxide is gradually substituted from the silicon dioxide, the silanol species starts to decrease gradually. Also, at high pH levels, the presence of free iron ions is typically suppressed due to the formation of a ferric hydroxide complex in SBF, resulting in a slight decrease in the pH of the solution.

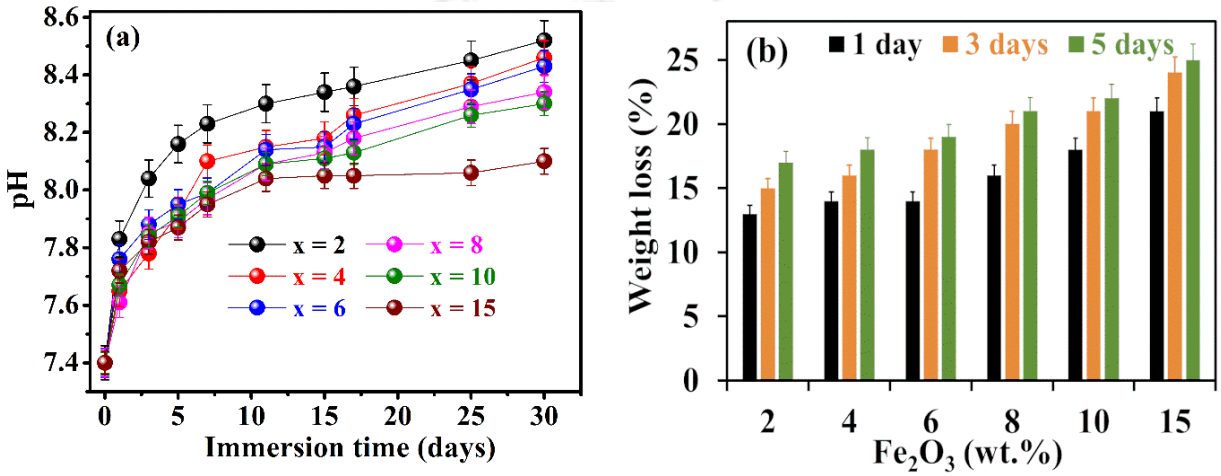

Figure 4.13: (a) Change in pH of MGC immersed in SBF with soaking time. (b) Weight loss in MGC measured before and after immersion in PBS for different days.

The measured weight loss of the MGC pellets before and after immersion for different days is displayed in Figure 4.13 (b). The weight loss gradually increased with immersion time and a large weight loss was observed after 1 day of soaking in the PBS due to rapid degradation of the samples. The weight loss generally increased with iron oxide concentration in the 45S5 composition. These studies indicate that the degradation of glass-ceramics increased with iron oxide content. Simultaneously, the formation of the HAp layer also increased, which counters the degradation by precipitation of the Ca-P rich layer over the surface of the samples. Thus, with increased iron oxide substitution in the 45S5 composition, a slight decrease in saturation value of pH and a slight increase in degradation are observed. Overall, all MGC compositions

show both good ion exchange in SBF and degradation in PBS, which qualify them as degradable bioactive materials.

4.8.2. Surface apatite layer formation

In vitro acellular bioactivity was assessed by immersing MGC pellets in SBF using the procedure outlined in section 2.2.10.1 of chapter 2. Figure 4.14 (a) to (f) show GI-XRD patterns of SBF treated MGC pellet surfaces recorded after 0, 1, 3, 5, 15, and 30 days of immersion. The XRD pattern labeled as '0 d' corresponds to the MGC pellet before immersion in SBF. On can notice the crystalline nature of the 0 day samples with XRD peaks from magnetite, hematite and combeite phase, as already discussed in the section on structural analyses of the MGCs. After immersion in SBF, an additional crystalline phase emerges in the XRD pattern, indicating the development of a crystalline layer on the surface of the MGC pellets. Two well-defined XRD peaks at 2θ values ~26° and ~32° develop on the surface of MGC pellet with x = 2 after 3 days of immersion in SBF. For MGC pellets with x = 4, 6, 8, 10, and 15, the emergence of these XRD peaks in SBF is only noticeable after 5 days of immersion. These two prominent peaks represent reflections from the (002) and (112) planes of HAp crystallites (reference ICDD 74-0565). The process of bone mineral phase formation through the ion exchange mechanism upon soaking in SBF has been used to explain HAp production on the sample surfaces (section 1.1.4 of chapter 1). The intensities of the newly developed crystalline (HAp) phase peaks increase with immersion time as displayed in Figure 4.14 (a) to (f). On the surface of MGC pellets, ions such as Ca^{2+} and PO_4^{3-} accumulate, which explains the increase in the HAp phase with immersion time. This HAp layer formation and increase in pH (already discussed in section 4.8.1) combinedly indicate the bioactive nature of all MGC compositions.

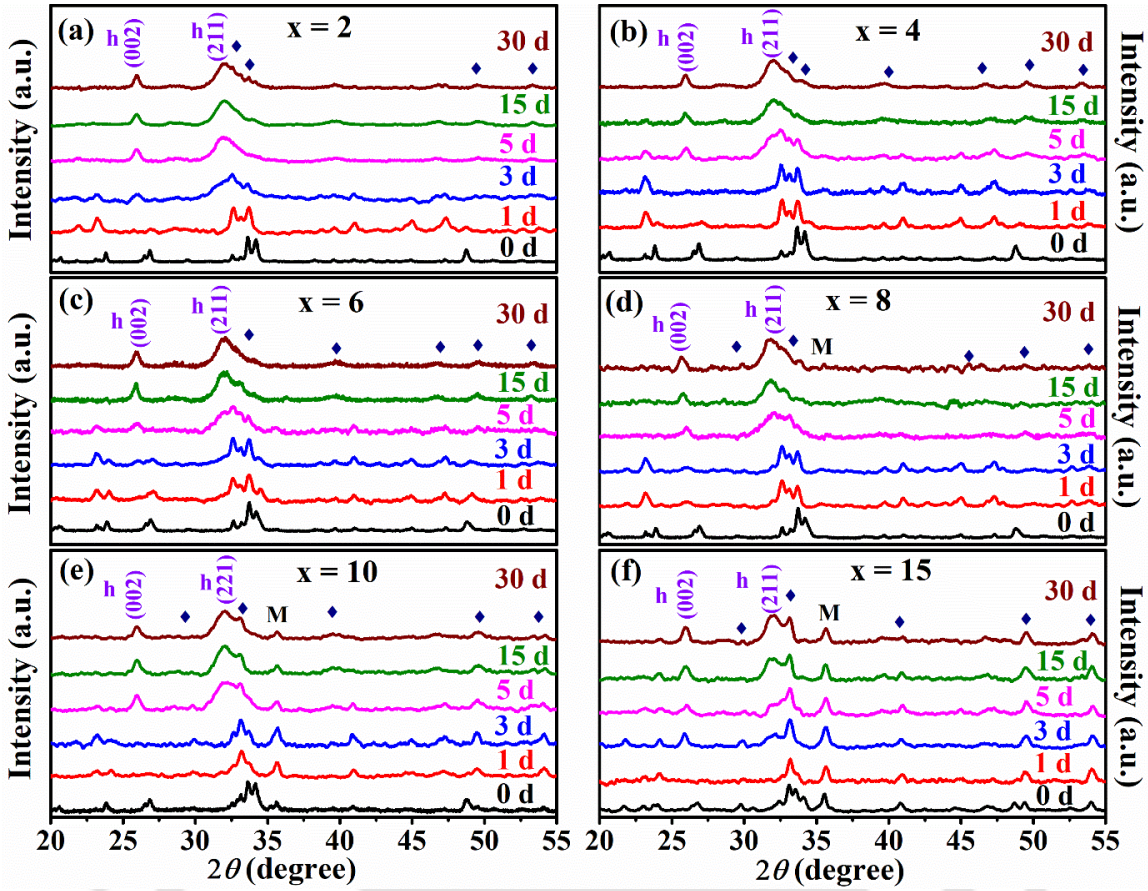

Figure 4.14: GI-XRD patterns of MGC pellets with (a) x = 2, (b) x = 4, (c) x = 6, (d) x = 8, (e) x = 10, and (f) x = 15 immersed in SBF for different days. Symbols M, h, and C represent magnetite, HAp, and combeite phases, respectively.

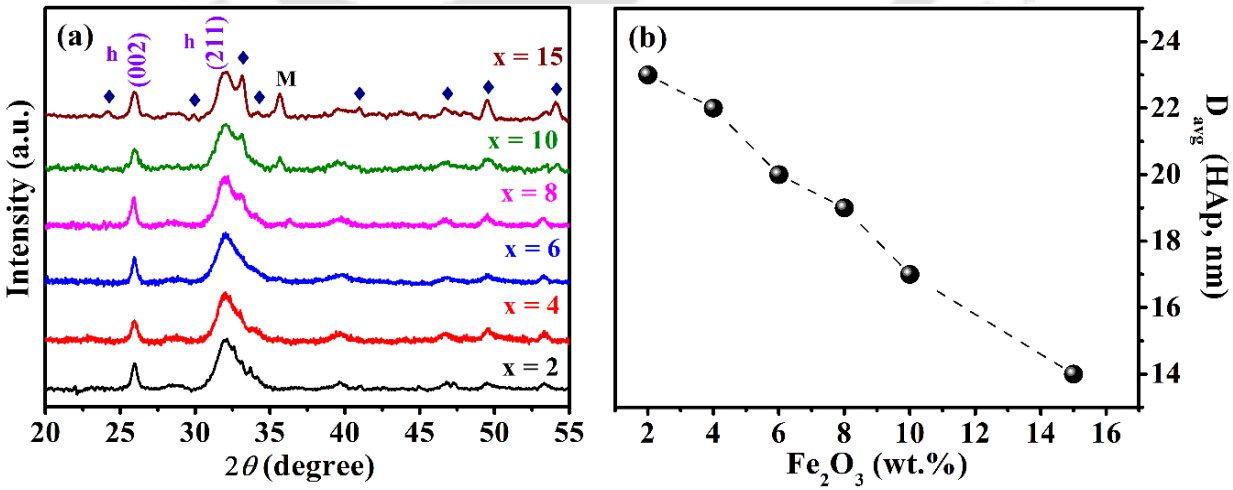

Figure 4.15: (a) XRD patterns, and (b) average crystallite size of HAp layer on the surface of MGC pellets of different compositions after 30 days of immersion in SBF.

Figure 4.14 (a-f) indicate a gradual development of the HAp layer with immersion time (days) and gradual suppression of the intensity of the underlying crystalline phases of each MGC sample. However, the crystallization of HAp layer depends upon the pH and Ca and P ions concentration of the solution. However, the thickness and the surface coverage of the deposited HAp layer decrease on the MGC surface as their iron oxide is increased. One can see that the HAp layer thickness and coverage over MGC pellets with x = 8, 10 and 15, are low and thus unable to completely suppress the appearance of the underlying glass-ceramic peaks in the GI-XRD patterns even after 30 days of immersion. Figure 4.15 (a) exemplifies the fact that the HAp layer is progressively thinner over the MGC pellets with x = 8, 10, and 15, indicating a slight decrement in the bioactivity in MGC with higher iron oxide content. The average HAp nanocrystallite size decreases substantially with an increase in x, as seen in Figure 4.15 (b). Hence, one can infer that the HAp layer growth (a) increases with immersion time for each MGC composition, and (b) slightly decreases for MGC with higher iron oxide content. The relative decrease of bioactivity of iron substituted glass-ceramic with increase in x could be explained in terms of variation in the crystalline phase percentages estimated in the XRD analysis of the MGC compositions (Figure 4.01). Substitution of iron oxide into the Hench composition increases the number of Fe^{2+} and Fe^{3+} ions at the cost of Si^{4+} ions. Reduction in Si^{4+} ions decrease the silanol group formation in SBF, which in turn decreases the HAp layer formation capacity or bioactivity of the MGC.

The FESEM images of the surface of the MGC pellets shown in Figure 4.16 (a) and (b), provide visual proof of the surface layer formation after 5 and 30 days of immersion in SBF. The grainy white layer signifies the HAp layer formed on the surface of immersed glass-ceramics. After soaking for 5 days, high density of spherical HAp grain formation is observed on the surface of the MGC pellets with x = 2 and x = 4. After 30 days of soaking, the HAp layer has expanded to cover the entire surface of all the MGC compositions (Figure 4.16 (b)). This growth

and complete coverage are correlated with the extended immersion time. Rapid layer formation of MGC samples with x = 2 and x = 4 describes the faster interchange of Ca^{2+} ions from the sample to the H_3O^+ ions from a physiological fluid. Furthermore, the primary determinant of the HAp layer production rate is the composition of the MGC. The surface mineralization was confirmed by EDS analysis, which shows the Ca/P ratio for all the samples after 30 days of soaking (*c.f.* Figure 4.16 (b)). The Ca/P ratio for the MGC pellets with x = 2, 4, 6, 8, and 10 are close to the Ca/P ratio of 1.67 reported for bulk HAp [SHAN2016]. The lower Ca/P ratio of the x = 15 sample suggests lower bioactivity, as also supported by the pH and XRD analyses of the SBF treated sample.

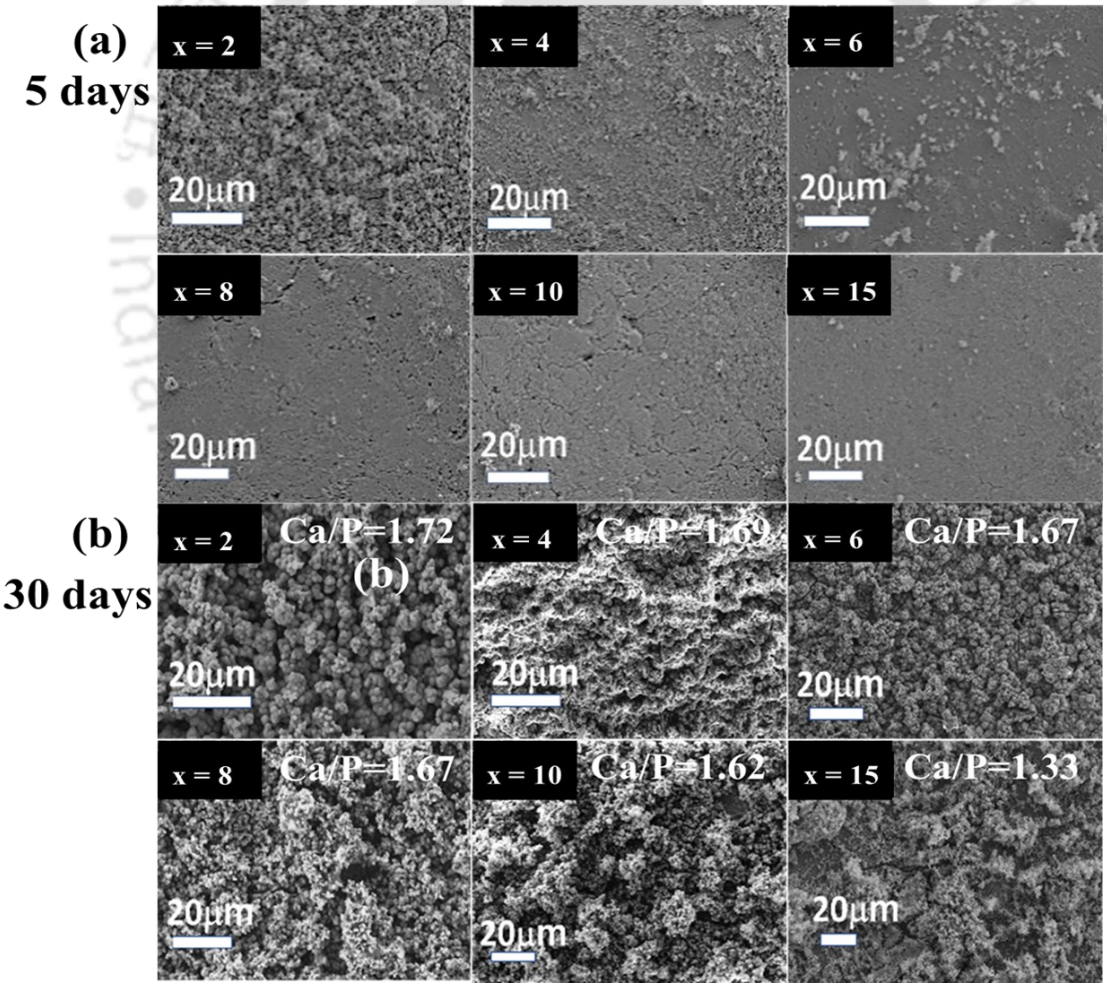

Figure 4.16: FESEM images of the surface of various MGC pellets after soaking in SBF for (a) 5 days, and (b) 30 days.

4.8.3. Osteoblast cell viability

The result of osteoblast (MG-63) cell viability tests is shown in Figure 4.17 (a) to (c). For the tested concentration range of 2 mg/ml to 0.25 mg/ml of 45S5 glass-ceramic without iron oxide, i.e., x = 0, the osteoblast cells showed excellent cytocompatibility and enhanced cell proliferation for 1 and 3 days of incubation as expected. After 1 day of incubation, MG-63 cells with x = 0 concentrations ranging from 2 mg/ml to 0.25 mg/ml exhibited viability ranging between ~91% and ~101%. After 3 days of incubation, the cell viability increased to ~92% to ~111% for the same concentration range of x = 0 sample.

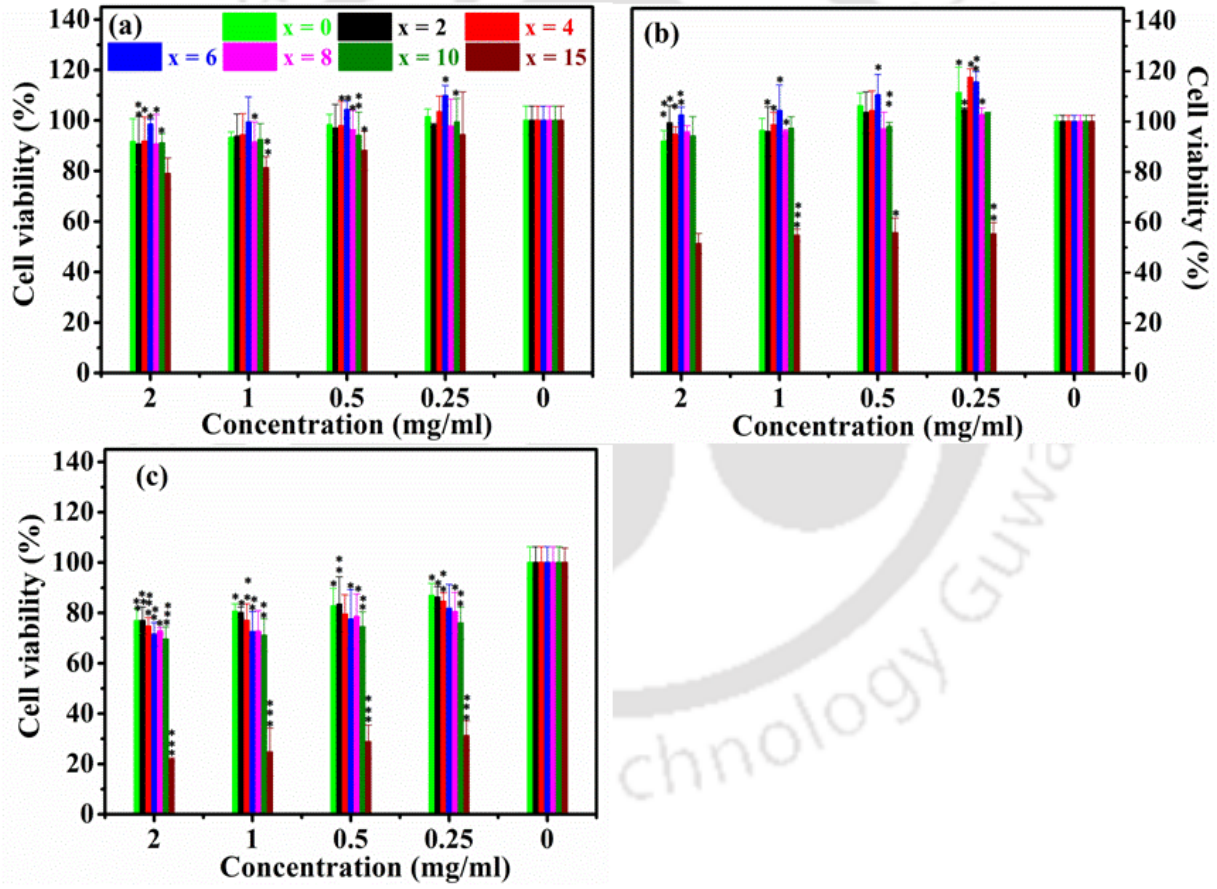

Figure 4.17: Viability of MG-63 cells incubated with MGC for (a) 1, (b) 3, and (c) 5 days. An asterisk indicates a significant difference in cell viability between different samples and control group (* $\rightarrow p < 0.05$, ** $\rightarrow p < 0.005$, *** $\rightarrow p < 0.001$, where p is the probability value or p-value).

The increment in cell viability can be attributed to the components of MGC such as Ca, P and Si which reportedly promote bone cells growth and proliferation [YADA2020]. Ca and P are key components of natural bone and Ca/P ratio of the MGC mimics the natural scaffold for osteoblast growth and proliferation. Ca supports the mineralization of extracellular matrix of bone and also increases the expression of growth factors such as IGF-I and IGF-II [MITR2018]. Si plays an essential role in cellular metabolic processes like bone tissue formation and calcification. Intake of Si also increases the bone mineral density and stimulates the collagen I formation [WANG2019, KIM02013]. These factors are responsible for the increased viability observed in case of MG-63 cells incubated with x = 0. Further, 5 days of incubation with x = 0 sample showed decreased viability of ~77% (2 mg/ml) to ~87% (0.25 mg/ml). This decrease in cell viability can be attributed to the reduction in bioavailability of x = 0 due to its biodegradation with time and over confluence of the culture plate well, leading to death of the osteoblast cells.

The multifunctional MGC incorporated with 2, 4, 6, 8, 10 and 15 wt.% iron oxide by replacing silicon oxide were also tested for their cytocompatibility and osteoblast cell growth for the same sample concentrations as done with x = 0. After 1 day of incubation, osteoblast cells showed none or slight increase in viability for the concentration range of 2 to 0.25 mg/ml of various MGC compositions. After incubation for 3 days, the cell viability of osteoblast was observed to significantly increase in the presence of these MGC samples. For the MGC with x = 2 with concentrations of 2 to 0.25 mg/ml, the cell viability increased from ~99% to ~105%. Similar increment in the cell viability was observed for the MGC with x = 4 and x = 6. However, the MGC with x = 8 and x = 10 exhibited a slight decrease in cell growth, ranging from ~94% to ~103%, across the tested concentrations (2 mg/ml to 0.25 mg/ml). In contrast, the MGC containing 15 wt.% iron oxide showed only ~55% cell viability indicating its toxic nature. The enhanced cell viability for MGC with 2 to 10 wt.% of iron oxide is attributed to the presence of Fe in the medium. Along with the desired magnetic behavior, Fe reportedly stimulates the growth

and proliferation of osteoblast cells and hence tends to increase the cell viability as observed in the MGC with iron oxide phases [FOPA2020].

Further, as discussed above, the incorporation of Fe results in proportionate decrease in Si, which lowers the collagen formation and thereby limits the cell proliferation rate. In the sample with x = 15, the reduced amount of Si may have resulted in the decreased bioavailability of MGC, thus leading to significant reduction in cell viability. After 5 days of incubation, the cell viability for all the samples, barring the one with x = 15, decreased up to ~70% for the highest concentration of 2 mg/ml of MGC. Such significant decrease in the cell number signifies extensive biodegradation of the MGC resulting in significant reduction in bioavailability of bioactive components like Ca, P and Si. Also, over confluence of culture wells might have affected the cell viability. In the case of the MGC with x = 15, the already low cell viability observed after 3 days of incubation period was further lowered to ~30%.

4.9. Summary

- Analysis of the XRD patterns of the sol-gel derived MGC nanopowders indicate the presence of three crystalline phases in all samples. The combeite phase diminishes, while the magnetic phases (hematite and magnetite) increase with higher levels of iron oxide substitution.
- The porous MGC samples exhibit an increase in surface area with the incorporation of iron oxide. The pore volume and pore size increase for the MGC containing up to 8 wt.% iron oxide and then decrease for the MGC with 10 wt.% iron oxide.
- Evolution of EPR parameters for the spectral line ($g \approx 2.0$) suggests a prevalence of super-exchange interaction over dipole-dipole interaction with increasing iron oxide content in the MGC nanopowders.

- Magnetization of the MGC displays an upward trend with an increase in iron oxide substitution. ZFC and FC curves show development of double exchange interaction at low temperatures in MGCs with higher iron oxide concentrations.
- Induction heating studies show that the MGC sample with 15 wt.% iron oxide has the highest *SAR* value and requires the least time (within 1280 s) to reach 42 °C from room temperature under the test conditions.
- Acellular bioactivity studies reveal a rapid degradation of the precipitated HAp surface layer due to a decrease in silanol groups with increased iron oxide substitution. Barring the MGC with x = 15, all other compositions are non-toxic to MG-63 osteoblast cells.
- The MGC sample with x = 10, exhibiting MG-63 cell viability of ~87% after 5 days of incubation, M_s of 0.82 emu/g, H_c of 149 Oe, *ILP* of 1.24 nHm^2kg^{-1}, emerges as a promising thermoseed for MH. Its higher *ILP* and bioactivity than the commercially available thermoseed fluid, FluidMag-CT, further supports its potential for use in.

Chapter 5

Magnetite nanoparticles substitution for SiO_2 in sol-gel 45S5 glass-ceramics

In chapter 4, it has been shown that the overall magnetic properties of 45S5 glass-ceramic increases with increase in iron oxide concentration. However, this also results in a reduction in the bioactivity of the ceramic. Moreover, 10 wt.% has been found to be the limiting concentration of iron oxide that can be incorporating in the 45S5 composition, without diminishing its bioactivity and turning it to be toxic to human cells. To achieve higher magnetic and bioactive properties suited for MH of bone cancer cells, it is essential to find an alternative magnetic oxide with these desired properties. In this context, MNP (Fe_3O_4 nanoparticles) are well-known for their exceptional biocompatibility and magnetic properties. SiO_2-coated Fe_3O_4 core-shell nanoparticles have also been investigated for biomedical applications [JIWE2001, ARCO2002, ARCO2003a, LI002006, HERN2006, BAIK2008, JIAN2011, VANE2011, HUI02011, DING2012, CHAR2015, GOH02015, CHAR2016, ANAN2016, ZELE2017, JI002018, NIKM2019, BIZA2020, YETI2020, YAZD2020, MADH2022]. There are also some studies on magnetite-based glass and glass-ceramics [ZHAN2022, ABE02010, BRET2005, LIU02012, HOU02021]. Surprisingly, there are no reports on MNP-substituted 45S5 glass-ceramic composition in the literature. However, there is one report by Rahman *et al.* [RAHM2020] on Fe_3O_4-SiO_2-CaO-Na_2O-P_2O_5 glass-ceramic, which has an overall composition different from that of45S5 composition. A systematic study of sol-gel derived 45S5 bioglass-ceramics synthesised by substituting MNP for SiO_2 is presented below.

5.1. Sample preparation

MNP were synthesized via the co-precipitation method as detailed in section 2.1 of this thesis. Subsequently, MNP-substituted glass-ceramics (MSGC) with compositions of (45-x)SiO_2-24.5CaO-24.5Na_2O-6P_2O_5-xFe_3O_4 (x = 5, 8, and 10 wt.%) were prepared using the sol-gel route. These were designated as S_{Fe5}, S_{Fe8}, and S_{Fe10}, corresponding ceramics with 5, 8, and 10 wt.% MNP, respectively. The aged gel was heated for 24 h at 100 °C to yield a dry gel nanopowder. The dried gel nanopowder was kept in an air oven for 3 days at 70 °C for thermal stabilization. As observed in section 3.2, heat treatment at 700 °C removed all traces of sodium nitrate phase in the ceramic and heat treatment above 450 °C induced conversion of magnetite to hematite of [SZOS2015, JAFA2015]. Therefore, a systematic heat treatment was conducted on S_{Fe5}, S_{Fe8}, and S_{Fe10}, samples at temperatures ranging from 450 °C to 700 °C for 1 h each.

5.2. Structural and magnetic properties of MNP

The XRD pattern of MNP recorded at room temperature is shown in Figure 5.01 (a). The most intense peak was found at $2\theta = 35.6°$, which corresponds to the reflection from the (311) plane of the magnetite spinal structure [sp. gp: Fd3m]. Other observed peaks at 2θ values of 30.1°, 43.1°, 53.4°, 57.2°, and 62.8° correspond to reflections from (220), (400), (422), (511), and (440) planes of magnetite, respectively. The average crystallite size (D_v) of magnetite was estimated to be 9 ± 1 nm using equation 2.03 and the peak width of the most prominent peak through profile analysis. The *M-H* loop for the MNP was recorded at room temperature, as illustrated in Figure 5.01 (b). M_s and H_c of the MNP are 64.33 emu/g and 11 Oe, respectively.

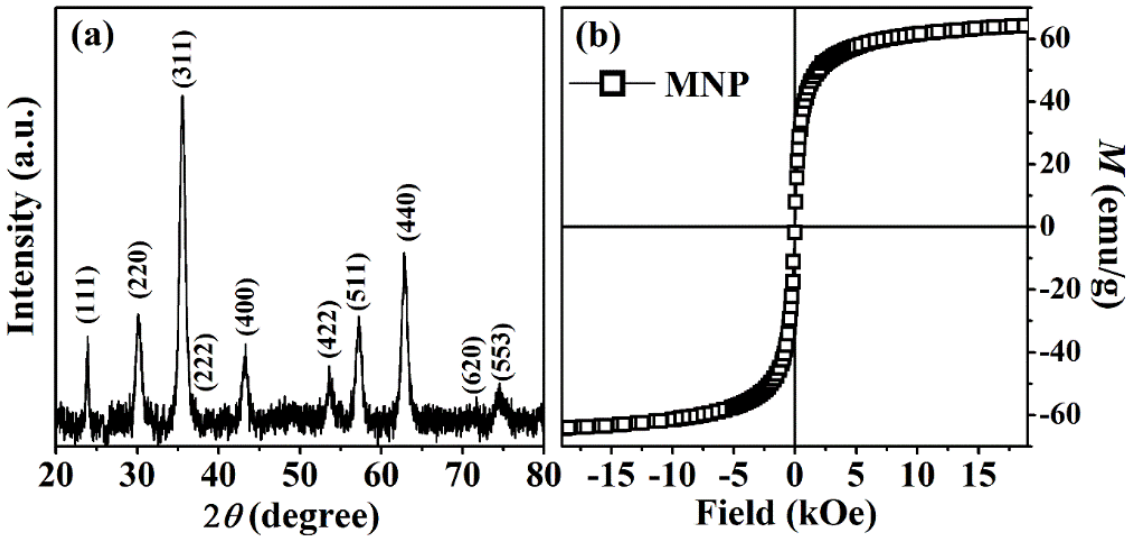

Figure 5.01: (a) XRD pattern, and (b) *M-H* loop of as-prepared MNP.

5.3. MNP-substituted glass-ceramics

5.3.1. Structural analysis

Figure 5.02 (a) presents the XRD patterns of as-prepared S_{Fe5}, S_{Fe8}, and S_{Fe10} MSGC nanopowders recorded at room temperature. The patterns indicate a significant presence of the sodium nitrate precursor phase ($NaNO_3$, ICDD-36-1474), suggesting that thermal stabilization at T_A = 70 °C is insufficient. Heat treatment up to T_A = 550 °C for 1 h did not induce any noticeable hematite phase in the MSGC nanopowders as seen from the XRD patterns in Figure 5.02 (b). However, sodium nitrate is still detectable in the XRD patterns along with combeite and magnetite, indicating incomplete reaction of the precursor. Only after heat treatment at 700 °C for 1 h, the sodium nitrate phase completely disappeared, leaving behind combeite ($Na_2Ca_2Si_3O_9$, PDF Card No.: 00-022-1455), magnetite (Fe_3O_4, PDF Card No.: -019-0629) and hematite (α-Fe_2O_3, PDF Card No.: -33-0664) phases as observed in Figure 5.02 (c). It is essential to point out here that the glass transition temperature range of the iron oxide-substituted bulk Hench glass is in the range of 500 to 650 °C [SHAN2016]. Hence, one can understand the inability to sustain the glassy phase after the above heat treatment and the emergence of glass-ceramics in the heat treated MSGC nanopowders. Table 5.01 lists the nominal composition and

the percentage of each crystalline phase in the MSGC nanopowders, as determined from the XRD data shown in Figure 5.02 (b and c). Table 5.01 also shows that the highly magnetic magnetite phase content is maximum in the MSGC nanopowders heat treated at 550 °C.

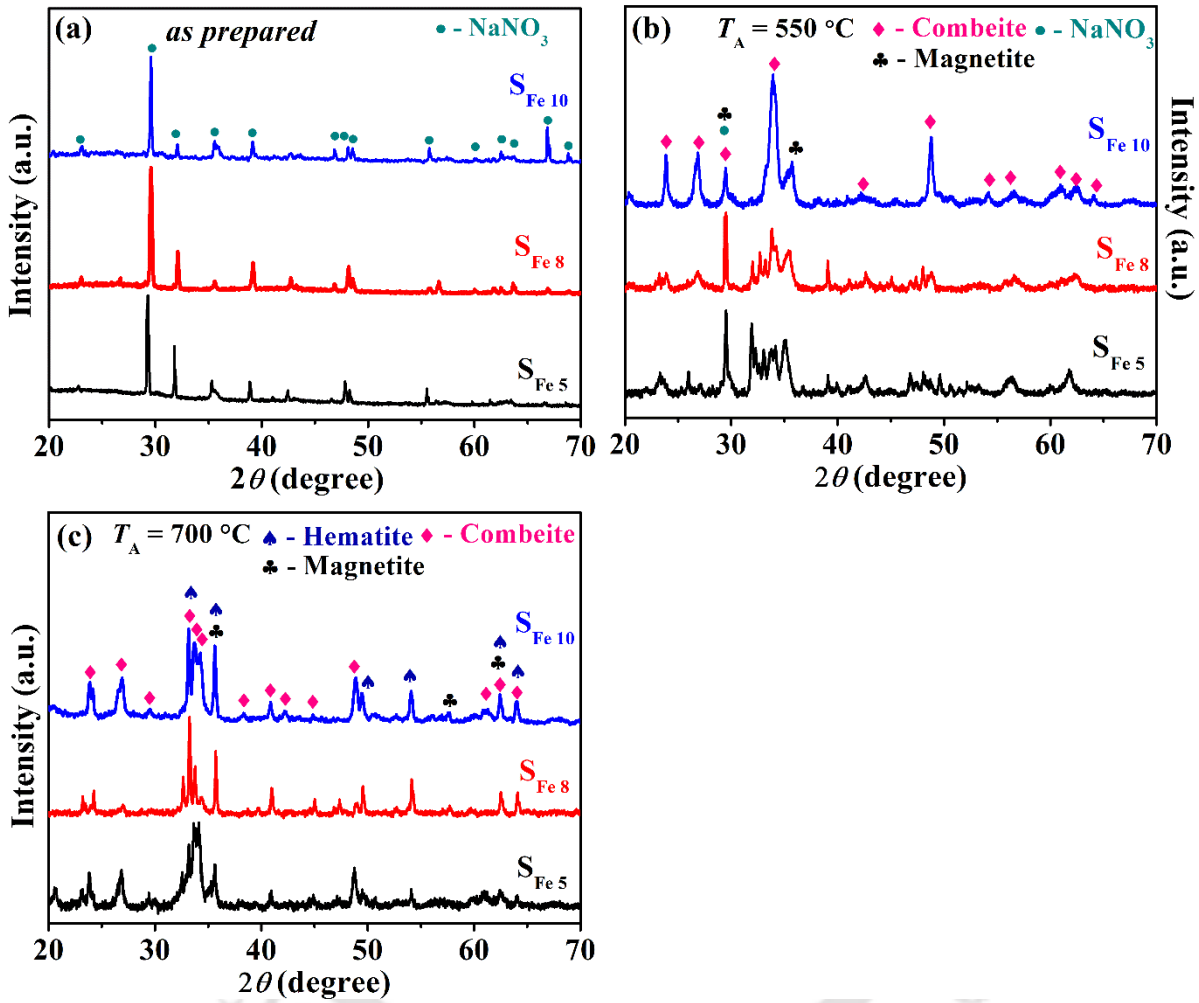

Figure 5.02: XRD patterns of (a) as prepared, and heat treated at (b) 550 °C, and (c) 700 °C MSGC with S_{Fe5}, S_{Fe8}, and S_{Fe10}.

Considering that no adverse effect has been reported on the bioactivity of the bioglass-ceramics containing sodium nitrate, the MSGC nanopowder S_{Fe5}, S_{Fe8}, and S_{Fe10} heat treated at 550 °C for 1 h appears to be the best candidates for MH application as they are expected have higher magnetic moment as well as better bioactivity as compared to the samples heated at higher temperatures on the basis of the relative percentages of the various crystalline phases present in

them. Hence, further studies would be limited to S_{Fe5}, S_{Fe8}, and S_{Fe10} nanopowders heat treated at 550 °C for 1 h.

Table 5.01: Nominal compositions and estimated crystalline phase percentages in various nanopowder samples after heat treatment at 550 °C and 700 °C. Symbol C, M, S, and H represent combeite, magnetite, sodium nitrate, and hematite phase, respectively.

Sample Code	**Nominal composition (wt.%)**					**Crystalline phase (%)**							
						T_A = 550 °C				**T_A = 700 °C**			
	SiO_2	CaO	Na_2O	P_2O_5	Fe_3O_4	C	M	S	H	C	M	S	H
S_{Fe5}	40	24.5	24.5	6.0	5.0	44	36	20	0	73	18	0	9
S_{Fe8}	37	24.5	24.5	6.0	8.0	42	40	18	0	68	21	0	11
S_{Fe10}	35	24.5	24.5	6.0	10.0	39	45	16	0	60	25	0	15

Figure 5.03 (a) depicts the FETEM image of near-spherical shaped S_{Fe8} MSGC nanopowder heat treated at 550 °C for 1 h. The particle size distribution of S_{Fe8} nanopowder is shown in Figure 5.03 (b) from which the average particle size was estimated to be 14 ± 1 nm with a full width at half maximum of 8 nm. The SAED pattern of the S_{Fe8} nanopowder reveals reflections originating from various crystallographic planes, including the (113), (006), and (217) planes of the combeite, the (104) plane of the sodium nitrate, as well as the (311), and (440) reflections from magnetite. Here, the reflection from magnetite's (311) plane overlaps with (105) reflection of combeite. HRTEM image and inverse fast Fourier transform (iFFT) of the HRTEM image reveal the lattice fringes corresponding (104) plane of sodium nitrate and (207) plane of combeite as displayed in Figure 5.03 (d).

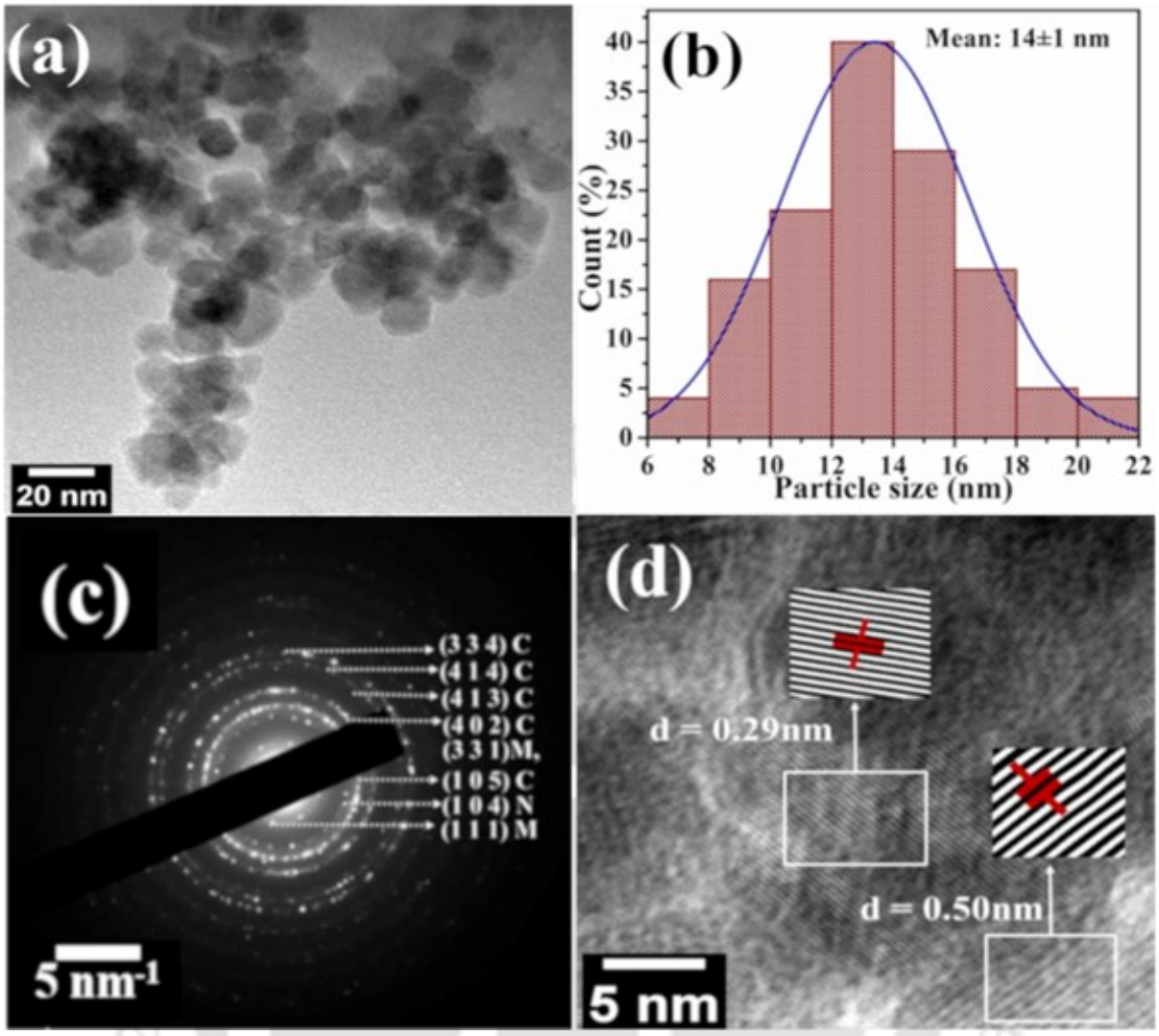

Figure 5.03: (a) FETEM image, (b) particle size distribution calculated from the TEM image, (c) SAED pattern, and (d) HRTEM image of S_{Fe8} MSGC nanopowder heat treated at 550 °C for 1 h. C, M, and N in (c) represent combeite, magnetite and sodium nitrate, respectively.

5.3.2. Morphology and compositional analysis

The particle size distribution and morphology of MNP, S_{Fe5}, S_{Fe8}, and S_{Fe10} MSGC nanopowders heat treated at 550 °C for 1 h were analysed using FESEM images, as shown in Figure 5.04. It was observed that all the tested MNP and MSGC nanopowders exhibited a morphology of agglomerated spherical particles. As the MNP content increased from 5 to 10 wt.%, both the surface area and magnetic moment increased, resulting in a higher degree of agglomeration. The

average particle sizes were estimated to be 12 ± 1 nm, 15 ± 1 nm, 18 ± 1 nm, and 43 ± 1 nm for the MNP, S_{Fe5}, S_{Fe8}, and S_{Fe10} MSGC nanopowder samples, respectively. The FETEM image (Figure 5.04 (b)) and FESEM image of S_{Fe8} MSGC nanopowders reveal particles with a spherical morphology and particle sizes of 18 ± 1 nm and 16 ± 1 nm, respectively, which are in good agreement considering the different sensitivity limits of the two techniques. The measured elemental compositions of each element in S_{Fe5}, S_{Fe8}, and S_{Fe10} MSGC nanopowders are tabulated in Table 5.02 against their nominal compositions. The observed compositions are slightly deviated from the nominal ones due the physically adsorbed oxygen. The presence of adsorbed oxygen leads to higher measured oxygen content, consequently reducing observed percentages of other elements compared to their nominal values.

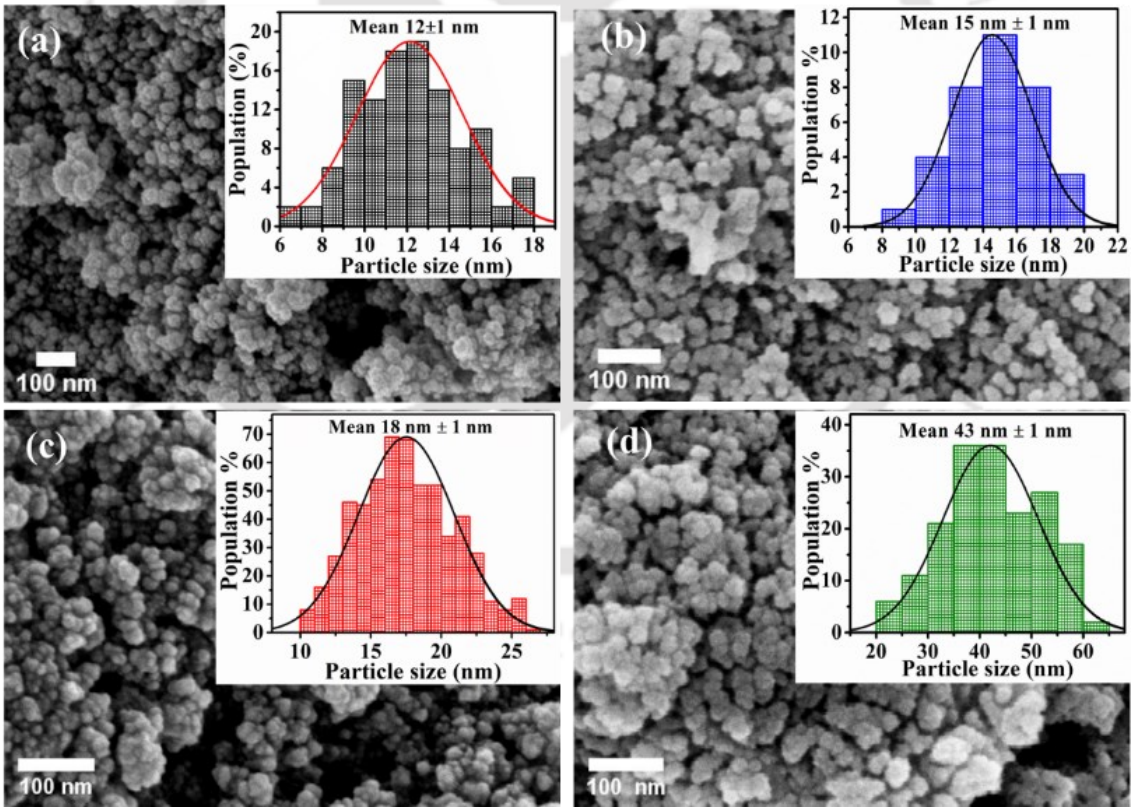

Figure 5.04: FESEM micrograph of (a) MNP, and (b) S_{Fe5}, (c) S_{Fe8}, and (d) S_{Fe10} MSGC nanopowders heated at 550 °C.

Table 5.02: Nominal and measured compositions of S_{Fe5}, S_{Fe8}, and S_{Fe10} MSGC nanopowder.

Sample code	Nominal Compositions (wt. %)						Measured Compositions (wt. %)					
	O	Si	Ca	Na	P	Fe	O	Si	Ca	Na	P	Fe
S_{Fe5}	39.3	15.3	13.4	15.4	5.1	11.5	41.1	13.8	14.4	14.1	4.7	10.4
S_{Fe8}	37.8	13.3	12.6	14.4	4.8	17.1	40.0	12.2	14.8	4.9	4.4	15.8
S_{Fe10}	36.7	10.3	12.0	13.8	4.6	22.6	39.2	10.0	14.5	4.7	4.3	21.4

5.3.3. Surface area analysis

The BJH isotherms and pore size distributions of the sol-gel-derived MSGC nanopowder samples are shown in Figure 5.05 (a and b). The hysteresis loops of S_{Fe5}, S_{Fe8}, and S_{Fe10} nanopowder samples heat treated at 550 °C showed H2-type isotherm, confirming the presence of an interconnected worm-like mesoporous structure in the MSGC nanopowders. The shape of isotherm does not significantly change when the concentration of MNP is increased from 5 to 10 wt.% in the nominal Hench composition. By using BET and BJH methods, the specific surface area, mean pore size and total pore volume were estimated and the same are listed in Table 5.03.

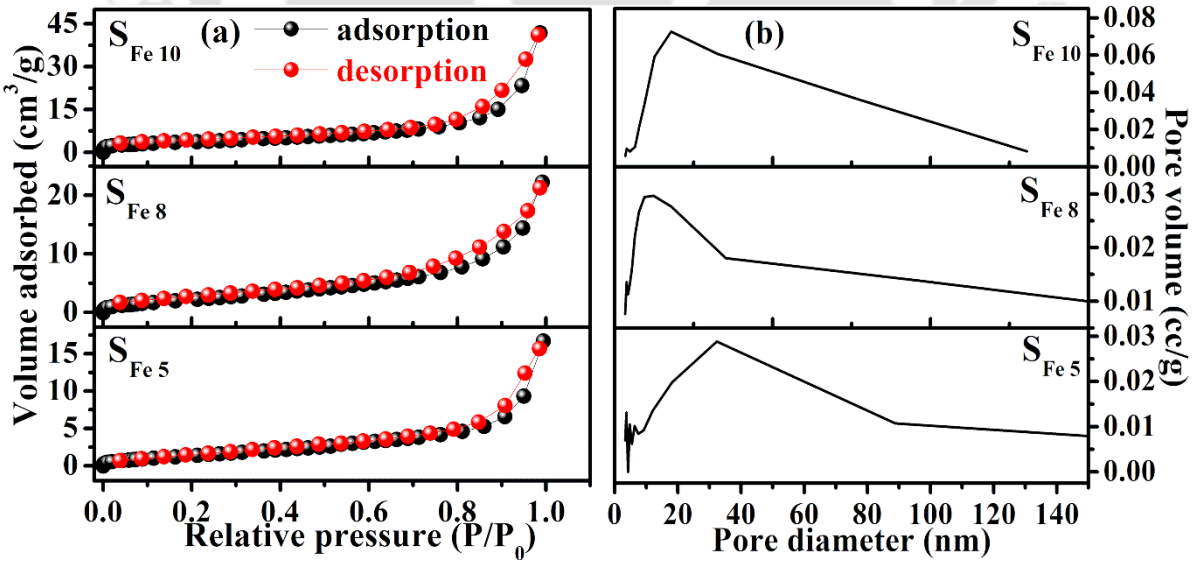

Figure 5.05: (a) N_2 adsorption-desorption isotherms, and (b) pore size distributions of S_{Fe5}, S_{Fe8}, and S_{Fe10} MSGC nanopowders.

It is evident from Table 5.03, that the textural parameters exhibit a composition dependence. The average pore size decreased from 16.9 nm to 14.9 nm, followed by an improvement to 19.2 nm, while the total pore volume increased from 0.025 cc/g to 0.065 cc/g when the concentration of MNP is increased from 5 to 10 wt.%. Additionally, the surface area of the MSGC nanopowder increased from 6.1 m^2/g to 13.5 m^2/g with the increase in MNP content from 5 to 10 wt.%. It can be seen that the addition of MNP to the MSGC resulted in an enhancement of their overall textural properties. Previous studies on sol-gel derived 45S5 glass and glass-ceramics have reported a maximum surface area of only 0.9 m^2/g [FAUR2015].

In the earlier chapter on iron oxide-substituted 45S5 glass-ceramics (MGC), it was pointed out that (i) an increase in iron oxide content led to an increase in surface area, (ii) the highest surface area obtained was 4.1 m^2/g for a 10 wt.% iron oxide content, and (iii) the overall textural properties deteriorated for glass-ceramics with iron oxide content higher than 10 wt.%. It may be noted that in the present work MNP were directly introduced during synthesis. On the other hand, in the earlier work, iron oxide was incorporated using the precursor $Fe(NO_3)_3.9H_2O$. It can be noticed that the specific area obtained in the present work is three time higher than that of iron oxide-substituted 45S5 MGC described in chapter 4. The high surface area to volume ratio of the MNP and their role as nucleation sites for pore formation during the drying process are possible reasons for the enhanced textural properties of the present MSGC nanopowders. It is evident from the experimental data that the surface area and the porosity of the sol-gel derived nanopowder increases with MNP content. It worthy to note that MSGC having higher surface area offers more sites for cells to adhere, leading to an increase in the interaction of the material with cells, which in turn increases the bioactivity required for bone regeneration. Therefore, the overall enhancement in the textural properties of mesoporous S_{Fe10} indicates its strong potential for biomedical applications.

Table 5.03: Textural properties of MSGC nanopowders processed at 550 °C.

Sample code	Surface area (m^2/g)	Pore size (nm)	Pore volume (cc/g)
S_{Fe5}	6.1	16.9	0.025
S_{Fe8}	9.2	14.9	0.034
S_{Fe10}	13.5	19.2	0.065

5.3.4. Surface Zeta potential and analysis of colloidal particles

ζ of aqueous suspensions of the MNP and MSGC nanopowders are displayed in Figure 5.06. ζ of the MSGC samples decreased in magnitude from -30.7 mV to -25.8 mV with an increase in MNP content from 5 wt.% to 10 wt.% in 45S5 composition. In contrast, bare MNP exhibited a ζ value of +24.8 mV. Based on the stability classification, ζ value of aqueous suspensions of MNP, S_{Fe5}, S_{Fe8} and S_{Fe10} lie within the range of stable suspensions. It can be noted that the aqueous suspension of MNP exhibits a positive ζ due to the multivalent positive Fe^{2+} and Fe^{3+} valence states, as well as the formation of hydroxyl groups. In contrast, the aqueous suspensions of MSGCs demonstrate a negative ζ attributed to the presence of oxygen and functional groups like SiO_2 and P_2O_5. These arguments are in line with the observations in earlier reports. Figure 5.06 indicates that ζ values show a systematic variation with the composition of the MSGC. As the MNP concentration was increased, ζ values decreased in magnitude which can be understood on the basis of the interaction of the magnetic particles dispersed in water. Structural studies discussed in section 5.3 have established that an increase in MNP concentration leads to a corresponding increase in the percentage of magnetic phases present in the MSGC nanopowder samples. As a result, the magnetization of the material also increases, which enhances the magnetic attraction between the particles. This in turn increases the aggregation and agglomeration of the particles. It is important to note that while magnetic interaction plays a significant role, it is not the only factor that influences the behavior of MSGC ceramic in the suspension. Other interactions between the ions, such as Van der Waals forces, hydrophilic and

hydrophobic interactions, *etc*., can also contribute towards the aggregation of particles in the suspension [OSS01983, LOPE1999, ZHAN2015]. Although all the MSGC colloids display a stable configuration, a closer observation of their properties indicates that S_{Fe10} may be more suitable for MH.

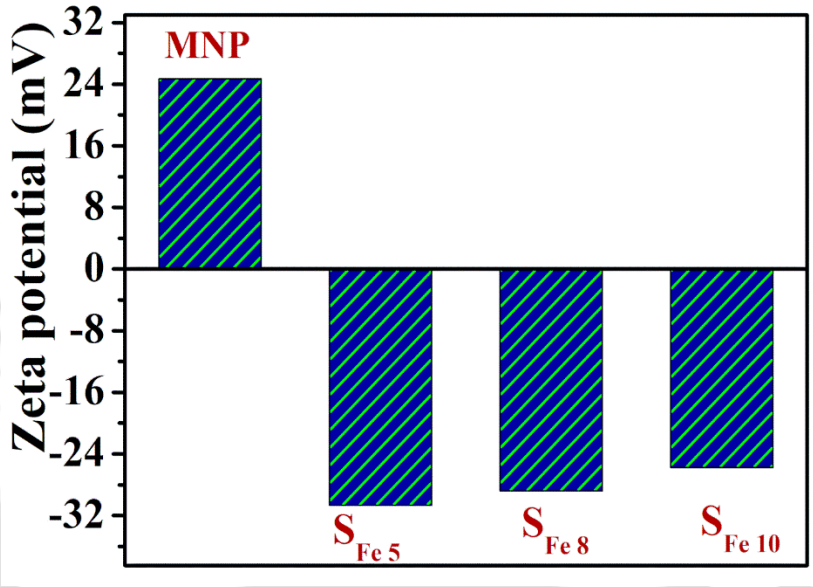

Figure 5.06: Zeta potential (ζ) of MNP, S_{Fe5}, S_{Fe8}, and S_{Fe10} recorded at room temperature.

The size distribution of colloidal particles in aqueous S_{Fe5}, S_{Fe8}, and S_{Fe10} samples was analysed using the DLS technique, and the results are presented in Figure 5.07. In the case of S_{Fe5} at a concentration of 1 mg/ml, the colloidal particle sizes ranged from 140 nm to 1220 nm, with an average value of ~870 nm. When the concentration was increased to 3 mg/ml, the colloidal particle distribution displayed a range from 240 nm to 2520 nm, with an average size of ~1585 nm. At a concentration of 5 mg/ml, the particle size distribution spanned from 282 nm to 4098 nm, with an average size of ~2780 nm. Similarly, in the case of S_{Fe8} at a concentration of 1 mg/ml, the colloidal particle sizes varied between 200 nm and 2100 nm with an average size of ~1280 nm. At higher concentrations of 3 mg/ml and 5 mg/ml, the particle sizes ranged from 204 nm to 2965 nm and 221 nm to 5220 nm with average sizes of ~1700 nm and ~2980 nm,

respectively. In the case of S_{Fe10} colloidal particles, the particle sizes varied from 160 nm to 2520 nm, 170 nm to 5666 nm, and 332 nm to 9210 nm at concentrations of 1 mg/ml, 3 mg/ml, and 5 mg/ml, respectively, with corresponding average sizes of ~1450 nm, ~3100 nm, and ~4240 nm, respectively. From these data, it is evident that the average size of the colloidal particles increased as the concentration was increased from 1 mg/ml to 5 mg/ml for each MSGC sample. This trend can be attributed to the increase in the magnetization as the magnetic content in the MSGC is increased.

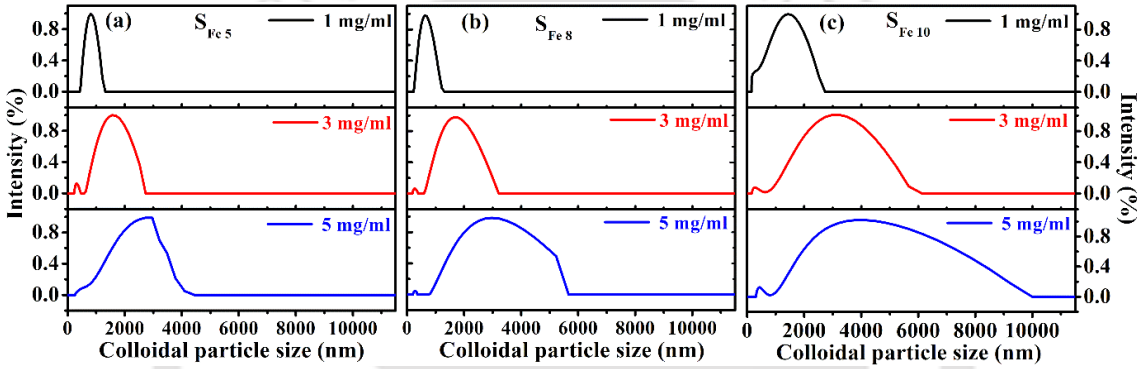

Figure 5.07: Colloidal particle size of (a) S_{Fe5}, (b) S_{Fe8}, and (c) S_{Fe10} MSGC in aqueous medium with different solute concentrations.

5.3.5. EPR studies

The EPR spectra of MSGC nanopowders depicted in Figure 5.08 (a) exhibit resonance absorptions cantered at $g \approx 2.1$, primarily attributed to the presence of Fe^{3+} ions. In chapter 4, two distinct spectral lines, $g \approx 2.0$ and $g \approx 4.3$, were found for lower x values (x = 2 and x = 4) in the compositions of $(45\text{-}x)SiO_2\text{-}24.5CaO\text{-}24.5Na_2O\text{-}6P_2O_5\text{-}xFe_2O_3$ ($2 \leq x \leq 15$). However, the $g \approx 4.3$ absorption is not present in the MNP-substituted 45S5 glass-ceramics. The absorption at $g \approx 2.1$ is indicative of Fe^{3+} ions grouped in clusters. Figure 5.08 (b) illustrates the variation in EPR parameters, ΔH and J of the $g \approx 2.1$ line as a function of MNP content (wt.%). Notably, the J value of the $g \approx 2.1$ spectral line increases while the ΔH decreases with increasing MNP content.

The increased intensity of the g ≈ 2.1 line with higher MNP content signifies the formation of iron clusters, which, in turn, enhances the super-exchange interactions between the iron ions. The variation of ΔH of the g ≈ 2.1 line indicates the presence of super-exchange interactions in MSGC with MNP (Fe_3O_4). The continuous increase in the total intensity of the g ≈ 2.1 line conveys that the number of spins increases with increment in MNP content in the MSGC samples. These findings highlight the possibility of tuning the magnetic interactions in MSGC by varying its MNP content.

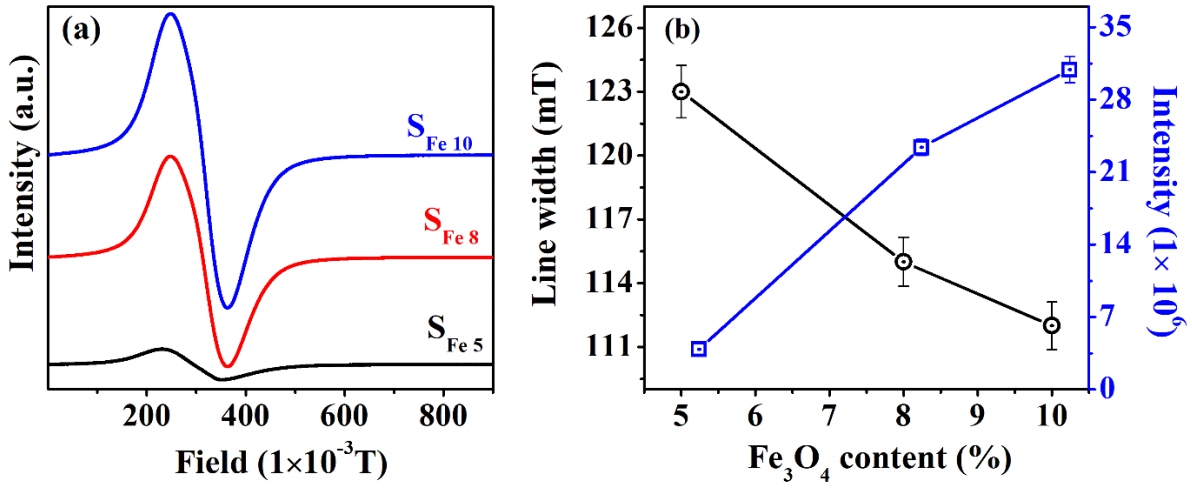

Figure 5.08: (a) Room temperature EPR spectra of all MSGC nanopowders. (b) Variations of linewidth (ΔH) and intensity (J) of g ≈ 2.1 line in S_{Fe5}, S_{Fe8}, and S_{Fe10} MSGC nanopowders.

5.3.6. Magnetic properties

Figure 5.09 (a) portrays the *M-H* loops of S_{Fe5}, S_{Fe8}, and S_{Fe10} nanopowder recorded in magnetic field range of ±20 kOe. Figure 5.09 (b) presents the minor *M-H* loops of S_{Fe5}, S_{Fe8}, and S_{Fe10} MSGC nanopowders recorded in clinically viable field range of ±500 Oe. Table 5.04 provides the magnetic parameters, including the M_s, H_c, M_r and hysteresis loop area of each MSGC nanopowder. Low values of H_c and M_r indicate the soft magnetic nature of all the MSGC nanopowder. As the MNP content is increased from 5 to 10 wt.% in the 45S5 composition, M_s

and M_r values show an increase from 3.67 emu/g to 14.01 emu/g and 0.17 emu/g to 0.25 emu/g, respectively. Conversely, H_c decreases with an increase in MNP concentration.

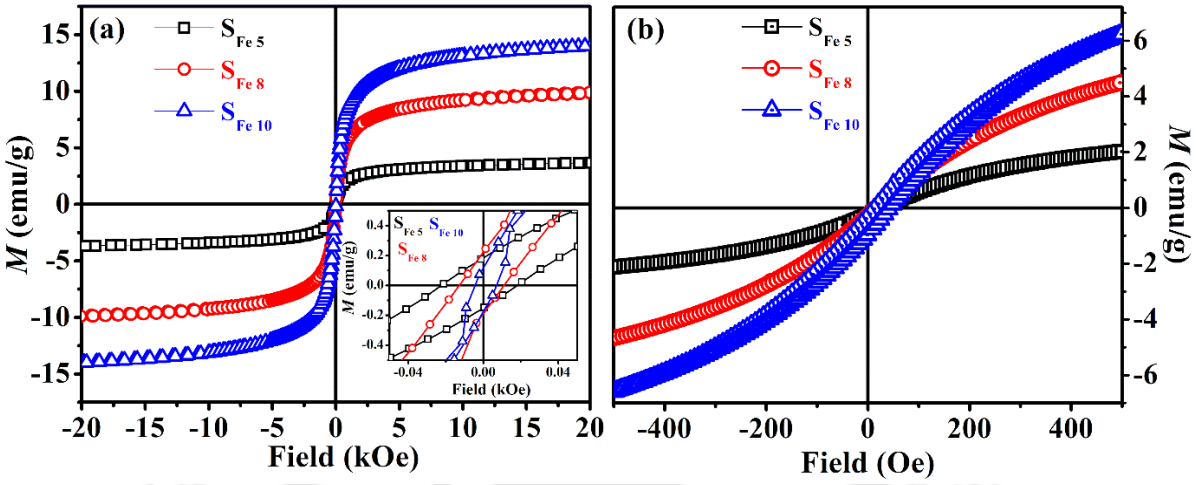

Figure 5.09: Room temperature *M-H* loops of heat treated S_{Fe5}, S_{Fe8}, and S_{Fe10} nanopowders recorded under (a) ±20 kOe, and (b) ±500 Oe field sweeps. Inset in (a) provides an enlarged view of data close to the origin.

Rahman *et al.* reported a sol-gel derived mesoporous magnetic glass-ceramic with a composition of $7Fe_3O_4$-$51SiO_2$-$18CaO$-$20Na_2O$-$4P_2O_5$ (mol%) containing Fe_3O_4 with average particle size of 50 ± 10 nm and M_s of ~13 emu/g [RAHA2020]. This composition is close to S_{Fe8} whose M_s is 9.88 emu/g. Both M_s values are comparable when one ignores the compositional variations between the two samples. The heat generated by the MSGC in an alternating magnetic field is directly related to the energy loss, which is defined by the hysteresis loop area. The magnetic properties of each MSGC presented in Table 5.04 suggest that samples with a high MNP content would be more appropriate for MH application. The minor *M-H* curves recorded at ±500 Oe exhibits a similar trend in M_s, H_c, M_r, and hysteresis loss when compared to the saturated *M-H* curves recorded at ±20 kOe.

Table 5.04: Magnetic parameters of MSGC nanopowders heat treated at 550 °C.

Magnetic and structural parameters	S_{Fe5}	S_{Fe8}	S_{Fe10}
Saturation magnetization, M_s (emu/g)	3.67	9.88	14.01
Coercive field, H_c (Oe)	20	12	9
Remnant magnetization, M_r (emu/g)	0.17	0.21	0.23
Average crystallite size of magnetite phase	12	15	18
Hysteresis loop area at ±20 kOe (erg/g)	260	700	996
Hysteresis loop area at ±500 Oe (erg/g)	8	22	35

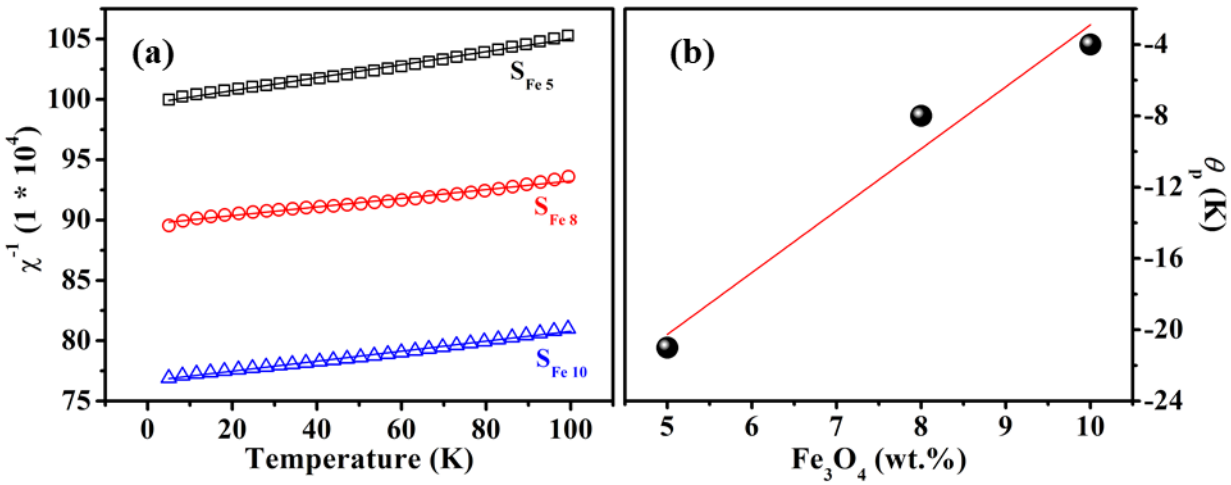

Figure 5.10: (a) Temperature dependent inverse reciprocal magnetic susceptibility, and (b) composition dependent paramagnetic Curie temperature (θ_p) of S_{Fe5}, S_{Fe8}, and S_{Fe10} nanopowders.

Figure 5.10 (a and b) display the inverse susceptibility versus temperature and paramagnetic Curie temperature (θ_p) versus MNP content curves of S_{Fe5}, S_{Fe8}, and S_{Fe10} MSGC nanopowder samples. Magnitude of θ_p decreases with MNP content in these MSGC. C_M was used to estimate effective magnetic moment as explained the chapter 2 (section 2.2.6). C_M increased and effective magnetic moment decreased with an increase in MNP content in MSGC. Table 5.05 lists the C_M and weight fraction of Fe^{2+} and Fe^{3+} ions in the MSGC samples. It can be observed from Table 5.05 that Fe ions exist in both $Fe^{2+}$and Fe^{3+} valence states in all MSGC

compositions. x_2 (weight fraction of Fe^{2+}) increases with MNP content, while x_1 (weight fraction of Fe^{3+}) decreases. The ratio of x_1 to total ions x shows the relative dominance of Fe^{3+} ion and a proportional reduction in Fe^{2+} ions in the MSGC nanopowders as a function of MNP content. This trend can be explained in terms of Fe^{2+}-Fe^{2+}, Fe^{2+}-Fe^{3+} and Fe^{3+}-Fe^{3+} exchange pairs in MSGC nanopowders.

Table 5.05: Experimental value of μ_{exp}, Molar Curie constant (C_M), weight fraction of iron ions in S_{Fe5}, S_{Fe8}, and S_{Fe10} MSGC nanopowder.

x (wt.%)	C_M (emuKOe^{-1})	μ_{exp} (μ_B)	x_1 (wt.% $Fe_2^{3+}O_3$)	x_2 (wt.% $Fe_2^{2+}O_3$)	$x1/(x_1 + x_2)$
S_{Fe5} (x = 5)	0.3810±0.0001	5.51±0.01	3.95±0.01	1.05±0.01	0.79
S_{Fe8} (x = 8)	0.5578±0.0001	5.27±0.01	6.69±0.01	1.31±0.01	0.84
S_{Fe10} (x = 10)	0.6489±0.0001	5.1±0.01	8.60±0.01	1.40±0.01	0.86

Just as done in the case of iron oxide-substituted 45S5 glass-ceramic, temperature dependent magnetization measurements at low temperatures were also performed on MSGC samples. The results, depicted in Figure 5.11 (a-c), present the ZFC and FC curves for S_{Fe5}, S_{Fe8}, and S_{Fe10} MSGC nanopowders in the temperature range of 5 K to 305 K. It can be observed that the ZFC and FC curves of all samples mimic the behavior of ferromagnet-like nanoparticles exhibiting superparamagnetism. Notably, the well-separated ZFC and FC curves display two features: T_B and T_{BF}, as explained in chapter 2. T_B increases from ~70 K to ~120 K as the MNP content increases from 5 to 10 wt.% in the MSGC. T_{BF} also shows an increase with MNP content [T_{BF} ~ 117 K for MSGC with 5 wt.% MNP, T_{BF} ~ 170 K for MSGC with 10 wt.% MNP, and T_{BF} ~ 270 K for MSGC with 10 wt.% MNP]. This increase in T_B and T_{BF} can be attributed to the rise

in D_V of magnetite phase (*c.f.*, Table 5.04), and the broadening of the particle size distribution with higher MNP content, as observed in section 5.3.2.

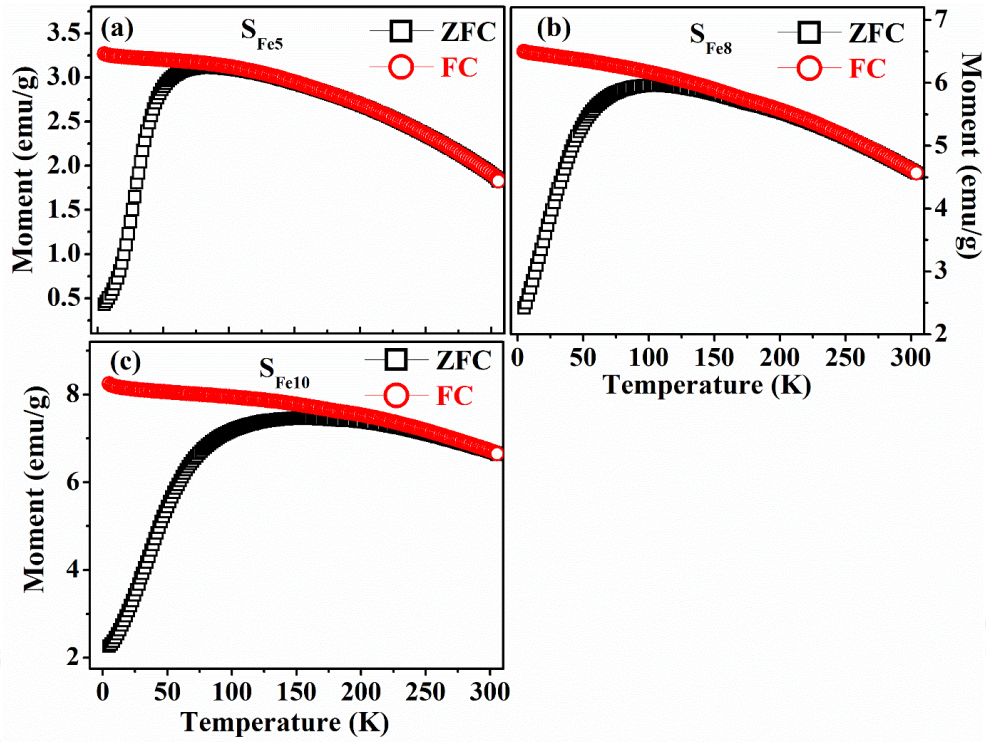

Figure 5.11: *M-T* curves of (a) S_{Fe5}, (b) S_{Fe8}, and (c) S_{Fe10} MSGC recorded under ZFC and FC modes.

5.3.7. Evaluation of induction heating capacity

Figure 5.12 illustrate the time-dependent temperature rise and the corresponding near infra-red camera images for five different concentrations of aqueous S_{Fe5}, S_{Fe8}, and S_{Fe10} MSGC fluids. When an alternating magnetic field was applied to S_{Fe5} magnetic fluid, the temperature of the fluid increased from ~33 °C to only ~42 °C for concentrations ranging from 1 - 9 mg/ml within 600 s of exposure time. Thus, the required temperature of 43 °C could not be attained with the highest concentration of S_{Fe5} sample even after 600 s of exposure to the field. In the case of S_{Fe8} and S_{Fe10} magnetic fluids, temperature increase from ~33 °C to ~45 °C and ~51 °C, respectively, could be achieved within 600 s for concentrations ranging from 1- 9 mg/ml. In fact, S_{Fe8} achieved

this temperature in 590 s with a concentration of 7 mg/ml and in 400 s with a concentration of 9 mg/ml. Interestingly, S_{Fe10} achieved the same feat within 600 s for a concentration of 3 mg/ml and within 200 s for a concentration of 9 mg/ml. In the case of the S_{Fe5}, S_{Fe8}, and S_{Fe10} nanopowder samples, the average dry particle sizes shown in Figure 5.04 fall within the range in which Néel and Brownian relaxation mechanisms are dominant. The colloidal particle size distribution of S_{Fe5}, S_{Fe8}, and S_{Fe10} at three different concentrations (1 mg/ml, 3 mg/ml, and 5 mg/ml) shown in Figure 5.07 would ultimately determine the dominant heat loss mechanism in this study. Considering the fact that the minimum colloidal particle size observed is well above 100 nm, the major contributor to the induction heating should be hysteresis loss.

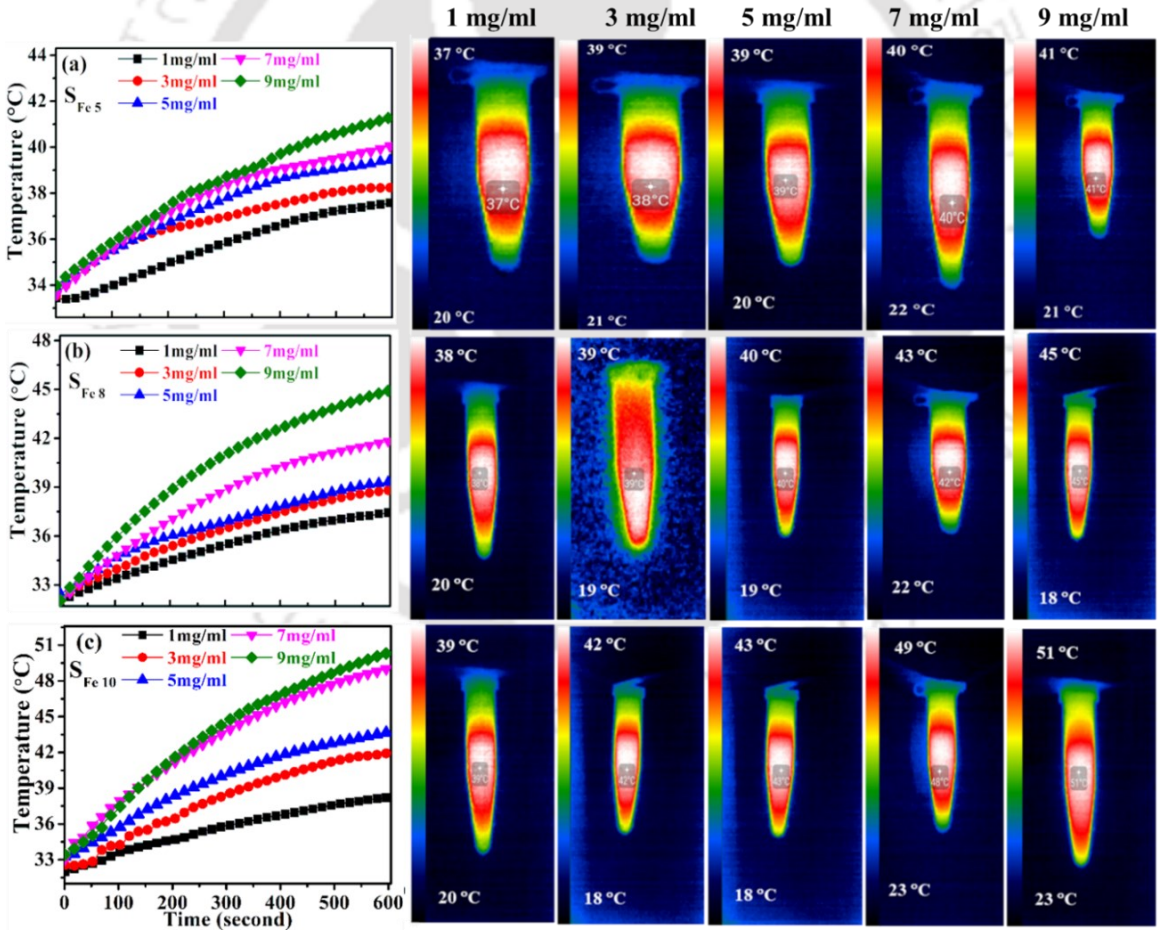

Figure 5.12: Induction heating curves and thermal images of aqueous colloids containing (a) S_{Fe5}, (b) S_{Fe8}, and (c) S_{Fe10} MSGC nanopowders of different concentrations.

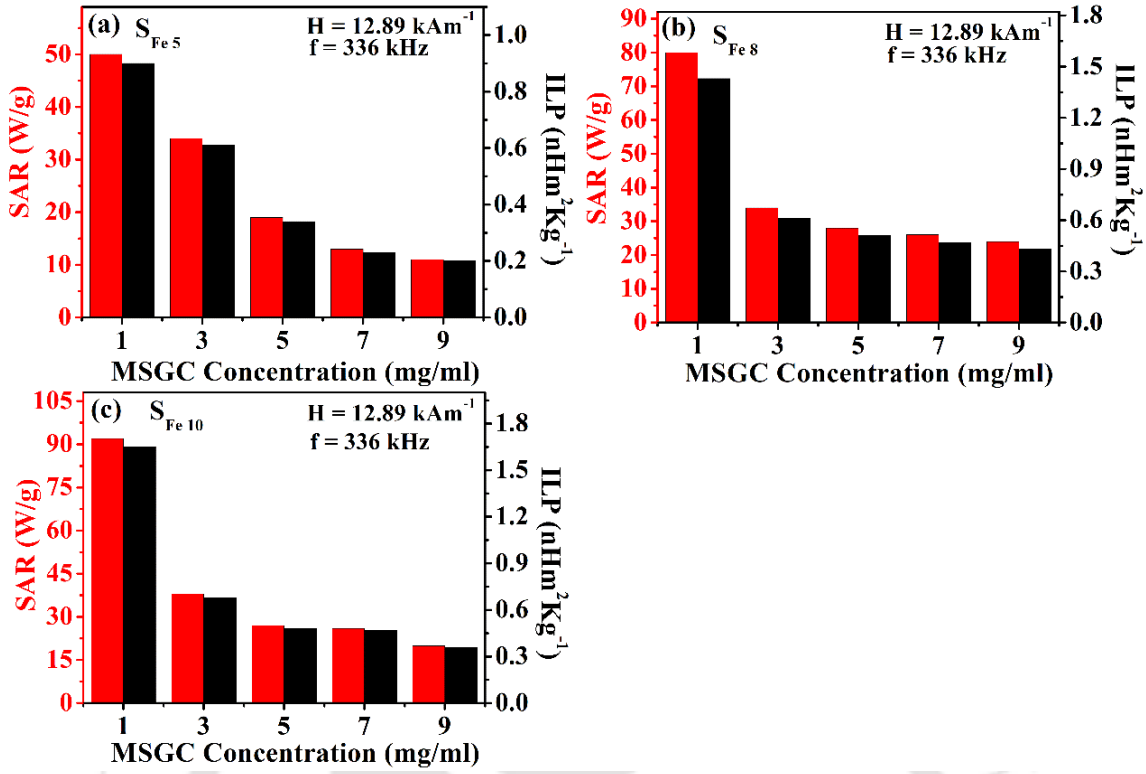

Figure 5.13: Calculated *SAR* and *ILP* values using BLM for aqueous fluids of (a) S_{Fe5}, (b) S_{Fe8}, and (c) S_{Fe10} with five different concentrations.

Furthermore, as the concentration is increased from 1 mg/ml to 5 mg/ml, more aggregation of particles occurs, leading to an increase in the average particle size. *SAR* and *ILP* values for aqueous fluids of S_{Fe5}, S_{Fe8}, and S_{Fe10} MSGCs were calculated using the BLM method, as illustrated in Figure 5.13. The data indicate a strong dependence of *SAR* values on the MSGC concentration in the magnetic suspension of all the samples. It can be seen that the magnetic fluid with the lowest MSGC content shows the highest *SAR* value in accordance with equation 2.20. This can be explained in terms of the change in the dipolar interaction between the particles in the fluid with concentration. As the MNP concentration increases, the separation between particles decreases, leading to a reduction in heat loss and improper heat exchange. *ILP* values (calculated using BLM) of aqueous fluids of S_{Fe5}, S_{Fe8} and S_{Fe10} with a concentration of 1mg/ml are 0.8 nHm^2kg^{-1}, 1.43 $nHm^2\ kg^{-1}$, and 1.82 nHm^2kg^{-1}, respectively. The *ILP* value of S_{Fe5} is slightly lower, while those of S_{Fe8} and S_{Fe10} are higher than the *ILP* value of 1.0 nHm^2kg^{-1} of the

commercially available magnetic fluid, FluidMag-CT. The heating capacity of the magnetic fluid increased appreciably when the MNP content was increased from 5 to 10 wt.%. Based on the results obtained, it can be observed that all the samples have potential for controlled heating of tumors. However, among the three samples tested, S_{Fe10} appears to be the most effective, since it achieved the highest temperature of 51 °C from 33 °C with a concentration of 9 mg/ml under the present test conditions.

5.3.8. *In vitro* bioactivity assessment

5.3.8.1. Ion exchange

The pH values were recorded periodically upon immersion of the MSGC pellets individually in SBF as shown in Figure 5.14. The ion-exchange mechanism causes the pH values of SBF to rise quickly during the first 3 days of immersion of the MSGC pellet in SBF, as seen in the inset of Figure 5.14. Subsequently, pH slowly stabilizes as the released ions reach saturation.

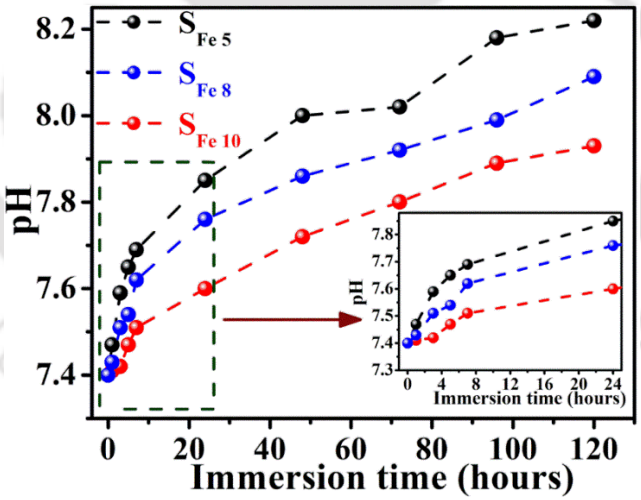

Figure 5.14: Change in pH of SBF upon immersion of the MSGC pellets.

After 7 days of soaking, the pH of the SBF increased from 7.40 to 8.25, 8.20, and 7.88 for the S_{Fe5}, S_{Fe8}, and S_{Fe10} MSGC, respectively. An increase in pH of the MSGC-immersed SBF demonstrates that all the MSGC samples are bioactive. A comparison of the pH curves of SBF

treated MSGC indicates a decrease in the saturation value of pH from 8.25 to 7.88 with increasing MNP content. This behavior is clearly related to the MNP content and immersion time on the release of Na, Ca, Fe, and P ions from the MSGC. As previously mentioned in chapter 4, the pH of the SBF solution is influenced by release of ions from the sample surface. Osteoblast cell proliferation tests discussed in section 5.3.8.3 will further confirm the bioactive nature of the MSGC samples.

5.3.8.2. Surface apatite layer formation

Figure 5.15 (a-c) show the GI-XRD patterns recorded from the surface of the MSGC pellets after 0, 1, 3, 5, and 7 days of immersion in SBF, respectively. The XRD pattern labeled as 0 d corresponds to that of the MSGC pellet prior to immersion in SBF, exhibiting the crystalline nature of the samples with reflections from combeite, sodium nitrate, and magnetite phases as discussed earlier in the structural analysis section 5.3.1.

Upon immersion in SBF, a new crystalline phase emerges in the XRD pattern, characterized by two distinct peaks at 2θ values of ~26° and ~32°. This indicates the formation of a crystalline HAp layer on the MSGC surface, as described in section 2.2.10.1 of chapter 1. The formation of the bone mineral phase HAp on the sample surface has already been explained through the ion exchange mechanism upon immersion in SBF (*c.f.* 2.2.10.2). Intensities of the newly developed crystalline (HAp) phase reflections increase with immersion time, as shown in Figure 5.15 (a-c). Both the formation of HAp layer and the increase in pH indicate the bioactive nature of all the MSGC samples.

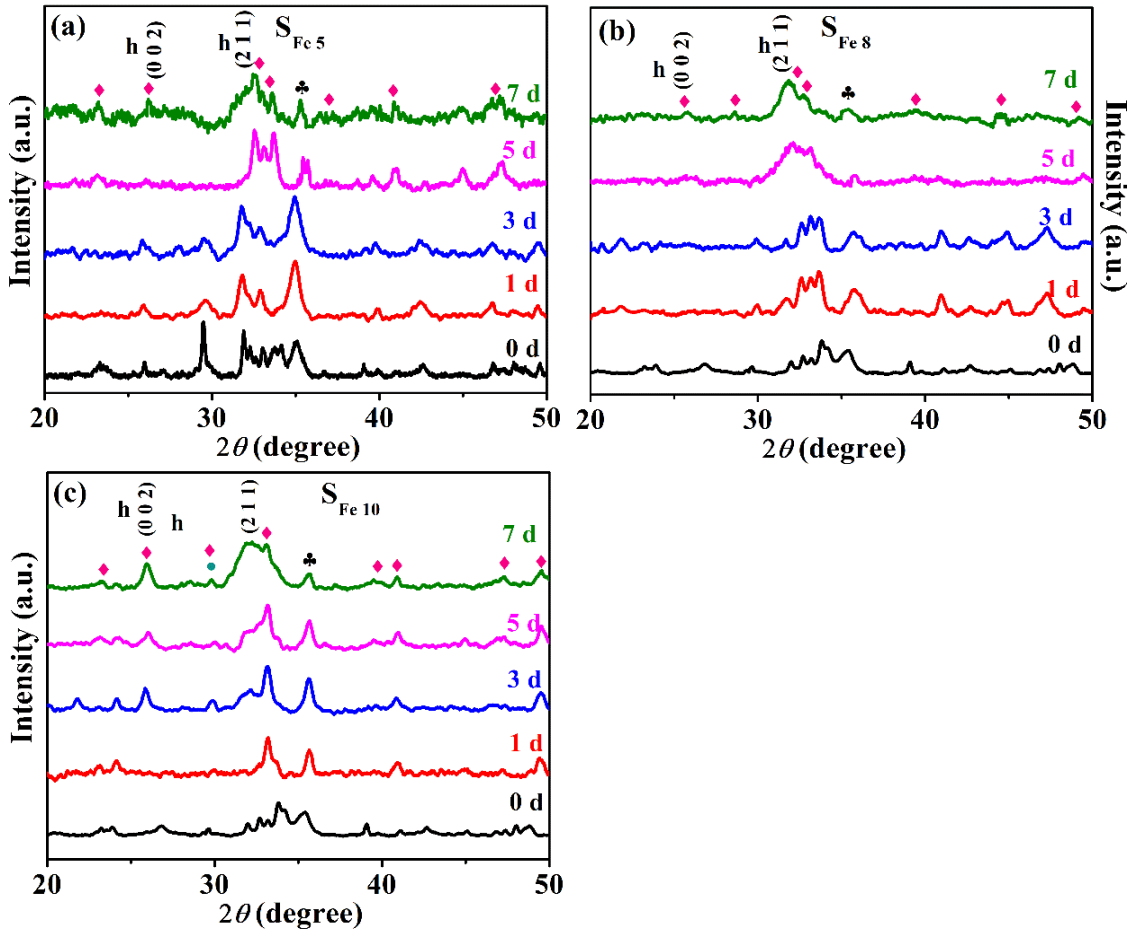

Figure 5.15: GI-XRD patterns of (a)S_{Fe5}, (b) S_{Fe8}, and (c) S_{Fe10} pellets immersed in SBF for different days. Symbols h, ♣, and ♦ represent HAp, magnetite, and combeite phases.

As mentioned in the previous section, increasing the MNP concentration from 5 to 10 wt.% leads to a decrease in the number of silanol groups (Si-OH), which affects the dissolution process. Consequently, the coverage or the extent of the newly formed HAp surface layer slightly decreases with an increase in MNP concentration. Consequently, the HAp layer thickness and coverage over S_{Fe5}, S_{Fe8}, and S_{Fe10} are relatively low, thereby exposing the underlying glass-ceramic peaks in the GI-XRD patterns even after 7 days of immersion. It can be observed that the growth of the HAp layer tends to increase with prolonged immersion time for each MSGC, which is a positive feature for long term implantation.

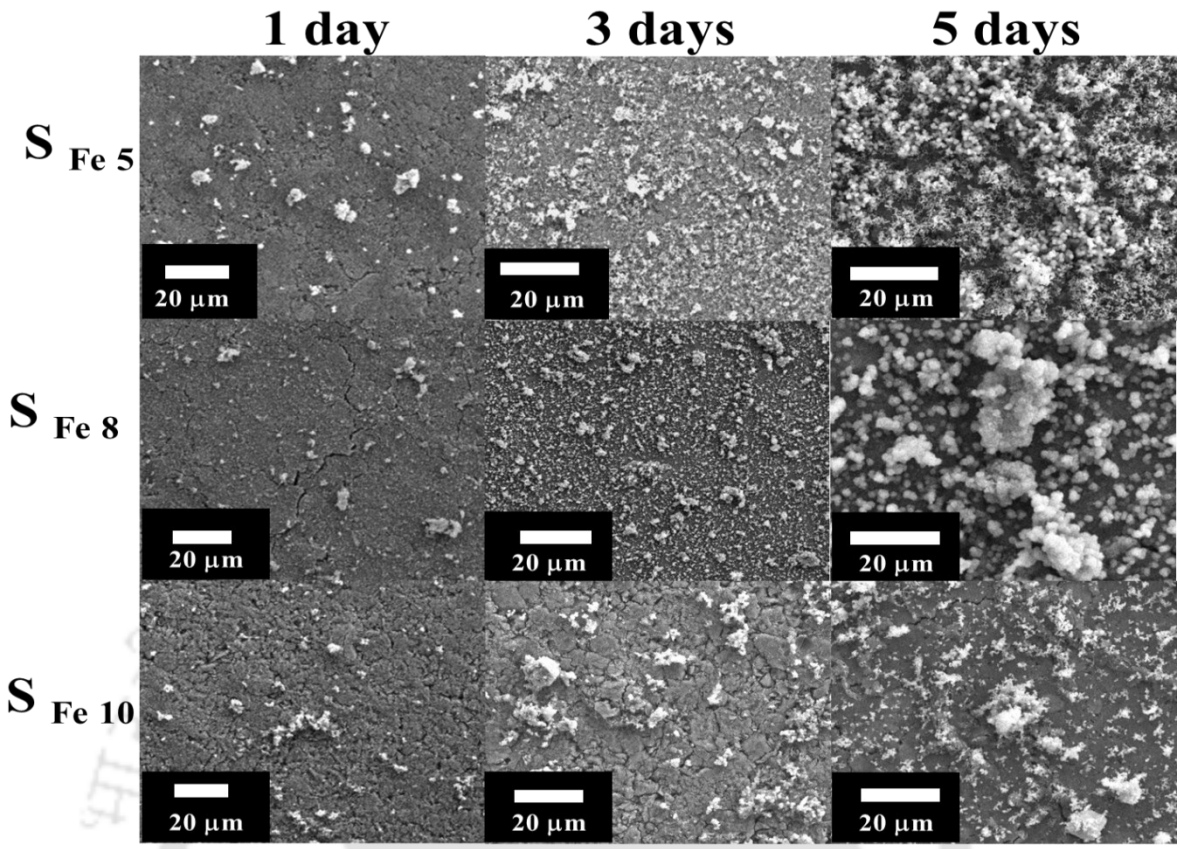

Figure 5.16: FESEM images of MSGCsurfaces after immersion in SBF for 1, 3, and 5 days.

Figure 5.16 displays FESEM images illustrating the surface of the MSGC after being immersed in for 1, 3, and 5 days. These images provide visual evidence of the growth of a surface layer. The presence of a grainy white layer indicates the formation of HAp layer on the surface of MSGC pellets during immersion. After a soaking period of 5 days, a high density of spherical HAp grains can be observed on the surfaces of all three MSGC samples. As the immersion time extends from 1 to 5 days, the growth of the HAp layer becomes more extensive. To confirm the surface mineralization, EDS analysis was conducted, revealing the Ca/P ratios of all samples after 5 days of soaking. The Ca/P ratios of S_{Fe5}, S_{Fe8}, and S_{Fe10} are close to the reported value of 1.67 for bulk Hench composition [SHAN2016].

5.3.8.3. Osteoblast cell viability

MNP have gained approval for clinical trials due to their potential capabilities in drug delivery and MH [WLOD2022, FULD2010]. The effect of incorporation of MNP in MSGC samples were evaluated through cell proliferation studies on the human osteoblast cell line, MG-63, as shown in Figure 5.17. Figure 5.17 (a) depicts the effects of the concentrations of S_{Fe5} MSGC on the viability of MG-63 osteoblast cells during an incubation period of up to 5 days. The cell viability exhibited an increasing trend with a decrease in MSGC concentration. The highest tested concentration of 2 mg/ml resulted in ~89% cell viability, while the lowest tested concentration, of 0.25 mg/ml yielded ~97% cell viability after 1 day of incubation. A similar pattern of increment in cell viability was observed during the incubation periods of 3 and 5 days. The maximum cell viability of ~109% was recorded for the 0.25 mg/ml concentration of S_{Fe5} during 5 days of incubation. The decrease in cell viability at higher concentrations can be attributed to reduced aggregation and acclimatization effect of cells at lower concentrations. The variation in cell viability with increasing Fe_3O_4 content in samples S_{Fe5}, S_{Fe8}, and S_{Fe10} at a concentration of 0.25 mg/ml is shown in Figure 5.17 (b). The percentage of viable cells increased as the MNP content was increased from 5 to 10 wt.%. Cell viability improved from ~97% (S_{Fe5} MSGC) to ~105% (S_{Fe10} MSGC) with an increase in Fe_3O_4content from 5 wt.% to 10 wt.% after 1 day of incubation. Similarly, cell viability improvement was observed for 3 days and 5 days of incubation, with a maximum of ~113% at 10 wt. % of Fe_3O_4. The observed rise in cell viability indicates the stimulation of osteoblast proliferation by the Fe_3O_4 present in the sample. Additionally, in Figure 5.17 (c), the viability of osteoblast cells after 1, 3, and 5 days of incubation is presented for samples S_{Fe5}, S_{Fe8}, and S_{Fe10} at concentrations of 0.25 mg/ml. As discussed previously, all the samples showed increasing cell viability with decreasing concentration. S_{Fe5}, S_{Fe8}, and S_{Fe10} exhibited cell viability of ~89%, ~93%, and ~92% for the maximum tested concentration of 2 mg/ml. In comparison, the cell viability was observed to

increase to ~97%, ~105%, and ~105%, respectively, for 0.25 mg/ml concentration of these samples.

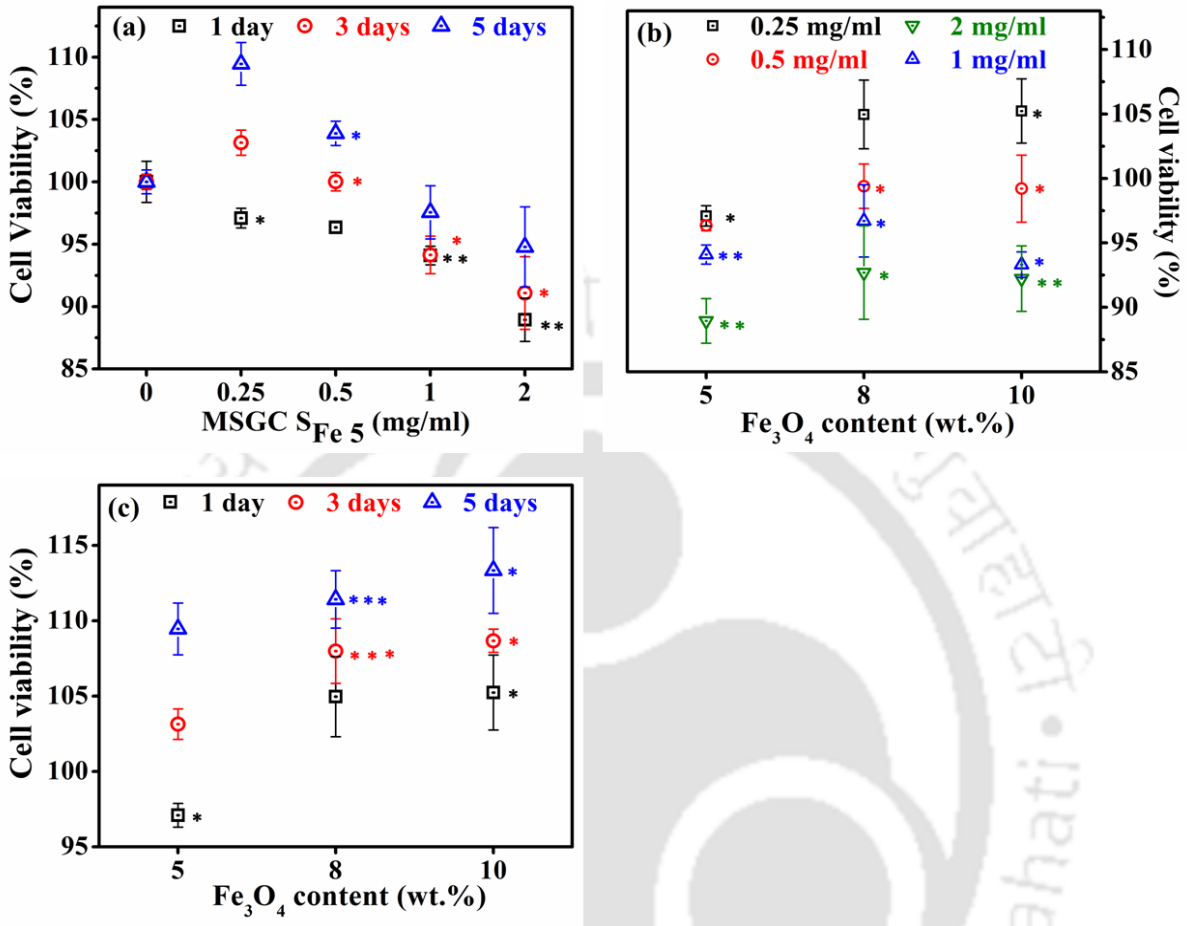

Figure 5.17: Cell viability studies performed on MG-63 cells to evaluate the effect on (a) various concentrations of S_{Fe5} during 5 days of incubation, (b) different MSGC samples with different concentrations after 1 day of incubation, and (c) different MSGC samples with same concentration (0.25 mg/ml) after 1, 3 and 5 days of incubation. An asterisk indicates a significant difference in cell viability between different samples and control group (* $\rightarrow p < 0.05$, ** $\rightarrow p < 0.005$, *** $\rightarrow p < 0.001$, where p is the probability value or p-value).

The roles of Si and Ca ions in this process are discussed in detail in section 4.7.3. Fe ions from the MNP reportedly stimulate the growth of the osteoblast cells, which explains the increase in the number of viable cells with increase in MNP content [FOPA2020, PANS2012, ULLA2020]. Cell viability remained above the acceptable threshold, even at the maximum

concentration of 2 mg/ml for all three MSGC. This confirms the suitability of all these samples for biological applications [FULD2010].

5.4. Summary

- Controlled heat treatment of MSGC nanopowders at 550 °C for 1 h yields the best combination of combeite, magnetite, and sodium nitrate phases.
- MNP-substituted 45S5 nanopowders demonstrate superior magnetic properties compared to iron oxide-substituted 45S5 nanopowders presented in chapter 4. Moreover, the heating capacity of the magnetic fluids containing MSGC nanopowders increased with the MNP content.
- MSGC nanopowders are non-toxic to MG-63 osteoblast cells and meet the threshold viability percentage at both low and high concentrations of S_{Fe5}, S_{Fe8}, and S_{Fe10}, making them suitable for bone regeneration applications.
- Among the tested MSGC, S_{Fe10} exhibited M_s of 14.01 emu/g, H_c of 9 Oe, and *ILP* of 1.82 nHm^2kg^{-1}, making it a promising candidate for use as thermoseed in MH treatment of cancer. These parameters are far superior to the commercially available thermoseed fluid, FluidMag-CT.

Chapter 6

Effect of selective substitutions of magnetite nanoparticles in 45S5 glass-ceramic

It has been shown in chapter 4 and chapter 5 that for making the sol-gel derived 45S5 glass-ceramic into a magnetic glass-ceramic suited for MH application, it is preferable to directly incorporate MNP during the sol-gel process rather than using an iron oxide precursor. Though these chapters discussed the introduction of iron oxide in 45S5 composition by replacing SiO_2, it is unclear if replacing silica with iron oxide (instead of CaO or Na_2O) is the correct choice to obtain an MGC with optimal properties for MH applications in bone cancer treatment. It may be noted that in the 45S5 ($45SiO_2$-24.5CaO-$24.5Na_2O$-$6P_2O_5$) composition, SiO_2 and P_2O_5 function as glass formers, while Na_2O and CaO act as glass modifiers. Barring P_2O_5, whose content is only 6 wt.%, the other three components, viz., SiO_2, CaO, and Na_2O are three potential components for substituting with MNP. To find an answer to this question, 8 wt.% MNP was substituted for SiO_2 or CaO or Na_2O in the 45S5 composition and the resulting properties of the glass-ceramics were evaluated. The choice of using 8 wt.% MNP as the optimal amount of substituent is based on inferences made from previous chapters (4 and 5) and the report of Singh *et al* [SING2009].

6.1. Sample preparation

MNP were prepared as explained in the chapter 2 (section 2.1). Following this, MNP-substituted glass-ceramics with three different compositions, viz., $37SiO_2$-24.5CaO-$24.5Na_2O$-$6P_2O_5$-$8Fe_3O_4$ (henceforth referred as MGCS), $45SiO_2$-16.5CaO-$24.5Na_2O$-$6P_2O_5$-$8Fe_3O_4$ (henceforth referred MGCC) and $45SiO_2$-24.5CaO-$16.5Na_2O$-$6P_2O_5$-$8Fe_3O_4$ (henceforth referred MGCN) were synthesized by sol-gel route. These compositions were designed such that 8 wt.% MNP are substituted for corresponding SiO_2, CaO and Na_2O, respectively, in the bioglass-ceramic $45SiO_2$-

24.5CaO-24.5Na_2O-6P_2O_5. The dried powders of the aged gel was provided an optimal heat treatment at 550 °C for 1 h before further studies were conducted on them.

6.2. Structural analysis

XRD patterns of the processed MGCS, MGCN, and MGCC samples at 550 °C for 1 h depicted in Figure 6.01. The Figure reveals that combeite ($Na_2Ca_2Si_3O_9$, ICDD-022-1445), magnetite (Fe_3O_4, ICDD-019-0629) and a small amount of sodium nitrate ($NaNO_3$, ICDD-33-306) phases have crystallized in all samples with no noticeable trace of hematite. The heat treatment temperature was restricted to 550 °C since magnetite begins to convert into hematite at higher temperatures, accompanied by a further reduction in the $NaNO_3$ phase [SZOS2015, JAFA2015]. Based on observations from earlier published reports and chapters 3 and 4, the formation of HAp under physiological conditions is not hindered by the presence of sodium nitrate and combeite phases [ADAM2013, THOM2016, PEIT2001].

The morphology of MGCS, MGCN and MGCC nanopowder particles can be visualized in the respective FETEM images presented in Figure 6.02 (a-c). All nanopowders exhibit near spherical morphology. However, MGCS and MGCN exhibit more regular shape than MGCC. The SAED pattern (Figure 6.02 (d)) of the MGCN sample consists of reflections originating from the (204), (205), (107), (217), and (334) planes of combeite, as well as the (104) plane of $NaNO_3$. The reflections from magnetite's planes (311) and (440) overlap with those of (105) and (215) planes of combeite. HRTEM image and inverse fast Fourier transform (iFFT) of HRTEM image show the lattice fringes of the (104) plane of $NaNO_3$ and the (204) plane of combeite phase in MGCN nanopowder, as displayed in Figure 6.02 (e). The estimated d-spacing of the two planes aligns with the XRD peak indexing shown in Figure 6.01.

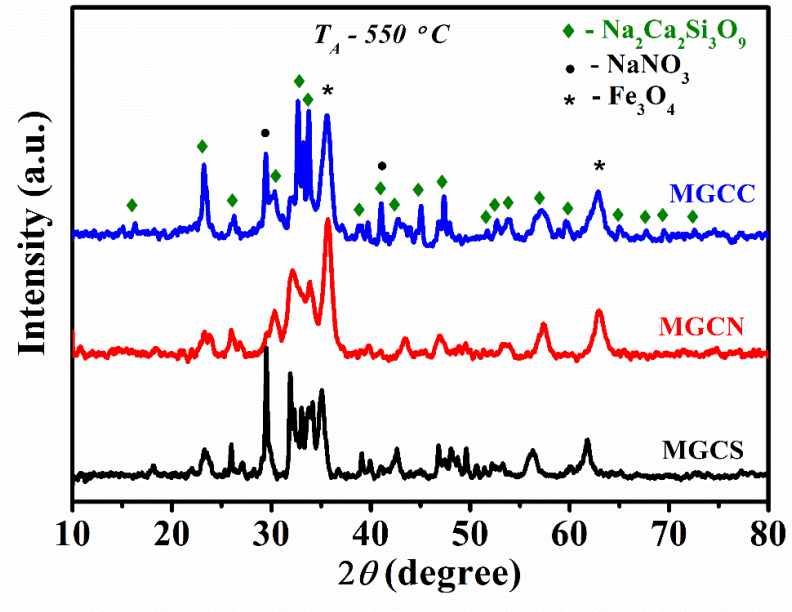

Figure 6.01: XRD patterns of heat treated MGCS, MGCN, and MGCC nanopowders.

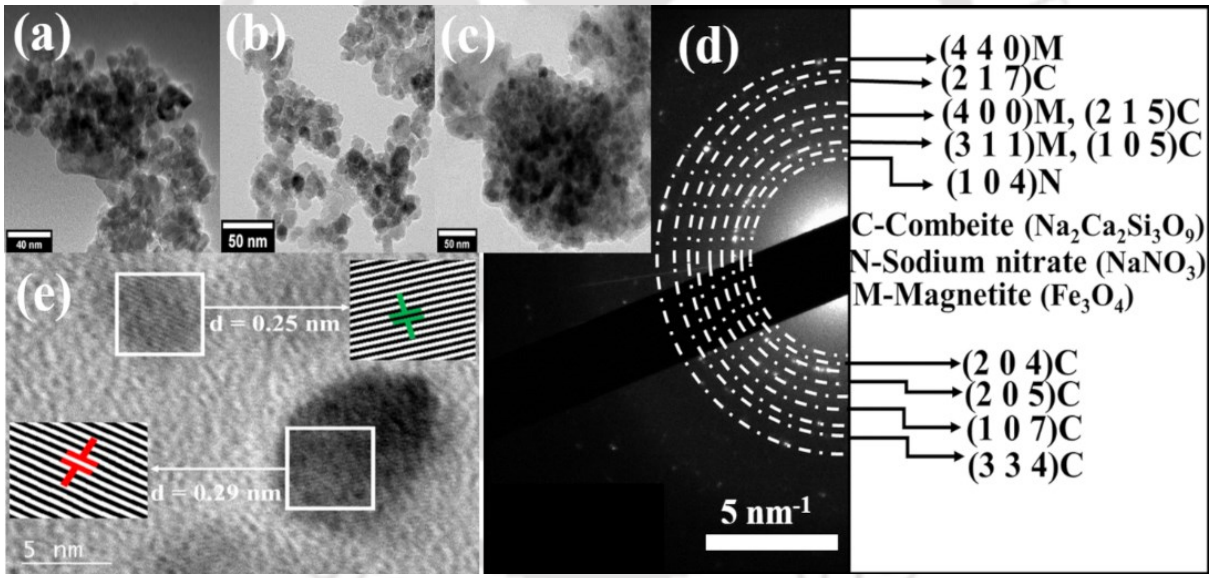

Figure 6.02: (a-c) FETEM images of heat treated MGCS, MGCN, and MGCC nanopowders. (d) SAED pattern, (e) HRTEM and iFFT images of heat treated MGCN nanopowder. C, M and N in (d) denote combeite, magnetite, and sodium nitrate, respectively.

6.3. Morphology analysis

The particle size distribution and morphology of MGCS, MGCN, and MGCC nanopowders were analysed using FESEM images shown in Figure 6.03 (a-c). Agglomerated spherical type of

morphology is observed in all the samples. This agglomeration is due to the high surface-to-volume ratio (shown in textural properties) and highly magnetic nature of the nanopowders. The average particle size of MGCS, MGCN, and MGCC are 18 ± 1 nm, 18 ± 1 nm, and 16 ± 1 nm, respectively. Even though MGCS, MGCN, and MGCC have the same MNP concentration, MGCC exhibits a slightly narrower size distribution.

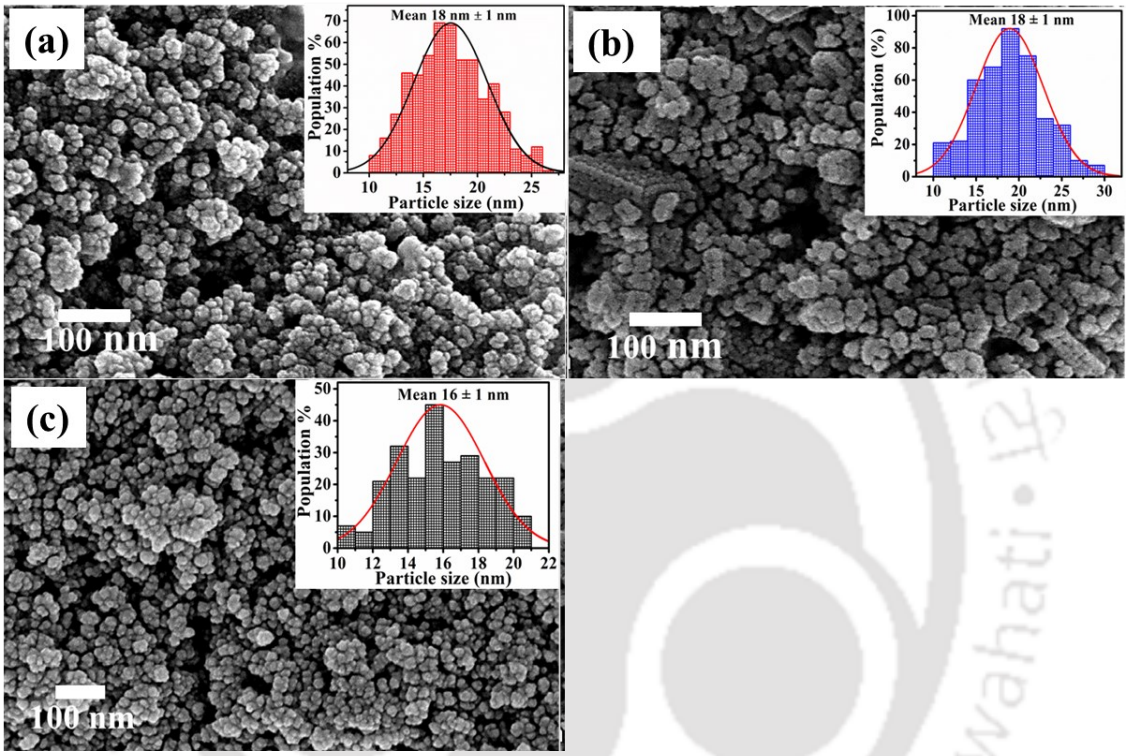

Figure 6.03: FESEM micrograph of heat treated (a) MGCS, (b) MGCN, and (c) MGCC nanopowders. Insets show the respective particle size distributions.

6.4. Surface area analysis

Figure 6.04 (a) and (b) display the BJH isotherms and the pore size distributions of MGCS, MGCN, and MGCC samples. The hysteresis loop of the isotherm curves of the all three samples exhibits H2-type isotherm, which belongs to type-IV isotherm. This specific shape of the hysteresis curve is indicative of the presence of interconnected and distorted wormlike pores in the samples. MGCS and MGCN display a bimodal pore size distribution with surface areas of

9.2 m^2/g and 13.08 m^2/g, respectively. The average size of the smaller pores is 3.7 nm for MGCS and 3.9 nm for MGCN. The larger pores have an average size of 14.9 nm for MGCS and 12.3 nm for MGCN. Additionally, the pore volumes of MGCS and MGCN are 0.035 cc/g and 0.050 cc/g, respectively. In comparison, MGCC features a surface area of 7.63 m^2/g, pore size of 12.3 nm, and pore volume of 0.030 cc/g.

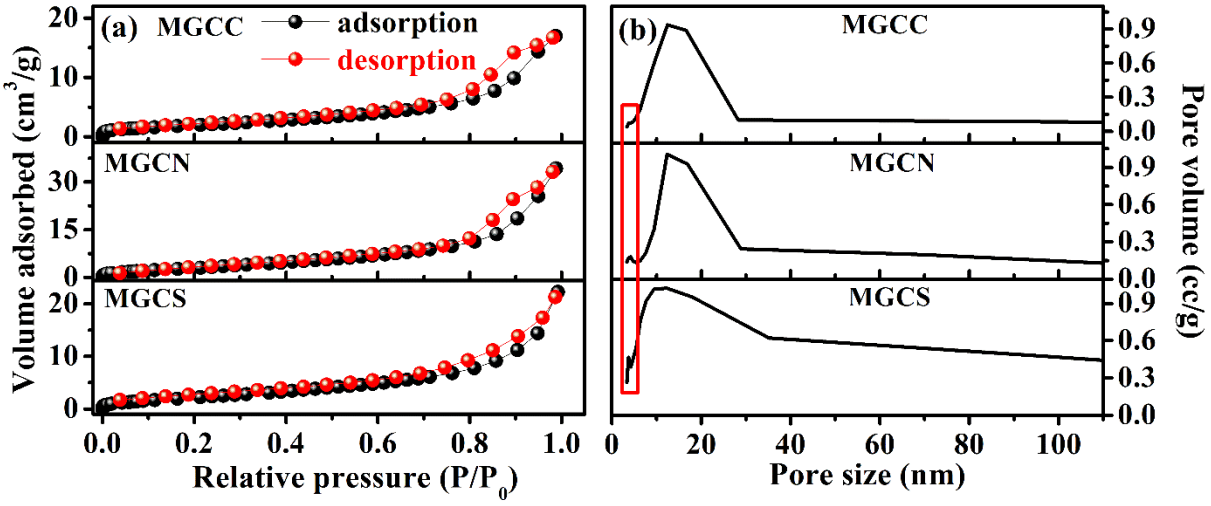

Figure 6.04: (a) N_2 adsorption-desorption isotherms, and (b) pore size distribution in MGCS, MGCN, and MGCC nanopowders.

As shown in chapters 4 and 5, the surface area of sol-gel-derived 45S5 glass-ceramic increases with the concentration of iron oxide precursor and MNP, with range of 1.81 m^2/g to 4.81 m^2/g and 5.60 m^2/g to 13.50 m^2/g, respectively. While all three MNP-substituted samples contain the same amount of MNP, variations in textural properties are observed due to differences in their network environment and constituent concentrations. The surface area of MGCN is significantly higher than MGCS. On the other hand, surface area of MGCC is lower than that of MGCS, but substantially higher than that of nanopowders of 45S5 glass-ceramic reported in the literature [FAUR2015]. Thus, MGCS, MGCN, and MGCC exhibit a notably higher surface area than 45S5 nanopowder and iron oxide-substituted 45S5 glass-ceramics as reported in the chapter 3 and chapter 4. Though bimodal porosity offers advantages for

bioactivity and magnetic hyperthermia, the ultimate results depend on the interplay between surface area and pore distribution. Thus, all three MGCS, MGCN and MGCC samples offer better textural properties as compared to the 45S5 glass-ceramic.

6.5. Surface Zeta potential and analysis of colloidal particles

The measured ζ values of aqueous suspensions of MGCS, MGCC, and MGCN are -29 mV, -28 mV, and -26 mV, respectively. Since the glass-ceramic constituents are the same for all three samples with only differing concentrations, the nature of the ζ is consistent across all samples, although the values differ. Certain bioactive glasses and glass-ceramics have been found to exhibit negative ζ values over a broad range [DOOS2011]. According to the colloidal stability limit of ζ described in chapter 4 (section 4.4), all the three samples are stable in aqueous medium [FAUR2015, ARJM2012]. The small differences in ζ values of the samples can be attributed to variations in the concentrations of Si, Na, and Ca ions in the respective colloidal solutions.

Figure 6.05 (a-c) demonstrate the average colloidal particle size distribution of MGCS, MGCN, and MGCC samples in aqueous medium. Table 6.01 presents the average colloidal particle sizes of MGCS, MGCN, and MGCC aqueous magnetic fluids of various solute concentrations. The data reveals a bimodal distribution of colloidal particles in all samples except MGCS at a concentration of 1 mg/ml. It is evident that there is a trend of increasing colloidal size distribution as the concentration rises from 1 mg/ml to 5 mg/ml for all samples. Notably, the MGCC samples display a smaller colloidal particle size distribution when compared to the MGCS and MGCN samples. The variation in colloidal size distribution of MGCS, MGCN, and MGCC fluids could be attributed to the variation in the concentration of various oxide constituents in different samples. The narrower colloidal distribution in the MGCC sample suggests a potential enhancement in its heating capacity as compared to the MGCS and MGCN samples.

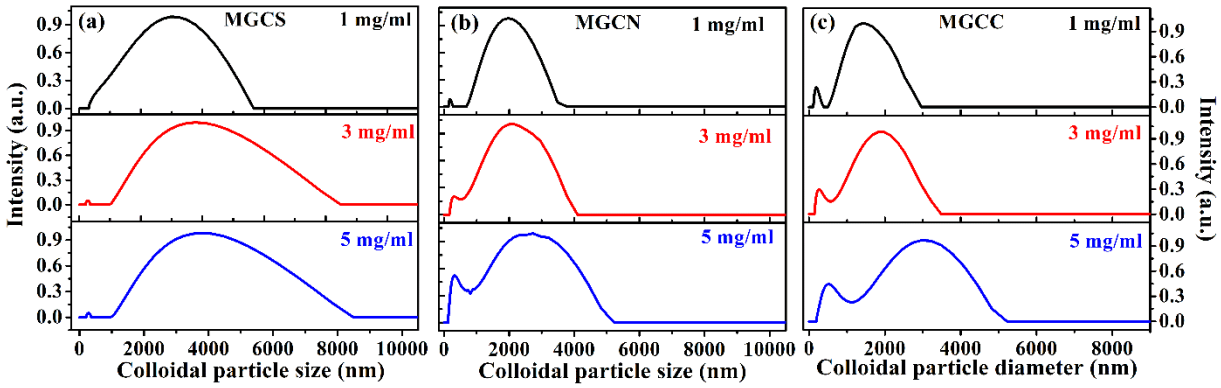

Figure 6.05: Colloidal particle size distribution in fluids with different concentrations of heat treated (a) MGCS, (b) MGCN, and (c) MGCC nanopowder.

Table 6.01: Average colloidal particle sizes of the three samples at various concentrations.

Fluid Concentration (mg/ml)	Average colloidal particle size (nm)		
	MGCS	MGCN	MGCC
1	~1585	~1650	~207, ~1443
3	~1690	~280, ~2095	~240, ~1650
5	~3000	~303, ~2620	~363, ~2590

6.6. EPR studies

The EPR spectra of MGCS, MGCN, and MGCC nanopowder samples recorded at room temperature are displayed in Figure 6.06 (a). Fe^{3+} ions display the same symmetry as described in chapter 5. All three samples exhibit a single resonance absorption line at g ≈ 2.1, indicating a cluster formation of Fe^{3+} ions within the ceramic network. Notably, the total intensity and line width are highest for MGCC and lowest for MGCS, as shown in Figure 6.06 (b). As discussed earlier in chapter 2, an increase in ΔH suggests that dipole-dipole interactions are dominant. Therefore, the highest dipole-dipole interaction is observed in the MGCC sample compared to MGCN and MGCS. Although all three samples were prepared with the same amount of MNP,

the dipole-dipole interaction between the iron ions in the MGCC sample is the highest among all investigated samples, which is also reflected in their magnetic properties.

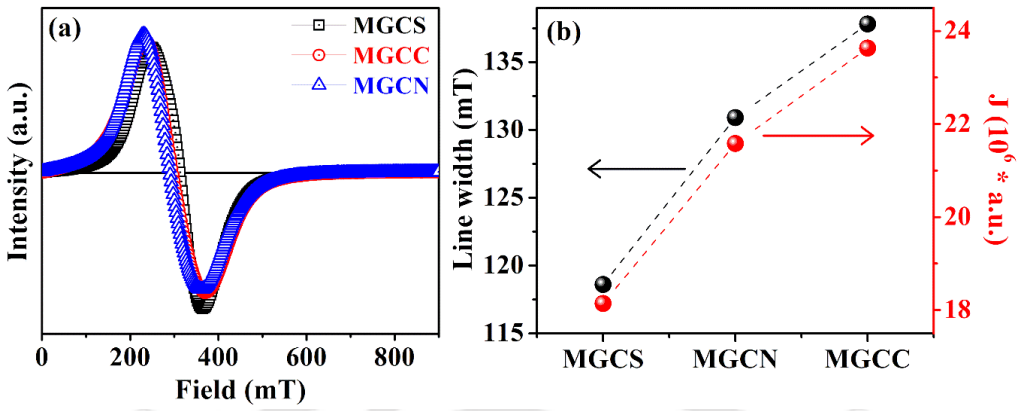

Figure 6.06: (a) Room temperature EPR spectra, and (b) variations in linewidth (ΔH) and intensity (J) of g ≈ 2.1 spectral line of MGCS, MGCN, MGCC nanopowders.

6.7. Magnetic properties

The room temperature *M-H* loops obtained for heat treated MGCS, MGCN, and MGCC nanopowders in a field sweep of ±20 kOe are depicted in Figure 6.07 (a). Figure 6.07 (b) displays the *M-H* loops of the same nanopowders recorded under clinically amenable range of ±500 Oe. Table 6.02 presents the magnetic parameters for heat treated MGCS, MGCN, and MGCC nanopowder samples, including M_s, H_c, M_r, and hysteresis loop area. Furthermore, the area enclosed by the hysteresis loop is 700 erg/g for MGCS, 895 erg/g for MGCN and 996 erg/g for MGCC. The low values of H_c and M_r indicate the soft magnetic character of these samples. Upon examining the magnetic parameters of MGCS, MGCN and MGCC, it becomes evident that MGCC and MGCN exhibit superior magnetic properties compared to MGCS, despite having the same MNP concentration. In the case of sol-gel based (45-x)SiO_2-24.5CaO-24.5Na_2O-6P_2O_5-xFe_2O_3 ($2 \leq x \leq 15$) glass-ceramics discussed in chapter 4, the highest M_s (= 1.54 emu/g) was obtained for the sample with x = 15 wt.% Fe_2O_3. This low M_s is due to the presence of the second magnetic phase, i.e., hematite, which has a low magnetic moment. On the other hand, Rahman

et al. reported a sol-gel derived mesoporous glass-ceramic composition of composition 7Fe_3O_4-51SiO2-18CaO-20Na_2O-4P_2O_5 (mol%) (corresponding to21Fe_3O_4-51SiO_2-18CaO-20Na_2O-4P_2O_5 in wt.%) based on Fe_3O_4 and obtained a high M_s of ~13 emu/g [RAHM2020]. Since their composition is entirely different from the current work, a direct comparison with the present results cannot be made. However, it can be noted that the MNP content in their system (21 wt.% Fe_3O_4) is considerably higher than the content (8 wt.% MNP) in the present samples. Since MNP is the only magnetic phase in both these sets of samples, one can compare their magnetic properties. The M_s value of MGCS is slightly lower, but MGCN shows a M_s value comparable to that of the earlier reported sample. Remarkably, MGCC exhibits the highest M_s value of 14.14 emu/g amongst all the samples, indicating significantly higher magnetization compared to the earlier reported value of ~13 emu/g.

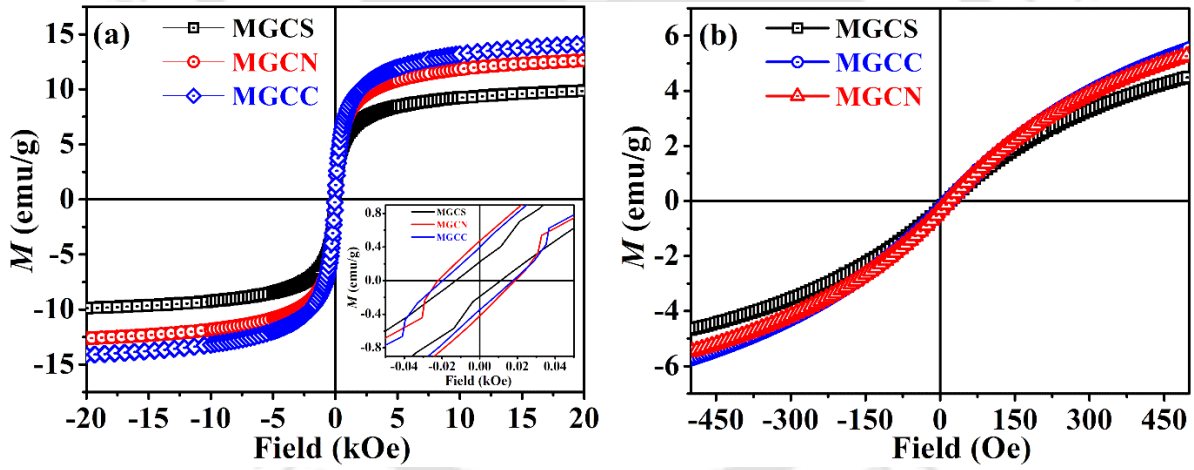

Figure 6.07: *M-H* curves of MGCS, MGCN, MGCC nanopowders recorded at (a) ±20 kOe, and (b) ±500 Oe.

This comparison also shows that all our three samples can be considered to be suitable for use as thermoseeds in MH. The minor *M-H* loops exhibit a similar trend in magnetic parameters, including M_s, H_c, M_r, and hysteresis loss, when compared to the *M-H* loop recorded with ±20 kOe. The heat generation capacity of a magnetic glass-ceramics in response to an

alternating magnetic field is directly linked to the energy loss, which is quantified by the area of the hysteresis loop. Hence, substituting MNP for CaO (MGCC) results in superior magnetic properties as compared to substitution for SiO_2 (MGCS) and Na_2O (MGCC). Thus, MGCC has displayed outstanding magnetic properties despite containing an equivalent amount of MNP, fostering optimism about its suitability as an excellent thermoseed in MH.

Table 6.02: Magnetic parameters of the three heated nanopowders.

Magnetic parameters	**MGCS**	**MGCN**	**MGCC**
Saturation magnetization, M_s (emu/g)	9.88	12.63	14.14
Coercivity, H_c (Oe)	0.21	0.45	0.37
Remnant magnetization, M_r (emu/g)	12	20	19
Hysteresis loop area at ±20 kOe (erg/g)	700	895	996

6.8. Evaluation of induction heating capacity

The temperature increase in the magnetic fluids of different concentrations was monitored for up to 600 s and the corresponding data are presented in Figure 6.08 (a-c), alongside near infra-red images that visually depict the temperature rise in the magnetic fluids. The safety limit has been followed throughout the experiment, as discussed in section 4.7 of chapter 4. When H (=12.89 kAm^{-1}) with f (=336 kHz) was applied to aqueous fluids of MGCS, MGCN and MGCC fluids, the temperature increased from ~32 °C to ~45 °C, ~46 °C and ~48 °C, respectively, for concentrations ranging from 1 - 9 mg/ml within 600 s of exposure. It can be noted that the temperature rise increases as the fluid concentration is increased from 1 mg/ml to 9 mg/ml. Table 6.03 provides a summary of the specific exposure times (t_H) required to reach ~42 °C for MGCS, MGCN, and MGCC within the 600 s time frame. To be more precise, aqueous fluids of MGCS and MGCN achieved this temperature in 528 s and 330 s at concentrations of 7 mg/ml, whereas it took them 350 s and 250 s at higher concentration of 9 mg/ml. On the other hand, the aqueous

fluid of MGCC accomplished the same outcome in 514 s at a concentration of 5 mg/ml and in 320 s at a concentration of 7 mg/ml. Impressively, it achieved this target in just 240 s at a concentration of 9 mg/ml. It can also be noted from Table 6.03 that lower concentrations of 1 mg/ml, 3 mg/ml, and 5 mg/ml of MGCS and MGCN fluids, as well as 1 mg/ml and 3 mg/ml of MGCC fluid, required more than 600 s to reach the desired temperature. Data presented are confined to 600 s of exposure as the search is for an efficient thermoseed requiring minimal exposure time. Three different mechanisms have been proposed to understand the heating capacity of magnetic fluids, as detailed in chapter 4.

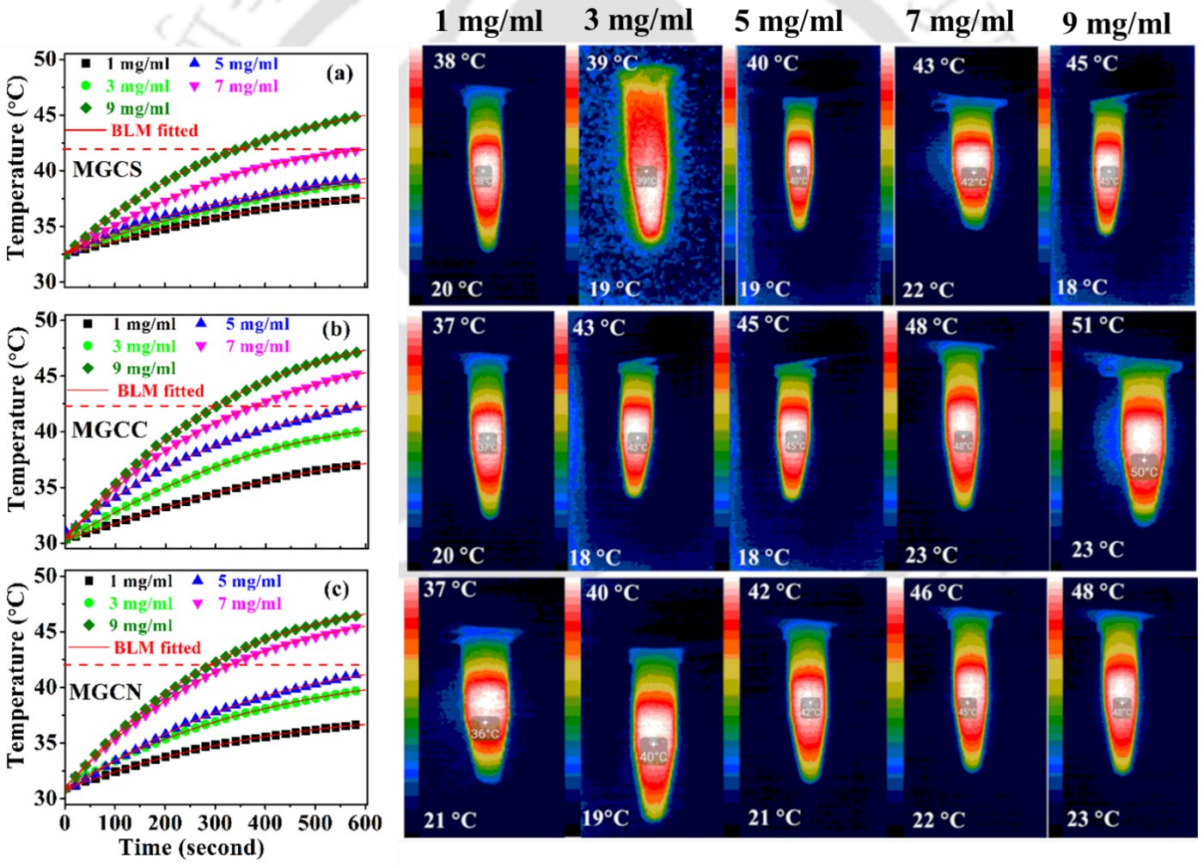

Figure 6.08: Temperature rise as a function of time in (a) MGCS, (b) MGCC, and (c) MGCN magnetic fluids at various concentrations. NIR camera image of each fluid is also displayed.

Table 6.03: Induction heating parameters of MGCS, MGCC, and MGCN fluids. t_H is exposure time required to reach the therapeutic temperature (42 °C) under specified test conditions.

	MGCS concentration (mg/ml)					**MGCN concentration (mg/ml)**					**MGCC concentration (mg/ml)**				
	1	3	5	7	9	1	3	5	7	9	1	3	5	7	9
SAR (W/g)	85	36	28	26	25	89	36	34	31	29	93	39	35	30	25
ILP ($nHm^2 g^{-1}$)	1.5	0.6	0.5	0.5	0.4	1.6	0.6	0.6	0.5	0.4	1.7	0.7	0.6	0.5	0.5
t_H(s)	-	-	-	528	350	-	-	-	330	250	-	-	514	320	240

The magnetic fluid stability and the average colloidal distribution of the three sets of colloidal particles in aqueous medium have already been discussed in this chapter. Hence, the combined analysis of the particle size distribution and magnetic parameters of MGCS, MGCN, and MGCC collectively reveal the dominance of both Brownian relaxation and hysteresis loss mechanisms in all concentration of the tested fluids.

To gain more insight on the fluid's heating behavior, *SAR* was calculated using the BLM, as discussed in chapter 2. Estimated *SAR, ILP* and exposure time (t_H) of magnetic fluids required to reach therapeutic temperature (42 °C) are tabulated in Table 6.03. The concentration of the magnetic fluid has an inverse effect on the *SAR* and *ILP* values of MGCS, MGCC, and MGCN. But t_H decreases with an increase in concentration. The decrease in *SAR* values with increase in concentration is due to an increase in magnetic interactions in the fluids as the MNP concentration rises. The *ILP* values at the lowest concentration of MGCS, MGCN and MGCC are all higher than the *ILP* value of 1.0 nHm^2kg^{-1} reported for the commercially available magnetic fluid, FluidMag-CT. It can be observed that MGCC stands out with significant advantages over MGCS and MGCN. This distinction may be attributed to the influence of distinct ceramic-network environments, which could alter the heat capacity of the magnetic fluid.

In conclusion, MNP substitution from CaO yields superior magnetic properties compared to substitution for SiO_2 and Na_2O for applications in MH.

6.9. *In vitro* bioactivity assessment

6.9.1 Ion exchange

The variation in the pH of SBF from the instant MGCS, MGCN and MGCC pellets are immersed is displayed in Figure 6.09. The rapid initial increase in pH is a consequence of the ion dissolution mechanism involving the exchange of the ions released from the sample surface with H_3O^+ as already pointed out in chapters 1 and 2. Over time, the pH gradually approaches saturation due to saturation in the release of ions from the sample. The pH of the samples immersed in SBF depends on ions such as Si, Ca, Na, Fe, and P. In this context, the concentrations of P and Fe ions remain constant in all the samples, while the concentrations of Si, Ca, and Na vary in each of the three samples. As discussed in chapter 1, Ca and Na ions directly increase the pH of the SBF solution, while Si influences the pH indirectly. However, it is difficult to determine which ion affects the pH more. The important conclusion drawn from the increase in pH of the SBF containing the MGCS, MGCN, and MGCC pellets is all the three compositions demonstrate bioactive nature.

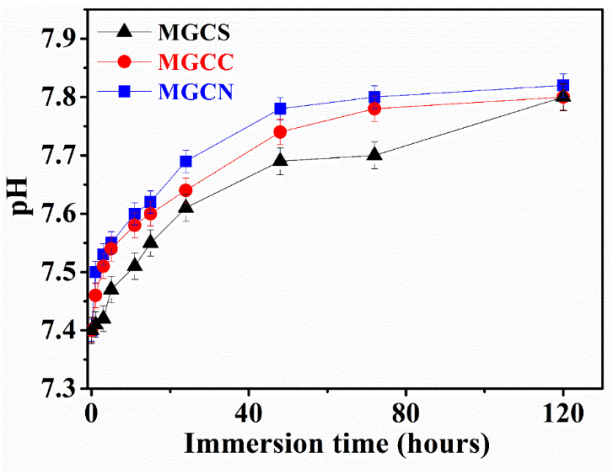

Figure 6.09: Change in pH value of SBF with soaking time of the three glass-ceramic pellets.

6.9.2. Surface layer formation

In vitro bioactivity assessments of MGCS, MGCN and MGCC nanopowder samples were done by treating them with SBF for 5 days. The GI-XRD patterns of SBF treated MGCS, MGCN and MGCC samples after 5 days of soaking are illustrated in Figure 6.10 (a). It can be observed that peaks at 2θ values of ~26° and ~32° represent reflections from the (002) and (112) planes of HAp crystallites. This confirms the precipitation of the HAp layer on the surfaces of the MGCS, MGCN, and MGCC pellets. The evolution of HAp layer is further confirmed by FESEM micrographs of SBF treated sample [*c.f.*, Figure 6.10 (b)]. The formation of this HAp layer indicates the bioactive nature of MGCS, MGCN and MGCC samples.

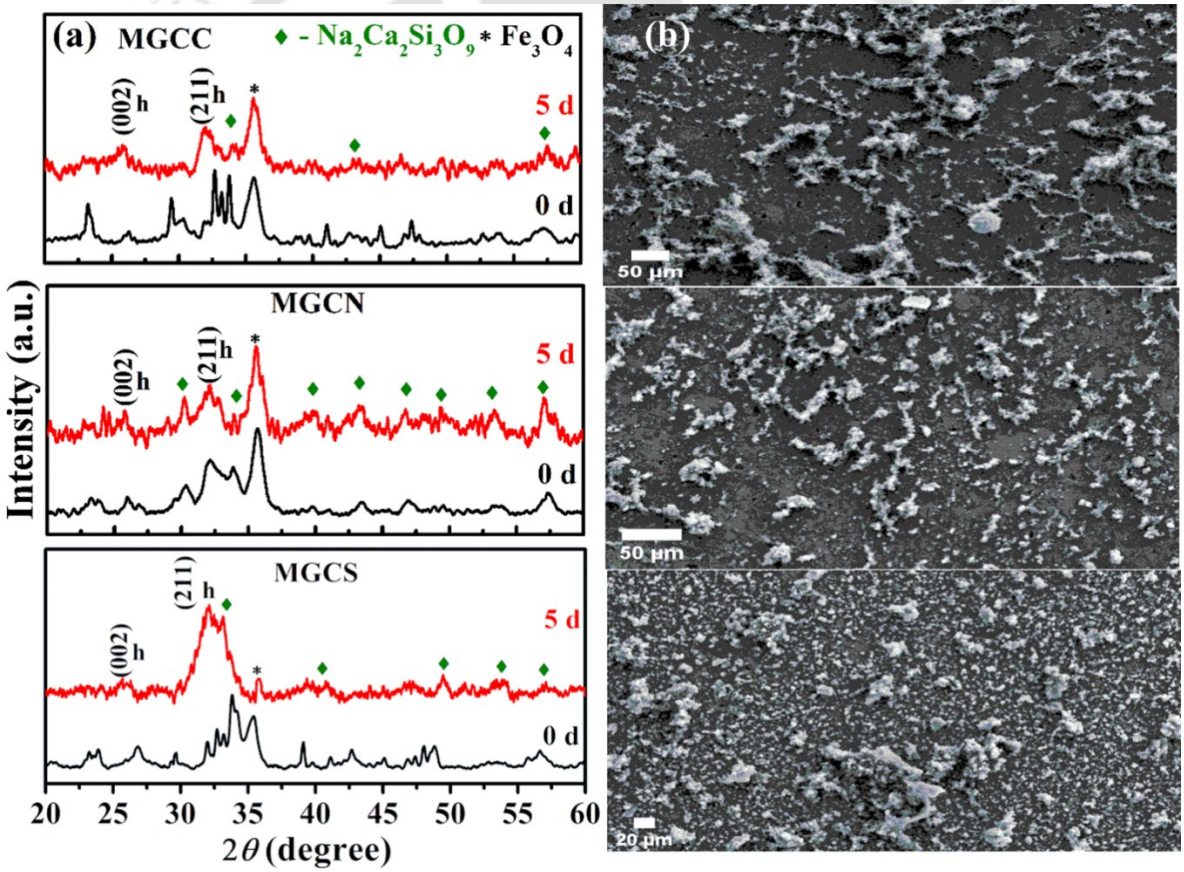

Figure 6.10: (a) GI-XRD pattern and (b) FESEM images of SBF treated MGCS, MGCN and MGCC pellets. Symbols ♦, ∗, and h represent combeite, magnetite, and HAp phases, respectively.

6.9.3. Osteoblast cell viability

To assess the impact of Si, Ca and Na ions on MG-63 cell viability, an extensive investigation was conducted, delving into the established roles of these ions, as elucidated by Hench *et al.* in the original Hench composition [KAUR2016]. However, the incorporation of MNP into Hench glass-ceramics by replacing SiO_2 (MGCS) or CaO (MGCC) or Na_2O (MGCN) led to distinct impacts on cell growth. The cytocompatibility of the samples was tested against the human osteoblast cells, MG-63 over a period of 5 days using four different sample concentrations, viz., 2, 1, 0.5 and 0.25 mg/ml. The observed results are shown in Figure 6.11.

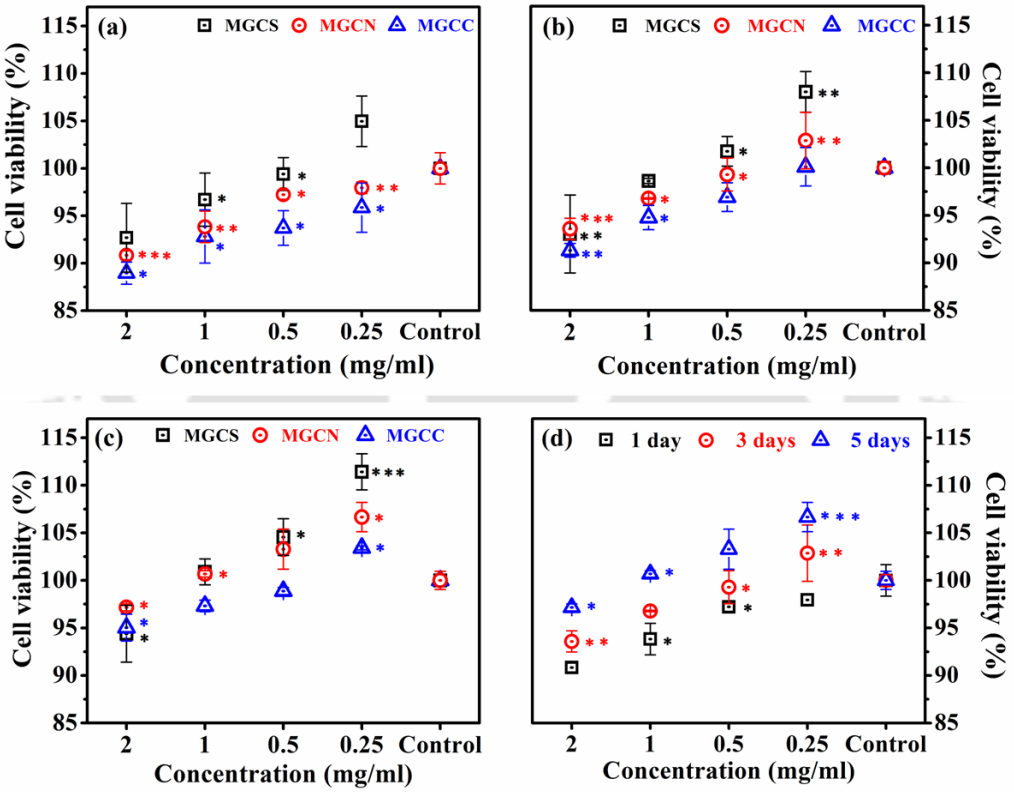

Figure 6.11: Viability of MG-63 osteoblast cells after incubation of different concentrations of MGCS, MGCC and MGCN nanopowders for (a) 1 day, (b) 3 days, and (c) 5 days. (d) Effect of concentration of MGCS nanopowders on the viability of MG-63 cells. An asterisk indicates a significant difference in cell viability between different samples and control group (* $\rightarrow p < 0.05$, ** $\rightarrow p < 0.005$, *** $\rightarrow p < 0.001$, where p is the probability value or p-value).

The MGCS sample showed excellent cytocompatibility against the osteoblast cells with cell viabilities of ~93% and ~105% for the concentrations of 2 and 0.25 mg/ml after 1 day of incubation (*c.f.*, Figure 6.11 (a)). On the other hand, MGCN and MGCC samples taken in 0.25 mg/ml concentration exhibited initial cell viability of ~98% and ~96%, which decreased to ~91% and ~89% at the highest concentration of 2 mg/ml, respectively, after 1 day of incubation. The increment in the cell viability with decrease in concentration may be attributed to the reduced aggregation and the acclimatization effect of cells at lower concentrations [FULD2010]. The cell viability improved with an increase in the period of incubation (Figure 6.11 (b, c and d)). After 3 days of incubation, the amount of viable cells increased from ~93 % to ~108 % in the case of MGCS, ~94 % to ~103 % in the case of MGCN, and ~91 % to ~100 % in the case of MGCC, as the concentration was diluted from 2 mg/ml to 0.25 mg/ml. After 5 days of incubation, the MGCS sample showed excellent cell viability of ~95% and ~111% for concentrations of 2 and 0.25 mg/ml. Similarly, cells showed consistent increase in the viability over 5 days, reaching up to ~107% to ~97% for MGCN and ~103% to ~95% for MGCC for concentrations of 0.25 and 2 mg/ml, respectively. The reason for the increase in cell viability with decreasing solute concentration and increasing incubation time has already been explained in detail in chapters 3 and 4. Overall, all the tested samples, *i.e.*, MGCS, MGCN and MGCC, showed excellent cytocompatibility within the acceptable limit prescribed [LI002015] for biomaterials and hence these samples can be used for biological applications.

6.10. Summary

- Mesoporous MGCS, MGCN, and MGCC nanopowders containing combeite, magnetite and a small amount of sodium nitrate were synthesized by sol-gel route.
- The colloidal size distribution and stable suspensions of MGCS, MGCN, and MGCC nanopowders have been identified for various solute concentrations in aqueous medium.

- MGCC exhibited the highest M_s (= 14.14 emu/g), and *ILP* (= 1.7 nHm^2kg^{-1}).
- Induction heating data indicated that MGCC outperformed MGCN and MGCS.
- All the three samples were found to be biocompatible and non-toxic to MG-63 osteoblast cells.
- Selective substitution of MNP for CaO (MGCC) results in a superior thermoseed for MH cancer therapy, particularly when compared to the *ILP* and bioactivity of the commercially available thermoseed fluid, FluidMag-CT.

Chapter 7

Optimization of the heating capacity of mesoporous MGCC glass-ceramic

Iron oxide-substituted MGCs reported in the literature exhibit various crystalline phases, whose concentrations alter their magnetic and bioactive properties [SING2008, SING2009, SIMO2014, SHAN2016]. No systematic processing of iron oxide/MNP-substituted sol-gel derived 45S5 MGC at elevated temperatures has been attempted so far to improve its bioactivity and induction heating capacity. Nisha *et al.* investigated the bulk 41CaO-44SiO_2-4P_2O_5-8Fe_2O_3-3Na_2O glass-ceramic under different heat treatment conditions and identified wollastonite, combeite, HAp, hematite, and magnetite crystalline phases [SHAN2013]. They reported that heat treatment at 1050 °C for 2 h showed the maximum M_s value, but beyond this point, magnetic properties decreased with further increases in heat treatment temperature and time. However, this study only demonstrated magnetic and structural properties and tested *in vitro* acellular bioactivity only for glass ceramic processed at 1050 °C. Since the above system is neither in nanoform nor the 45S5 composition, it can be concluded from previous studies (Chapters 3, 4, and 5) and the study by Nisha *et al*. that a systematic heat treatment study is needed to understand the effect of the relative presence of magnetic and non-magnetic phases on bioactive and magnetic properties for MH applications. This chapter presents a systematic heat treatment study of the promising thermoseed MGCC with a view to further enhance its efficacy for MH treatment of cancer and bone regeneration.

7.1. Sample preparation

MNP-substituted magnetic glass-ceramic with the composition of $45SiO_2$-16.5CaO-$24.5Na_2O$-$6P_2O_5$-$8Fe_3O_4$ (MGCC) has been prepared, as discussed in chapter 6. To investigate the optimum heat treatment, a process ranging from 550 °C to 700 °C was conducted.

7.2. Structural analysis

Figure 7.01 depict the room temperature XRD patterns of MGCC nanopowders subjected to heat treatment at temperatures ranging from T_A = 550 °C to T_A = 700 °C for 1 h each. XRD patterns confirmed the presence of three crystalline phases viz., sodium nitrate ($NaNO_3$, ICDD-33-306), magnetite (Fe_3O_4, ICDD-019-0629), and combeite ($Na_2Ca_2Si_3O_9$, ICDD-002-1445) in MGCC nanopowders processed at T_A = 550 °C. When T_A was raised from 550 °C to 700 °C, a progressive increase in the combeite phase along with a gradual decrease in the magnetite and sodium nitrate phases, and the emergence of the hematite phase can be seen. The relative phase percentages are estimated from the XRD patterns and displayed in Table 7.01. Table 7.01 shows the complete suppression of sodium nitrate phase and the presence of combeite, magnetite and hematite (α-Fe_2O_3, ICDD-33-0664) phases in MGCC nanopowders processed at T_A = 700 °C. Emergence of hematite phase from magnetite at high temperatures has already been discussed in section 5.3.1. At T_A = 700 °C, the non-magnetic combeite becomes the most dominant phase (as also observed earlier in Fe_2O_3 substituted 45S5 MGCs in chapter 4).

The SAED pattern (Figure 7.02 (a)) of the MGCC nanopowder processed at 550 °C displays reflections from various crystallographic planes of combeite, including (204), (402), (305), (207), (217), and (334). Additionally, the reflection from (104) plane of $NaNO_3$ and (311) plane of magnetite [overlapping with the (105) plane of combeite] are also observed. For the MGCC processed at 700 °C, the SAED pattern exhibits reflections from all the crystallographic planes observed in the MGCC processed at 550 °C except the one from (104) plane of $NaNO_3$.

Apart from these, two reflections from hematite, viz., (300) and (214) are also apparent. These reveal the complete suppression of $NaNO_3$ phase and the partial conversion of magnetite into the hematite at 700 °C. This observation is in concurrence with the XRD results summarized in Table 7.01. HRTEM micrographs and their inverse fast Fourier transforms (iFFT) depicted in Figure 7.02 (c-e), provide details of the various lattice planes (or lattice fringes) in the processed MGCC nanopowders. Peaks from (204) and (003) planes of combeite, (331) plane of magnetite and (104) plane of $NaNO_3$, can be visualized.

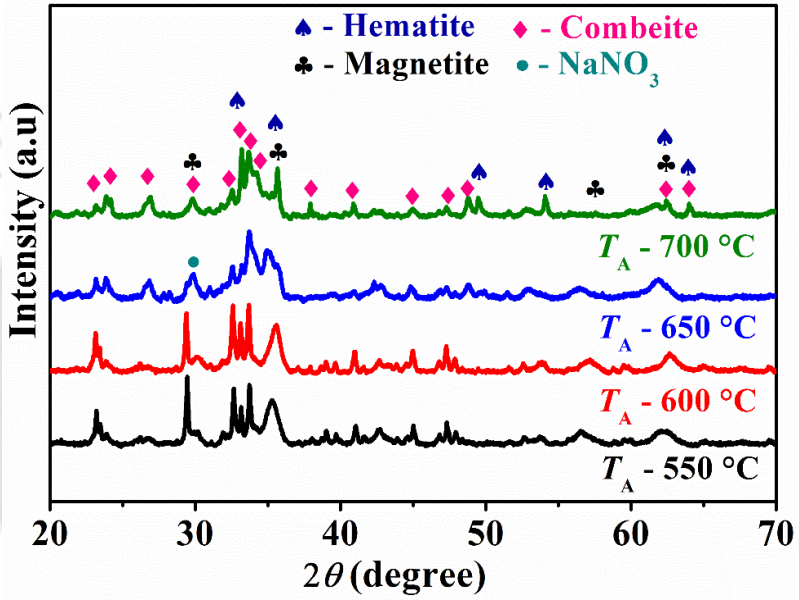

Figure 7.01: XRD patterns of MGCC nanopowders processed at various temperatures.

Table 7.01: Calculated crystalline phase percentages in MGCC nanopowders processed at different temperatures (T_A).

T_A (°C)	Relative % of various crystalline phases in MGCC			
	Combeite	Hematite	Magnetite	Sodium nitrate
550	34	0	47	19
600	48	6	30	16
650	51	8	28	13
700	71	9	20	0

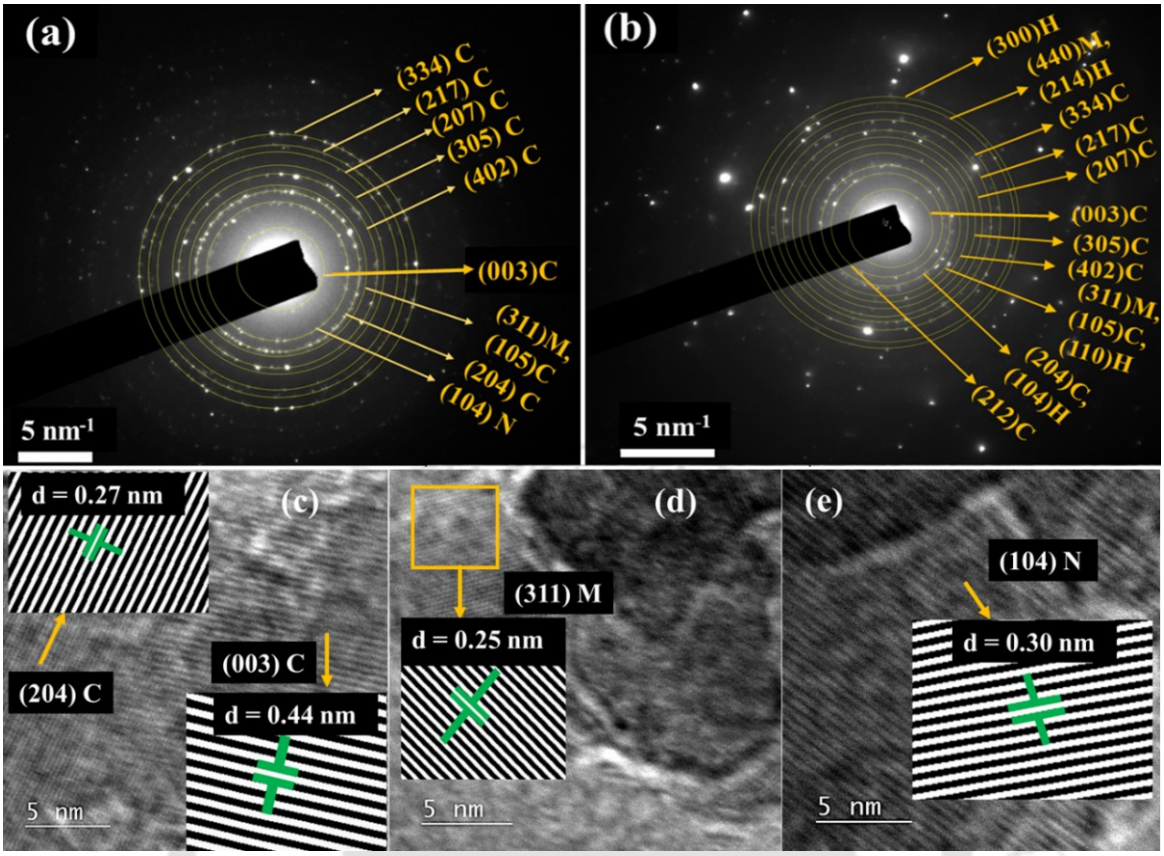

Figure 7.02: SAED pattern of MGCC processed at (a) 550 °C, and (b) 700 °C. (c-e) HRTEM and images of MGCC processed at 550 °C. C→ combeite, M→ magnetite and N → $NaNO_3$.

7.3. Morphology analysis

The morphology and average particle size distribution of MGCC nanopowders processed at different T_As were probed using FESEM micrographs (*c.f.* Figure 7.03). The micrographs revealed an agglomerated particle with near spherical morphology in all the samples. The estimated average particle sizes are 16 ± 1 nm, 19 ± 1 nm, 21 ± 1 nm, and 27 ± 1 nm for MGCC heated at 550 °C, 600 °C, 650 °C, and 700 °C, respectively. With the elevation of heat treatment temperature, the magnetic moment decreases and the average particle size increases.

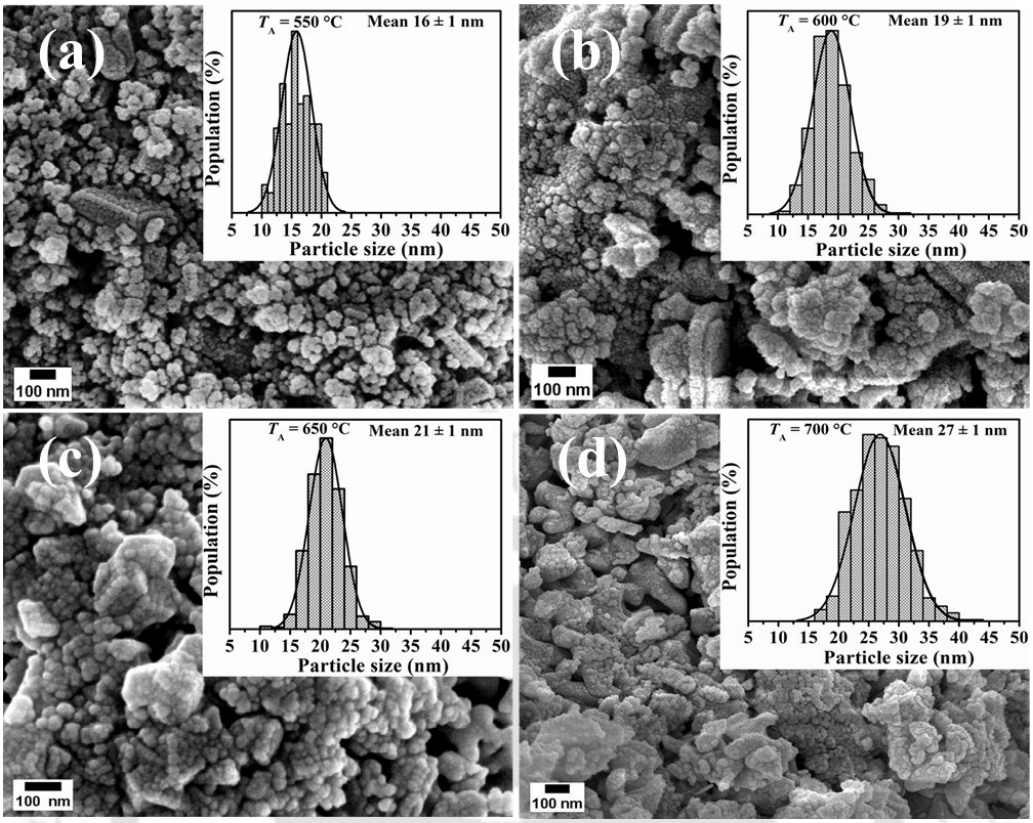

Figure 7.03: FESEM micrograph of MGCC nanopowder processed at (a) 550 °C, (b) 600 °C, (c) 650 °C, and (d) 700 °C. Insets show the respective particle size distributions.

7.4. Surface area analysis

Figure 7.04 (a and b) represent the BJH isotherms and pore size distribution curves of the MGCC nanopowders processed at, 550 °C and 700 °C, respectively. Type-IV isotherms were observed, and both isotherms exhibit hysteresis curves, indicative of the mesoporous nature of the samples processed at T_A = 550 °C and T_A = 700 °C. The surface area and pore volume are 7.63 m²/g and 2.625e^{-02} cc/g, respectively, for the nanopowder processed at 550 °C. They increased to 26.50 m²/g and 4.296e^{-02} cc/g, respectively, when T_A was raised to 700 °C. On the other hand, the average pore size reduced from 12.33 nm to 3.05 nm with an increase in T_A from 550 °C to 700 °C.

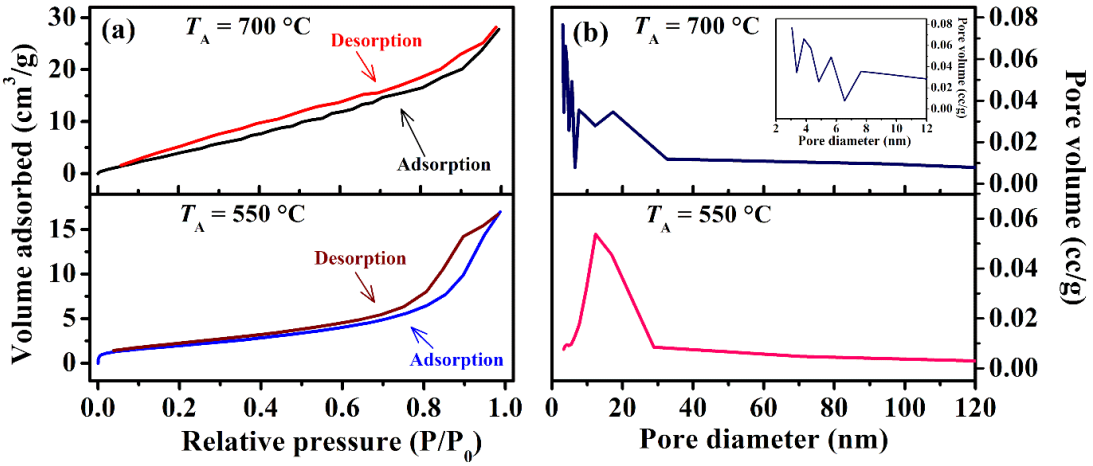

Figure 7.04: (a) N_2 adsorption-desorption isotherms, and (b) pore size distribution of MGCC nanopowders processed at 550 °Cand 700 °C.

The differences in the hysteresis observed between the adsorption and desorption curves of the nanopowders processed at 700 °C and 550 °C are evident. It can be seen that the hysteresis phenomenon appears even at a lower relative pressure of 0.1 for MGCC nanopowder processed at 700 °C, whereas it initiates in the nanopowder processed at 550 °C only after a relative pressure of 0.5. This observation suggests that the increase in temperature induces an overall growth in the particle size. Consequently, adsorbed molecules become pinned at the entrances of the pores, leading to a delay in the initiation of the desorption curve. The increment in the surface area of the MGCC sample is accompanied by a decrease in the average pore size. This is a consequence of the inverse relationship between particle size and surface area [PAND2021]. However, at T_A = 700 °C, the combeite and hematite phases undergo growth, the latter at the cost of magnetite phase, while $NaNO_3$ phase vanishes. So, determining the predominant phase that influences the overall textural properties becomes a challenge. The surge in surface area may be linked to the expansion of the combeite and hematite crystallites. Interestingly, at T_A = 700 °C, the pore size decreases below 10 nm, in contrast to sizes larger than 10 nm observed at T_A = 550 °C. The discussion on particle size growth in section 7.3 highlights its impact on pore size distribution.

While a higher surface area favours bioactivity, a reduction in pore size hinders the formation of HAp layers under physiological conditions. Thus, surface area and pore size play crucial roles in determining the surface reactions, which ultimately affect the bioactivity of the mesoporous samples.

7.5. Surface Zeta potential and analysis of colloidal particles

The measured ζ values for aqueous suspensions of MGCC nanopowder processed at T_A = 550 °C, 600 °C, 650 °C, and 700 °C are -26 mV, -27 mV, -28 mV, and -27 mV, respectively, as depicted in Figure 7.05 (a). The graphics indicate a slight increase in ζ up to T_A = 650 °C, followed by a slight decrease at T_A = 700 °C. Considering the stability scale, MGCC processed at all temperatures exhibit stable colloidal behavior in aqueous medium. The slight reduction in ζ values after T_A = 650 °C may be attributed to the removal of $NaNO_3$ phase in this temperature range.

In Figure 7.05 (b), the average colloidal particle size distributions of MGCC nanopowders subjected to heat treatment from 550 °C to 700 °C in aqueous medium are shown. All measurements were performed with a solute concentration of 1 mg/ml. Figure 7.05 (b) shows that all the tested magnetic fluids exhibit a bimodal distribution of colloidal particle sizes. In the case of the MGCC processed at 550 °C, the particle distribution covers ranges between 89 - 350 nm and 505 - 2525 nm, with average sizes of ~190 nm and ~1473 nm, respectively. For the fluid with solute processed at 600 °C, the first range contracts to 89 - 296 nm, while the second range expands to 575 - 2415 nm, with average sizes of ~173 nm and ~1405 nm. In the case of the fluid with MGCC sample processed at 650 °C, the average particle sizes vary from 91 - 375 nm and 595 - 2595 nm, with averages of ~210 nm and ~1505 nm. Similarly, in the case of the fluid with MGCC processes at 700 °C, the particle distribution spans from 110 - 394 nm and 550 - 2918 nm, with average sizes of ~227 nm and ~1665 nm. Thus, the colloidal particle size distribution

shifts towards the right (i.e., high sizes side) for solutes processed at higher T_A. Remarkably, the MGCC powder processed at 600 °C displays a narrower colloidal size distribution when compared to the one processed at 550 °C. This can be attributed to the rearrangement of iron ions and the corresponding change in the magnetic interactions between Fe^{2+} and Fe^{3+} ions resulting from the partial conversion of magnetite to hematite. Also, the colloidal size distribution broadens for solutes processed at higher T_A containing higher hematite phase %.

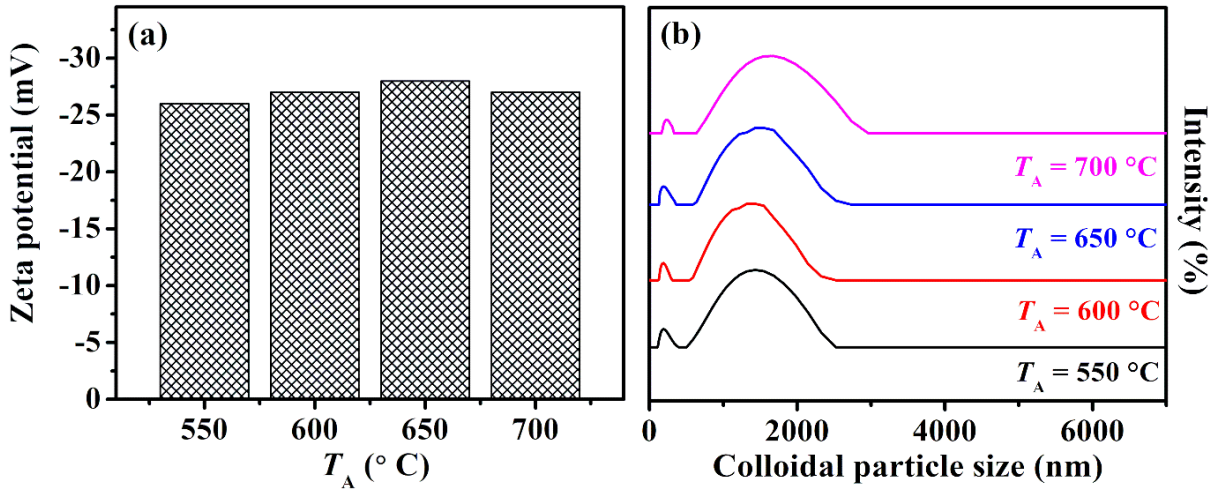

Figure 7.05: (a) Zeta potential and (b) particle size distribution curves in aqueous colloidal solutions containing different MGCC nanopowders of same concentration (1 mg/ml).

7.6. EPR studies

Figure 7.06 (a) portrays the room temperature EPR spectra arising from Fe ions in the processed MGCCs nanopowder samples. In these absorption spectra, resonance absorption centred around g ≈ 2.1 is evident, signalling the presence of Fe^{3+} ion clusters. Figure 7.06 (b) depicts the variations in ΔH and J of the g ≈ 2.1 line of MGCC nanopowder processed at T_A. From this plot, it can be inferred that the intensity of the spectral line at g ≈ 2.1 decreases with increasing in T_A value, while the linewidth initially increases up to T_A = 600 °C and then decreases for higher T_As. The observed variation in ΔH of the g ≈ 2.1 line suggests that dipole-dipole interactions prevail in MGCC nanopowders processed up to 600 °C. This may be associated with the onset

of conversion of magnetite into hematite. However, super-exchange type interactions become dominant in MGCC nanopowders processed at higher T_As. The persistent decline in the total intensity of the g ≈ 2.1 spectral line indicates a reduction in the number of spins in MGCC processed at higher T_A. This decrease is associated with the emergence of the nonmagnetic hematite phase at $T_A \geq 600$ °C. These arguments are supported by XRD and magnetization data of these nanopowders. Hence, it is possible to tune the magnetic interactions in this MGCC by appropriate heat treatment. Since the ability to control dipole-dipole interactions in nanocrystalline thermoseeds dispersed in body fluid is crucial for managing the heat generating capacity of magnetic fluids, MGCC emerges as a promising candidate for MH application.

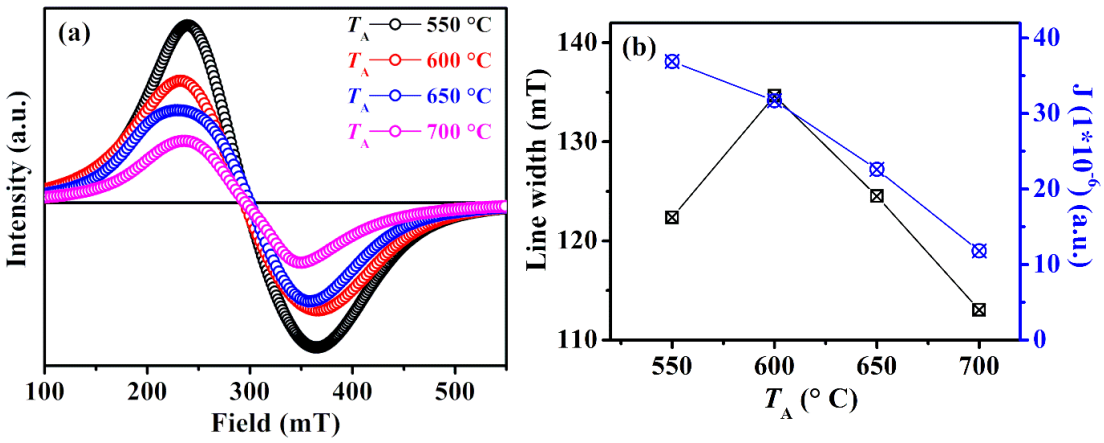

Figure 7.06: (a) Room temperature EPR spectra of all processed MGCC nanopowders. (b) Variations in ΔH and J of g ≈ 2.1 line in MGCC nanopowders processed at different T_A.

7.7. Magnetic properties

Figure 7.07 illustrates the *M-H* curves recorded at room temperature for MGCC nanopowders. Table 7.02 presents M_s, M_r, H_c and the area under the loop of MGCC nanopowder processed at various T_A's. The maximum M_s (= 14.14 emu/g) and H_c (= 20 Oe) were observed for the MGCC processed at 550 °C. Increasing T_A from 550 to 700 °C, results in a gradual decrease in M_s with simultaneous decrease in H_c and M_r values from 19 Oe to 3 Oe and from 0.37 emu/g to 0.01

emu/g, respectively. The gradual conversion of magnetite and growth of the hematite phase is the main reason for the reduction in H_c and M_r values with increasing T_A.

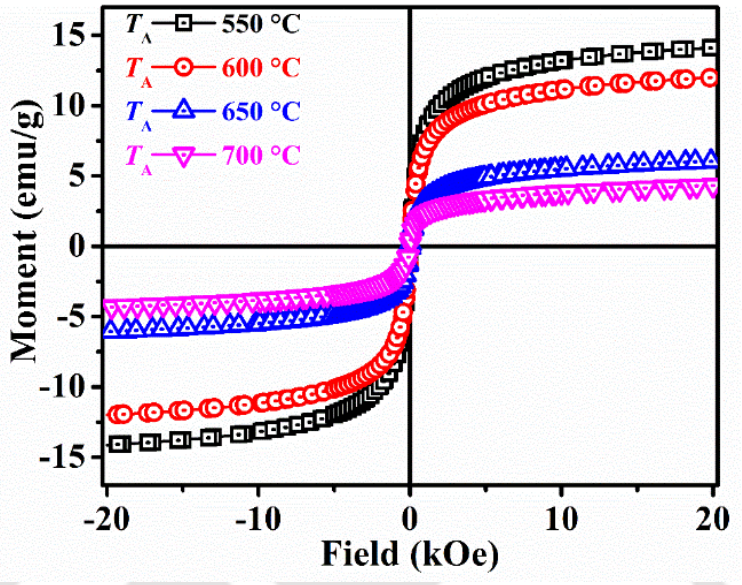

Figure 7.07: Room temperature *M-H* loop of MGCC heated from T_A = 550 °C to T_A = 700 °C.

The variations in these magnetic parameters can be related to the relative variation in the iron oxide phase percentages (magnetite and hematite) of samples processed at different temperatures. Additionally, the area enclosed by the hysteresis loop decreases from 995 erg/g to 290 erg/g as the processing temperature is raised from 550 °C to 700 °C. The MGCC nanopowders exhibit soft magnetic properties, as evidenced by their consistently low H_c and M_r values. It can be observed from Figure 7.07 and Table 7.01 that the overall magnetic properties decline with increasing T_A. This reduction is attributed to the progressive conversion of the highly magnetic phase (magnetite) to the less magnetic phase (hematite) with increase in T_A. The hysteresis loop area quantifies the ability of MGCC to generate heat in response to an alternating magnetic field, since it is directly correlated with the energy loss. The magnetic properties of MGCC processed at lower T_A are notably superior when compared to those processed at higher T_A. As a result, the MGCC powders processed at 550 °C and 600 °C demonstrate excellent magnetic characteristics indicating their potential as thermoseeds in MH.

Table 7.02: Magnetic parameters of MGCC nanopowders processed at different temperatures.

Magnetic parameters	**T_A = 550 °C**	**T_A = 600 °C**	**T_A = 650 °C**	**T_A = 700 °C**
Saturation magnetization, M_s (emu/g)	14.14	12.00	6.05	4.32
Coercive field, H_c (Oe)	20	13	5	3
Remnant magnetization, M_r (emu/g)	0.37	0.24	0.03	0.01
Hysteresis loop area at ±20 kOe (erg/g)	995	841	441	290

ZFC and FC curves of the MGCC samples processed at different T_A's are shown in Figure 7.08. It can be observed that the ZFC and FC curves of all the samples exhibit superparamagnetic-like features. It can be noted that the well-separated ZFC and FC curves exhibit three features, as explained in chapter 2, section 2.2.6, representing T_B, T_{BF}, and a cusp in the FC curve below 100 K. The observed T_B for MGCC processed at 550 °C is 122 K. T_B of ~130 K has been reported for 8 nm MNP [CAI02014]. It is also evident from the literature that T_B of magnetite nanoparticles is influenced by its crystallite size [CAI02014, FELI2017]. Thus, one can infer that the slightly lower T_B observed in this case as compared to the one reported in the literature is due to the difference in crystallite size of the two magnetite nanoparticles. Establishing T_B values for MGCC processed at T_A> 550 °C is challenging due to the coexistence of two magnetic phases (magnetite and hematite), leading to complex magnetic behavior. The temperatures at which FC and ZFC T_{BF} shows an increase with T_A [T_{BF} ~ 150 K for T_A = 550 °C, T_{BF} ~ 170 K for T_A = 600 °C, T_{BF} ~ 249 K for T_A = 650 °C, and T_{BF} ~ 253 K for T_A = 700 °C]. It can be noted that the cusp-like feature is absent for MGCC powders processed at 550 °C and 600 °C. In MGCC nanopowders processed above 650 °C, the sharpness of this feature increases, and it also shifts towards higher temperatures. This shift and enhanced sharpness of this feature can be explained on the basis of the steady conversion of magnetite to hematite with increase in T_A. Huang *et al.* observed similar features in $BiFeO_3$ nanoparticles and attributed them to

superparamagnetism relaxation process and spin glass transition behavior [HUNG2013]. They also attributed the absence of the cusp in the ZFC curve to the superposition of a broad maximum peak originating from the blocking state. However, Vijayasundaram *et al.* disproved any association of the mentioned cusp with spin glass or phase transitions in $BiFeO_3$ nanoparticles [VIJA2016]. They proposed that this cusp corresponds to changes related to the magnetic domain structure. Koksharov *et al.* also identified a similar feature in iron oxide nanoparticles at 40 K, interpreting it as a spin glass transition [KOKS2001]. In our case, the appearance of the cusp-like feature in MGCC nanoparticles is clearly linked to the emergence of the hematite phase, which alters the magnetic interactions of Fe ions in the ceramic network.

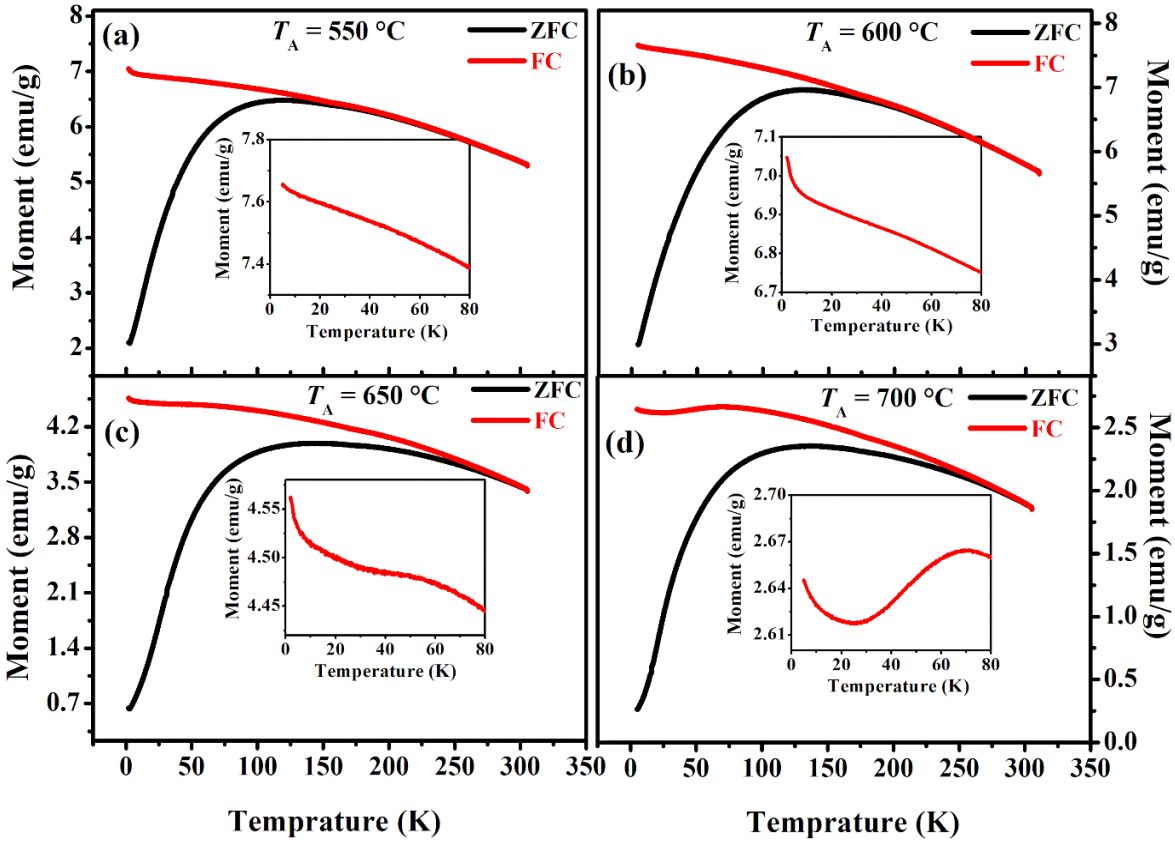

Figure 7.08: *M-T* curves of MGCC nanopowder processed at (a) 550 °C, (b) 600 °C, (c) 650 °C, and (d) 700 °C. Insets provide an enlarged view of the FC curve at lower temperatures.

7.8. Evaluation of induction heating capacity

The temperature rise in aqueous MGCC solutions containing different concentrations of MGCC nanopowders processed at (a) T_A = 550 °C, (b) T_A = 600 °C, (c) T_A = 650 °C, and (d) T_A = 700 °C under induction heating is depicted in Figure 7.09. The rate of rise in temperature increased in colloidal fluids containing MGCC nanopowder processed up to 600 °C and then decreased in those with MGCC powders processed at higher T_A values.

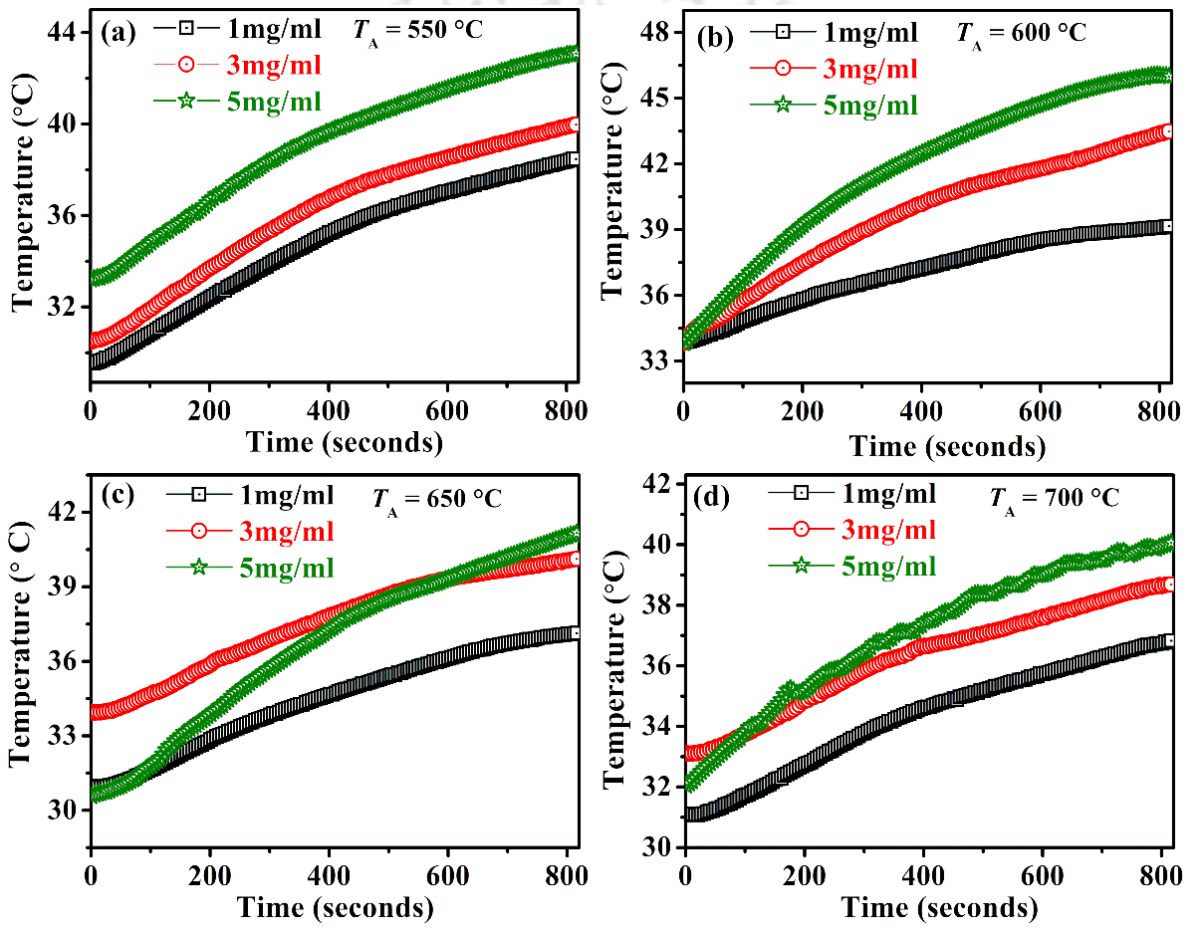

Figure 7.09: Temperature rise in aqueous colloids containing MGCC nanopowders processed at (a) T_A = 550 °C, (b) T_A = 600 °C, (c) T_A = 650 °C, and (d) T_A = 700 °C as a function of time.

The temperature of the magnetic fluid containing MGCC nanopowder processed at 550 °C rose from ~30 °C to ~43 °C when the concentration was increased from 1 to 5 mg/ml after exposure to H of 12.89 kA/m and f of 336 kHz for 600 s. When the maximum concentration of

MGCC nanoparticles (5 mg/ml) processed at T_A = 550 °C was exposed to the field for 600 s, the clinically required temperature of 43 °C was reached. However, the fluid temperature containing MGCC processed at 600 °C increased from ~33 °C to ~39 °C, ~43 °C, and ~51 °C as concentrations varied from 1 mg/ml to 5 mg/ml within 600 s of exposure time. As for the fluid consisting of MGCC processed at 650 °C, its temperature increased from ~33 °C to ~37 °C, ~40 °C, and ~42 °C for the fluid concentrations of 1, 3 and 5 mg/ml. However, for the fluid containing MGCC processed at 700 °C, the temperature of the magnetic fluid did not reach the threshold value of 43 °C in 600 s. This reduction in heating efficiency of MGCC processed at T_A> 600 °C can be attributed to the reduction in magnetite phase percentage and appearance of hematite phase in these MGCC samples. The findings from DLS studies along with the magnetic parameters suggest that both relaxation and hysteresis mechanisms contribute to the induction heating process in these fluids.

The *SAR* and *ILP* values of fluids containing MGCC nanopowder processed at different T_As were estimated by the BLM method and the same are displayed in Figure 7.10. As the fluid concentration of MGCC processed at 550 °C was raised from 1 to 5 mg/ml, the *SAR* values exhibited a decline from 93 W/g to 35 W/g. Similar trend was observed for all fluids containing MGCC processed at other T_As too. The MGCC fluid with the lowest concentration displayed the highest *SAR*. This is attributed to the dipolar interaction among magnetic particles suspended within the fluid. *SAR* values initially increased for fluids containing MGCC nanopowder processed at 600 °C and then decreased for other fluids. The maximum *SAR* of 97 W/g was found for 1 mg/ml fluid containing MGCC processed at 600 °C. Moreover, the *SAR* value decreased as the fluid concentration was increased from 1 to 5 mg/ml. *SAR* decreased from 97 W/g to 53 W/g for fluids containing MGCC processed from 600 °C to 700 °C. The maximum *ILP* of 1.8 nHm^2kg^{-1} was achieved in the 1 mg/ml fluid containing MGCC processed at 600 °C. *ILP*

variation with samples followed the same trend as observed for *SAR*. *ILP* of fluids containing 1 mg/ml of MGCC processed at 550 °C, 600 °C, and 650 °C are 1.7 nHm^2kg^{-1}, 1.8 nHm^2kg^{-1} and 1.1 nHm^2kg^{-1}, respectively. The *ILP* values of these fluids, which surpass the *ILP* value (=1.0 nHm^2kg^{-1}) of FluidMag-CT, a commercially available magnetic fluid for MH. Interestingly, the maximum *SAR* was found at the lowest concentration of MGCC processed at 600 °C. This intriguing result can be understood with the help of narrowest colloidal size distribution of aqueous MGCC with 1 mg/ml concentration. Since wider colloidal size reduces the heating capacity, the heating capacity of MGCC diminishes when processed above 600 °C.

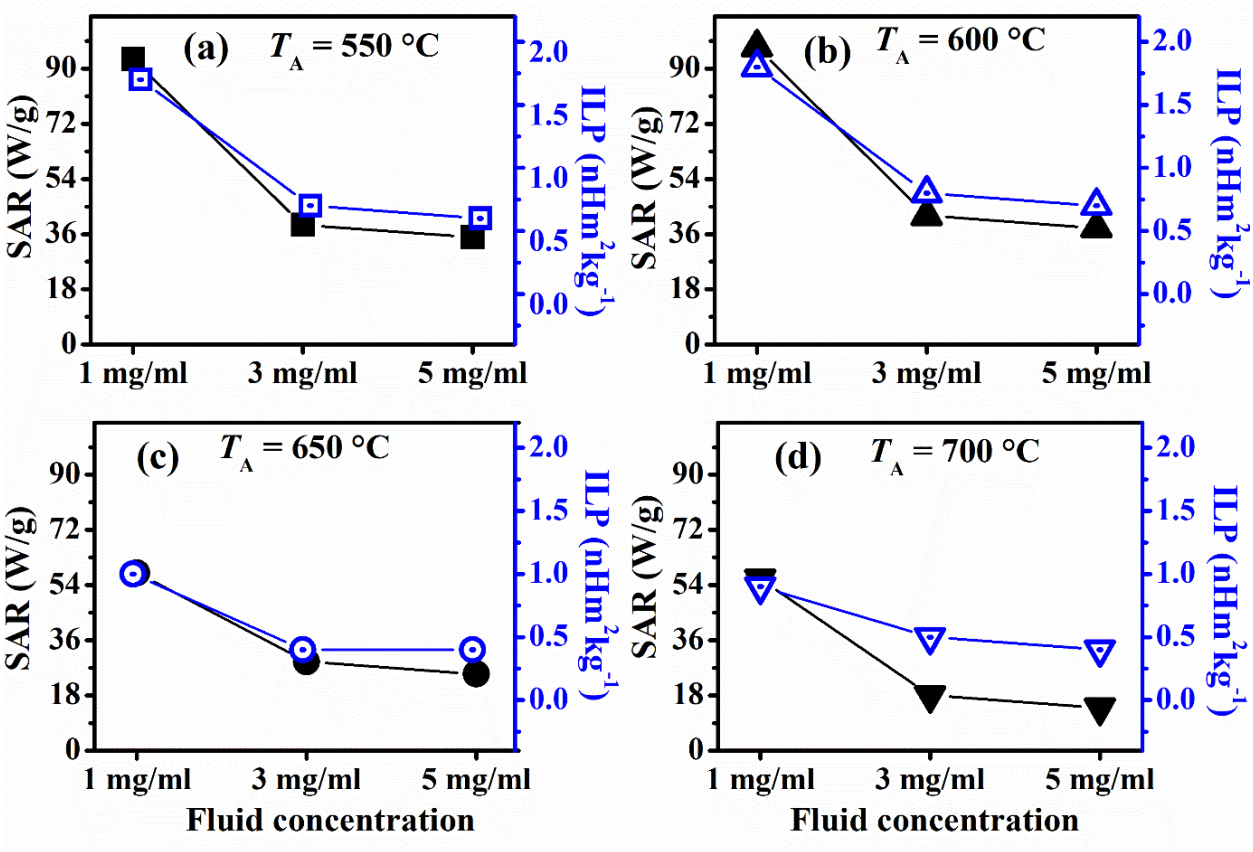

Figure 7.10: Estimated *SAR* and *ILP* values of fluids containing MGCC nanopowder processed at (a) T_A = 550 °C, (b) T_A = 600 °C, (c) T_A = 650 °C, and (d) T_A = 700 °C using BLM.

7.9. *In vitro* bioactivity assessment

7.9.1. Ion exchange

The ion exchange mechanism is responsible for the rapid rise in pH values in SBF during the initial days of immersion as illustrated in Figure 7.11. Once the discharged ions reach saturation, the pH value as saturates. After soaking for 11 days, the MGCC nanopowder processed at 550 °C, 600 °C, 650 °C, and 700 °C showed increase in pH from 7.40 to 8.05, 8.08, 8.20, and 8.29, respectively.

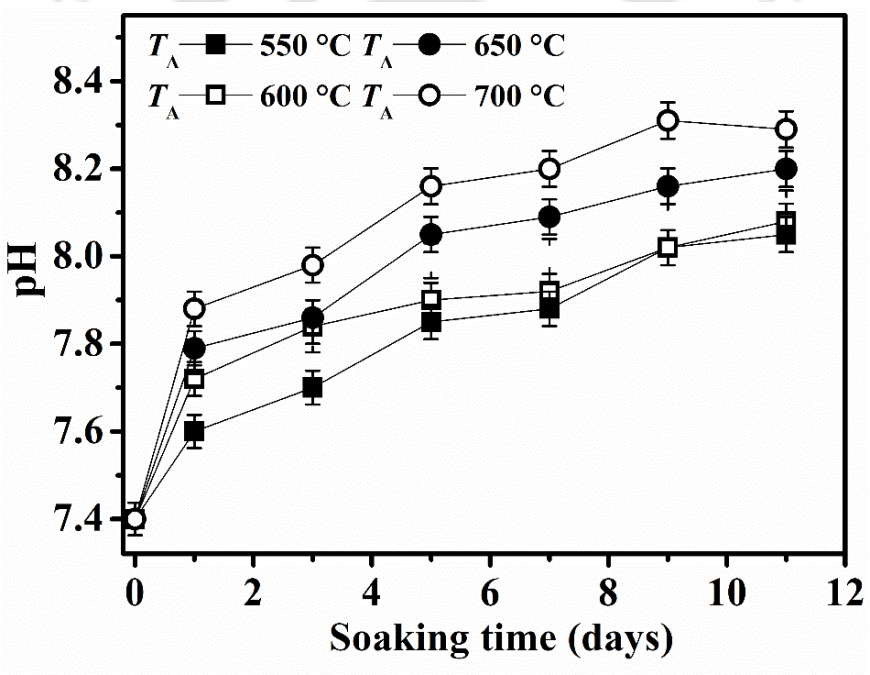

Figure 7.11: Change in pH of SBF with immersion time of different MGCC pellets.

The increasing pH levels observed in the MGCC immersed in SBF suggest that all MGCC samples exhibit bioactivity. However, a comparative analysis of pH curves at different samples reveals an initial increase in MGCC processed at higher T_A. The dominance of the combeite phase at higher T_A, which favours effective crystallization and growth of the HAp layer on the surface of MGCC, is considered to be the prominent factor for the upward trend in pH

value [KOKU2006]. This, in turn, facilitates the deposition of a HAp surface layer by enhancing the ionic activity of the fluid. As the T_A is raised from 550 °C to 700 °C, the swift elevation in the pH of SBF favours the nucleation of the HAp surface layer over the MGCC sample. It is to be noted that iron ions do not directly contribute to the pH of SBF, but their indirect influence is acknowledged [ARCO2003a]. The data in Table 7.01 illustrate a sharp increase in the combeite phase upon heat treatment at 700 °C. In summary, the overall increase in the pH of SBF with varying T_A suggests an enhancement in the bioactivity of MGCC processed at higher T_A.

7.9.2. Surface apatite layer formation

The GI-XRD patterns of MGCC pellets captured after immersion at regular intervals from 0 to 5 days of immersion are showcased in Figure 7.12 (a–d). The appearance of a new crystalline phase in the XRD pattern upon immersion in SBF indicates the formation of a crystalline layer on the surface of the MGCC pallets.GI-XRD patterns of the MGCC pellets show peaks at 2θ values of ~26° and ~32°, corresponding to the reflections from (002) and (112) planes of HAp (ICDD 74-0565) after 5 days of immersion. All MGCC samples exhibit bioactivity as evidenced by the deposition of the HAp layer in SBF and the concurrent rise in pH.

The FESEM images of the surface of MGCC pellets treated with SBF are displayed in Figure 7.13. These images visually confirm the development of a HAp surface layer. The HAp layer's development becomes more pronounced with an increase (a) in soaking time from 1 to 5 days of each sample and (b) processing temperature of the MGCC. Thus, a noticeable variation in the coverage of the HAp layer over the MGCC sample surface is observed with varying soaking times and T_A values. These findings collectively indicate that MGCC samples processed at all $T_A$values exhibit bioactive nature.

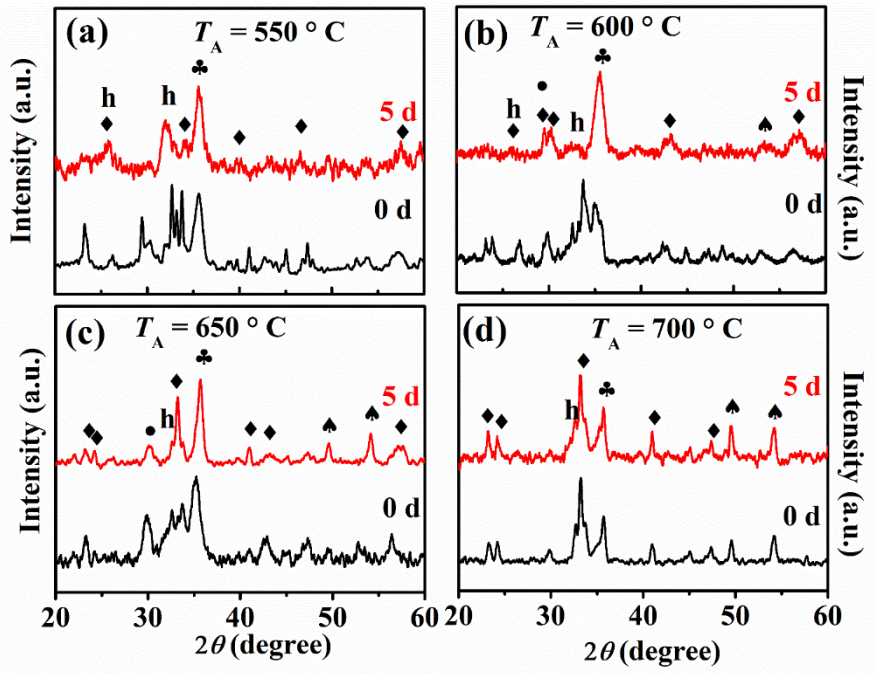

Figure 7.12: GI-XRD patterns of SBF treated MGCC processed at (a) 550 °C, (b) 600 °C, (c) 650 °C, and (d) 700 °C. Symbols ♦, ♣, ♠, •, and h represent combeite, magnetite, hematite, sodium nitrate and HAp phases, respectively.

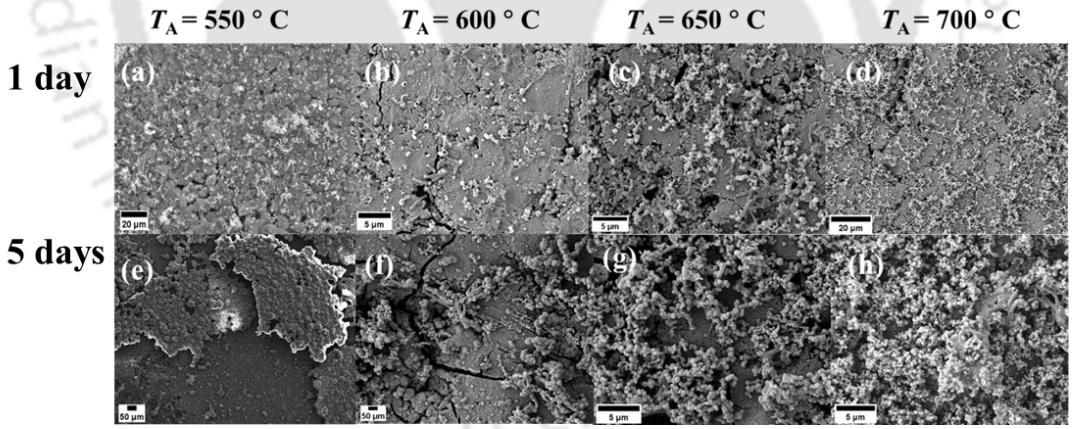

Figure 7.13: FESEM micrographs of MGCC after soaking in SBF for 1 and 5 days.

7.10. Summary

- The magnetic and bioactive properties of MGCC nanopowder can be tuned through controlled heat treatment in the temperature range of 550 to 700 °C.

- M_s of MGCC nanopowder gradually decreases as the processing temperature is increased beyond 550 °C, due to the conversion of magnetite into hematite.
- MGCC processed at 600 °C exhibited the narrowest colloidal size distribution and superior overall magnetic and induction heating properties.
- *In vitro* bioactivity assessments of MGCC nanopowders processed at all T_A values revealed their bioactive nature.
- Substituting MNP for CaO in the 45S5 composition followed by heat treatment at 600 °C for 1 h makes MGCC nanopowder an excellent thermoseed for MH in cancer therapy.

Chapter 8

Conclusions and scope for future work

The key discoveries made, and conclusions drawn in this thesis work on the structural, magnetic and bioactive characteristics of the sol-gel derived iron oxide / MNP-substituted 45S5 bioglass-ceramic nanopowders are highlighted in this chapter. Future directions of research and development in these areas have also been pointed out in this chapter.

8.1. Conclusions

The primary objective of this thesis is to develop a functional bioglass-ceramic capable of targeting bone cancer cells using MH therapy, while simultaneously promoting the healing and regeneration of normal cells and tissues close to the treatment site. To achieve this goal, various challenges have been addressed in this study. Chapters 3 to 7 of the thesis highlight the notable features observed in synthesized magnetic bioglass-ceramic nanopowders. The following are the major key points emanating from this thesis work and their implications:

- Chapter 3 of this thesis addresses the prevalent, yet unresolved challenges encountered in stabilizing the glassy state without compromising on the Na_2O content in sol-gel derived 45S5 nanopowders, which is primarily responsible for the superior bioactivity of the 45S5 composition. Controlled heat treatment of the as-synthesized revealed that the vitreous state could be maintained for a maximum amount of 12 wt.% Na_2O, by heat treating the as-synthesized powders at 700 °C for 2 h.

- Chapters 4 and 5 focus on adopting two strategies to enhance the magnetic properties of sol-gel derived 45S5 composition for applications involving bone regeneration and MH by incorporating iron oxide and MNP into the bioglass-ceramic. Two series of magnetic bioglass-ceramics have been prepared by systematically introducing iron oxide and MNP in the place of SiO_2 in 45S5 composition. In the first strategy, a heat treatment recipe was

formulated to dissolve sodium nitrate completely and crystallize desired amounts of magnetite and hematite. The relative crystalline phase percentages played a decisive role in identifying the best M_s values of 0.82 and 1.54 emu/g, achieved with 10 wt.% and 15 wt.% iron oxide, respectively. Additionally, in the second strategy, a small percentage of sodium nitrate was allowed to remain at the cost of preventing the magnetite to hematite by appropriate heat treatment process. Interestingly, the maximum M_s achieved was 14.01 emu/g for 10 wt.% MNP in 45S5 bioglass-ceramic. The maximum heat absorption capacity of both iron oxide and MNP variants in 45S5 bioglass-ceramic was evaluated in terms of *ILP*, which was found to be 1.24 and 1.82 nHm^2kg^{-1}, respectively. Bioglass-ceramics containing up to 10 wt.% iron oxide or MNP were not toxic as revealed by viability tests with MG-63 bone cells. However, the 45S5 bioglass-ceramic with 10% MNP was found to be superior for MH, as it offers higher M_s, *ILP*, and cell viability values.

- After recognizing the potential use of the MNP variant in 45S5 bioglass-ceramics, 8 wt.% MNP was chosen in chapter 6 to optimize the substitution site. MNP was substituted for the glass former (SiO_2) and the two glass-modifiers (CaO or Na_2O). Surprisingly, it was observed that 8 wt.% MNP substitution for CaO exhibited comparable M_s and *ILP* values to 10 wt.% MNP substitution for SiO_2 under the same heat treatment conditions, while maintaining an acceptable range of MG-63 osteoblast cell viability. This finding encourages one to explore MNP substitution for CaO in 45S5 composition more to further enhance the induction heating and bioactive qualities of this bioglass-ceramic. Chapter 7 expanded this work by exploring different heat treatment temperatures, resulting in a combination of magnetite, combeite, sodium nitrate and a small amount of hematite (~6%) and ended up by realizing M_s values compared to the 10 wt.% MNP variants with SiO_2. Even with 8 wt.% MNP substitution for CaO followed heat treatment

at 600 °C, the magnetic bioglass-ceramic showcased a biomaterial that surpasses the *ILP* value of commercially available FluidMag-CT (= 1.0 nHm^2kg^{-1}).

8.2. Scope for future work

After five decades since the discovery of MH therapy for bone cancer cells, no bioglass-ceramic has been found to effectively destroy cancer cells without causing any side effects. This work represents a step forward, focusing on primary investigations to broaden the application of magnetic 45S5 bioglass-ceramic for effective MH therapy in bone cancer therapy. Limited time has constrained further advancements in studying these bioglass-ceramics, which could be explored by future research to develop them into efficient implant materials. The following aspects suggestions are placed to take this work forward:

- Having found that the substitution of the 8 wt.% MNP variant provides superior results, it suggests that substitution beyond 8 wt.% MNP could be attempted to achieve even better properties for MH.
- The heating capacity was tested for a limited time under a fixed alternating magnetic field and frequency, which are well below the accepted safety limits for patients. By varying these parameters, it may be possible to achieve a higher efficacy in heating capacity while remaining within the safety limits.
- The heat absorption capacity of the magnetic bioglass-ceramics was measured in an aqueous solvent, which is comparable to the *in vitro* environment. However, in the presence of cells and tissues near the cancer site, additional heat absorption occurs. Therefore, evaluating the absorption capacity under *in vivo* conditions would provide more confidence in adapting these materials as implants.
- *In vitro* bioactivity, bone cell viability, and heating capacity studies are conducted separately to understand the behavior of these bioglass-ceramics. However, these aspects

collectively influence the performance of these bioglass-ceramics in *in vivo* conditions. Therefore, it is crucial to conduct all these investigations in *in vivo* environment to comprehensively evaluate the overall performance of these bioglass-ceramics.

References

[ABE02010] T. Abe, T. Kisi, A. Yasumori, *J. Phys. Conf. Ser.,* 232, (2010), 012018.

[ADAM2013] L.A. Adams, E.R. Essien, R.O. Shaibu, A. Oki, *J. Glas. Ceram.*, 3, (2013) 11–15.

[ADHI2023] J. Adhikari, S. Dasgupta, A. Barui, M. Ghosh, P. Saha, *J. Sol-gel Sci. Technol.,* 106, (2023), 757-774.

[AGRA2023] R. Agrawal, A. Kumar, M.K. Mohammed, S. Singh, *J. Zhejiang Univ. Sci.,* (2023), 1-16.

[AHMA2018] A. Ahmad, H. Bae, I. Rhee, *J. Korean Phys. Soc.,* 73, (2018), 125–129.

[AJAY2007] A.K. Gupta, R.R. Naregalkar, V.D. Vaidya, *Nanomed.,* 2, (2007), 23.

[ALBO2008] C. Albon, D. Muresan, R.E. Vandenberghe, S. Simon, *J. Non. Cryst. Solids.,* 354, (2008), 4603–4608.

[ALTE2021] S.S. Alterary, A. Alkhamees, *Green Process. Synth.,* 10, (2021), 384–391.

[ANAN2023] V. Anand, A. Chaudhary, Meenakshi, G. Bhatia, P. Heera, S. Thakur, *J. Asian Ceram. Soc.*11, (2023), 526-534.

[ANDE1992] O.H. Andersson, *J. Mater. Sci.: Mater. Med.,* 3, (1992), 326–328.

[ANAN2016] V. Anand, K. Singh, K. Kaur, H. Kaur, G. Bhatia, S. Singh, D.S. Arora, *J. Am. Ceram. Soc.,* 99, (2016), 3632–3638.

[ANTU2019] A. Antuzevics, *Experimental Methods in the Physical Sciences, Academic Press,* 50, (2019), 161-190.

[ARCO2002] D. Arcos, R.P. Del Real, M. Vallet-Regí, *Biomater.,* 23, (2002), 2151–2158.

[ARCO2003a] D. Arcos, R.P. Del Real, M. Vallet-Regí, *J. Biomed. Mater. Res. - Part A.,* 65, (2003), 71–78.

[ARCO2003b] D. Arcos, D.C. Greenspan, M. Vallet-Regí, *J. Biomed. Mater. Res. - Part A* 65A, (2003), 344–351.

[ARDE1997] I. Ardelean, M. Peteanu, S. Filip, V. Simon, G. Györffy, *Solid State Commun.* 102, (1997), 341–346.

[ARJM2012] N. Arjmandi, W.V. Roy, L. Lagae, G. Borghs, *Anal. Chem.* 84, (2012), 8490–8495.

[ARST2007] H. Arstila, E.V.H. Arstila, E. Vedel, L. Hupa, M. Hupa, *J. Eur. Ceram. Soc.,* 27, (2007), 1543.

[ASTH2014] G. Asthana, S. Bhargava, *Sch. J. App. Med. Sci.,* 2, (2014), 3231-3237.

[ASUH2011] S. Asuha, B. Suyala, X. Siqintana, S. Zhao, *J. Alloys Compd.,*509, (2011), 2870-2873

[BADA2012] P. Badanayak, J.V. Vastrad, *J. Pharm. Innov.,* 10, (2012), 1023-1027.

[BAIK2008] Baikousi, S. Agathopoulos, I. Panagiotopoulos, A.D. Georgoulis, M. Louloudi, and M.A. Karakassides, *J. Sol-Gel Sci. Technol.,* 47, (2008), 95–101.

[BAIN2018] F. Baino, S. Hamzehlou, S. Kargozar, *J. Funct. Biomater.,* 9, (2018), 25.

[BAIN2019] F. Baino, E. Fiume, *Mater. Lett.,* 245, (2019), 14-17.

[BAND1980] A.K. Bandyopadhay, J. Zarzycki, P. Auric, J.Chappert, *J. Non. Cryst. Solids.,* 40, (1980), 353–368.

[BANS2023] P.V. Bansode, S.D. Pathak, M.B. Wavdhane, V. Lohate, *Inter. J. Den. Med. Sci. Res.,* 5, (2023), 610-616.

[BIZA2020] D. Bizari, A. Yazdanpanah, F. Moztarzadeh, *Mater. Chem. Phys.,* 241, (2020), 122439.

[BLIT1990] C.A. Blitterswijk, S.C. Hesseling, J.J. Grote, H.K. Korerte, K. Groot, *J. Biomed. Mater. Res.,* 24, (1990), 433-453.

[BONF1995] W. Bonfield, *In Bioceramics 8, ed. J. Wilson, D. Greenspan & L. L. Hench. Elsevier Science, Oxford,* (1995), 3755382.

[BORR1981] N.F. Borrelli, A.A. Luderer, J.N. Panzarino, *Eur. Pat. Appl.,* 2, (1981), 20040512.

[BOSE2018] S. Bose, D. Ke, H. Sahasrabudhe, A. Bandyopadhyay, *Prog. Mater. Sci.,* 93, (2018), 45-111.

[BRET2005] O. Bretcanu, S. Spriano, E. Verne, M. Coisson, P. Tiberto, P. Allia, *Acta Biomater.,* 1, (2005), 421-429.

[BRET2006a] O. Bretcanu, E. Verné, M. Cöisson, P. Tiberto, P. Allia, *J. Magn. Magn. Mater.,* 305, (2006), 529–533.

[BRET2006b] O. Bretcanu, S. Spriano, C.B. Vitale, E. Verné, *J. Mater. Sci.,* 41, (2006), 1029–1037.

[BURZ1979] E. Burzo, *Phys Magn Phenom. Romania.,* 1, (1979), 79.

[CACC2012] I. Cacciotti, M. Lombardi, A. Bianco, A. Ravaglioli, L. Montanaro, *J. Mater. Sci: Mater. Med.,* 23, (2012), 1849–1866.

[CAI02014] Y. Cai, *Brigham Young University.* (2014), 3982

[CAI02020] W. Cai, M. Guo, X. Weng, W. Zhang, G. Owens, Z. Chen, *Mater. Sci. Eng. C.,* 112, (2020), 110900.

[CANN2021] M. Cannio, D. Bellucci, J.A. Roether, D.N. Boccaccini, V. Cannillo, *Mater.,* 14, (2021), 1–25.

[CAO01996] W. Cao, L.L. Hench, *Ceram. Int., 22*, (1996), 493-507.

[CART2005] D. Carta, D.M. Pickup, J.C. Knowles, M.E. Smith, R.J. Newport, *J. Mater. Chem.,* 15, (2005), 2134–2140.

[CATT2013] R. Catteaux, I. Lebecq, F. Désanglois, F. Chai, J.C. Hornez, S. Hampshire, C. Follet, *Chem. Eng. Res. Des.,* 91, (2013), 2420-2426.

[CHAJ2015] S. Chajri, S. Bouhazma, S. Herradi, H. Barkai, S. Elabed, S.I. Koraichi, B.E. Bali, M. Lachkar, *J. Mater. Environ. Sci.,* 6, (2015), 1882-1897.

[CHAR2015] T. Charoensuk, W. Limphirat, C. Sirisathitkul, W. Tangwatanakul, P. Jantaratana, U. Boonyang, *Nanomater. Nanotechnol.,* 5, (2015), 34.

[CHAR2016] T. Charoensuk, C. Sirisathitkul, W. Tangwatanakul, S. Pinitsoontorn, U. Boonyang, *J. Ceram. Sci. Technol.,* 7, (2016), 139–144.

[CHEN2010] Q.Z. Chen, Y. Li, L.Y. Jin, J.M. Quinn, P.A. Komesaroff, *Acta Biomater.,* 10, (2010), 4143–4153.

[CHEN2014] J. Chen, H. Zhang, X. Zhang, G. Yang, L. Lu, X. Lu, C. Wan, K. Ijiri, H. Ji, Q. Li, *Mol. Biol. Rep.,* 4, (2014), 2161-2169.

[CHON2023] E.J. Chong, J.W. Ng, P.C. Lee, *Bio. Integr.,* 4, (2023), 54-61.

[CLAR1974] A.E. Clark, *Gainesvile: Univ. Florida*, 1974. Dissertation.

[CULL1956] B.D. Cullity, S.R. Stock, Elements of X-ray diffraction, Third, Addision-*Wesley Publishing Company Inc., Massachusetts,* (1956).

[DANE2021] S.S. Danewalia, K. Singh, *Mater. Today Bio.,* 10, (2021), 100100.

[DATT2017] J. Datta, A. Dey, S.K. Neogi, M. Das, S. Middya, R. Jana, S. Bandyopadhyay, A. Layek, P.P. Ray, *Electronic and Magnetic Devices.,* 64, (2017), 1–7.

[DEAT2014] A.E. Deatsch, B.A. Evans, *J. Magn. Magn. Mater.,* 354, (2014), 163–72.

[DENI1989] H.W. Denissen, W. Kalk, A.A.H. Van Den Hoof, *J. Prosthe. Dent.,* 61, (1989), 706-712.

[DEY02016] T. Dey, A. Maljuk, D.V. Efremov, O. Kataeva, S. Gass, C.G.F. Blum, *Phys Rev B.,* 93, (2016), 1–7.

[DING2012] H.L. Ding, Y.X. Zhang, S. Wang, J.M. Xu, S.C. Xu, G.H. Li, *Chem. Mater.,* 24, (2012), 4572–4580.

[DOOS2011] A. Doostmohammadi, A. Monshi, R. Salehi, M.H. Fathi, Z. Golniya, A.U. Daniels, *Ceram. Int.,* 37, (2011), 2311-2316.

[DOWN1991] R.N. Downes, S. Vardy, T.E. Tanner, W. Bonfield, I*n Bioceramics 4, ed. W. Bonfield, G. W. Hastings & K. E. Tanner. Butterworth-Heinmann Ltd, Oxford, England*, (1991), 23-246.

[EBIS1990] Y. Ebisawa, T. Kokubo, K. Ohura, T. Yamamuro, *Biomater.,* 24, (1990), 721-734.

[EBIS1992] Y. Ebisawa, T. Kokubo, K. Ohura, T. Yamamuro, *J. Mater. Sci. Med.,* 4, (1992), 225-232.

[FADL2019] A. Fadli, K. Komalasari, A. Adnan, I. Iwantono, Rahimah, A.S. Addabsi, *IOP Conf. Ser.: Mater. Sci. Eng.,* 622, (2019), 012013.

[FAUR2015] J. Faure, R. Drevet, A. Lemelle, N. Ben Jaber, A. Tara, H. El Btaouri, H.A. Benhayoune, *Mater. Sci. Eng. C.,* 47, (2015), 407–412.

[FELI2017] L.L. Félix, J.A.H. Coaquira, M.A.R. Martínez, G.F. Goya, J. Mantilla, M.H. Sousa, L.D.L.S. Valladares C.H.W. Barnes, P.C. Morais, *Sci. Rep.,* 7, (2017), 1–8.

[FERR2020] S. Ferraris, S. Yamaguchi, N. Barbani, M. Cazzola, C. Cristallini, M. Miola, E. Vernè, S. Spriano, *Acta Biomater.,* 102, (2020), 468-480.

[FILH1996] O.P. Filho, G.P. LaTorre, L.L. Hench, *J. Biomed. Mater. Res.,* 30, (1996), 509-514.

[FIUM2020] E. Fiume, C. Migneco, E. Verné, F. Baino, *Mater.,* 13, (2020), 540.

[FONE1959] S. Foner, *Rev. Sci. Inst.* 30, (1959), 548.

[FOPA2020] R. Fopase, V. Saxena, P. Seal, J.P. Borah, L.M. Pandey, *Mater. Sci. Eng. C.,* 116, (2020), 111163.

[FORO2021] R. Foroutan, S.J. Peighambardoust, S. Hemmati, A. Ahmadi, E. Falletta, B. Ramavandi, C. Bianchi, *RSC. Advan.,* 11, (2021), 27309-27321.

[FU002011] Q. Fu, E. Saiz, M.N. Rahaman, A.P. Tomsia, *Mater. Sci. Eng. C.,* 31, (2011), 1245–1256.

[FU002020] S. Fu, Q. Fang, A. Li, Z. Li, J. Han, X. Dang, W. Han, *Sci. J. Energy Eng.,* 9, (2020), 80-100.

[FULD2010] S. Fulda, A.M. Gorman, O. Hori, A. Samali, *Int. J. Cell Biol.,* 2010, (2010), 20182529.

[GALG1990] P.N. Galgut, I.M. Waite, S.M.B. Tinkler, *Clin. Mater.,* 6, (1990), 150-121.

[GAO02023] Y. Gao, M.A. Seles, M. Rajan, *Review Adv. Mater. Sci.,* 62, (2023), 20220318.

[GERH2010] L.C. Gerhardt, A.R. Boccaccini, *Mater.,* 3, (2010), 3867-3910.

[GHAN2001] A. El-Ghannam, E. Hamazawy, A. Yehia, *J. Biomed. Mater. Res.,* 55, (2001), 387-395.

[GILC1957] R.K. Gilchrist, R. Medel, W.D. Shorey, R.C. Hanselman, J.C. Parrott, C.B. *Taylor, Ann. Surg.,* 146, (1957), 596–606.

[GIRO2011] A.L. Girot, F.Z. Mezahi, M. Mami, H. Oudadesse, A. Harabi, M.L. Floch, *J. Non-Cryst. Solids.,* 357, (2011), 3322-3327.

[GOH02015] Y.F. Goh, M. Akram, A.Z. Alshemary, R. Hussain, *Mater. Sci. Eng. C.,* 53, (2015), 29–35.

[GROO1983] K. de Groot, *CRC Press, Boca Raton, FL.,* 1, (1983).

[GROS1993] U.M. Gross, C. Muller-Mai, C. Voigt, *Wilson World Scientific, London,* (1993), 105-123.

[HENC1982a] L.L. Hench, E.C. Ethridge, *Academic Press, New York.,* (1982).

[HENC1982b] L.L. Hench, A.E. Clark, *CRC Press, Florida,* (1982).

[HENC1982c] L.L. Hench, *Williams, D.F. cd. Boca Raton: CRC Press,* 1, (1982), Chapter 4.

[HENC1990] L.L. Hench, J. K. West, *Chem. Rev.,* 90, (1990), 33.

[HENC1991] L.L. Hench, *J. Am. Ceram. Soc.,*74, (1991), 1487–1510.

[HENC1998a] L.L. Hench, D.L. Wheeler, D.C. Greenspan, *J. Sol-Gel Sci. Technol.*, 13, (1998), 245-250.

[HENC1998b] L.L. Hench, *J. Am. Ceram. Soc.,* 81, (1998), 1705–1728.

[HENC2002] L.L. Hench, J.M. Polak, *Scie.,* 295, (2002), 1014–1017.

[HENC2006] L.L. Hench, *J. Mater. Sci: Mater. Med.,* 17, (2006), 967-978.

[HERN2006] E. Ruiz-hernandez, M. Serrano, D. Arcos, M. Vallet-Regi, *J. Biomed. Mater. Res. Part A.,* 79, (2006), 533–543.

[HOLA1983] W. Holand, J. Naumann, W. Vogel, J. Gummael, *Naturwiss,* 32, (1983), 571.

[HOLA1993] W. Holand, W. Vogel, *Wilson World Scientific, London,* (1993), 125-137.

[HOU02021] Y. Hou, Y. Wang, G.H. Zhang, K.C. Chou, *J. Eur. Ceram. Soc.,* 41, (2021) 5201–5213.

[HUAN2013] F. Huang, Z. Wang, X. Lu, J. Zhang, K. Min, W. Lin, R. Ti, T. Xu, J. He, C. Yue, J. Zhu, *Sci. Rep.,* 3, (2013), 2907.

[HUI02011] C. Hui, C. Shen, J. Tian, L. Bao, H. Ding, C. Li, Y. Tian, X. Shi, H.J. Gao, *Nanoscale.,* 3, (2011), 701–705.

[HUO02020] W. Huo, X. Zhang, E. Tervoort, S. Gantenbein, J.Yang, A.R. Studar, *Adv. Funct. Mater.,* 30, (2020), 2003550.

[HUSL2017] D.J. Hulsen, N.A. van Gestel, J.A.P. Geurts, J.J. Arts, *Woodhead Publishing: Sawston, UK,* (2017), 9780081002421.

[HUSS2022] K.I. Hussein, A.M. Al-Syadi, M.S. Alqahtani, N. Elkhoshkhany, H. Algarni, M. Reben, E.S. Yousef, *Mater.,* 15, (2022), 2403.

[IAVE2015] I. A. Vedernikova, *Rev. J. Chem.,* 5, (2015), 256.

[ILON1988] G. Ilonca, I. Ardelean, O. Cozar, *J. Phys. Colloq.,* 49, (1988), 1107-1108.

[ISLA2017] M.T. Islam, R.M. Felfel, E.A. Neel, D.M. Grant, I. Ahmed, K.M.Z. Hossain, *J. Tissue Eng. Regen. Med.,* 8, (2017), 1 –16.

[JEON2019] J. Jeong, J.H. Kim, J.H. Shim, N.S. Hwang, C.Y. Heo, *Biomater. Res.,* 23, (2019), 30675377.

[JI002018] P.T. Ji, Y.Y. Wang, M.R. Zhang, B. Li, G.X. Zhang, *Int. J. Appl. Ceram. Technol.,* 15, (2018), 1261–1267.

[JIAN2011] Y. Jiang, J. Ou, Z. Zhang, Q.H. Qin, *J. Mater. Sci. Mater. Med.,* 22, (2011), 721–729.

[JIAN2020] C. Jiang, S. Cai, L. Mao, Z. Wan, *Mater.,* 13, (2020), 140.

[JIWE2001] Z. Jiwe, Y. Xi, Z. Liangying, *Ferroelectrics.,* 262, (2001), 25-30.

[JOHN2021] S.P. John, J. Mathew M, *J. Alloys Compd.,* 869, (2021), 159242.

[JONE2013] J.R. Jones, *Acta Biomater.,* 9, (2013), 4457–4486.

[JONE2015] J.R. Jones, *J. Biomater.*, 23, (2015), 53–82.

[JOY02019] N.O. Joy-anne, Y. Su, X. Lu, P.H. Kuo, J. Du, D. Zhu, *Bioact. Mater.,* 4, (2019), 261-270.

[JUNG2000] J.H. Jung, Y. Ono, S. Shinka, *Chem. Int. Ed.,* 10, (2000), 1862-1865.

[KANG2022] M.A. Kang, J. Fang, A. Paragodaarachchi, K. Kodama, D. Yakobashvili, Y. Ichiyanagi, H. Matsui, *Nano Lett.,* 22, (2022), 8852–8859.

[KARI2018] A.Z. Karimi, E. Rezabeigi, R.A.L. Drew, *J. Non-Crystal. Sol.,* 502, (2018), 176-183.

[KAUR2016] G. Kaur, G. Pickrell, N. Sriranganathan, V. Kumar, D. Homa, *J. Biomed. Mater. Res. - Part B Appl. Biomater.,*104, (2016), 1248–1275.

[KAUR2019] G. Kaur, V. Kumar, F. Baino, J.C. Mauro, G. Pickrell, I. Evans, O. Bretcanu, *Mater. Sci. Eng. C.,* 104, (2019), 109895.

[KIM02013] E.J. Kim, S.Y. Bu, M.K. Sung, M.K. Choi, *Biol. Trace. Elem. Res.,* 152, (2013), 105–112.

[KOKS2001] Y.A. Koksharov, S.P. Gubin, I.D. Kosobudsky, G.Y. Yurkov, D.A. Pankratov, L.A. Ponomarenko, M.G. Mikheev, M. Beltran M, Y. Khodorkovsky, A.M. Tishin, *Phys. Rev. B*, 63, (2001), 012407.

[KOKU1990a]T. Kokubo, *Biomater.,* 12, (1990), 155–163.

[KOKU1990b]T. Kokubo, *J. Jpn. Soc Powder Powder Metall.,* 37, (1990), 324–328.

[KOKU2006] T. Kokubo, T. Hiroaki, *Biomater.,* 27, (2006), 2907-2915

[KOMA1980] T. Komatsu, N. Soga, *J. Chem. Phys.,* 72, (1980), 1781–1785.

[KOML2002] V.S. Komlev, S.M. Barinov, *J. Mater. Sci. Mater. Med.,* 13, (2002), 295–299.

[KUMA1994] B. Kumar, C.H. Chen, *J. Appl. Phys.,* 75, (1994), 6760–6762.

[KUMA2018] R. Kumar, A. Chauhan, S.K. Jha, B.K. Kuanr, *J. Mater. Chem. B.,* 6, (2018), 5385–5399.

[LACE1986] W.R. Lacefield, L.L. Hench, *Biomater.,* 7, (1986), 104-108.

[LADA2012] A.K. Ladavos, A.P. Katsoulidis, A. Iosifidis, K.S.Triantafyllidis, T.J. Pinnavaia, P.J. Pomonis, *Microporous Mesoporous Mater.,* 151, (2012), 126-133.

[LAFT2020] S.H. Lafta, *J. Supercond. Nov. Magn.,* 33, (2020), 3765–3772.

[LANG1993] R. Langer, J.P. Vacanti, *Science.* 260, (1993), 920–926.

[LANI2019] O.L. Lanier, O.I. Korotych, A.G. Monsalve, D. Wable, S. Savliwala, N.W.F. Grooms, C. Nacea, O.R. Tuitt, J. Dobson, *Int. J. Hyperth.,* 36, (2019), 687–701.

[LEGR1991] R.Z. LeGeros, H. Myers. *S. Karger, Basel, Switzerland,* 15, (1991)

[LEVE2005] T. Leventouri, A.C. Kis, J.R. Thompson, I.M. Anderson, *Biomater.,* 26, (2005), 4924–4931.

[LI001991] R. Li, A.E. Clark, L.L. Hench, *J. Appl. Biomater.,* 2, (1991), 231-239.

[LI002006] M. Li, M. J. Mondrinos, X. Chen, M R. Gandhi, F.K. Ko, P.I. Lelkes, *J. Biomed. Mater. Res. Part A.,* 79, (2006), 963–973.

[LI002007] J.P. Li, H. Kajiya, F. Okamoto, A. Nakao, T. Iwamoto, K. Okabe, *Endocrinology*, 148, (2007), 2116-2125.

[LI002015] W. Li, J. Zhou, Y. Xu, *Biomed. Reports.,* 3, (2015), 617–620.

[LIST1867] J. Lister, *Br. Med. J.,* 351, (1867), 246–248.

[LIU02006] X. Liu, M.D. Kaminski, Y. Guan, H. Chen, H. Liu, A.J. Rosengart, *J. Magn. Magn. Mater.,* 306, (2006), 248-253.

[LIU02012] J.A. Liu, M.M. Zhang, X.N. Yang, W. He, *Adv. Mater. Res.,* 535-537, (2012), 855-860.

[LIU02020] S.S. Liu, M. Li, J.M. Wu, A.N. Chen, Y.S. Shi, C.H. Li, *Ceram. Int.,* 46, (2020), 4240-4247.

[LOBE1995] K. Lobel, *Chapman and Hall, London,* (1995), 215-236.

[LOH02023] Z.W. Loh, M.H.M. Zaid, M.M.A. Kechik, Y.W. Fen, K.M. Amin, W.M. Cheong, *J. Mater. Res. Tech.,* 24, (2023), 3815-3825.

[LOPE1999] M.A. Lopes, F.J. Monteiro, J.D. Santos, A.P. Serro, B. Saramago, *J. Biomed. Mater. Res.,* 45, (1999), 370–375.

[LOVE1971] D. Loveridge, S. Parke, *Phys. Chem. Glas.,* 12, (1971), 19–27.

[LU002000] H.H. Lu, S.R. Pollack, P. Ducheyne, *J. Biomed. Mater. Res.,* 51, (2000), 80-87.

[LUCA2011] A. Lucas-girot, F.Z. Mezahi, M. Mami, H. Oudadesse, A. Harabi, M.L. Floch, *J. Non-Crystal. Sol.,* 357, (2011), 3322–3327.

[LUDE1983] A.A. Luderer, N.F. Borrelli, J.N. Panzarino, G.R. Mansfield, D.M Hess, J.L. Brown, E.H. Barnett, E.W. Hahn, *Radiat. Res.,* 94, (1983), 190–198.

[MADH2022] Madhavi, M. Kumar, J.R. Ansari, V. Kumar, S. Nagar, A. Sharma, *Metals.,* 12, (2022), 2145.

[MAHA2014] A. Mahajan, E. Ramana, *Recent Patents Mater. Sci.,* 7, (2014), 109–130.

[MAUR2020] I. Maurin, C. Vichery, J.M. Nedelec, *Appl. Mater. Interfaces,* 12 (2020) 47820−47830.

[MAZZ2021] E. Mazzoni, M.R. Iaquinta, C. Lanzillotti, C. Mazziotta, M. Maritati, M. Montesi, S. Sprio, A. Tampieri, M. Tognon, F. Martini, *Front.Bioeng. Biotechnol.,* 9, (2021), 613787.

[MCKE2021] L.W. McKeen, *William Andrew Publishing.*, 53, (2021), 9780323228053.

[MEKK2001] A. Mekki, *Phys. Status Solidi Appl. Res.,* 184, (2001), 327–333.

[MITR2018] V. Mitran, R. Ion, F. Miculescu, M.G. Necula, A.C. Mocanu, G.E. Stan, I.V. Antoniac, A. Cimpean, *Mater.,* 11, (2018).

[MONT2016] M. Montazerian, E.D. Zanotto, *J. Biomed. Mater. Res. - Part A.,* 104, (2016), 1231–1249.

[MOSM1983] *T.* Mosmann, *J. Immunol. Methods.* 65, (1983), 55–63

[MOST2021] A.A. Mostafa, M.M.H. El-Sayed, A.N. Emam, A.A. Abd-Rabou, R.M. Dawood, H. Oudadesse, *RSC Adva.,* 11, (2021), 25628-25638.

[MULL1957] Mullin, J. W., & Webb, K. L. (1957). *Analytical Chemistry*, 29(11), 1702-1706.

[MUSG2014] J.D. Musgraves, S. Danto, K. Richardson, (2014), 9780857093561.

[NEIL2018] E. O'Neill, G. Awale, L. Daneshmandi, O. Umerah, K.W. Lo, *Drug Discov. Today.,* 4, (2018), 879-890.

[NERE1991] R.M. Nerem, *Ann Biomed Eng.,* 91, (1991), 529–545.

[NIH0] https://www.nibib.nih.gov/science-education/science-topics/biomaterials.

[NIH02017] NIH, 2017. Biomaterials. https://www.nibib.nih.gov/science-education/science (2017)

[NIKM2019] A. Nikmah, A. Taufiq, A. Hidayat, *IOP Conf. Ser. Earth Environ. Sci.,* 276, (2019), 012046.

[OKUD2009] M. Okuda, M. Takeguchi, Ó.Ruairc, M. Tagaya, Y. Zhu, A. Hashimoto, N. Hanagata, W. Schmitt, T. Ikoma, *J. Electron Microsc. Tech.,* 59, (2009), 173-179.

[ONO01988] K. Ono, T. Yamamuro, T. Nakamura, Y. Kakutani, T. Kitsugi, K. Hyakuna, T. Kokubo, *J. Biomed. Mater. Res. 22,* (1988), 869-885.

[OPPE1998] A. Oppermann, M.J. Crimp, D.M. Bement, *J. Biomed. Mater. Res.,* 42, (1998), 412–416.

[ORGA1988] F. Orgaz-Orgaz, *J. Non-Cryst. Solids.,* 100, (1988), 115.

[OSS01983] C.J. Oss, D.R. Absolom, *Int. J. Clin. Transfus.,* 44, (1983), 183–190.

[OYAN2003] A. Oyane, H.M. Kim, T. Furuya, T. Kokubo, T. Miyazaki, T. Nakamura, *J. Biomed. Mater. Res.* 65, (2003), 188-195.

[PAND2021] M. Pandey, M. Singh, K. Wasnik, S. Gupta, S. Patra, P.S. Gupta, D. Pareek, N.S.N. Chaitanya, S. Maity, A.B.M. Reddy et al. *ACS Omega,* 6, (2021), 31615–31631.

[PANS2012] S. Panseri, C. Cunha, T.D. Alessandro, M. Sandri, G. Giavaresi, M. Marcacci, C.T. Hung, A. Tampieri, *J. Nanobiotech.,* 10, (2012), 1.

[PART2022] B.H. Parte, I. Rodrigo, J.G. Basoa, S.I. Correcher, C.M. Medina, J.J. Echevarría-Uraga, J.A. Garcia, F. Plazaola, I. García-Alonso, *Cancers.,* 14, (2022), 1–14.

[PAVI2014] L. Pavic, M.P.F. Graca, Z. Skoko, A. Mogu-Milankovic, M.A. Valente, *J. Am.*

Ceram. Soc., 97, (2014), 2517–2524.

[PAVA2019] P.M.V. Raja, A.R. Barron, Rice University via OpenStax CNX, (2019).

[PEIT2001] O. Peitl, E.D. Zanotto, L.L. Hench, *J. Non. Cryst. Solids.,* 292, (2001), 115–126.

[PEIT2012] O. Peitl, E.D. Zanotto, F.C. Serbena, L.L. Hench, *Acta Biomater.,* 8, (2012), 321–332.

[PIRA2013] H. Pirayesh, J.A. Nychka, *J. Am. Ceram. Soc.,* 96, (2013), 1643–1650.

[POPA2013] A. Popa, R. Stefan, M. Bosca, V. Dan, V. Pop, P. Pascuta*, AIP Conf. Proc.,* 1565, (2013), 250–254.

[PRAK2017] M. Prakasam, J. Locs, K. Salma-Ancane, D. Loca, A. Largeteau, L. Berzina-Cimdina, *J. Funct. Biomater.,* 8, (2017), 44.

[PROE2011] M.P. Proenca, C.T. Sousa, A.M. Pereira, P.B. Tavares, J. Ventura, M. Vazquez, J.P. Araujo, *Phys. Chem. Chem. Phys.,* 13, (2011), 9561–9567.

[PRYC2003] R.S. Pryce, L.L. Hench, *Key Eng. Mate.,* 240, (2003), 201-204.

[QIUH2015] Q. Yang, M. Gong, S. Cai, T. Zhang, J.T. Douglas, V. Chikan, N.M. Davies, P. Lee, I.Y. Choi, S.Ren, M.L. Forrest. *Ther. Deliv.,* 68, (2015), 1195-1210.

[RADA2011] S. Rada, A. Dehelean, M. Stan, R. Chelcea, E. Culea, *J. Alloys Compd.,* 509, (2011), 147–151.

[RAHA2011] M.N. Rahaman, D.E. Day, B.S. Bal, Q. Fu, S.B. Jung, L.F. Bonewald, A.P. Tomsia, *Acta Biomater.,* 7, (2011), 2355-2373.

[RAHA2020] M.S. Ur Rahman, M.A. Tahir,S. Noreen, M. Yasir, I. Ahmad, M.B. Khan, K.W. Ali, M. Shoaib, A. Bahadur, S. Iqbal, *RSC Adv.,*10, (2020), 21413–21419.

[RAJY2012] C. Rajyasree, P. Srinivasa Rao, P.M.V. Teja, A. Ramesh Babu, S. Yusub, D. Krishna Rao, *J. Non. Cryst. Solids.,* 358, (2012), 2597–2605.

[RAO02022] H.M. Rao, K. Rajkumar, V. Narayana, M. Akash, J. Sabu, R. Ramadoss, *J. Pharm. Negat. Results.,* 13, (2022), 7.

[RECK1994] R. Reck, *Laryngoscope,* 2, (1994), 1-54.

[REZA2014] E. Rezabeigi, P.M. Wood-Adams, R.A.L. Drew, *Mater. Sci. Eng. C.,* 40, (2014), 248–252.

[RING2020] H.L. Ring, A. Sharma, R. Ivkov, J.C. Bischof, *Int. J. Hyperth.,*37, (2020), 100–107.

[ROBE2020] A.P. Roberts, X. Zhao, D. Heslop, A. Abrajevitch, Y.H. Chen, P. Hu, Z. Jiang, Q. Liu, B.J. Pillans, *Geosci. Lett.,* 7, (2020).

[RUMP2012] K. Rumpf, P. Granitzer, P.M. Morales, P. Poelt, M. Reissner, *Nanoscale Res. Lett.,* 7, (2012), 2–5.

[RWJO1989] R.W. Jones, *The Institute of Metals, London*, (1989).

[SAKK1985] S. Sakka, *J. Non-Cryst. Solids.,* 73, (1985), 651.

[SARI2018] E.O. Sari, A. Fadli, A. Amri, *Jurnal. Sains. Materi. Indonesia.*, 19, (2018), 9-13.

[SEDI2022] O. Sedighi, A. Alaghmandfard, M. Montazerian, F. Baino, *J. Am. Ceram. Soc.,* 105, (2022), 1723–1747.

[SHAN2014] N. Shankhwar, R.K. Singh, G.P. Kothiyal, A. Srinivasan, *IEEE Trans. Magn.,* 50, (2014), 4003504.

[SHAN2016] N. Shankhwar, A. Srinivasan, *Mater. Sci. Eng. C.,*62, (2016), 190-196.

[SHCH2020] A. Shchelokova, V. Ivanov, A. Mikhailovskaya, E. Kretov, I. Sushkov, S. Serebryakova, E. Nenasheva, I. Melchakova, P. Belov, A. Slobozhanyuk, A. Andreychenko, *Nat. Commun.,* 11, (2020), 7395080.

[SHEA2023] A. Shearer, M. Montazerian, J.C. Mauro, *J. Non-Cryst. Solids.,* 608, (2023), 122228.

[SHEL1997] J.E. Shelby, *The Royal Society of Chemistry, Cambridge, UK*, (1997), 85404-533-3.

[SING2000] V. Singh, S.S. Yadav, V. Chauhan, S. Shukla, R. Ranjanay, K.K. Vishnolia, (2020), 221-236.

[SING2008a] R.K. Singh, G.P. Kothiyal, A. Srinivasan, *J. Non-Cryst. Solids.,* 354, (2008), 3166-3170.

[SING2008b] R.K. Singh, G.P. Kothiyal, A. Srinivasan, *J. Magn. Magn. Mater.,* 320, (2008), 1352–1356.

[SING2009] R.K. Singh, G.P. Kothiyal, A. Srinivasan, *Appl. Surf. Sci.,* 255, (2009), 6827–6831.

[SING2010] R.K. Singh, A. Srinivasan, *Ceram. Int.,* 36, (2010), 283–290.

[SIMO2004] V. Simon, D. Eniu, M. Neuman, S. Simon, *Int. J. Mod. Phys. B,* 18, (2004), 2215-2221.

[SIQU2011] R.L. Siqueira, O. Peitl, E.D. Zanotto, *Mater. Sci. Eng. C.,* 31, (2011), 983–991.

[SOET2017] F. Soetaert, S.K. Kandala, A. Bakuzis, R. Ivkov, *Sci. Rep.,*7, (2017), 1–15.

[STAN1995] H.R. Stanley, A.E. Clark, L.L. Hench, *Chapman and Hall, London,* (1995), 255-270.

[STEP2021] G. Stéphane, D. Jean-Marc, A. Frédéric S. Sophie, *Mater. Degrad.,* 5, (2021), 2397-2106.

[TAKA2004] H. Takadama, M. Hashimoto, M. Mizuno, T. Kokubo, *Phos. Res. Bull.* 17, (2004), 119-125.

[THOM2016] A. Thomas, J. Bera, *J. Sol-Gel Sci. Technol.*, 80, (2016), 411–416.

[ULLA2020] I. Ullah, W. Zhang, L. Yang, M.W. Ullah, O.M. Atta, S. Khan, B. Wu, T. Wu, X. Zhang, *Mater. Sci. Eng. C.,* 110, (2020), 110633.

[VANE2011] E. Vanea, M. Tămăşan, C. Albon, V. Simon*, J. Non. Cryst. Solids.,* 357, (2011), 3791–3796.

[VELA2019] M.V. Velasco, M.T. Souza, M.C. Crovace, A.J. Aparecido de Oliveira, E.D. Zanotto, *Biomed. Glasses.*, 5, (2019), 148–177.

[VIJA2016] S.V. Vijayasundaram, G. Suresh, R.A. Mondal, R. Kanagadurai, *J. Magn. Magn. Mater.,* 418, (2016), 30–36.

[WANG2016] R.Y. Wang, S.H. Yang, W.H. Xu, Chin. *Med. J. (Engl).,* 129, (2016), 594–600.

[WANG2019] Z. Wang, H.W. Bao, *Am. J. Transl. Res.,* 11, (2019), 4984–4991.

[WEDG1976] F.A. Wedgwood, A.C. Wright, *J. Non. Cryst. Solids.,*21, (1976), 95–105.

[WILL1986] D.F. Williams, *Proc. Consensus Conference of the European Society for Biomaterials, Elsevier, New York* (1986).

[WILS1993] J. Wilson, A. Yli-urpo, R.P. Happonen, *World scientific, London,* (1993), 63-73.

[WILS1994] J. Wilson, A.F. Clark, E. Douek, J. Kriegger, W.K. Smith, J.S. Zamet, *Butterworth-Heinemann, Oxford,* 7, (1994), 415-422.

[WLOD2022] A. Włodarczyk, S. Gorgoń, A. Radoń, K.B. Rusinek, *Nanomater.,* 12, (2022), 1–23.

[WORK2022] A.B. Workie, S.J. Shih, *RSC Adv.,* 12, (2022), 23143–23152.

[WU002015] X. Wu, G. Meng, S. Wang, F. Wu, W. Huang, Z. Gu, *Mater. Sci. Eng. C.,* 52, (2015), 242–250.

[WU002017] L. Wu, B.J.C. Luthringer, F. Feyerabend, Z. Zhang, H.G. Machens, M. Maeda, H. Taipaleenmäki, E. Hesse, R. Willumeit-Römer, A.F. Schilling, *Osteoporos. Int.,* 28, (2017), 3215–3228.

[XIAO2023] L. Xiaorui, Z. Fuyin, W. Xudong, G. Xuezheng, Z. Shudong, L. Hui, D. Dandan, L. Yubing, W. Lizhen, F. Yubo, *Int. J. Bioprinting.,* 9, (2023), 649.

[XU002019] H.S. Xu, Y.W. Yang, R.L. Wang, H.B. Xiao, L.F. Xu, S.H. Liang, et al., *Solid State Phys.,* 383, (2019), 125837.

[YADA2020] V.S. Yadav, M.R. Sankar, L.M. Pandey, *J. Magnes. Alloy.,* 8, (2020), 999-1015.

[YAMA1984] T. Yamamuro, J. Shikata, H. Okumuro, T. Kitsugi, Y. Kakutani, T. Matsui, T. Kokubo, *Cleveland: ISAO press, OH,* (1984), 810-814.

[YAMA1993] T. Yamamuro, *Wilson World Scientific, London,* (1993), 89-103.

[YANG2020] M. Yang, J. Li, Y. Man, Z. Peng, X. Zhang, X. Luo, *Mater. Des.,* 186, (2020), 108334.

[YAZD2020] A. Yazdanpanah, F. Moztarzadeh, S. Arabyazdi, *Phys. B Condens. Matter.,* 593, (2020), 412298.

[YETI2020] N.K. Yetim, F.K. Baysak, M.M. Koç, D. Nartop, *J. Mater. Sci. Mater. Electron.,*31, (2020), 18278–18288.

[YOLA2015] Y. Piñeiro, Z. Vargas, J. Rivas, M.A. López-Quintela, *Eur. J. Inorg. Chem.,* 10, (2015), 4495.

[ZELE2017] I.V. Zelepukin, V.O. Shipunova, A.B. Mirkasymov, P.I. Nikitin, M.P. Nikitin, S.M. Deyev, *Acta Naturae.,* 9, (2017), 58–65.

[ZHAN2015] M. Zhang, B. qiang Liao, X. Zhou, Y. He, H. Hong, H. Lin, *J. Chen, Bioresour. Technol.,* 175, (2015), 59–67.

[ZHAN2022] Z. Zhang, N. Zhang, X. Li, G. Li, K. Zhang, A. Jing, J. Li, H. Tang, *J. Aust. Ceram. Soc.,* 58, (2022), 1729–1745.

[ZHAO2021] Y. Zhao, Z. Zhang, Z. Pan, Y. Liu, *J. Sci. Explor.,* 1, (2021), 20210089.

Publications/Presentations

[1] **Nitu,** R. Fopase, L.M. Pandey, P. Seal, J.P. Borah, and A. Srinivasan, Assessment of sol-gel derived iron oxide substituted 45S5 bioglass-ceramics for biomedical applications, *J. Mater. Chem. B., 11*, (2023), 7502–7513. https://doi.org/10.1039/D3TB00287J.

[2] **Nitu,** and A. Srinivasan, Influence of iron oxide substitution on the magnetic interactions in sol-gel derived 45S5 bioactive glass-ceramics, *J. Am. Ceram.,* 106, (2023), 5806-5813. https://doi.org/10.1111/jace.19265.

[3] **Nitu,** R. Fopase, L.M. Pandey, and A. Srinivasan, Effect of systematic substitution of Na_2O for SiO_2 on devitrification and bioactivity of sol-gel derived 69.5SiO_2-24.5- CaO-6P_2O_5 ceramics, *Mater. Chem. Phy.,* 313, (2024), 128731. https://doi.org/10.1016/j.matchemphys.2023.12871.

[4] **Nitu,** R. Fopase, L.M. Pandey, K.P. Hazarika, J.P. Borah, R.K. Singh A. Srinivasan, Enhancement in the induction heating efficacy of sol–gel derived SiO_2-CaO-Na_2O-P_2O_5 bioglass-ceramics by incorporating magnetite nanoparticles, *J. Mater. Chem. B.,*12, (2024), 3494–3508. https://doi.org/10.1039/d3tb03014h.

[5] **Nitu,** R. Fopase, L.M. Pandey, J.P. Borah, A. Srinivasan, Enhancement of induction heating capability of bioactive SiO_2-CaO-Na_2O-P_2O_5 glass-ceramics by selective substitution with magnetite nanoparticles, *Biomed. Mater.,* 19, (2024), 045038. https://doi.org/10.1088/1748-605X/ad51c0.

[6] **Nitu,** M. Jamir, J.P. Borah, and A. Srinivasan, Impact of Iron Oxide Phases on the Magnetic Induction Heating Capacity of Mesoporous 45SiO_2-16.5CaO-24.5Na_2O-

$6P_2O_5$-$8Fe_3O_4$ Glass-Ceramics, *J. Phys. Chem. B,* 128, (2024). https://doi.org/10.1021/acs.jpcb.4c02485.

[7] **Nitu,** and A. Srinivasan, Influence of magnetite nanoparticles substitution on the magnetic interactions in sol-gel derived 45S5 bioactive glass-ceramics. (under preparation)

Presentations in conferences:

[1] **Nitu,** and A. Srinivasan, "Role of sodium oxide concentration on structure of Hench bioglass composition" International conference on advanced material and mechanical characterization (ICAMMC 2021), 2-4 December 2021, SRM Institute of Science and Technology Chennai, virtual (**Poster**).

[2] **Nitu,** and A. Srinivasan, "Self-crystallization of sol-gel derived bioglass and glass-ceramic", International conference on functional glasses/ glass-ceramic (ICFGGC 2022), 24-25 November 2022, C-MET Pune, virtual (Poster) **(Best Poster Award**).

[3] **Nitu,** J. Molongnenla, J.P. Borah and A. Srinivasan, "Influence of iron oxide phases on the magnetic and induction heating properties of sol-gel derived $45SiO_2$-$16.9CaO$-$24.5Na_2O$-$6P_2O_5$-$8Fe_3O_4$ glass-ceramic", International Conference on Magnetic Materials and Applications (ICMAGMA-2023), 4-6 December 2023, Hyderabad (**Poster**).

*****